UNIVERSITY OF CALIFORNIA SAN DIEGO

Drug Delivery, Imaging and Sensing using Porous Silicon Materials

A dissertation submitted in partial satisfaction of the requirements for the degree Doctor of Philosophy

in

Materials Science and Engineering

by

Joanna Wang

Committee in charge:

Professor Michael J. Sailor, Chair
Professor Gerald Boss, Co-Chair
Professor Karen Christman
Professor Neal Devaraj
Professor Donald Sirbuly

2019

The Dissertation of Joanna Wang is approved, and it is acceptable in quality and form for publication on microfilm and electronically:

_____

_____

_____

_____

Co-chair

_____

Chair

University of California San Diego

2019

DEDICATION

To my family and cats.

TABLE OF CONTENTS

LIST OF FIGURES

Chapter Two

Chapter Three

Chapter Four

Chapter Five

Chapter Six

Appendix A

LIST OF TABLES

Chapter Two

Chapter Three

Chapter Four

Chapter Five

Chapter Six

ACKNOWLEDGEMENTS

I would like to thank my advisor, Michael J. Sailor for being an amazing and helpful mentor who was always open to discussing new ideas or offer helpful suggestions/constructive criticism. Chatting with him about research is very intellectually stimulating, fun and impressive as he is an expert in many fields and seems to know endless facts about materials and chemistry. He set a good example of an ethical and professional scientist/researcher and treated his colleagues and mentees with respect. He is invested in me and my lab members success and gave career advice that was instrumental to helping me figure out my next steps. His passion for teaching is contagious and he encourages us to participate in scientific outreach activities both in (e.g. summer school for nanotechnology) and out of the lab. He hosts dinner parties at his house for special occasions and makes the best grilled salmon and lamp chops (the only ones I will ever eat). It has been a great pleasure to work in his lab and, as much as I am excited for my future career, I will miss the Sailor lab dearly.

I would like to thank Tushar Kumeria who is the best collaborator anyone can ask for. He is very proactive/motivated, knowledgeable and helpful in the lab and has an endless list of great ideas. His passion for science and discovery brings energy and excitement to our work. Together, we were able to complete many projects and his expertise/work ethic has been critical/instrumental to its success. Additionally, Tushar is a patient and fun collaborator/friend and contributes to a welcoming, positive and exciting lab environment/culture. I treasure our time together and hope we continue to collaborate in the future.

I would like to thank all other collaborators and lab members who helped me in my projects over the years. In particular, I want to acknowledge Emily Anglin for her mentorship when I first joined the Sailor lab. I want to thank BJ Kim, Jinyoung Kang and Hankyeol Jung for the fun times

we had together. Getting a PhD can be, at times, challenging and I am truly grateful for their friendship, patience, support and encouragement. I also want to thank the Cheng and Freeman Lab at Shiley Eye Center for collaborating on multiple projects.

Chapter 3, in full, is a reprint of the material as it appears Wang, J., Kumeria, T., Bezem, M.T., Wang, J. and Sailor, M.J. Self-reporting Porous Silicon Microparticles for Drug Delivery. Appl. Mater. Interfaces 2017, 10 (4), 3200–3209. The dissertation author was the primary investigator and author of this paper.

Chapter 4, in part is currently being prepared for submission for publication of the material. Wang, J., Warther, D., Kumeria, T., Ying, X., Huffman, K., Cheng, L., Freeman, W.R. and Sailor, M.J. Self-Reporting Porous Silicon Microparticles for Sustained Delivery of Intraocular Therapeutics. The dissertation/thesis author was the primary investigator and author of this material.

Chapter 5, in full, is a reprint of the material as it appears Wang, J., Lee, G.Y., Kennard, R.M, Barillaro, G., Bisiewicz, R.H., Cortez Lemus, N.A., Cao, X.C., Anglin, E.J., Park, J.S., Potocny, A., Bernhard, D. Li, J., and Sailor, M.J. Engineering the Properties of Polymer Photonic Crystals with Mesoporous Silicon Templates. Chem. Mater. 2017, 29 (3), 1263-1272. The dissertation author was the primary investigator and author of this paper.

Chapter 6, in full, is a reprint of the material as it appears Kumeria, T., Wang, J. (co-first author), Chan, N., Harris, T.J., and Sailor, M.J. A Visual Sensor for Alcohol Sterilization of Plastic Fixtures Using a Porous Silicon Photonic Crystal Template. ACS Sensors 2017, 3 (1), pp 143–150. The dissertation author was the primary investigator and author of this paper.

Appendix A, in part is currently being prepared for submission for publication of the material. Wang, J,. Ying, X., Huffman, K., Cheng, L., Freeman, W.R. and Sailor, M.J. Controlling

the Release of Dual-Drug Loaded Porous Silicon for Ophthalmic Combination Therapy. The dissertation/thesis author was the primary investigator and author of this material.

VITA

May 2013	Bachelor of Science Department of Materials Science and Engineering University of Illinois at Urbana-Champaign Urbana-Champaign, Illinois
June 2014	Master of Science Materials Science and Engineering Program University of California at San Diego San Diego, California
September 2019	Doctor of Philosophy Materials Science and Engineering Program University of California at San Diego San Diego, California

PUBLICATIONS

1. **Wang, J.**, Kumeria, T, Bezem, M.T, and Sailor, M.J. Self-reporting Porous Silicon Microparticles for Drug Delivery. *Appl. Mater. Interfaces* **2017,** 10 (4), 3200–3209
2. Kumeria, T., **Wang, J. (co-first author),** Chan, N. and Sailor, M.J. A Visual Sensor for Alcohol Sterilization of Plastic Fixtures Using a Porous Silicon Photonic Crystal Template. *ACS Sensors* **2017,** 3 (1), pp 143–150
3. **Wang, J.**, Lee, G.Y., Kennard, R.M, Bisiewicz, R.H., Cortez Lemus, N.A., Cao, X.C., Anglin, E.J., Park, J.S., Potocny, A., Bernhard, D. Li, J., and Sailor, M.J. Engineering the Properties of Polymer Photonic Crystals with Mesoporous Silicon Templates. *Chem. Mater.* **2017,** 29 (3), 1263-1272
4. **Wang, J.**, Joo, J., Kennard, R., Lee, S., and Sailor, M.J. Thermolytic Grafting of Polystyrene to Porous Silicon. *Chem. Mater.* **2016**, 28 (1), 79-89.
5. Zuidema, J.M., Kumeria, T., Kim, D., Kang, J., **Wang, J.**, Hollet, G.I., Zhang, X., Roberts, D., Chan, N., Dowling, C., Suarez, E.B., Allen, N.J., Tuszynski, M.H., and Sailor, M.J. Nanofibrous Tissue Scaffolds of Protein-loaded Porous Silicon in Polycaprolactone by Spray Nebulization. *Adv. Mater.* **2018**
6. Robbiano, V., Mariani,S., Iglio, R., La Mattina, A.A., Nadimi, P., Wang, J., Kim, B., Kumeria, T., Sailor, M.J., and Barillaro, G. Moldless Printing of High-Magnification Silicone Lenses With Embedded Nanostructured Optical Filters. *Submitted to Adv. Funct. Mater.*
7. **Wang, J.**, Kumeria, T., Ying, X., Li, F., Huffman, K., Zou, Y., Wang, Y., Kozake, D., Choi, S., Park, M., Choi, N.H., Cheng, L., Freeman, W.R. and Sailor, M.J. Continuous Flow Apparatus for In Vitro Release Testing of Ophthalmic Suspensions.
8. **Wang, J.**, Warther, D., Kumeria, T., Ying, X., Huffman, K., Cheng, L., Freeman, W.R. and Sailor, M.J. Self-Reporting Porous Silicon Microparticles for Sustained Delivery of Intraocular Therapeutics.
9. **Wang, J.,** Ying, X., Huffman, K., Cheng, L., Freeman, W.R. and Sailor, M.J. Controlling the Release of Dual-Drug Loaded Porous Silicon for Ophthalmic Combination Therapy.
10. Kumeria, T., **Wang, J.**, Kim, B., Park, J.H., Zuidema, J., Klempner, M., Cavacini, L., Wang, Y. and Sailor, M.J. Enteric Polymer Coated Porous Silicon Nanoparticles for Site Specific Oral Protein Delivery.
11. Kumeria, T., **Wang, J.** and Sailor, M.J. Protecting the Color of Porous Silicon Photonic Crystals through Structural Engineering.
12. Hollett G., Leonard, H., Kumeria, T., Kim, B., Martin, T., Ipekci, I., Palomba, J., **Wang, J.**, Chan, N., Pierron, A., Ayres, J., and Sailor, M.J. Longer Acting Injectables: Continuous, Linear Release of a Crystalline Contraceptive from a Porous Silicon Host.
13. Zuidema, J.M., Dumont, C.M., **Wang, J.**, Kang, J., Bertucci, A., Shea, L.D., and Sailor, M.J. Porous Silicon Loading Chemistries Protect Therapeutics Embedded in Poly(lactic-co-glycolic acid) Nanofibers to Enhance Neurite Extension.

ABSTRACT OF DISSERTATION

Drug Delivery, Imaging and Sensing using Porous Silicon Materials

By

Joanna Wang

Doctor of Philosophy in Materials Science and Engineering

University of California San Diego, 2019

Professor Michael J. Sailor, Chair
Professor Gerald Boss, Co-Chair

By leveraging its structural, chemical and photonic properties, porous silicon materials were employed to develop platform drug delivery, theranostic and sensing systems. For drug

delivery applications, oxidative and magnesium/calcium trapping strategies were investigated to physically immobilize small molecule and protein payloads within the silicon skeleton. The trapping chemistry utilized the pore volume of porous silicon for hosting payload so that high loading efficiency and near 0-order release kinetics was achieved. This strategy also alters the mechanism of payload release from diffusion to particle degradation and substantially minimizes or eliminates burst release. The intrinsic luminescence of silicon was employed as a self-reporting tool for real-time monitoring of payload release from the skeleton and activated by either thermal oxidation or aqueous aging. Correlations between pharmacokinetics and luminescence decay were demonstrated in both *in vivo* and *in vitro* studies for intraocular delivery applications.

Polymer-silicon composite photonic crystals were investigated for sensing applications by utilizing the change in structural color as a signal output. The molecular weight dependence on polymer melt infiltration into porous silicon templates enabled fabrication of free-standing polymer photonic crystals with different porosities and optical signatures. Porous silicon films were embedded into polymer catheter devices as sterilization sensors using simple manufacturing methods. Bacteria testing revealed that by wiping the tip of the catheter hub with an alcohol swab and upon observing a complete color change from green to red (and back to green) the catheter device was sterile and confirmed the sensing ability of the porous silicon film.

CHAPTER ONE

Introduction

1.1 Using Materials to Improve Therapies

Complex formulations that combines materials science, chemistry and physics has created a new paradigm to traditional molecular medicine in improving therapeutic and diagnostic systems. The first example began with iron oxide nanoparticles for managing anemia in the 40-50s.[1] Iron was administered parenterally to humans in the 30-40s in the form of a salt in attempts to elevate hemoglobin levels in the blood and caused severe acute toxicity.[2-3] To mitigate flocculation of iron in the blood, the first complex formulation was fabricated by simply encapsulating the iron salt in carbohydrate.[4-5] The carbohydrate coating reduced aggregation of colloidal iron and in turn significantly improved its safety profile and increased the maximum tolerated dose. This formulation made a lasting significance as its improved forms are still used in the clinic today[1, 6] and introduced the concept that, instead of finding an alternative therapy or performing molecular modifications, existing therapeutics can be combined with materials to have significantly better biological properties. Now, materials are employed to "deliver" therapeutics and improve properties including pharmacokinetics/dynamics, biocompatibility, bioavailability, biodistribution and this concept has also been applied to other types of clinical applications such as imaging and diagnostics.[7-8]

1.2 Porous Silicon as a Drug Delivery and Imaging Material

Many different classes of materials are employed as carriers for drug delivery applications including polymers,[9-11] dendrimers,[12-14] porous systems (silica,[15-17] silicon[18-19] and other inorganics[20-21]), carbon nanotubes,[22-23] liposomes[24-26]/membranes[27] and viral vectors[28-29] and each system has its unique strength and limitations. This thesis focuses on leveraging the chemical, structural and photonic properties of porous silicon materials for long-term drug delivery, theranostic and sensing applications. Porous silicon has been employed in many biological

applications due its biodegradability[30] and biocompatibility[31-32] and has an excellent safety profile[33] which is partially owed to the fact that is the 15th most abundant element in the body and accounts for 0.001% of a person's mass.[34-35] In biological environments, silicon oxidizes and dissolves into silicic acid,[36-37] which can then be excreted from the body.

The high surface area structure of silicon has enabled it to act as a sponge for concentrating and hosting therapeutic cargo.[19] Additionally, its fabrication process allows it to take different forms and size such as films, ribbons,[38] micro-particles and nanoparticles. During the 2-electron electrochemical etching process in ethanolic HF (Equation 1.1), silicon selectively dissolves in the <100> direction and generates pores that perpendicular to the wafer face.[39-41]

$$Si + 6F^- + 2H^+ + 2h^+ \rightarrow SiF_6^{2-} + H_2 \qquad (1.1)$$

The instantaneous porosity and pore size that is formed during the etch is determined by the applied current so that complex structures could be formed. The silicon film can be removed by electropolishing in the using the 4-electron oxidation reaction (Equation 1.2) where the bulk-to-porous silicon interface is dissolved in its entirety and without forming pores.

$$Si + 6F^- + 4h^+ \rightarrow SiF_6^{2-} \qquad (1.1)$$

These films can be employed as implants or broken up into micro/nanoparticles for injectable delivery vehicles for depot or targeted delivery.

Compared to other systems, porous silicon has unique and versatile chemistries that enables it to carry many classes of payloads and at high loading effieicneis.[19, 42] Additionally, these

chemistries play a significant role in defining the pharmacokinetics for the formulation. The most basic method of loading is adsorption loading, where molecules adhere to the surface of the skeleton due to electrostatic interactions. Because most of the area resides on the interior of the particle or film, the payload is protected from the harsh environment of its surroundings. While silicon is hydrophobic immediately after functionalization, it readily oxidizes in air or buffer to become hydrophilic. Additionally, it is relatively unstable and degrades quickly, which is not desirable for long-term applications. For adsorption loading purposes, the silicon surface is typically modified by thermal oxidation, carbonization,[43] hydrosilylation and silane chemistries[44] to convert the surface of the silicon surface to hydrophobic or charged surfaces[45] and improve payload adhesion and particle stability (for sustained release applications). In Chapter 4, alkoxy silane functionalization was employed for the loading a hydrophobic small molecule drug, triamcinolone acetonide, for ophthalmic therapeutics. A particular highlight in the field is functionalization with heterocyclic silanes.[46] These molecules react with hydroxylate surface groups on the silicon surface by an ring-opening click reaction without the production of any byproduct. Additionally, these simple reactions occur under mild conditions, short times (1-2hrs) and common organic solvents (e.g. dichloromethane) and achieve high yield. These grafting chemistries also cover the surface with functional groups (e.g. primary amines) that can undergo further modifications to graft targeting peptides or PEG groups for long circulation of nanoparticles. In Appendix A, primary amines were grafted to silicon using alkoxy silanes and was further modified using EDC/NHS and DIC/DMAP chemistries to covalently graft two drugs, daunorubicin and dexamethasone onto porous silicon for combination therapy. Due to the strong bond to the particles, sustained release of therapeutic concentrations of each drug was achieved.

Recently, new forms of drug loading have been developed to achieve near 0-order release profile of drug. This is especially ideal for sustained release because it allows therapeutic concentrations to be delivered at long time-scales while preventing burst release, which may cause side effects, and the long "tail" where drug concentration is still detected but is below the therapeutic limit. Trapping chemistries, discussed in Chapter 2, allows therapeutics to be physically immobilized within the particles by pore swelling during oxidation of the silicon skeleton[47] or formation of an inorganic precipitate.[48-49] These chemistries allow high loading efficiency of payloads including small molecules, protein, and oligonucleotides. Because the payloads are physically trapped, they are immobilized until degradation of the silicon skeleton. The presumed degradation mechanism of porous silicon particles is by thinning of the disk so that the exposed surface area remains relatively constant over time and, by using trapping chemistries, enables the release profile to more closely resemble 0-order pharmacokinetics.

Trapping mechanism is especially advantageous when loading proteins. Protein based molecules such as enzymes or antibodies have posed a delivery challenge for many systems because they denature in organic solvents and cannot be easily formulated. In the case of silicon, proteins are excellent payloads because they are made up of amino acids and rich in amine groups, which are known to facilitate the degradation silicon and reprecipitation of silicic acid into silica. As a result, proteins tend naturally "self-trap" and have high loading efficiencies in silicon and sustained release profile. The inorganic nature of silicon also protects the protein so that it maintains activity even when soaked in harsh environments (e.g. organic solvents).[50]

Lastly, melt-infiltration has enabled high loading efficiencies of small molecule hydrophobic drugs and long-term sustained release.[51] Like the trapping mechanism, melt loading utilizes the pore volume in its entirety rather than only its surface and, due to the anisotropic

degradation mechanism of the pSi particles, maintain therapeutic concentrations of drug for long times.

1.3 Theranostic Systems

Theranostic models combine both therapeutic and imaging modalities into a single system enabling patients to undergo fewer procedures while maximizing the benefits and patient disease information.[52-53] While theranostic systems are exciting, like many multiplex or multimodality systems, it is important to consider the benefits carefully. For certain systems the optimal dosage and conditions for each modality is different and combining them may inevitably compromise the effectiveness of one or both modes and limiting its benefits. Additionally, for many diagnostic systems, the constraints for toxicity are much more stringent and rigid. Taking all these considerations into account, theranostic systems may be the more beneficial in cases where the patient has already been diagnosed with a disease and where the imaging element informs on the treatment progress or patient response. Lastly, a platform system that can combine an imaging system with the desired therapeutic is desirable for treating different types of diseases.

Porous silicon is an excellent material for designing theranostic systems because the skeleton itself can display luminescence in the visible-NIR range. Its luminescence property does not alter the biodegradability of the particles or require any additional additives or complex processing.[54] The luminescence of silicon comes from quantum confinement of the skeleton[55] after thinning the silicon walls by oxidation or matrix dissolution.[56-60] By tuning the particle luminescence to the red-NIR range, silicon can overcome a major limitation of many fluorescent probes and be easily detected within optical window in vivo, which has minimal absorption.[61] Additionally, as the particles degrade, emitting centers are dissolved and the silicon walls becomes narrower so that the luminescence spectra blue shifts and decreases in intensity.[60, 62-65] Using this

property, the luminescence of the particles can conveniently "self-report" or provide feedback signal that informs its degradation by fluorescence imaging.[54] A major thrust of this thesis (Chapter 3-4) utilizes the change in luminescence signature to indirectly monitor the release of a payload in vitro and in vivo. These self-reporting formulations allow physicians to probe the real-time pharmacokinetics of the therapeutic so that they can customize treatment plans to individual patients.

The indirect bandgap of silicon allows it to have a long radiative lifetime on the order of 1-100μs.[32] This property allows silicon to have a unique imaging advantage because it can blank out tissue autofluorescence and most background signals under time-resolved conditions, where fluorescence signal is collected nano-microseconds after a pulsed excitation light is turned off.[66-67] Using time-gated imaging, a signal to noise ratio of >100 fold has been reported, making silicon an excellent fluorescence contrast agent. The lifetime of silicon is dependent on the wavelength of the emission where higher energy emitters have shorter lifetimes. Consequently, the overall luminescent lifetime decreases as the particles degrades so that the fate of particles could be tracked in vivo.[68]

1.4 Composites

Composites consisting of porous silicon and polymers has enabled applications requiring more complex, flexible or robust structures.[69-70] For example, porous silicon particles have been encapsulated in oriented polymer fiber scaffolds for directed neural growth and repair.[50] The particles were able to protect sensitive growth factors from denaturing during the scaffold formulation process in organic solvent and delivering the proteins to neurons. While composites provide improved stability and functionality to porous silicon systems, the parameters governing composite material synthesis is not well studied. In Chapter 5 of this thesis, properties of polymer

flow into porous silicon was investigated as a function of molecular weight and monitored using the photonic properties of silicon films. In chapter 6, porous silicon photonic crystals were incorporated into polymer catheter hubs as simple color change sterilization sensors.

1.5 Looking to the Future

There are many more exciting advances within the drug delivery, theranostic and sensing field to be investigated using porous silicon. Based on the work of this thesis, the author lists a few potential directions. Self-reporting has primary been investigated in intraocular therapeutics but can still be explored for other tissues delivery systems including subcutaneous, intramuscular and intestinal (using a probe), The luminescence of silicon can be further exploited for more uses other than self-reporting such as triggering the release of a payload, BRET by blue luciferase trapping, in vivo diagnostic, cell tracking studies.

1.6 References

1. Macdougall, I. C., EVOLUTION OF IV IRON COMPOUNDS OVER THE LAST CENTURY. *Journal of Renal Care* **2009,** *35* (s2), 8-13.

2. Heath, C. W.; Strauss, M. B.; Castle, W. B., QUANTITATIVE ASPECTS OF IRON DEFICIENCY IN HYPOCHROMIC ANEMIA: (The Parenteral Administration of Iron). *The Journal of clinical investigation* **1932,** *11* (6), 1293-1312.

3. Goetsch, A. T.; Moore, C. V.; Minnich, V., OBSERVATIONS ON THE EFFECT OF MASSIVE DOSES OF IRON GIVEN INTRAVENOUSLY TO PATIENTS WITH HYPOCHROMIC ANEMIA. *Blood* **1946,** *1* (2), 129.

4. Nissim, J., INTRAVENOUS ADMINISTRATION OF IRON. *The Lancet* **1947,** *250* (6463), 49-51.

5. McLean Baird, I.; Podmore, D. A., INTRAMUSCULAR IRON THERAPY IN IRON-DEFICIENCY ANÆMIA. *The Lancet* **1954,** *264* (6845), 942-946.

6. Coyne, D. W.; Auerbach, M., Anemia management in chronic kidney disease: Intravenous iron steps forward. *American Journal of Hematology* **2010,** *85* (5), 311-312.

7. Allen, T. M.; Cullis, P. R., Drug delivery systems: entering the mainstream. *Science* **2004,** *303* (5665), 1818-1822.

8. Langer, R., Drug delivery and targeting. *NATURE-LONDON*- **1998**, 5-10.

9. Mora-Huertas, C. E.; Fessi, H.; Elaissari, A., Polymer-based nanocapsules for drug delivery. *International Journal of Pharmaceutics* **2010,** *385* (1), 113-142.

10. Liechty, W. B.; Kryscio, D. R.; Slaughter, B. V.; Peppas, N. A., Polymers for drug delivery systems. *Annu Rev Chem Biomol Eng* **2010,** *1*, 149-173.

11. Hoare, T. R.; Kohane, D. S., Hydrogels in drug delivery: Progress and challenges. *Polymer* **2008,** *49* (8), 1993-2007.

12. Esfand, R.; Tomalia, D. A., Poly(amidoamine) (PAMAM) dendrimers: from biomimicry to drug delivery and biomedical applications. *Drug Discovery Today* **2001,** *6* (8), 427-436.

13. Svenson, S., Dendrimers as versatile platform in drug delivery applications. *European Journal of Pharmaceutics and Biopharmaceutics* **2009,** *71* (3), 445-462.

14. Gillies, E. R.; Fréchet, J. M. J., Dendrimers and dendritic polymers in drug delivery. *Drug Discovery Today* **2005,** *10* (1), 35-43.

15. Barbé, C.; Bartlett, J.; Kong, L.; Finnie, K.; Lin, H. Q.; Larkin, M.; Calleja, S.; Bush, A.; Calleja, G., Silica Particles: A Novel Drug-Delivery System. *Advanced Materials* **2004,** *16* (21), 1959-1966.

16. Lu, J.; Liong, M.; Li, Z.; Zink, J. I.; Tamanoi, F., Biocompatibility, biodistribution, and drug-delivery efficiency of mesoporous silica nanoparticles for cancer therapy in animals. *Small (Weinheim an der Bergstrasse, Germany)* **2010,** *6* (16), 1794-805.

17. Slowing, I. I.; Vivero-Escoto, J. L.; Wu, C.-W.; Lin, V. S. Y., Mesoporous silica nanoparticles as controlled release drug delivery and gene transfection carriers. *Advanced Drug Delivery Reviews* **2008,** *60* (11), 1278-1288.

18. Salonen, J.; Laitinen, L.; Kaukonen, A. M.; Tuura, J.; Björkqvist, M.; Heikkilä, T.; Vähä-Heikkilä, K.; Hirvonen, J.; Lehto, V. P., Mesoporous silicon microparticles for oral drug delivery: Loading and release of five model drugs. *Journal of Controlled Release* **2005,** *108* (2), 362-374.

19. Anglin, E. J.; Cheng, L.; Freeman, W. R.; Sailor, M. J., Porous silicon in drug delivery devices and materials. *Advanced Drug Delivery Reviews* **2008,** *60* (11), 1266-1277.

20. Horcajada, P.; Chalati, T.; Serre, C.; Gillet, B.; Sebrie, C.; Baati, T.; Eubank, J. F.; Heurtaux, D.; Clayette, P.; Kreuz, C.; Chang, J.-S.; Hwang, Y. K.; Marsaud, V.; Bories, P.-N.; Cynober, L.; Gil, S.; Férey, G.; Couvreur, P.; Gref, R., Porous metal–organic-framework nanoscale carriers as a potential platform for drug delivery and imaging. *Nature Materials* **2009,** *9*, 172.

21. Gultepe, E.; Nagesha, D.; Sridhar, S.; Amiji, M., Nanoporous inorganic membranes or coatings for sustained drug delivery in implantable devices. *Advanced Drug Delivery Reviews* **2010,** *62* (3), 305-315.

22. Bianco, A.; Kostarelos, K.; Prato, M., Applications of carbon nanotubes in drug delivery. *Current Opinion in Chemical Biology* **2005,** *9* (6), 674-679.

23. Liu, Z.; Chen, K.; Davis, C.; Sherlock, S.; Cao, Q.; Chen, X.; Dai, H., Drug delivery with carbon nanotubes for in vivo cancer treatment. *Cancer Res* **2008,** *68* (16), 6652-6660.

24. Anselmo, A. C.; Mitragotri, S., Nanoparticles in the clinic. *Bioeng Transl Med* **2016,** *1* (1), 10-29.

25. Sharma, A.; Sharma, U. S., Liposomes in drug delivery: progress and limitations. *International journal of pharmaceutics* **1997,** *154* (2), 123-140.

26. Allen, T. M.; Cullis, P. R., Liposomal drug delivery systems: from concept to clinical applications. *Advanced drug delivery reviews* **2013,** *65* (1), 36-48.

27. Thanuja, M. Y.; Anupama, C.; Ranganath, S. H., Bioengineered cellular and cell membrane-derived vehicles for actively targeted drug delivery: So near and yet so far. *Advanced Drug Delivery Reviews* **2018,** *132*, 57-80.

28. Muzyczka, N., Use of Adeno-Associated Virus as a General Transduction Vector for Mammalian Cells. In *Viral Expression Vectors*, Muzyczka, N., Ed. Springer Berlin Heidelberg: Berlin, Heidelberg, 1992; pp 97-129.

29. Daya, S.; Berns, K. I., Gene Therapy Using Adeno-Associated Virus Vectors. *Clinical Microbiology Reviews* **2008,** *21* (4), 583.

30. Shabir, Q., Biodegradability of Porous Silicon. In *Handbook of Porous Silicon*, Canham, L., Ed. Springer International Publishing: Cham, 2014; pp 395-401.

31. Low, S. P.; Voelcker, N. H., Biocompatibility of porous silicon. *Handbook of Porous Silicon* **2014**, 381-393.

32. Low, S. P.; Voelcker, N. H.; Canham, L. T.; Williams, K. A., The biocompatibility of porous silicon in tissues of the eye. *Biomaterials* **2009,** *30* (15), 2873-2880.

33. Tanaka, T.; Godin, B.; Bhavane, R.; Nieves-Alicea, R.; Gu, J.; Liu, X.; Chiappini, C.; Fakhoury, J. R.; Amra, S.; Ewing, A.; Li, Q.; Fidler, I. J.; Ferrari, M., In vivo evaluation of safety of nanoporous silicon carriers following single and multiple dose intravenous administrations in mice. *International journal of pharmaceutics* **2010,** *402* (1-2), 190-197.

34. Emsley, J., *Nature's Building Blocks: An A-Z Guide to the Elements*. Oxford University Press: 2001.

35. Jugdaohsingh, R., Silicon and bone health. *The journal of nutrition, health & aging* **2007,** *11* (2), 99-110.

36. Canham, L. T., Bioactive silicon structure fabrication through nanoetching techniques. *Advanced Materials* **1995,** *7* (12), 1033-1037.

37. Anderson, S.; Elliott, H.; Wallis, D.; Canham, L.; Powell, J., Dissolution of different forms of partially porous silicon wafers under simulated physiological conditions. *physica status solidi (a)* **2003,** *197* (2), 331-335.

38. Pérez, K. S.; Warther, D.; Calixto, M. E.; Méndez-Blas, A.; Sailor, M. J., Harnessing the Aqueous Chemistry of Silicon: Self-Assembling Porous Silicon/Silica Microribbons. *ACS Applied Materials & Interfaces* **2019,** *11* (30), 27162-27169.

39. Loni, A., Porous Silicon Formation by Anodization. In *Handbook of Porous Silicon*, Canham, L., Ed. Springer International Publishing: Cham, 2018; pp 13-24.

40. Uhlir Jr, A., Electrolytic Shaping of Germanium and Silicon. *Bell System Technical Journal* **1956,** *35* (2), 333-347.

41. Unagami, T., Formation mechanism of porous silicon layer by anodization in HF solution. *Journal of the electrochemical society* **1980,** *127* (2), 476-483.

42. Salonen, J.; Kaukonen, A. M.; Hirvonen, J.; Lehto, V.-P., Mesoporous silicon in drug delivery applications. *Journal of pharmaceutical sciences* **2008,** *97* (2), 632-653.

43. Mäkilä, E.; Kivelä, H.; Shrestha, N.; Correia, A.; Kaasalainen, M.; Kukk, E.; Hirvonen, J.; Santos, H. A.; Salonen, J., Influence of Surface Chemistry on Ibuprofen Adsorption and Confinement in Mesoporous Silicon Microparticles. *Langmuir* **2016,** *32* (49), 13020-13029.

44. Kim, D.; Joo, J.; Pan, Y.; Boarino, A.; Jun, Y. W.; Ahn, K. H.; Arkles, B.; Sailor, M. J., Thermally Induced Silane Dehydrocoupling on Silicon Nanostructures. *Angew Chem Int Ed Engl* **2016,** *55* (22), 6423-6427.

45. Tieu, T.; Dhawan, S.; Haridas, V.; Butler, L. M.; Thissen, H.; Cifuentes-Rius, A.; Voelcker, N. H., Maximizing RNA Loading for Gene Silencing Using Porous Silicon Nanoparticles. *ACS Applied Materials & Interfaces* **2019,** *11* (26), 22993-23005.

46. Kim, D.; Zuidema, J. M.; Kang, J.; Pan, Y.; Wu, L.; Warther, D.; Arkles, B.; Sailor, M. J., Facile Surface Modification of Hydroxylated Silicon Nanostructures Using Heterocyclic Silanes. *Journal of the American Chemical Society* **2016,** *138* (46), 15106-15109.

47. Fry, N. L.; Boss, G. R.; Sailor, M. J., Oxidation-Induced Trapping of Drugs in Porous Silicon Microparticles. *Chem Mater* **2014,** *26* (8), 2758-2764.

48. Kang, J.; Joo, J.; Kwon, E. J.; Skalak, M.; Hussain, S.; She, Z.-G.; Ruoslahti, E.; Bhatia, S. N.; Sailor, M. J., Self-Sealing Porous Silicon-Calcium Silicate Core–Shell Nanoparticles for Targeted siRNA Delivery to the Injured Brain. *Advanced Materials* **2016,** *28* (36), 7962-7969.

49. Wang, J.; Kumeria, T.; Bezem, M. T.; Wang, J.; Sailor, M. J., Self-Reporting Photoluminescent Porous Silicon Microparticles for Drug Delivery. *ACS applied materials & interfaces* **2018,** *10* (4), 3200-3209.

50. Zuidema, J. M.; Kumeria, T.; Kim, D.; Kang, J.; Wang, J.; Hollett, G.; Zhang, X.; Roberts, D. S.; Chan, N.; Dowling, C.; Blanco-Suarez, E.; Allen, N. J.; Tuszynski, M. H.; Sailor, M. J., Oriented Nanofibrous Polymer Scaffolds Containing Protein-Loaded Porous Silicon Generated by Spray Nebulization. *Advanced Materials* **2018,** *30* (12), 1706785.

51. Wang, M.; Coffer, J. L.; Dorraj, K.; Hartman, P. S.; Loni, A.; Canham, L. T., Sustained antibacterial activity from triclosan-loaded nanostructured mesoporous silicon. *Molecular pharmaceutics* **2010,** *7* (6), 2232-2239.

52. Kelkar, S. S.; Reineke, T. M., Theranostics: Combining Imaging and Therapy. *Bioconjugate Chemistry* **2011,** *22* (10), 1879-1903.

53. Sharma, R.; Mody, N.; Agrawal, U.; Vyas, S. P., Theranostic Nanomedicine; A Next Generation Platform for Cancer Diagnosis and Therapy. *Mini reviews in medicinal chemistry* **2017,** *17* (18), 1746-1757.

54. Park, J.-H.; Gu, L.; von Maltzahn, G.; Ruoslahti, E.; Bhatia, S. N.; Sailor, M. J., Biodegradable luminescent porous silicon nanoparticles for in vivo applications. *Nature materials* **2009,** *8* (4), 331-336.

55. Cullis, A. G.; Canham, L. T.; Calcott, P. D. J., The structural and luminescence properties of porous silicon. *J. Appl. Phys.* **1997,** *82* (3), 909-965.

56. Petrova-Koch, V.; Muschik, T.; Kux, A.; Meyer, B. K.; Koch, F.; Lehmann, V., Rapid thermal oxidized porous Si- the superior photoluminescent Si. *Appl. Phys. Lett.* **1992,** *61* (8), 943-945.

57. Gelloz, B.; Koshida, N., Highly enhanced photoluminescence of as-anodized and electrochemically oxidized nanocrystalline p-type porous silicon treated by high-pressure water vapor annealing. *Thin Solid Films* **2006,** *508* (1-2), 406-409.

58. Ray, M.; Sarkar, S.; Bandyopadhyay, N. R.; Hossain, S. M.; Pramanick, A. K., Silicon and silicon oxide core-shell nanoparticles: Structural and photoluminescence characteristics. *J. Appl. Phys.* **2009,** *105* (7).

59. McInnes, S. J. P.; Voelcker, N. H., Silicon-polymer hybrid materials for drug delivery. *Future Med. Chem.* **2009,** *1* (6), 1051-1074.

60. Joo, J.; Cruz, J. F.; Vijayakumar, S.; Grondek, J.; Sailor, M. J., Photoluminescent Porous Si/SiO2 Core/Shell Nanoparticles Prepared by Borate Oxidation. *Adv. Funct. Mater.* **2014,** *24*, 5688-5694.

61. Park, J.-H.; Gu, L.; Maltzahn, G. v.; Ruoslahti, E.; Bhatia, S. N.; Sailor, M. J., Biodegradable luminescent porous silicon nanoparticles for in vivo applications. *Nat. Mater.* **2009,** *8*, 331-336.

62. Wolkin, M. V.; Jorne, J.; Fauchet, P. M.; Allan, G.; Delerue, C., Electronic states and luminescence in porous silicon quantum dots: The role of oxygen. *Phys. Rev. Lett.* **1999,** *82* (1), 197-200.

63. Sa'ar, A., Photoluminescence from silicon nanostructures: The mutual role of quantum confinement and surface chemistry. *J. Nanophotonics* **2009,** *3*, 032501.

64. Wilson, W. L.; Szajowski, P. F.; Brus, L. E., Quantum Confinement in Size Selected, Surface-Oxidized Si Nanocrystals. *Science* **1993,** *262*, 1242-1244.

65. Zacharias, M.; Heitmann, J.; Scholz, R.; Kahler, U.; Schmidt, M.; Blasing, J., Size-controlled highly luminescent silicon nanocrystals: A SiO/SiO2 superlattice approach. *Appl. Phys. Lett.* **2002,** *80* (4), 661-663.

66. Gu, L.; Hall, D. J.; Qin, Z.; Anglin, E.; Joo, J.; Mooney, D. J.; Howell, S. B.; Sailor, M. J., In vivo time-gated fluorescence imaging with biodegradable luminescent porous silicon nanoparticles. *Nature Communications* **2013,** *4*, 2326.

67. Joo, J.; Liu, X.; Kotamraju, V. R.; Ruoslahti, E.; Nam, Y.; Sailor, M. J., Gated Luminescence Imaging of Silicon Nanoparticles. *ACS Nano* **2015,** *9* (6), 6233-6241.

68. Jin, Y.; Kim, D.; Roh, H.; Kim, S.; Hussain, S.; Kang, J.; Pack, C.-G.; Kim, J. K.; Myung, S.-J.; Ruoslahti, E.; Sailor, M. J.; Kim, S. C.; Joo, J., Tracking the Fate of Porous Silicon Nanoparticles Delivering a Peptide Payload by Intrinsic Photoluminescence Lifetime. *Adv Mater* **2018,** *30* (35), e1802878-e1802878.

69. Bonanno, L. M.; Segal, E., Nanostructured porous silicon-polymer-based hybrids: from biosensing to drug delivery. *Nanomedicine (London, England)* **2011,** *6* (10), 1755-70.

70. Li, Y. Y.; Cunin, F.; Link, J. R.; Gao, T.; Betts, R. E.; Reiver, S. H.; Chin, V.; Bhatia, S. N.; Sailor, M. J., Polymer Replicas of Photonic Porous Silicon for Sensing and Drug Delivery Applications. *Science* **2003,** *299* (5615), 2045.

CHAPTER TWO

Chemistries for Payload Loading in Porous Silicon Microparticles

2.1 Introduction

Sustained release system has provided a new way of delivering therapeutics in for a wide range of clinical applications[1] such as cardiovascular conditions,[2] asthma,[3] eye disease[4] and birth control.[5-6] For most of these applications, the drug concentration within the patient needs to be maintained within a "therapeutic window" to continuous provide the benefits of the therapeutic over long time scales.[7-8] If the concentration exceeds the "maximum tolerated dose", the patient may experience severe toxicity and side effects. Below the "therapeutic limit" the drug does not provide therapeutic benefit to the patient. To maintain therapeutic concentrations, many complex formulations have been developed including hydrophobic small molecule crystals, polymer-drug composites, etc. to enable long-term drug delivery to the desired tissue.

Due to its versatile surface chemistry and pore morphology, porous silicon particles have been employed as a platform sustained delivery system[9-11] to host many different types of payloads including small molecule, oligo nucleotide,[12-14] proteins and peptides. For most of these payloads, the dominate mechanism of loading is by adsorption following diffusion into the pores.[11] Consequently, like mesoporous silica, a major limitation of the porous silicon delivery system is high burst release in initial time points. To encourage adsorption and increase electrostatic interaction, many surface chemistries[15-16] have been employed to convert the pore surface to the desired charge or hydrophobicity. While these chemistries improve the pharmacokinetics, the mechanism of payload adsorption and diffusion remains the same and, as a result, the release profile typically still includes a strong burst followed by steady state release.

Instead of improving electrostatic interactions, a major thrust of this work seeks to change the paradigm of the loading chemistry so that the mechanism of payload release is no longer based on diffusion but particle degradation. Because porous silicon particles are in the shape of a disc,

the degradation is presumably anisotropic so that the particle becomes thinner overtime while the planer dimensions remains the same. As a result, the exposed surface area is relatively consistent overtime and enables a near 0-order pharmacokinetics. This provides substantial pharmacokinetic advantage because the drug concentration can be tuned by the dosage and maintained within the therapeutic window for long time scales. At the end of the release, the anisotropic degradation profile causes the entire particle to disintegrate quickly and minimizes the "tail", where drug is still being released from the formulation, but the concentration falls below the therapeutic limit. As a result, this delivery system can prevent side effects from residue drug concentrations or toxicity from high drug concentrations following another therapeutic dosage.

Two major types of loading chemistries explored in this work include trapping and covalent grafting. Trapping chemistries involve immobilizing the particles within the pores by inducing pore shrinkage after the payload is loaded.[17-18] These chemistries are mainly performed in aqueous environments and employed to load most classes of payloads besides for hydrophobic small molecule drugs. In the second method (see Appendix A), covalent grafting was explored to load multiple types of small molecule therapeutics within the same particle for combination therapy.

2.2 Oxidative Trapping using Aqueous Buffers

2.2.1 Background

Porous silicon readily oxidizes in aqueous environments to form a hydrated oxide shell. Unlike thermal oxidation, the hydrated oxide, which occurs due to a combination of oxygen diffusion into the skeleton and reprecipitation of SiO_2, causes the silicon walls to swell and the pores to shrink substantially. Previous work has leveraged oxidative trapping using nitride to physically trap rhodamine B and cobinamide, a small molecule derived from vitamin B 12, into microporous silicon.[17] By doing so, more sustained release was observed. While this method works

well for small molecules that are not sensitive to nitrite, the solvent conditions may cause denaturation for more sensitive and larger molecules such as proteins.

In this work, we explored changes in pore size following soaking in buffered solution. We then tested whether this would allow encapsulation of enzymes that can turn over substrate to produce bioluminescence. We use bioluminescence and this trapping method as a means for probing protein activity within the silicon skeleton and potential for imaging and cell assay applications.

2.2.2 Porous Silicon Synthesis

Porous silicon was synthesized from electrochemical etching of single crystalline silicon wafers (Virginia Semiconductors, polished on the (100) face, boron-doped (p-type), resistivity < 1.5 mΩ•cm). The etch was performed under ethanolic HF (3:1 HF to ethanol) under a constant current supply of 70 mA/cm^2 for 600 s. Porous silicon films were removed from the bulk Si wafer by an electropolishing step with 3.33% HF (diluted in ethanol) under a constant current supply of 8 mA/cm^2 for 300 s. The porous silicon films were sonicated in ethanol for 10 minutes to yield particles of between 10-100 μm.

2.2.3 Skeleton Wall Swelling by Oxidation and Silica Reprecipitation in Buffers

To test if there is a significant reduction in pore size for payload trapping, porous silicon chips and particles were soaked in Tris buffered saline for 24 hrs and washed 3 times with ethanol. The chips before and after oxidation were imaged under a scanning electron microscope (SEM) after sputtering with iridium (Denton Desk IV Sputter Coater) for 4s. The pore size, surface area, and volume were quantified for pSi particles before and after oxidation with nitrogen absorption (5 point analysis, Micromeritics ASAP2020).

The imaging results with SEM shows significant pore shrinkage and appears to have reprecipitation of SiO_2 (Figure 2.2.1). The pore shrinkage is validated with nitrogen absorption measurements, which revealed that the pore size and volume shrank by ~50% and thus shows the potential of trapping (Figure 2.2.2, Table 2.2.1). It's important to note that the particles were oxidized in tris buffer, which is composed of amine-based molecules and known to accelerate the degradation and reprecipitation of SiO_2. While oxidative trapping has been previously demonstrated with nitride, trapping by using biocompatible and biologically friendly solutions such as TBS is advantageous because it enables the stabilization of sensitive payloads such as enzymes and antibodies. Additionally, due to the non-toxic nature of buffers, an optimized process with high loading efficiency will eliminate the need for wash steps to ensure removal of organic solvents commonly employed for small molecule loading.

(a)

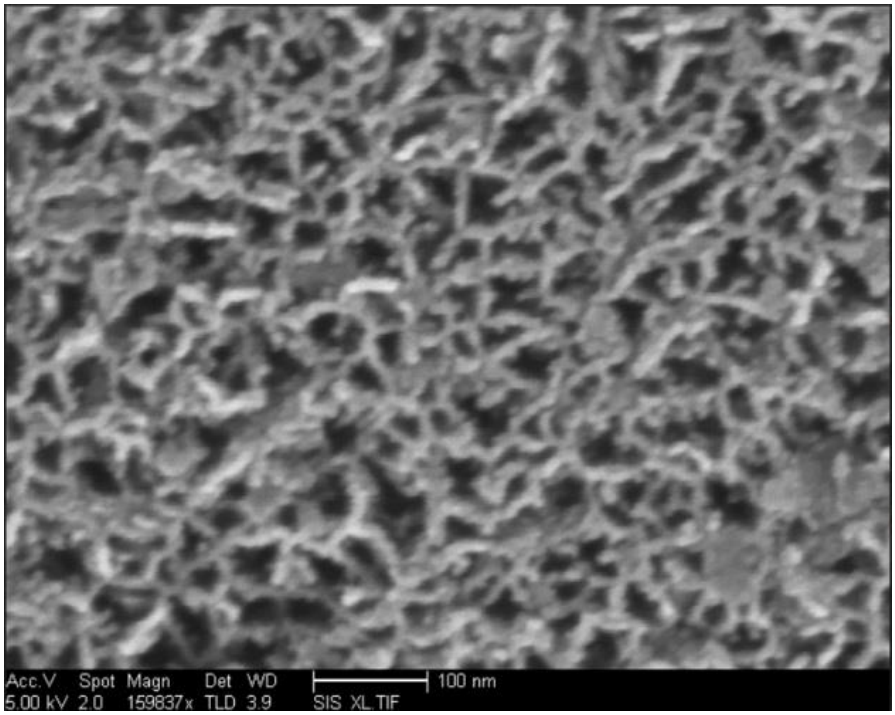

(b)

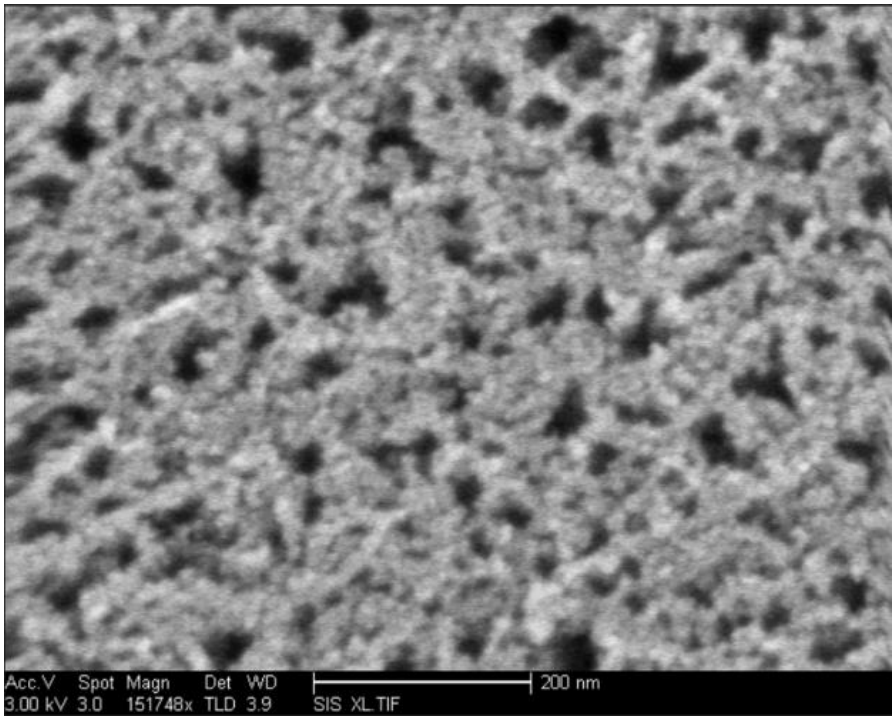

Figure 2.2.1. The scanning electron images of porous silicon chips (a) before and (b) after soaking in Tris buffered saline for 24 hrs. After soaking, obvious pore shrinkage and skeleton wall swelling is be observed.

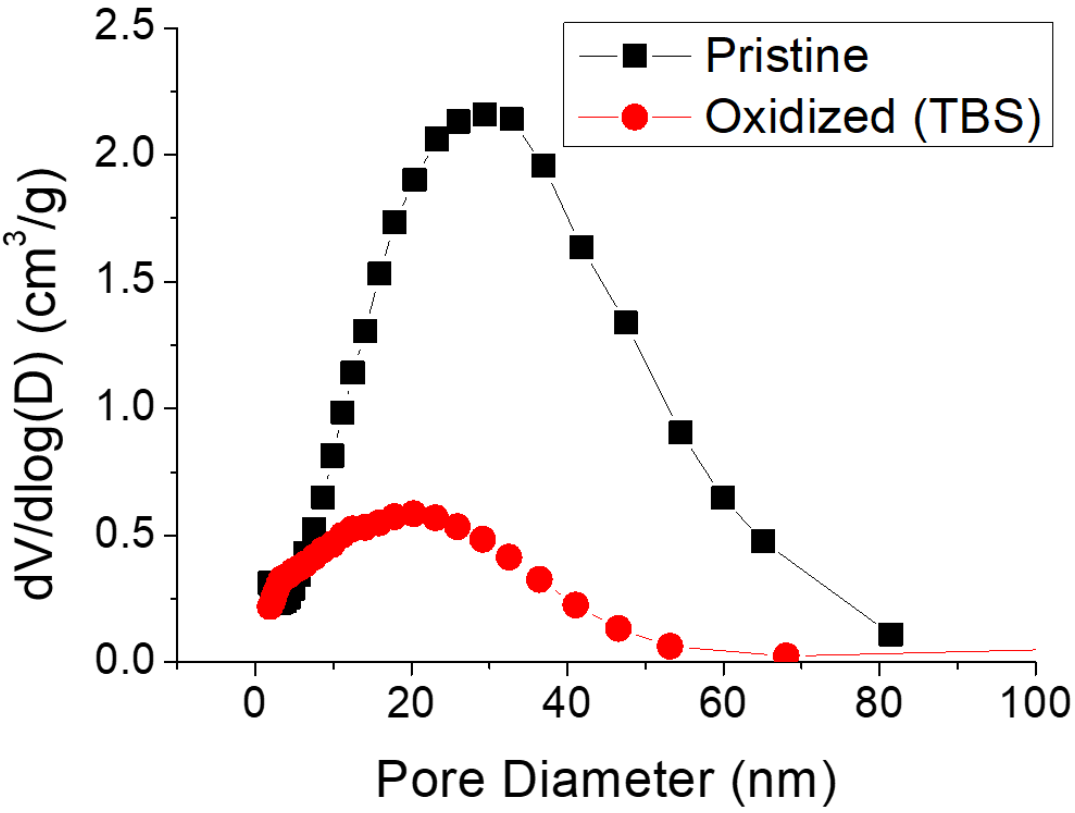

Figure 2.2.2. The pore volume versus pore diameter plot following the BJH approximation of the nitrogen adsorption isotherms. After oxidizing in Tris buffer, significant decrease in pore volume and diameter is observed.

Table 2.2.1. The summary of surface area, pore diameter and volume of porous silicon particles characterized by nitrogen adsorption.

	Pristine	**TBS Oxidation**
[a]**BET Surface Area**	526 m^2/g	399 m^2/g
[a]**BET Pore Width**	11.9 nm	6.23 nm
[b]**BJH Cumulative Pore Volume**	1.54 cm^3/g	0.72 cm^3/g

[a] Brunnauer-Emmett-Teller (BET) analysis of the adsorption isotherms from nitrogen adsorption isotherms.

[b] Barrett, Joyner, and Halenda (BJH) analysis of the adsorption isotherms from nitrogen adsorption isotherms.

2.2.4 Immobilization of Bioluminescent Enzymes in Porous Silicon Particles

While the trapping mechanism was demonstrated for long-term for drug delivery applications, we tested this for potential imaging and diagnostic applications by loading the particles with bioluminescent enzymes NanoLuc and NanoLuc-GFP.[19-20] When active, these enzymes emit a photon when turning over substrate and enables real-time visualization and tracking of enzymatic activity when immobilized within the particles. Porous silicon particles were synthesized by electrochemical etching of Siltronix wafers (polished on the (100) face, boron-doped (p-type), resistivity <1.1 mΩ·cm) with ethanolic HF (1:1 ethanol:HF) and under a perforated etch with an oscillating square wave of 25 mA/cm^2 for 45s, 150 mA/cm^2 for 2s and 45 repeats. Porous silicon films were removed from the bulk Si wafer by an electropolishing step with 3.33% HF (diluted in ethanol) under a constant current supply of 2.67 mA/cm^2 for 300 s. The films were subjected to a series of ultrasonication and settling times to obtain particles between 1-10 μm (diameter) and ~1 μm thick. The particle size was confirmed by SEM imaging (Zeiss) (Figure 2.2.3).

Following sonication, particles were stored in ethanol to prevent extensive oxidation. Prior to loading, the particles were washed three times in water followed by water oxidation (1 mg/mL) for 24 hrs while agitated on a spinning wheel to passivate the surface with a uniform and thin oxide. The water was removed following centrifugation of the particles. Particles were then soaked in the NanoLuc, BSA and PBS solution for 24 hrs and agitated on a rotating wheel. Three different loading solutions (NanoLuc 0.5 μg/mL BSA 99.5 μg/mL; NanoLuc 1 μg/mL BSA 99 μg/mL; NanoLuc 2 μg/mL BSA 98 μg/mL) were tested and the total protein added corresponded to 10 wt% of the particles. NanoLuc only accounted for a small fraction of loading because of its high cost and difficulty in quantification in high concentrations due to rapid turnover rate of substrate

and short bioluminescence signals (few seconds) (dilution will cause low particle concentration and silicon dissolution). As a result, BSA was added to encourage pore shrinkage, which in turn prevents leakage, and help stabilize the NanoLuc. Following loading, particles were washed three times (1 mg/mL) with 0.1% PBS-BSA.

Successful loading was demonstrated by measuring the NanoLuc concentration in the supernatant of the loading solution and of particles (100 μg) dispersed in PBS buffer (100 μL) (Figure 2.2.4). Bioluminescence was collected after adding substrate (100 μL of NanoGlow - diluted 1000X from stock, Promega) and measured in a fluorescence plate reader and at 460 nm. The intensity readings of the particles (Figure 2.2.4a) suggests that NanoLuc was loaded. The supernatant of the loading solution had low intensity signal and minimal change (Figure 2.2.4b), which is comparable to background noise (not shown), and indicates that nearly all of the added enzyme was encapsulated. To test the amount of enzyme leakage, particles were soaked in PBS pH 7.4 buffer for 24hr (1 mg/mL) and, following centrifugation, the supernatant was collected for bioluminescence analysis. The intensity plots of the leakage test solution are comparable to background and reveals that NanoLuc was tightly trapped within the silicon skeleton (Figure 2.2.5a). The sensitivity of bioluminescence measurement is greater than 0.5 nM as shown in Figure 2.2.5b. The bioluminescence intensity decay trend appears to be different between free (Figure 2.2.5b) and loaded NanoLuc. For free NanoLuc, the intensity decays exponentially at initial time points which is represented by the near linear trend on the exponential scale in Figure 2.2.5b. The loaded NanoLuc displays a plateau or slight increase in intensity before decaying in a non-linear trend. This may be attributed to diffusion of the substrate into the pores that suppresses the turnover rate of substrate by the NanoLuc.

While bioluminescence was observed, the relative intensity counts and decay trend suggests that less than ~10% of loaded NanoLuc was turning over substrate (by comparing with pure NanoLuc solution). This may be attributed to suppression of intensity signal due to absorption of the silicon particles. However, it is also possible that a large amount of the loaded protein was inactive when trapped within the particles because immobilization within the skeleton may restrict space that the proteins requires to orient and turnover substrate. As enzymes are rich in amine groups, which is known to facilitate degradation of Si into silicic acid and reprecipitation back to silica, it is possible that these biological macromolecules are more tightly immobilized to the scaffold. Lastly, proteins have specific folding structure to optimize its transport, binding, and activity for its function. Regions that are rich in cationic amino acid sequences (e.g. lysine, arginine or histidine) may preferentially orient towards the silicon and cause the active site to be inactive.

To test the activity of the enzyme in the particles after trapping, a droplet of NanoLuc-GFP-pSi was placed between a glass slide and coverslip and imaged under an Andor camera connected to a homemade microscope setup (iCCD, cooled to -30°C) (Figure 2.2.4). No features and minimal signal were acquired to ensure that there was minimal background and no scatting from the particles (Figure 2.2.4a). The microscope setup was then connected to a 450 nm LED to excite the GFP. The strong contrast between the particles and background indicates successful loading of the protein and minimal leakage into the surrounding medium (Figure 2.2.4b). Camera exposure time was shortened prevent saturation of the CCD. Immediately after, the LED was switched off and a 1 uL droplet of concentrated substrate was added and the camera was allowed to collect the image under the same settings as the background control (Figure 2.2.4c). While the signal is much weaker than fluorescence, clear bioluminescence was clearly visualized from the particles demonstrating successful diffusion of the substrate into the particles and enzymatic

activity of the NanoLuc. Since the camera was focused in the same sample and location, the particle bioluminescence was validated by comparing to the fluorescent images (Figure 2.2.4b and c). Since the particles were not fixed onto the slide, slight movement was observed.

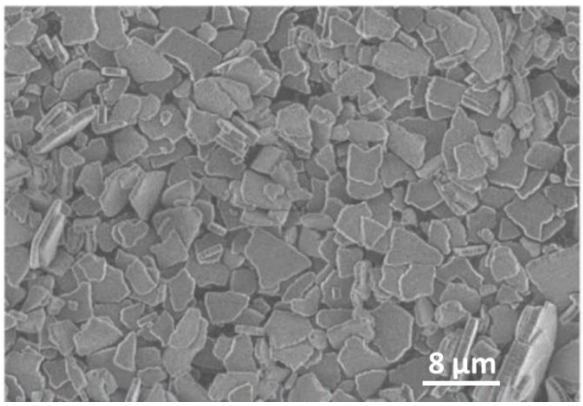

Figure 2.2.3. Scanning electron microscope of empty particles that were employed for enzyme loading studies. Particles ranged from ~1-10 µm.

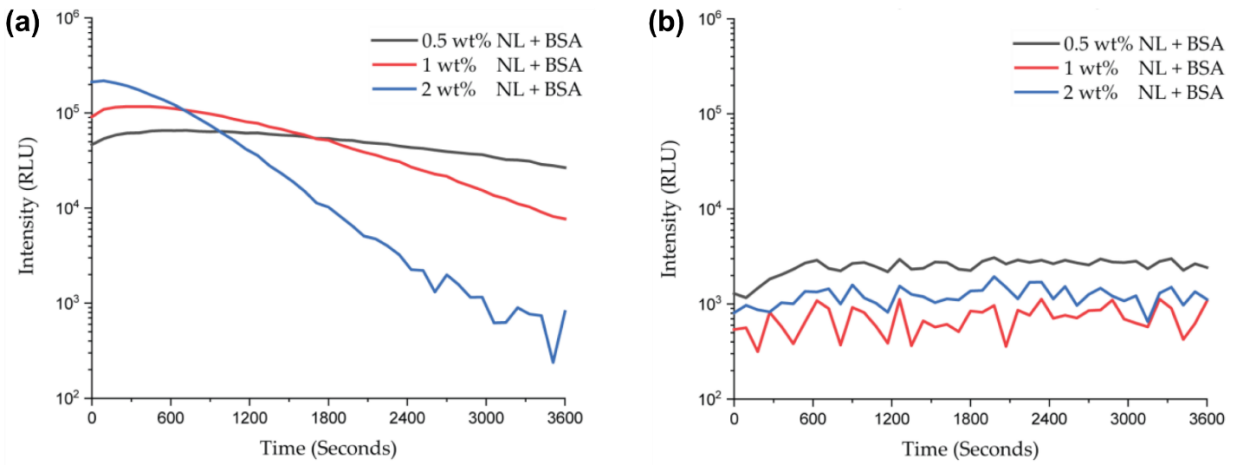

Figure 2.2.4. The bioluminescence kinetics following the addition of NanoGlow substrate in (a) 0.5, 1 and 2 wt% NanoLuc loaded porous silicon microparticles and (b) the supernatant of the loading solution after loading. The particles displayed obvious bioluminescence and both the higher intensity and faster decay reflects the stronger presence of NanoLuc at higher wt% loading. The low intensity and minimal change in intensity in (b) is comparable to background signal and suggests that nearly 100% of the added NanoLuc was loaded into the particles. Intensity measurements were performed on a 96 well plate and in a fluorescence plate reader at 460 nm.

.

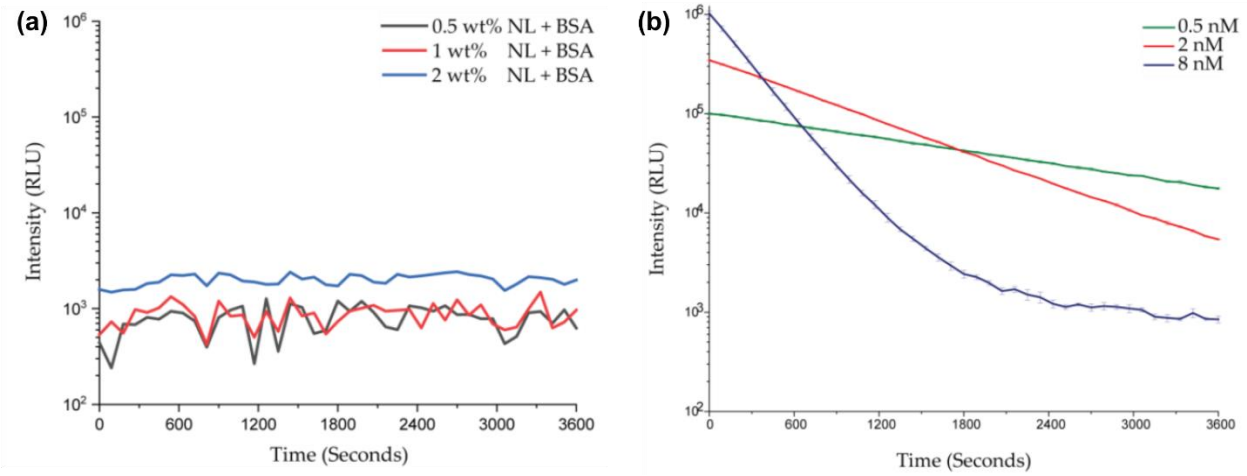

Figure 2.2.5. The bioluminescence kinetics following the introduction of NanoGlow substrate in (a) the leakage test solution of 0.5, 1 and 2 wt% NanoLuc loaded porous silicon microparticles and (b) the pure NanoLuc with 0.5, 2 and 8 nM concentrations. Intensity measurements were performed on a 96 well plate and in a fluorescence plate reader at 460 nm.

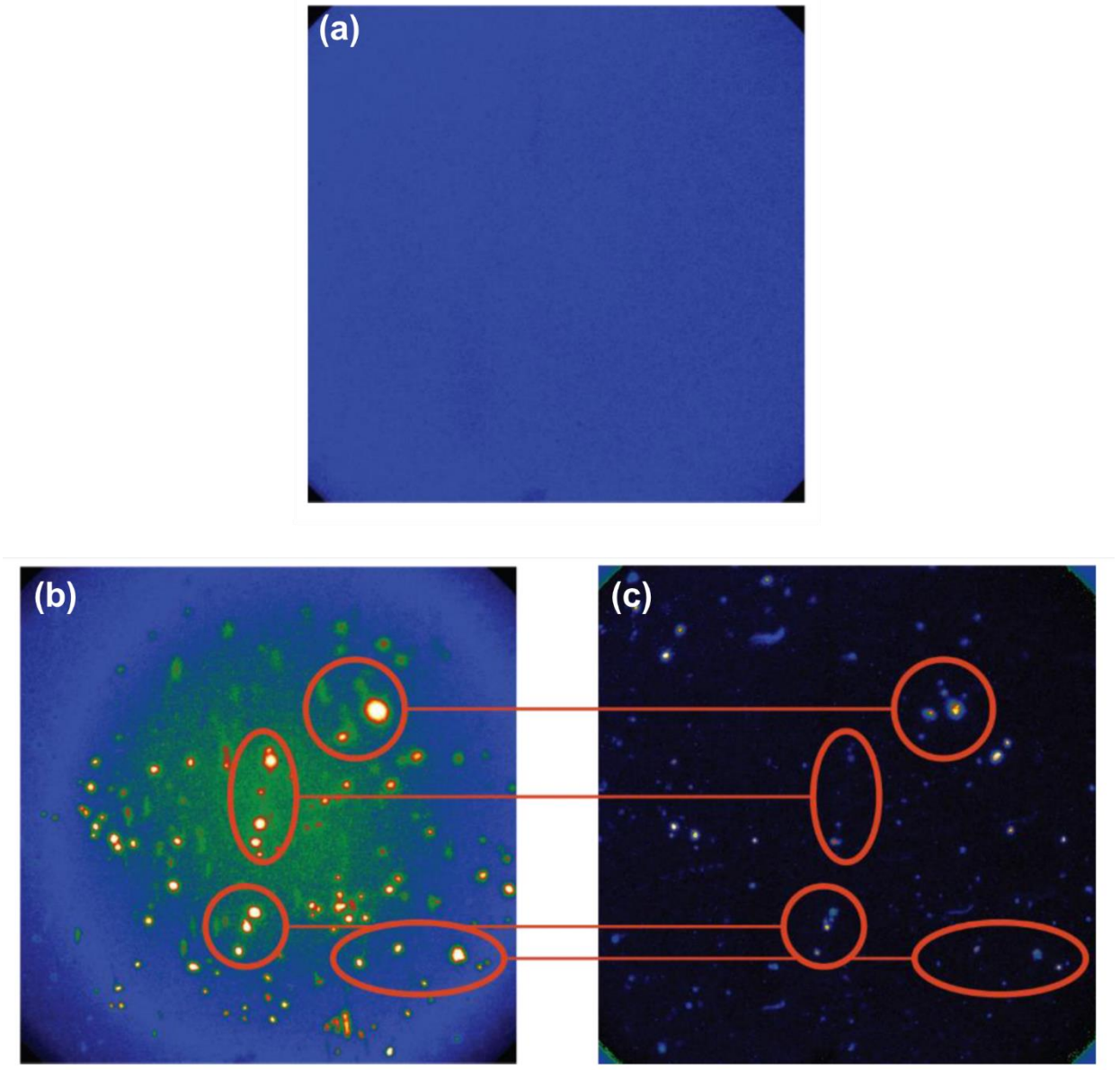

Figure 2.2.6. False color intensity images from an Andor camera of (a) NanoLucGFP loaded pSi (no light), (b) illuminated with a 365 nm LED (Ocean Optics) excitation source and (c) following the addition of NanoGlow substrate (no excitation light).

2.3 Calcium and Magnesium Loading

2.3.1 Background

In aqueous environment and biological conditions, porous silicon readily oxidize and dissolve into solution in the form of silicic acid.[21] However, in the presence calcium and phosphate ion containing solutions, dissolution of pSi is inhibited due to the mineralization and precipitation of calcium phosphate formation on the surface of the pSi.[22] In this work, we demonstrate the formation of silicates on the surface of pSi during its dissolution by introducing high concentrations of group two alkaline metals, calcium and magnesium. The silicate shell improves the stability of the particle and immobilizes payloads within the silicon skeleton. In particular, calcium silicate is insoluble and well known for its stability in cement chemistry and fabrication.[23] We compare the loading efficiency and pharmacokinetic profile of anionic and cationic molecules using these trapping chemistries with porous silicon microparticles.[24]

2.3.2 Materials

Highly boron-doped p-type Si wafers (1 mΩ•cm resistivity, <100> orientation, 525 ± 25 μm thick) were obtained from Virginia Semiconductor. Aqueous 48% hydrofluoric acid, potassium hydroxide, Tris buffer saline pH7.4, and ethanol were purchased from Fisher Scientific. Tris(2,2-bipyridine)ruthenium(II) hexafluorophosphate (Ru(bpy)), rhodamine B (RhB) and bovine serum albumin tagged with fluorescein isothiocyanate was purchased from Sigma Aldrich. Phosphate buffered saline was purchased from life technologies.

2.3.3 Experimental Methods

2.3.3.1 Fabrication of pSi Films and Microparticles.

For optical testing and microparticle, porous silicon was synthesized by electrochemical etching in a Teflon etch cell (8.6 cm^2) and with 12 mL of 3:1 48%-HF: EtOH solution. For the

optical characterization studies, a constant current supply of 70 mA/cm^2 for 600s was applied. For microparticle fabrication, the current was modulated between 200 to 800 mA and at a period of 4 sec and 2.7 sec per cycle (i.e. current cycling from 200 to 800 mA) to form a composite sinusoidal structure with stop bands at approximately 450 and 560 nm. The porosity and thickness of the porous silicon layer was approximately 57% and 20 µm, respectively. This porous silicon film was removed from bulk silicon by an electropolishing step using 3.33 *v/v* % of 48%-HF in ethanol and etching at 150 mA for 150 sec. These films were then ultrasonicated in ethanol for approximately 5 – 7 min to get particles of desired size (i.e. 20 × 60 × 60 µm). After sonication the suspension was centrifuged for 5 min at 14000 rpm. Then the supernatant was discarded and the pallet at the bottom was transferred to a silica boat (ceramic). The oxidation of the pSi particles was carried out at 800 °C for 1 h in muffle furnace to fully convert the skeleton to silicon dioxide.

2.3.3.2 Preparation of Magnesium and Calcium Ion Loading Solution and Particle Treatment

Magnesium or calcium chloride was dissolved in deionized water to obtain a 4M ion solution. Minimal volumes of hydrochloric acid or aqueous potassium hydroxide was added to the solution so that the pH was adjusted to 8.5-9. For characterization and pore shrinking studies, particles (10 mg) were soaked in 3 mL of either the magnesium/calcium solution or borate buffer (pH 9) and sonicated for 16 hrs. The particles were washed three times in milliQ water (1 mg/mL) and dried in a vacuum desiccator.

2.3.3.3 XRD Characterization

Powder X-ray diffraction spectra were collected at ambient temperature on a Bruker D8 Advance diffractometer using Cu Kα (λ=1.5418 Å) radiation (40 kV, 40 mA), using a step size of 0.02° in 2Θ, and a 2Θ range of 10-90°.

2.3.3.4 Loading and Release of Rhodamine B (RhB) and Ruthenium Bipyridine (Ru-bpy)

Porous silicon particles (10 mg) were ultrasonicated for 24 hours after adding 3 mL of either pH 9 borate buffer (Sigma-Aldrich), 4M magnesium chloride hexahydrate, or 4 M calcium chloride and 750 μL of dye solution (11 mg/mL, Rhodamine B (RhB) or ruthenium bipyridine (Ru(bpy))). Each solution was adjusted with low volumes of hydrochloric acid or potassium hydroxide to pH 8.5-9 in order to promote higher reactivity of the pSi surface and alkaline-silicate core-shell formation. After loading, the particles were centrifuged and washed 3-5 times in water (10 mL).

Dried RhB and Ru-bpy loaded particles were split into three different samples (~3 mg/sample). Release studies were performed in 1 mL of Tris buffer (pH 7.4) and incubated at 37°C. Every 24 hours, 1 mL of buffer was sampled and replaced. The supernatant of each time point was characterized by UV-Vis plate reader (RhB – 553 nm, Ru-bpy – 291 nm). After the release for 9 days, particles were soaked in 0.5M KOH to fully dissolve the particles and quantify unreleased dye.

2.3.4 Magnesium and Calcium Induced Trapping

Oxidized silicon readily degrades into silicic acid in aqueous solutions (eq 2.1).

$$SiO_2 + 2H_2O \rightarrow Si(OH)_4 \quad (2.1)$$

Concentrated magnesium or calcium salt enabled fast reaction with the silicic acid to form Mg/Ca silicate (eq 2,3).

$$Si(OH)_4 + 2Mg^{2+} + 4OH^- \rightarrow Mg_2SiO_4 + 4H_2O \quad (2.2)$$

$$Si(OH)_4 + 2Ca^{2+} + 4OH^- \rightarrow Ca_2SiO_4 + 4H_2O \quad (2.3)$$

To test the formation of silicate precipitation and pore shrinkage, the reflectance spectrum of pSi chips was monitored using a tungsten white light (Ocean Optics) and spectrometer (USB4000).

PSi chips were first fully oxidized at 800°C for 1 hr to eliminate any signal from oxidative pore swelling. Baseline optical characterization of the chips were collected in water. Prior to spectral collection, water was removed and the chips were immediately subjected to 5 mL of 4M $MgCl_2/CaCl_2$ adjusted to pH 9 with KOH or HCl and pH 9 borate buffer as a control. High pH was selected to encourage dissolution of the silicon matrix for silicic acid formation. The optical reflectance spectrum of each chip was collected over eight hours (Figure 2.3.1). The shrinkage of the pore volume was analyzed by taking the Fourier transform of these reflectance spectra to obtain $2nL$ (n – refractive index, L – layer thickness), or the effective optical thickness (EOT) of the pSi film.[25] By assuming minimal changes in the thickness, the $2nL$ values were used to probe how the refractive index (n) of the matrix changes over time.

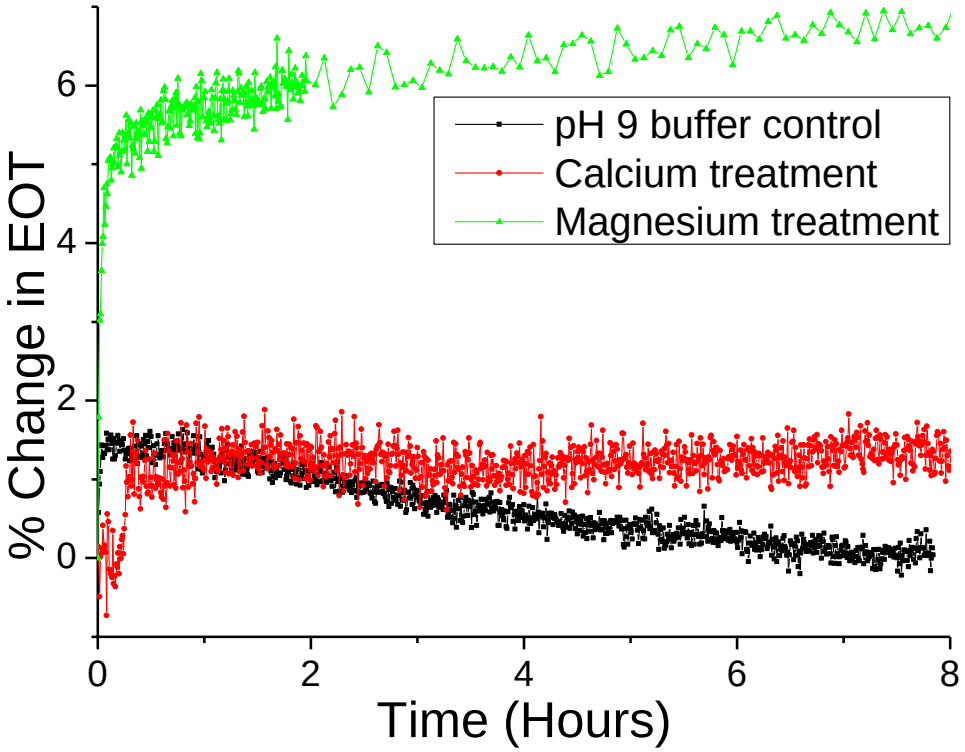

Figure 2.3.1. The percent change in the effective optical thickness of fully oxidized porous silicon films when soaked in pH 9 borate buffer, 4M magnesium chloride or 4M calcium chloride.

As expected, the *2nL* values continuously decreased over time when the chip was exposed to pH 9 buffer. The dissolution of the matrix allows more aqueous buffer (n≈1.3) to infiltrate the pores and reduce the overall refractive index of the film [silicon oxide (n=1.54)]. However, in the presence of magnesium, the effective optical thickness increases rapidly during initial time points before becoming slower and more progressive. This is attributed to fast degradation of the silicon dioxide skeleton during initial time points that allow rapid reprecipitation of silicic acid in the form of magnesium silicate. As more and more magnesium silicate form, it presumably passivates the surface and prevents the particles from degrading, which is attributed to the slow increase at later time points. In the case of calcium treatment, the EOT remained relatively consistent over time. Because the solution was elevated to pH 9, the solubility of silica is elevated and, as the pH 9 borate treatment showed, the SiO_2 should degrade and decrease in EOT value. The consistent EOT values suggests the formation of calcium silicate that prevented the particle from degrading. Overall, the change in EOT was more significant for magnesium treatment and suggests a higher pore shrinkage compared to calcium. This can be due to a thicker magnesium silicate shell formation or more extensive particle degradation in the calcium treated particles.

2.3.5 Characterization of Porous Silicon's Structure after Mg/Ca Treatment

To validate the optical experiments and test whether the calcium and magnesium treatment enabled pore shrinkage, we performed nitrogen adsorption measurements on particles (prepared and treated by the same conditions) and quantified by the BJH model (Figure 2.3.2). After overnight (16 hr) sonication of fully oxidized pSi particles, the pore volume displayed a significant reduction compared to the pristine and pH 9 buffer controls (Table 2.3.1). Because the particles were fully oxidized, pore swelling due to oxidation of the silicon skeleton was eliminated and pore reduction is attributed to silicate precipitation.

Additional characterization of silicate formation was performed by X-Ray diffraction (Figure 2.3.3) with pSi particles that were not oxidized and treated under the same conditions. Oxidation was not performed so that silicon peaks could be visualized to understand particle oxidation and degradation during the reaction. Silicon crystalline peaks were present in the magnesium treated particles, indicating the preservation of the silicon skeleton. The X-ray pattern of calcium treated particles revealed peaks of calcium carbonate and silicon peaks. The formation of carbonate is attributed to diffusion of carbon dioxide into the calcium chloride powder or the reaction solution. The silicon peaks are no longer present indicating oxidation of the skeleton. In both magnesium and calcium treatment, no crystalline phase is observed in the silicate precipitate indicating an amorphous phase. In the case of pH 9 buffer, no crystal pattern is observed suggesting oxidation and degradation of the skeleton.

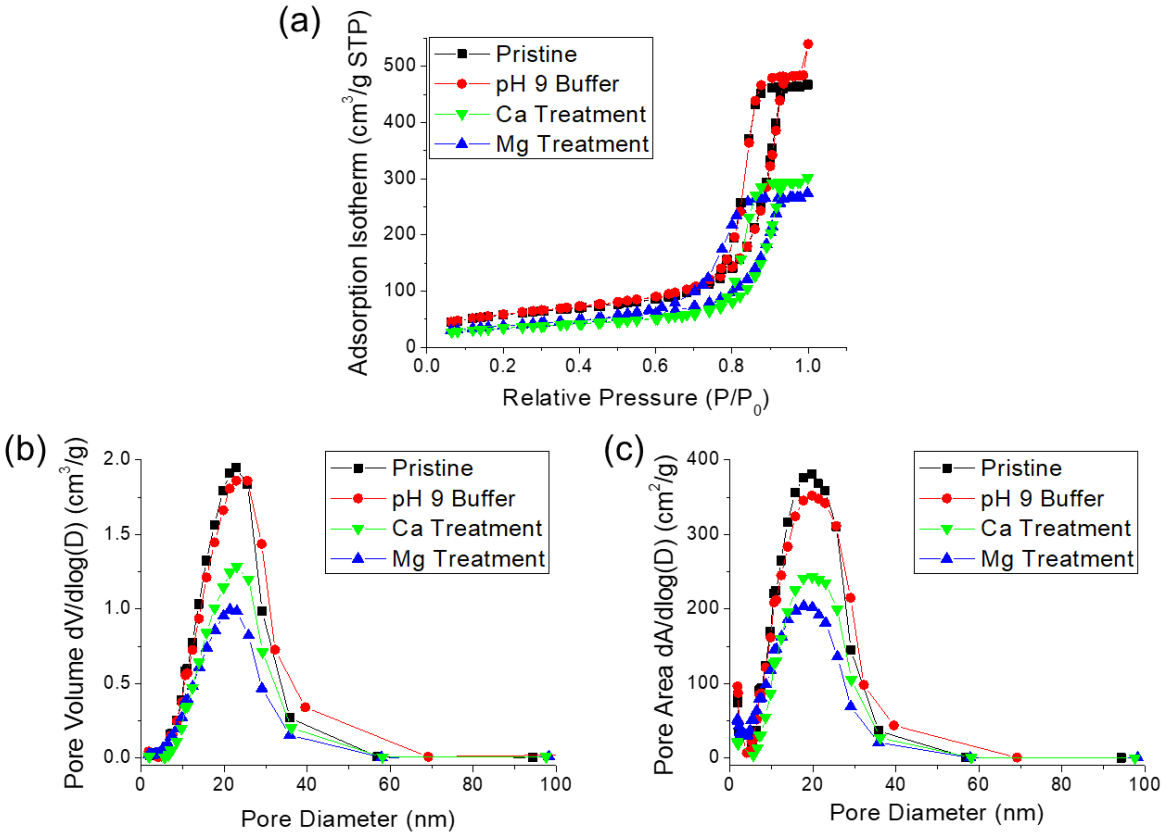

Figure 2.3.2. (a) The nitrogen adsorption isotherms and the BJH approximation for (b) pore volume and (c) pore surface area versus pore diameter.

Table 2.3.1. The summary of the nitrogen adsorption experiments of pristine and pH 9 buffer, 4M Mg and 4M Ca treatment.[24]

	Pristine	**pH9 Buffer Treatment**	**Mg Treatment**	**Ca Treatment**
BET Surface Area	210.1 m^2/g	211.8 m^2/g	136.9 m^2/g	122.7 m^2/g
BJH Adsorption Cumulative Pore Volume	0.709 cm^3/g	0.822 cm^3/g	0.416 cm^3/g	0.460 cm^3/g
BJH Adsorption Average Pore Diameter	15.9 nm	19.99 nm	13.8 nm	17.2 nm

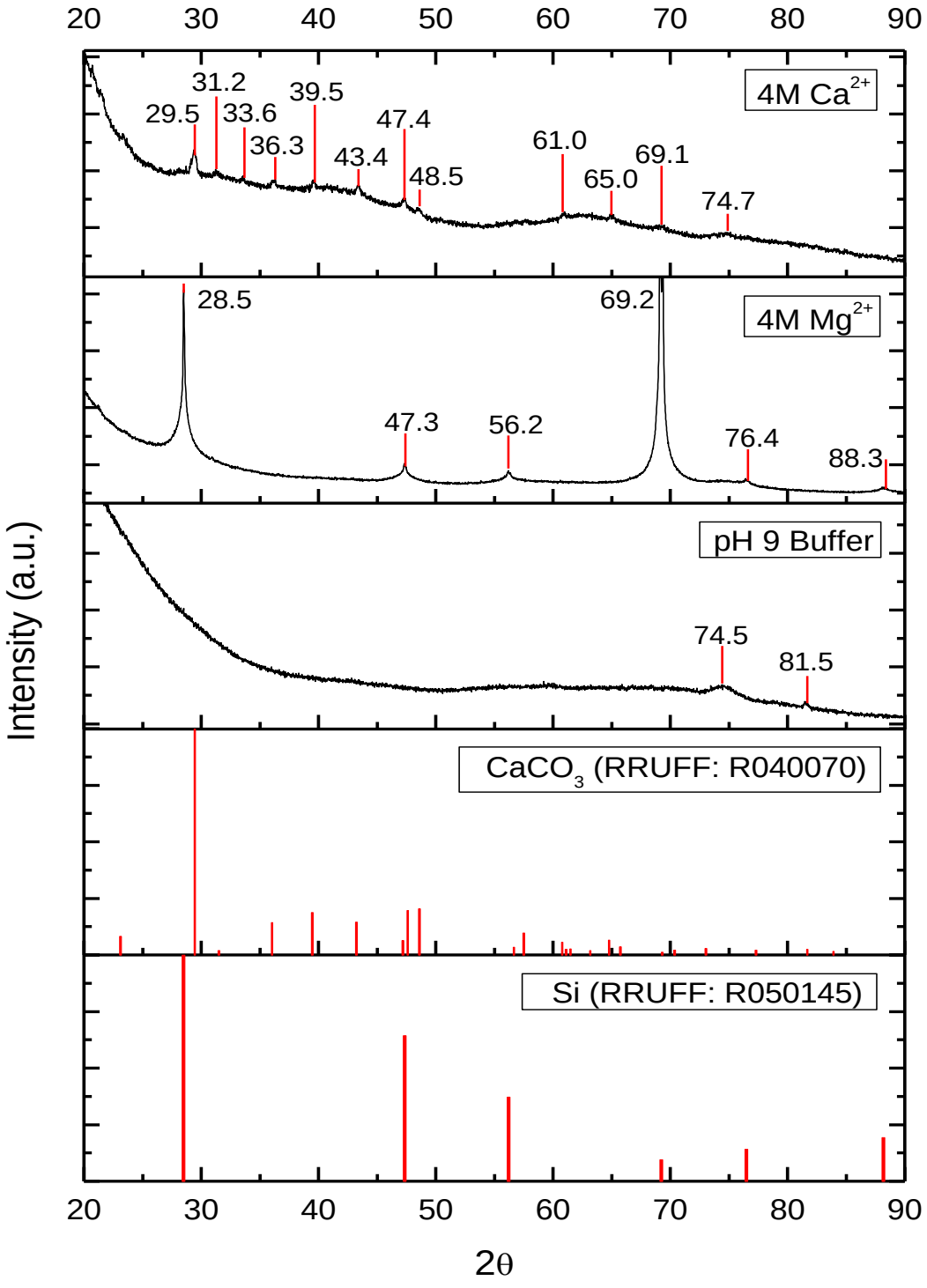

Figure 2.3.3. The powder XRD data of silicon particles treated with 4M calcium chloride, 4M magnesium chloride and pH 9 borate buffer. [24]

2.3.6 Magnesium and Calcium Enhanced Trapping of Small Molecule Dyes

To test the effect of charge on loading, rhodamine B (RhB) and Ru-bpy, were selected as the neutral and cationic model payloads. Rose bengal was initially tested as an anionic payload but, due to severe precipitation of the dye in concentrated calcium and magnesium solution, RhB was selected instead for comparison (neutral). Each dye was loaded in the presence of pH 9 borate buffer or 4M magnesium or calcium chloride solutions adjusted to pH 9 and sonicated for 16 hrs. After loading, the particles were washed 5 times with deionized water.

The RhB and Ru-bpy loaded particles were subject to release studies for 9 days in Tris buffer at pH7.4. Tris buffer was selected to prevent calcium or magnesium phosphate formation during the release. The release solution was sampled hourly for the first six hours and daily thereafter to prevent saturation at initial time points. The particles remaining at the end of the release study was treated with 0.5M KOH to fully dissolve the particles and extract the remaining payload. The loading efficiency was calculated by summing the amount of dye remaining in the particles and released during the dissolution study.

The loading of RhB was significantly higher in magnesium and calcium than the pH 9 buffer treated formulation due to stronger electrostatic interaction with a positively charged surface (Table 2.3.2). At high pH, RhB is zwitterionic and has limited electrostatic attraction with the pSi as seen in the pH 9 loaded formulation. When comparing the pharmacokinetics, the Mg/Ca treated samples displayed much longer sustained release presumably because the silicate crust physically immobilized the dye molecules within the skeleton structure (Figure 2.3.4a). These results are consistent with prior findings[18] where oligonucleotides (siRNA), well known to have a negative charge due to the outer phosphate groups, achieved higher loading efficiency in the presence of concentrated calcium solution.

On the other hand, Ru-bpy had the highest loading efficiency in porous silicon when dissolved in pH9 buffer. Because Ru-bpy is a positively charged molecule, the calcium and magnesium may displace the dye to prevent efficient accumulation within the pores. However, when loaded in the presence of Mg/Ca, longer sustained release of Ru-bpy was observed and suggests that formation of the silicate can still immobilize cationic payloads (Figure 2.3.4b). Additionally, the extended pharmacokinetics (by release percentage) may also be an artifact of poor loading.

2.3.7 Conclusion

While trapping with anionic molecules has already been shown in porous silicon systems,[18] this work compares the loading efficiency and release kinetics of calcium and magnesium treated silicon particles. Due to the trapping mechanism and positively charged surface of the silicate precipitate, calcium and magnesium treatment enabled high loading efficiency of neutral molecules and caused low loading of cationic payloads. However, the trapping chemistry enabled more sustained release for both payloads. Additionally, by using fully oxidized particles, we confirm that the pore shrinkage and trapping mechanism is a consequence of oxidation in high ionic strength solution but due to silicate/silica formation. We expect that this type of trapping strategy may also occur with other cationic metals such as copper, iron, zinc, and manganese. In addition to drug delivery, formation of silicate with certain metals may also enable other applications such as imaging and self-reporting systems.

Table 2.3.2. The mass loading efficiencies of RhB and Ru(bpy) in pH 9 borate buffer, 4M Mg, or 4M Ca solution. The mass loading was calculated by dividing the mass of the dye by the total mass of the loaded particles (particle + dye).[24]

	pH 9 Buffer	**Mg Treatment**	**Ca Treatment**
RhB	6.9%	22%	13%
Ru-pby	6.2%	1.2%	3.2%

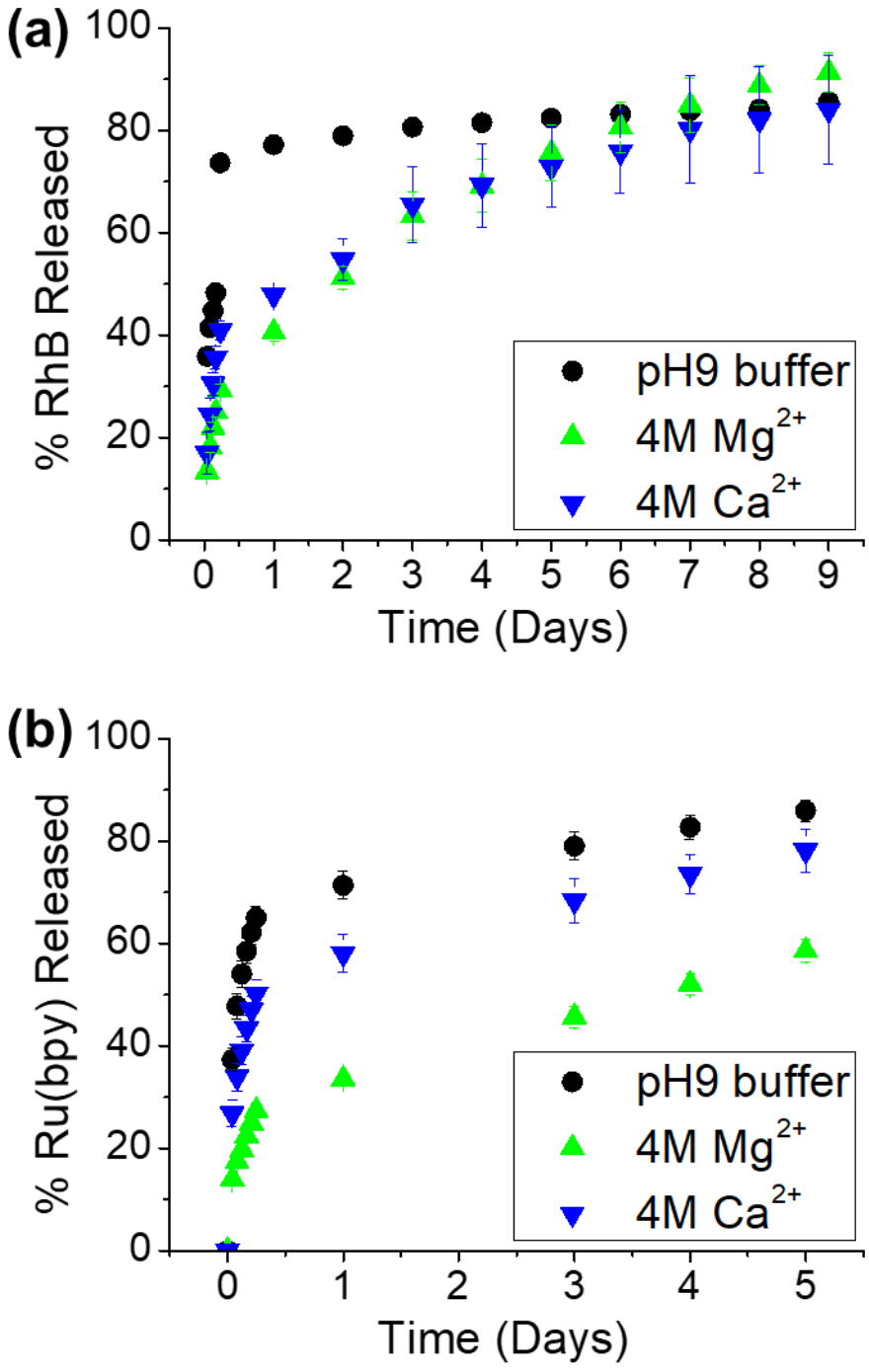

Figure 2.3.4. The cumulative release of (a) RhB and (b) Ru(bpy) from oxidized porous silicon particles treated with pH 9 borate buffer, 4M Mg and 4M Ca.[24]

2.4 References

1. Anselmo, A. C.; Mitragotri, S., An overview of clinical and commercial impact of drug delivery systems. *Journal of Controlled Release* **2014,** *190*, 15-28.

2. Nellore, R. V.; Singh Rekhi, G.; Hussain, A. S.; Tillman, L. G.; Augsburger, L. L., Development of metoprolol tartrate extended-release matrix tablet formulations for regulatory policy consideration. *Journal of Controlled Release* **1998,** *50* (1), 247-256.

3. Edwards, D. A.; Ben-Jebria, A.; Langer, R., Recent advances in pulmonary drug delivery using large, porous inhaled particles. *Journal of Applied Physiology* **1998,** *85* (2), 379-385.

4. Chang-Lin, J.-E.; Attar, M.; Acheampong, A. A.; Robinson, M. R.; Whitcup, S. M.; Kuppermann, B. D.; Welty, D., Pharmacokinetics and Pharmacodynamics of a Sustained-Release Dexamethasone Intravitreal Implant. *Investigative Ophthalmology & Visual Science* **2011,** *52* (1), 80-86.

5. Hubacher, D.; Kavanaugh, M., Historical record-setting trends in IUD use in the United States. *Contraception* **2018,** *98* (6), 467-470.

6. Stunning popularity of LARCs with good access and quality: a major opportunity to meet family planning needs. *Glob Health Sci Pract* **2015,** *3* (1), 12-13.

7. Rowland, M.; Tozer, T. N., *Clinical pharmacokinetics/pharmacodynamics*. Lippincott Williams and Wilkins Philadelphia:: 2005.

8. Brody, T., Chapter 4 - Dose Modification and Dose Titration. In *FDA's Drug Review Process and the Package Label*, Brody, T., Ed. Academic Press: 2018; pp 101-151.

9. Anglin, E. J.; Cheng, L.; Freeman, W. R.; Sailor, M. J., Porous silicon in drug delivery devices and materials. *Advanced drug delivery reviews* **2008,** *60* (11), 1266-1277.

10. Salonen, J.; Kaukonen, A. M.; Hirvonen, J.; Lehto, V.-P., Mesoporous Silicon in Drug Delivery Applications. *Journal of Pharmaceutical Sciences* **2008,** *97* (2), 632-653.

11. Prestidge, C. A.; Barnes, T. J.; Lau, C.-H.; Barnett, C.; Loni, A.; Canham, L., Mesoporous silicon: a platform for the delivery of therapeutics. *Expert Opinion on Drug Delivery* **2007,** *4* (2), 101-110.

12. Rytkönen, J.; Arukuusk, P.; Xu, W.; Kurrikoff, K.; Langel, Ü.; Lehto, V.-P.; Närvänen, A., Porous Silicon–Cell Penetrating Peptide Hybrid Nanocarrier for Intracellular Delivery of Oligonucleotides. *Molecular Pharmaceutics* **2014,** *11* (2), 382-390.

13. Kim, B.; Pang, H.-B.; Kang, J.; Park, J.-H.; Ruoslahti, E.; Sailor, M. J., Immunogene therapy with fusogenic nanoparticles modulates macrophage response to Staphylococcus aureus. *Nature Communications* **2018,** *9* (1), 1969.

14. Kafshgari, M. H.; Delalat, B.; Tong, W. Y.; Harding, F. J.; Kaasalainen, M.; Salonen, J.; Voelcker, N. H., Oligonucleotide delivery by chitosan-functionalized porous silicon nanoparticles. *Nano Research* **2015,** *8* (6), 2033-2046.

15. Li, W.; Liu, Z.; Fontana, F.; Ding, Y.; Liu, D.; Hirvonen, J. T.; Santos, H. A., Tailoring Porous Silicon for Biomedical Applications: From Drug Delivery to Cancer Immunotherapy. *Advanced Materials* **2018,** *30* (24), 1703740.

16. Tieu, T.; Alba, M.; Elnathan, R.; Cifuentes-Rius, A.; Voelcker, N. H., Advances in Porous Silicon–Based Nanomaterials for Diagnostic and Therapeutic Applications. *Advanced Therapeutics* **2019,** *2* (1), 1800095.

17. Fry, N. L.; Boss, G. R.; Sailor, M. J., Oxidation-Induced Trapping of Drugs in Porous Silicon Microparticles. *Chemistry of Materials* **2014,** *26* (8), 2758-2764.

18. Kang, J.; Joo, J.; Kwon, E. J.; Skalak, M.; Hussain, S.; She, Z.-G.; Ruoslahti, E.; Bhatia, S. N.; Sailor, M. J., Self-Sealing Porous Silicon-Calcium Silicate Core–Shell Nanoparticles for Targeted siRNA Delivery to the Injured Brain. *Advanced Materials* **2016,** *28* (36), 7962-7969.

19. Hall, M. P.; Unch, J.; Binkowski, B. F.; Valley, M. P.; Butler, B. L.; Wood, M. G.; Otto, P.; Zimmerman, K.; Vidugiris, G.; Machleidt, T., Engineered luciferase reporter from a deep sea shrimp utilizing a novel imidazopyrazinone substrate. *ACS chemical biology* **2012,** *7* (11), 1848-1857.

20. Boute, N.; Lowe, P.; Berger, S.; Malissard, M.; Robert, A.; Tesar, M., NanoLuc Luciferase – A Multifunctional Tool for High Throughput Antibody Screening. *Frontiers in Pharmacology* **2016,** *7* (27).

21. Anderson, S. H. C.; Elliott, H.; Wallis, D. J.; Canham, L. T.; Powell, J. J., Dissolution of different forms of partially porous silicon wafers under simulated physiological conditions. *Physica Satus Solidi* **2003,** *197* (2), 331-335.

22. Canham, L. T., Bioactive Silicon Structure Fabrication Through Nanoetching Techniques. *Adv. Mater.* **1995,** *7* (12), 1033-1037.

23. Chen, J. J.; Thomas, J. J.; Taylor, H. F. W.; Jennings, H. M., Solubility and structure of calcium silicate hydrate. *Cement and Concrete Research* **2004,** *34* (9), 1499-1519.

24. Sailor, M. J.; Kang, J.; Joo, J.; Anglin, E.; Kwon, E.; Skalaks, M.; Bhatia, S. N. Porous silicon materials comprising a metal silicate for delivery of therapeutic agents. WO2017181115A1, 2017.

25. Lin, V. S. Y.; Motesharei, K.; Dancil, K.-P. S.; Sailor, M. J.; Ghadiri, M. R., A Porous Silicon-Based Optical Interferometric Biosensor. *Science* **1997,** *278* (5339), 840.

CHAPTER THREE

Self-Reporting Porous Silicon Microparticles

3.1 Abstract

A porous Si (pSi) microparticle-based delivery system is investigated, and the intrinsic luminescence from the particles is employed as a probe to monitor the release of a model protein payload, bovine serum albumin (BSA) (Figure 3.1). The microparticles consist of a core Si skeleton surrounded by a SiO_2 shell. Two types of pSi are tested, one with smaller (10 nm) pores and the other with larger (20 nm) pores. The larger pore material yields a higher mass loading of BSA (3 vs 20%). Two different methods are used to load BSA into these nanostructures: the first involves loading by electrostatic physisorption, and the second involves trapping of BSA in the pSi matrix by local precipitation of magnesium silicate. Protein release from the former system is characterized by a burst release, whereas in the latter system, release is controlled by dissolution of the pSi/magnesium silicate matrix. The protein release characteristics are studied under accelerated (0.1 M aqueous KOH, 21 °C) and physiologically relevant (phosphate-buffered saline, pH 7.4, 37 °C) conditions, and the near-infrared photoluminescence signal from the pSi skeleton is monitored as a function of time and correlated with protein release and silicon dissolution. The thickness of the Si core and the SiO_2 shell are systematically varied, and it is found that the luminescence signature can be tuned to provide a signal that either scales with protein elution or that changes rapidly near the end of useful life of the delivery system. Although payload release and particle dissolution are not driven by the same mechanism, the correlations between luminescence and payload elution for the various formulations can be used to define design rules for this self-reporting delivery system.

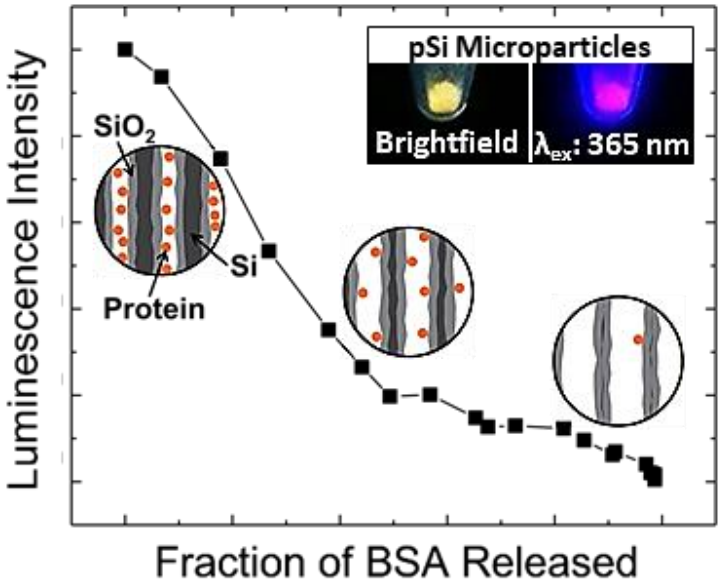

Figure 3.1. The photoluminescence of porous silicon acts as a self-reporting probe for the release of a model protein payload, bovine serum albumin. Photoluminescence disappears as the quantum-confined Si domains within the skeleton dissolve, and this correlates with protein release.

3.2 Introduction

Hollow, or porous nanomaterials are attractive as drug delivery vehicles because they can provide the advantages of sustained release, lower systemic toxicity, and tissue-specific targeting while protecting the drug payload from degradation.[1-4] Inorganic materials such as porous silicon (pSi),[5-6] nanoporous anodic alumina,[7] and mesoporous silica[8-9] have been exploited as materials to deliver drugs via many different administration routes; of interest in this study are intraocular, intramuscular, and subcutaneous delivery, where larger, depot based formulations are typically used.[10-15] Controlling the kinetics of drug release from such nanomaterials is crucial for optimal treatment, and it poses a substantial challenge due to patient-to-patient variability and other physiological characteristics that affect release kinetics.[16-17] There is a particular need to monitor drug burden in developmental stages and during clinical trials, and indirect methods of drug quantification by sampling bodily fluids such as blood or urine are limited due to cost and complexity. Theranostic systems that are self-reporting, such that they indicate the status of the delivery vehicle in terms of local drug concentration or residual drug capacity,[18-24] is a poorly developed area that could provide substantial benefits in personalized medicine.[25-26]

Compared to other systems, a unique dimension of pSi is that it contains intrinsic photoluminescent domains as part of the nanostructure. It is one of few semiconductor "quantum dot" materials that is nontoxic and degrades to nontoxic byproducts.[27-30] For self-reporting drug-delivery applications, advantages of pSi include: (1) the photoluminescence appears at tissue-penetrating near-infrared wavelengths;[30] (2) the measurement of light emission from pSi has little to no angular dependence or directional light scattering (unlike photonic crystals, for example);[18, 31] and (3) the long-lived (micro seconds) excited state of pSi enables elimination of interfering background fluorescence by time-gated imaging.[32-33] In this work, we explore the possibility of

using this intrinsic luminescence from pSi particles to self-report carrier degradation and drug delivery.

3.3 Materials and Experimental Methods

3.3.1 Materials

Silicon wafers, polished on the (100) face, boron-doped (p-type), resistivity <1.5 mΩ·cm were obtained from Virginia Semiconductor, Inc. or from Siltronix. Absolute ethanol (200 proof) was obtained from Rossville Gold Shield Chemicals. Potassium hydroxide (ACS grade) and sodium sulfite (ACS grade) were obtained from Fisher Scientific. Ammonium molybdate tetrahydrate (crystal, ACS grade) was obtained from Spectrum Chemicals. Magnesium chloride (6-hydrate, crystalline, ACS grade), concentrated sulfuric acid (ACS grade), and hydrofluoric acid (48% aqueous, ACS grade) were obtained from Macron Chemicals. Micro BCA protein assay kit (No. 23235) was obtained from Thermo-Fisher Scientific. Bovine serum albumin from porcine gastric mucosa (lyophilized powder, 32004500 units/mg protein), 4-(methylamino)phenol hemisulfate salt (ACS grade, 99%), and oxalic acid dehydrate (ACS grade, >99%) were obtained from Sigma-Aldrich Chemicals.

3.3.2 Fabrication of Luminescent Porous Silicon (pSi) Microparticles.

Porous Si microparticles were prepared by electrochemical etch of highly boron-doped single-crystalline Si wafers as previously described.[34] A wafer was mounted in a sealed etching cell that exposed a circular area of 60 cm^2. The cell was fitted with a copper slab that served as a back contact for the Si wafer. For the small (~10 nm) pore formulation, a 3:1 (v:v) 48% aqueous HF:absolute ethanol electrolyte was used and the wafer was etched at a constant current density of 70 mA/cm^2 for 600 s. For the large (~20 nm) pore formulation, a 1:1 (v:v) 48% aqueous HF:absolute ethanol electrolyte was used and the wafer was etched at a constant current density of

30 mA/cm^2 for 720 s. These conditions generated a porous Si layer of thickness approximately 20 μm and porosity approximately 60% or 70% for the small-pore or large-pore formulations, respectively. The electrolyte was replaced with an electrolyte consisting of 1:20 (v:v) 48% aqueous HF:absolute ethanol, and the porous Si film was removed from the wafer by an electropolishing step consisting of a current density of 4.17 mA/cm^2 applied for 550 s. The freestanding porous Si layer was rinsed with absolute ethanol three times, removed by gentle agitation, and the fragments were placed in a sealed vial containing absolute ethanol (20 mL). The vial was suspended in an ultrasonic bath (1.9 L Ultrasonic Cleaner, No. 97043, VWR, inc.) and the porous layer was subjected to ultrasonic fragmentation for 20 min, resulting in a suspension of nano and microparticles. The nanoparticles were removed from the suspension by removing the supernatant after the microparticles were allowed to settle for 20 min in the vial. The microparticles were dried under vacuum for 1 h and then placed in a ceramic boat and inserted into the hot zone of a preheated tube furnace at 700 °C for 25, 35, or 45 min (for small-pore samples) or 15, 20, or 30 min (for large-pore samples) to activate photoluminescence. After heating for the desired times, the boat containing the particles was moved to the edge of the tube furnace to cool for 2 min, and it was then removed to a ceramic surface and allowed to cool to room temperature.

3.3.3 Characterization of pSi Particles

Attenuated total reflectance Fourier transform infrared (ATR-FTIR) spectra were collected using a Thermo Scientific Nicolet 6700 FTIR instrument with a Smart iTR diamond ATR fixture. Raman spectra were collected using a Renishaw inVia Raman microscope with a 100 mW 532 nm laser excitation source. Nitrogen adsorption/desorption isotherms were recorded with a Micromeritics ASAP2020.

3.3.4 Adsorption Loading of Bovine Serum Albumin (BSA).

Porous silicon particles (5 mg) were placed in 5 mL Falcon tubes (Corning, inc.) and soaked in a 1.5 mL solution of BSA (8 mg/mL) in acetate buffer (pH 4) for 16 h while agitating on a spinning wheel. The particles were washed 5 times with 1 mL of acetate buffer and dried under vacuum for 1 h.

3.3.5 Loading by Silicate Trapping.

Bovine serum albumin was loaded into the pSi particles from aqueous solutions containing a magnesium salt. The loading solution was adjusted to pH 9 with potassium hydroxide (KOH) and consisted of 1.0 mL of 12 mg/mL BSA in Tris buffer and 0.5 mL of 4 M (for the small-pore samples) or 600 mM (for the large-pore samples) MgCl2 in deionized water. The loading solution (1.5 mL) was added to 5 mg of particles in a Falcon tube (5 mL). The mixture was agitated on a spinning wheel for 16 h. After the particles were loaded, they were washed 5 times with 1 mL of Tris buffer and dried under vacuum for 1 h.

3.3.6 BSA Release and Luminescence Decay Studies.

Loaded pSi particles (1−2 mg) were immersed in 0.1 M KOH (1.5 mL) in plastic cuvettes. Luminescence spectra (λ_{ex}: 365 nm, 375 ± 5 nm band-pass filter) were collected hourly with an Ocean Optics QE-Pro TE cooled CCD spectrometer using a 515 nm long pass filter. The cuvettes were stirred constantly (via magnetic stir bar) during spectral acquisition to disperse the particles. The stirring was stopped after spectral acquisition, the particles were allowed to settle for 55 min, the supernatant release medium (1 mL) was collected for Si and protein assays, and the cuvette was then replenished with fresh 0.1 M aqueous KOH solution. The study was carried out until the photoluminescence spectrum was no longer detectable. After the last time point for data collection, the sample was left overnight to ensure complete dissolution of silicon prior to final assay.

Concentration of protein was quantified using the commercial micro BCA assay kit following the protocol described by the vendor. Dissolved Si was quantified using molybdenum blue assay (see below). The total mass loading of BSA and mass of Si were quantified by summing the amounts measured at each time point during the release assay and the final measurement, after all pSi particles had been dissolved. The long-term (30 day) release studies were performed using the same protocol but using aqueous PBS at pH 7.4 as the dissolution medium, maintaining the temperature at 37 °C, and sampling/replacing 1.2 mL every 1−3 days.

3.3.7 Molybdenum Blue Assay

Dissolved silicon content was determined using the published molybdenum blue assay.49 Two solutions (A and B) were prepared for this assay. Solution A consisted of 16.2 mM ammonium molybdate and 0.72 M HCl. Solution B consisted of 0.16 M oxalic acid, 7.7 mM of 4-(methylamino)phenol hemisulfate, 6.3 mM of sodium sulfite, and 1.8 M of sulfuric acid. To quantify the silicic acid concentration, 100 μL of Solution A was added to 400 μL of each sample (prediluted by a factor of 100−1000) and allowed to react for 15 min. Then, 500 μL of Solution B was added to each sample and the mixture was allowed to react for 1 h. The optical absorbance at 810 nm of each sample was quantified with a UV−vis plate reader (Spectra Max Plus 384, Molecular Devices). A standard curve was prepared from a serially diluted standard silicon solution (Sigma-Aldrich Si Standard for ICP, TraceCERT, 1000 mg/mL), and the working range was 0.5−20 ppm in water and 1−10 ppm in PBS at pH 7.4 (diluted from stock 10 times).

In Vitro Imaging Studies. Luminescent porous silicon particles (35 min oxidation) were treated in 2 M KOH (2 mg pSi/200 μL KOH) in a 96-well plate (UV-transparent). A higher concentration of base was used in these accelerated aging experiments relative to the other experiments described in this paper in order to reduce the time duration of the experiments.

Luminescence images were collected as a function of time using a Point Gray IR camera fitted with a 600 nm long pass filter and a 240 mm lens (λex: 365 nm). The automatic exposure settings on the camera were disabled to maintain constant image acquisition parameters during the experiment. The images were processed with ImageJ software (NIH) to quantify the luminescence intensity. Intensity of pixels was integrated within a selected square frame. The frame included the image of the entire well.

3.4 Results and Discussion

3.4.1 Synthesis and Characterization of Luminescent Porous Silicon Microparticles

Microparticles of pSi were prepared by anodic electrochemical etch of highly p-doped single-crystal silicon wafers in an electrolyte consisting of aqueous hydrofluoric acid (HF) and ethanol. The porous film was removed from the silicon substrate by electrochemical lift-off and subjected to ultrasonic fracture to form irregular microparticles of sizes ranging from 15 to 110 μm (Figure 3.2a). The thickness and open porosity (obtained by spectroscopic liquid infiltration method, or SLIM),[35] of the porous silicon layers prior to particle formation were ∼20 μm and ∼60−70%, respectively. Scanning electron microscope images revealed pores with diameters of 5−50 nm and wall thickness of∼10 nm (Figure 3.2 b,c). In the present work, three types of core−shell luminescent Si−SiO_2 structures were prepared by systematically varying the SiO_2 shell thickness. This was achieved by controlling the duration of thermal oxidation (25, 35, or 45 min) at 700 °C (Figure 3.3a), designated “thin shell”, “medium shell”, and “thick shell”.[36] Because the shell was formed by partial conversion of the crystalline Si walls to oxide, the longer oxidation times resulted in a simultaneously thicker oxide shell and a thinner Si core for a given pore wall thickness. This depletion of the Si core was evident in the visual appearance of the particles; the optical density progressively decreased with increasing oxidation time, ranging from dark brown

for the as-etched particles to a light ochre color for material treated at 700 °C for 45 min. Material oxidized for 1 h at 800 °C had the pure white appearance of silica and showed no evidence of crystalline silicon by Raman spectroscopy.

The growth of the oxide shell resulted in minimal changes in the overall pore size and porosity, as determined by nitrogen adsorption/desorption measurements (Figure 3.4) and was accompanied by a shift in the emission maximum of photoluminescence to the blue (Table 3.1). The photoluminescence of porous Si originates from quantum confinement in the crystalline silicon skeleton,[37] and the SiO_2 shell serves to passivate the Si surface, increasing the photoluminescence quantum yield of the material.[36, 38-41] Consistent with extensive prior work with porous Si, the blue shift in the photoluminescence spectrum is attributed to a reduction in size of the quantum-confined Si features. The values of average thickness (d) of the emissive crystalline Si features in the skeleton were estimated from photoluminescence and Raman measurements. The photoluminescence data were fit to the inverse power law of Equation 3.1, taken from published theoretical calculations on Si quantum dots:[46-47]

$$E_{PL} = E_g + \frac{3.73}{d^{1.39}} \qquad (3.1)$$

where E_{PL} and E_g (E_g of Si = 1.12 eV) are the energies (in eV) of the emission maximum and of the silicon bandgap, respectively. The values of d are depicted in Figure 3.3a and listed in Table 3.1. The reported average sizes of the particles are consistent with Raman measurements, which displayed a shift of the 520 cm^{-1} band associated with the lattice optical phonon mode of crystalline Si to lower energy by between 5 and 20 cm^{-1} (Figure 3.4), suggesting average Si feature sizes of 5 nm or smaller.[48-49] Characteristic of nanophase silicon, this band was broadened on the low

energy side relative to the porous Si starting material, indicative of some loss of crystallinity.[50] Conversion of Si to silicon oxide was confirmed by Fourier-transform infrared (FTIR) spectroscopy (Figure 3.4). After thermal treatment, the vibrational stretching modes from surface bound Si−H species at ∼2100 cm^{-1} were no longer observable, and an intense band associated with Si−O stretching modes was observed at ∼1100 cm^{-1} indicating that all three particle formulations displayed a similar oxide surface chemistry.

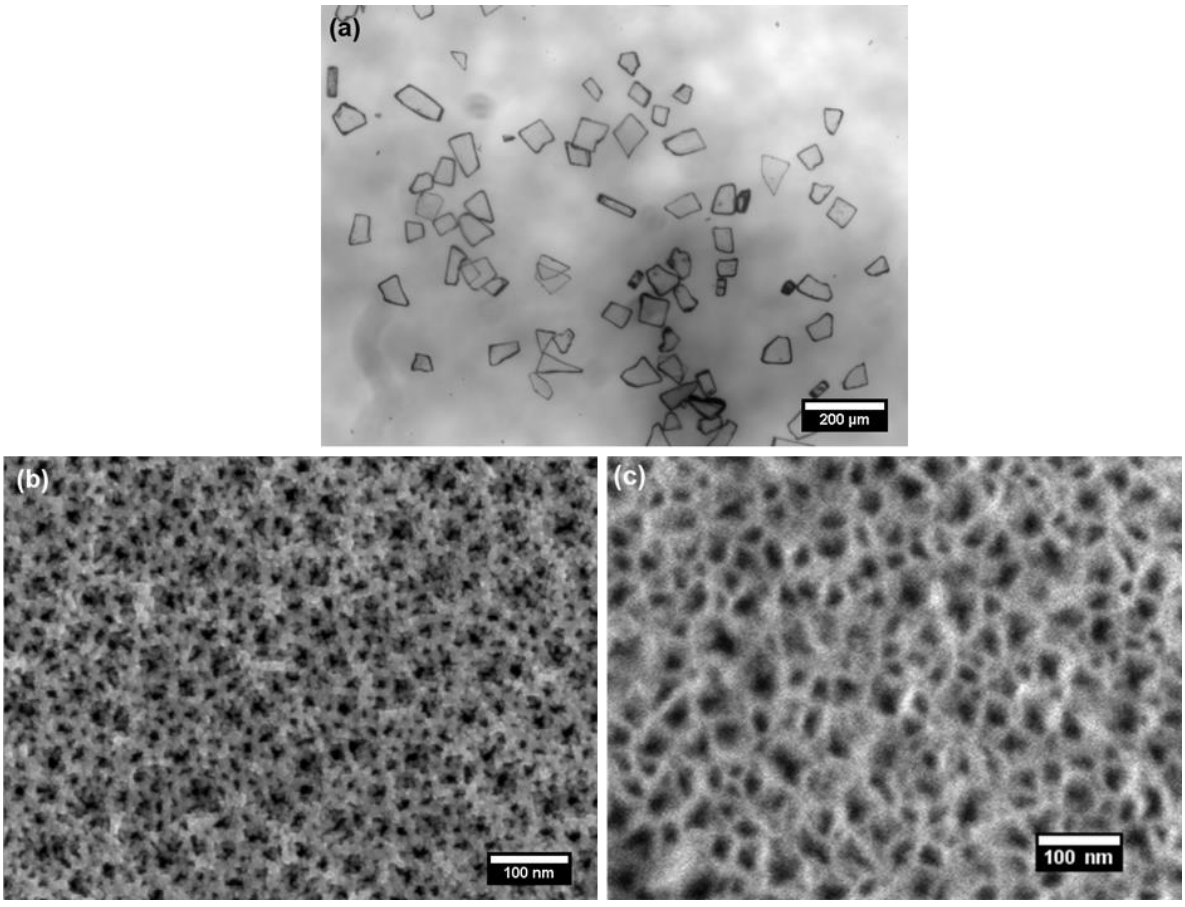

Figure 3.2. Microscope and SEM imaging of pSi particles. Representative (a) optical microscope images of oxidized (700°C for 45 min) pSi particles (5X); (b) SEM image of the pores, obtained as a plan-view of the pSi film etched into a silicon wafer prior to microparticle formation and subsequent oxidation, and (c) plan-view SEM image of pSi microparticles prepared at a higher average current density than the sample in (b), resulting in larger pores.

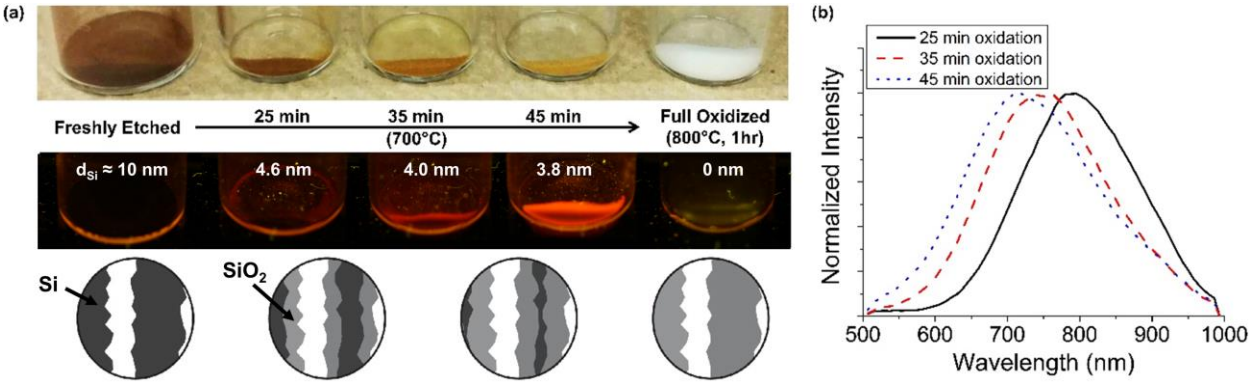

Figure 3.3. Thermal oxidation decreases the size of the Si skeletal core and increases the thickness of the SiO_2 shell. (a) Top: Photographs of thermally treated porous silicon microparticles as a function of thermal oxidation time. The brownish color observed derives from the crystalline Si core, which is completely oxidized when the material is treated at a temperature of 800 °C for 1 h ("Full Oxidized"). Middle: The particles illuminated with UV (365 nm) light display differing degrees of luminescence intensity. Only the partially oxidized particles displayed detectable photoluminescence. Values of pSi indicate average size of the luminescent Si features, estimated from Eq 3.1. Bottom: A schematic depicting the proposed nanostructural changes is shown below the relevant images; the crystalline Si core decreases in diameter and the SiO_2 shell increases in thickness with increasing extent of oxidation. (b) Relative photoluminescence spectra of the pictured samples (λ_{ex} = 365 nm, 500 nm long-pass filter). The photoluminescence spectra exhibit a blue shift as the Si core oxidizes, corresponding to a reduction in average size of the crystalline Si domains in the sample.

Table 3.1. Characteristics of protein-loaded porous Si-SiO_2 core-shell particles (small pores).

	Sample		
	thin shell	**medium shell**	**thick shell**
Oxidation Time[a]	25 min	35 min	45 min
Surface area (m^2/g)[b]	265 ± 30	267 ± 30	246 ± 30
Pore volume (cm^3/g)[c]	0.71 ± 0.08	0.68 ± 0.08	0.65 ± 0.08
Pore diameter (nm)[b]	11.5 ± 1	11.9 ± 1	11.9 ± 1
Photoluminescence λ_{max} (nm)[d]	795	748	724
Si feature size (nm)[e]	4.6	4.0	3.8
% BSA loaded by adsorption[f]	5.5 ± 0.7	5.2 ± 0.5	3.6 ± 0.3
% BSA loaded by Mg silicate trapping[g]	2.5 ± 0.2	2.5 ± 1	2.7 ± 0.8

[a]Time that pSi samples (in microparticulate form) were oxidized in air at 700 °C to generate the SiO_2 shell. Preparation parameters for the particles prior to oxidation were the same for all sample types.

[b]Measured by nitrogen adsorption and determined using BET (Brunnauer-Emmett-Teller) analysis of the adsorption isotherms.

[c] Measured by nitrogen adsorption and determined using BJH (Barrett, Joyner, and Halenda) analysis of the adsorption/desorption isotherms.

[d]Measured with λ_{ex} = 365 nm.

[e]Average size of the luminescent Si features in the sample, estimated from PL spectrum using eq. 1 ($E_{g,Si}$=1.12eV).

[f]Mass percentage. BSA loaded from pH 4 acetate buffer by electrostatic adsorption. Each value represents mean ± standard deviation (n=3).

[g]Mass percentage. BSA loaded from pH 9 tris buffer in the presence of 1.3 M $MgCl_2$(aq). Each value represents mean ± standard deviation (n=3).

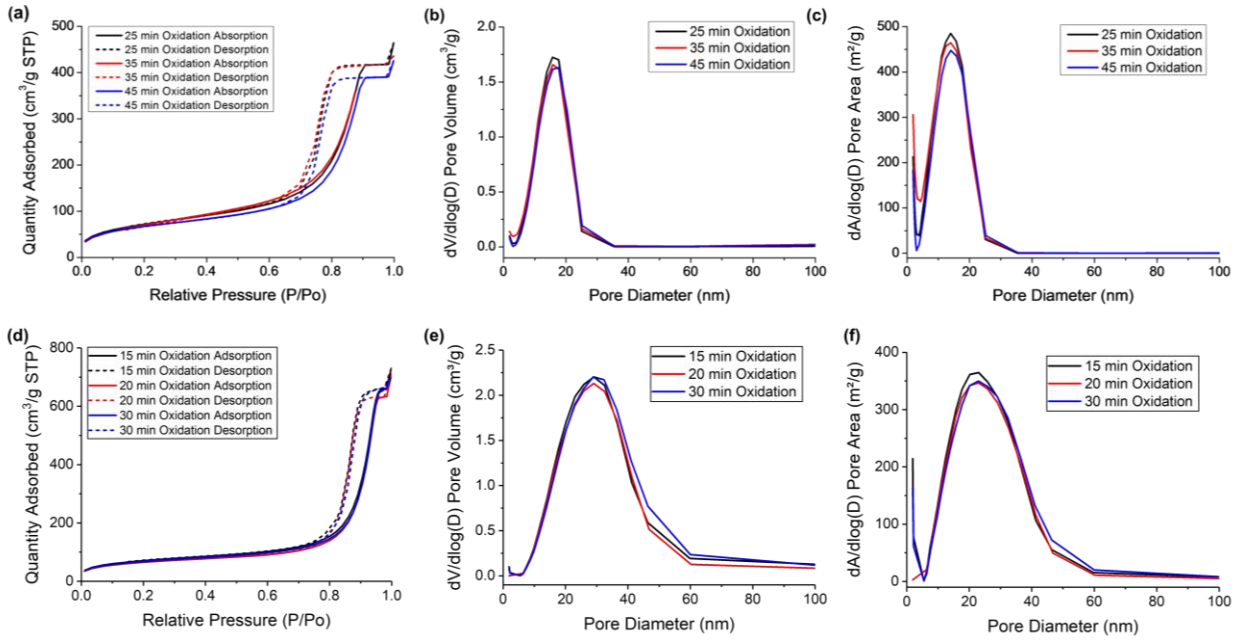

Figure 3.4. Characterization of porous silicon particles by nitrogen adsorption/desorption isotherms. These particles were characterized prior to thermal oxidation, and represent the two types of etching conditions used in this study: "small pores" (a-c) and "large pores" (d-f). Adsorption-desprption isotherms shown in (a) and (d); Calculated BJH pore volume with respect to pore diameter shown in (b) and (e); pore area with respect to pore diameter shown in (c) and (f). The "small pores" samples of (a), (b), and (c) were prepared by etching the Si wafers at a constant current density of 70 mA/cm^2 for 600 s in 3:1 (v:v) 48% aqueous HF:absolute ethanol and their properties are summarized in Table 3.1 of the main text. The "large pores" samples of (d), (e), and (f) were prepared by etching the Si wafers at a constant current density of 30 mA/cm^2 for 720 s in 1:1 (v:v) 48% aqueous HF:absolute ethanol and their properties are summarized in Table 3.2 of the main text.

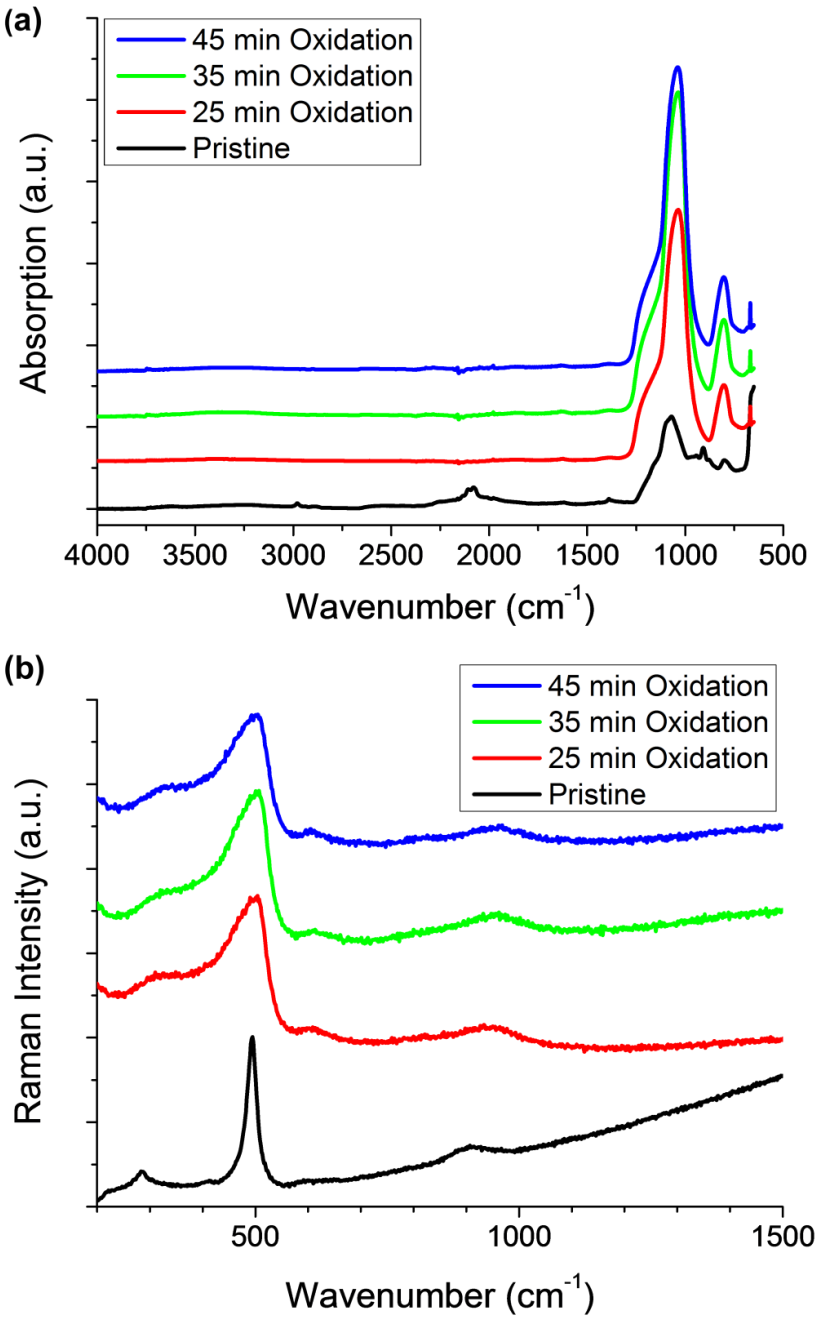

Figure 3.5. Characterization of porous silicon particles before ("Pristine") and after thermal oxidation at 700°C for the indicated times. (a) Attenuated total reflectance Fourier-transform infrared (ATR-FTIR) spectra reveal the removal of surface Si-H groups and conversion to Si-O-Si after oxidation. (b) Raman spectra obtained after oxidation shows the Si lattice mode associated with the crystalline silicon skeleton.

3.4.2 Luminescence Correlation and Comparison of BSA Release and by Trapping or Absorption Loading Methods

Next the luminescent core−shell nanomaterials were loaded with bovine serum albumin (BSA) as a surrogate for a biologic therapeutic. Two methods of loading the model drug payload within the pores were compared: the first was based on simple electrostatic adsorption, and the second was based on physical trapping of the protein (Figure 3.6). Adsorption loading was employed to represent a common release model, wherein the elution kinetics display an initial burst followed by a slower steady-state release. To promote strong electrostatic adsorption of BSA to the silicon oxide surface during loading, the solution pH was adjusted to 4, which is lower than the isoelectric point of BSA (pI = 4.8).[51] These conditions have been shown to yield strong adsorption of BSA onto oxidized porous Si surfaces.[52] In the second loading method, the loaded protein was trapped in the pores using localized deposition of magnesium silicate. This chemistry follows a previously reported approach involving the ability of added calcium ion to form a silicate precipitate that traps the drug payload within the pores.[53] In the present case, we found that the alkaline earth metal magnesium behaved similarly to calcium in the ability of its dictation to form an insoluble silicate salt. In this mechanism, the formation of magnesium silicate results from reaction of a relatively high concentration (1.3 M) of Mg^{2+} ion with silicic acid that is locally generated by dissolution of the SiO_2 shell (at pH = 9) of the porous Si−SiO_2 core−shell particles (Figure 3.6b).[53-55] The presence of magnesium in the nanomaterials was confirmed in the scanning electron microscope images using energy dispersive spectroscopy EDS-SEM (not shown).

We tested both methods of protein loading (electrostatic adsorption and magnesium silicate trapping) on two different types of pSi microparticles, one in which the average pore diameter was ∼10 nm (small pores) and another in which the average pore diameter was ∼20 nm (large pores).

It was found that the “small pore” (Table 3.1) samples loaded substantially less BSA than the “large pore” samples (Table 3.2) with either loading method. For pSi particles of a given pore size, the mass loading of BSA showed no strong dependence on oxide shell thickness. Both loading methods preserved the photoluminescence of the original core−shell nanomaterial, with little change in the wavelength maximum or efficiency of photoluminescence. Next, the photoluminescent BSA-loaded formulations were tested under aqueous dissolution conditions. The mechanism of protein release can be split into two pathways, related to the method used to load the protein into the nanomaterial. A schematic depicting hypothetical release processes for the two classes of samples is given in Figure 3.7. For material that was loaded by the electrostatic adsorption process of Figure 3.6a, release of BSA can be considered to proceed primarily via desorption (Figure 3.7a). For material loaded by the trapping method, where the protein was trapped in the pSi matrix by precipitation of magnesium silicate (Figure 3.6b), we consider that BSA release is more closely tied to degradation of the carrier matrix (Figure 3.7b).

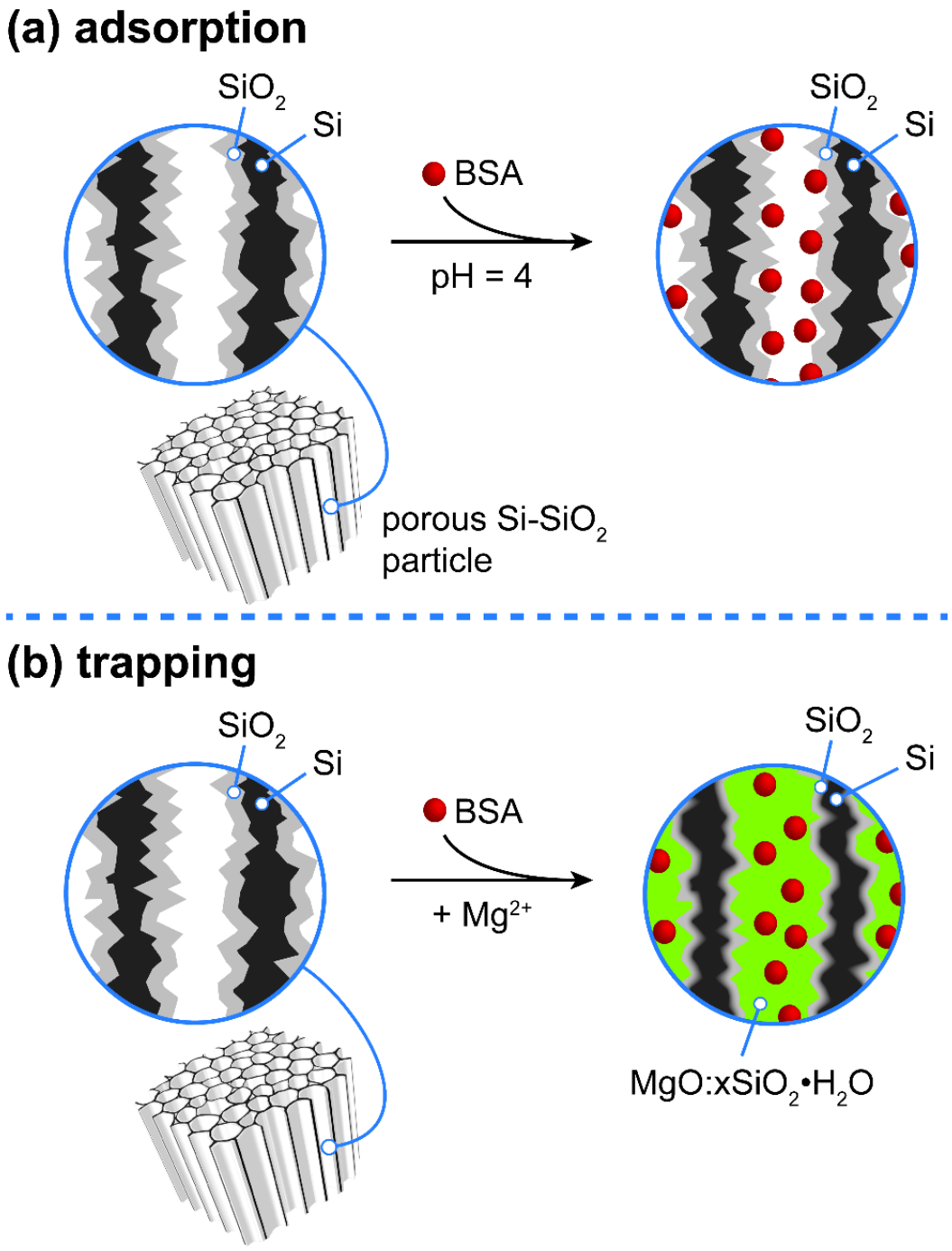

Figure 3.6. Schematics depicting the two approaches used to load the test protein bovine serum albumin (BSA). (a) Adsorption loading is performed at pH 4, which is lower than the isoelectric point of BSA. The cationic charge on the protein displays a strong electrostatic attraction to the negatively charged surface oxide of the particles. (b) Trapping of BSA is accomplished by loading the protein in the presence of high concentration of magnesium ion at pH 9. The orthosilicate product of SiO_2 dissolution reacts with magnesium ions to form a stable silicate that immobilizes the protein within the pores.

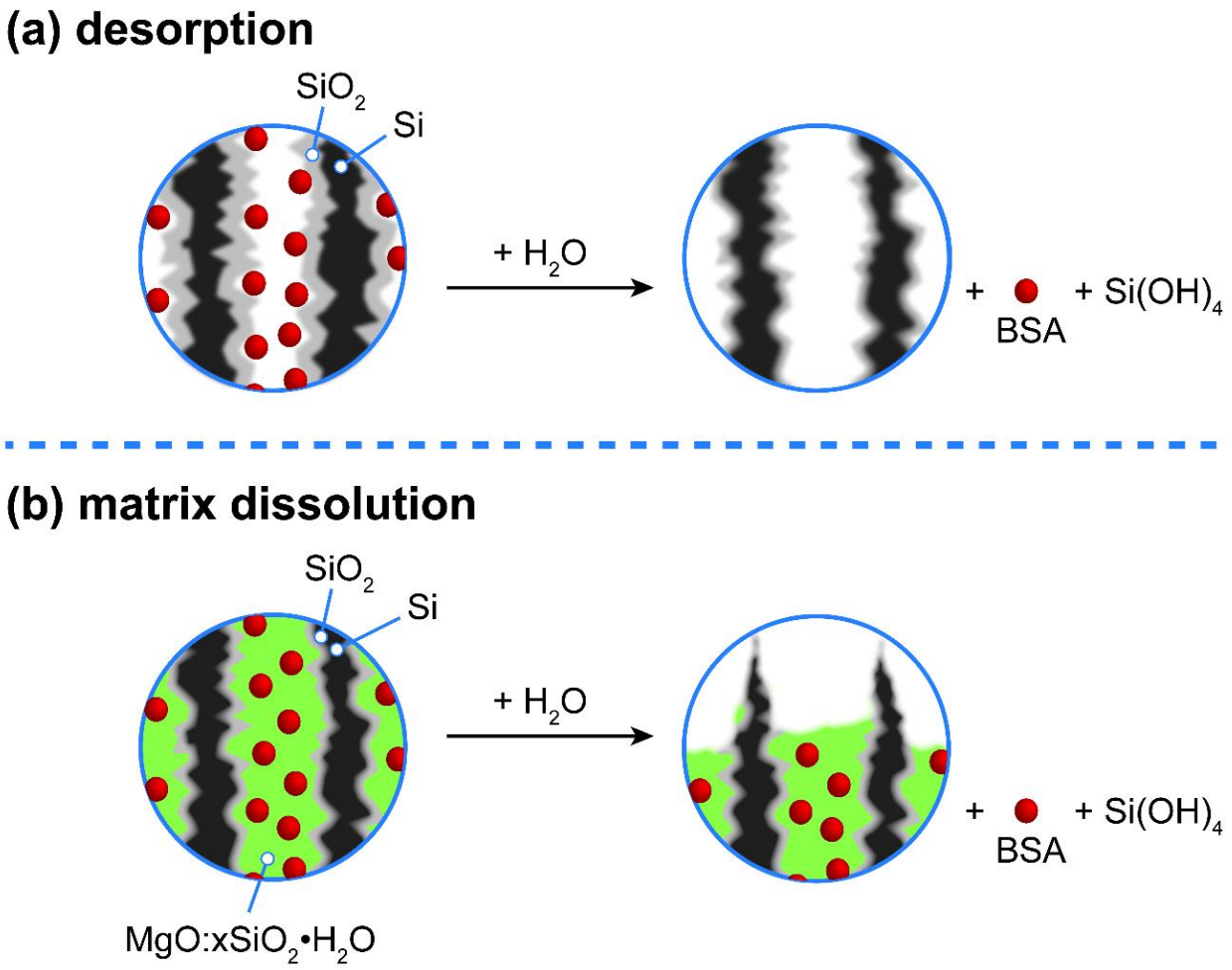

Figure 3.7. Schematics depicting the two proposed mechanisms for protein release from (a) adsorption-loaded porous Si-SiO_2 particles and (b) matrix-trapped porous Si-SiO_2 particles. Images depict cross-sections of the mesopores with bovine serum albumin (BSA) protein depicted with red spheres. (a) With adsorption-loaded porous Si-SiO_2, the protein is weakly bound to the matrix and it is released prior to degradation/dissolution of the photoluminescent Si core. A burst release is observed, and photoluminescence from the Si skeleton degrades on a slower timescale. (b) With matrix-trapped porous Si-SiO_2, the protein is embedded in a magnesium silicate matrix. Because the protein is trapped in this insoluble magnesium silicate phase, the release of protein is more closely tied to degradation of the carrier. A more controlled release is observed, and photoluminescence from the Si skeleton degrades on a similar timescale.

Table 3.2. Characteristics of protein-loaded porous Si-SiO_2 core-shell particles (large pores).

	Sample		
	thin shell	**medium shell**	**thick shell**
Oxidation Time[a]	15 min	20 min	30 min
Surface area (m^2/g)[b]	239 ± 16	206 ± 30	237 ± 10
Pore volume (cm^3/g)[c]	1.04 ± 0.06	1.05 ± 0.04	1.05 ± 0.08
Pore diameter (nm)[b]	21± 1	22 ± 0.2	21± 0.5
Photoluminescence λ_{max} (nm)[d]	823	783	747
Si feature size (nm)[e]	5.1	4.5	4.0
% BSA loaded by adsorption[f]	19 ± 1.7	17 ± 1.1	16 ± 1.0
% BSA loaded by Mg silicate trapping[g]	29 ± 2.5	27 ± 3.6	33 ± 2.1

[a]Time that pSi samples (in microparticulate form) were oxidized in air at 700 °C to generate the SiO_2 shell. Preparation parameters for the particles prior to oxidation were the same for all sample types.

[b]Measured by nitrogen adsorption and determined using BET (Brunnauer-Emmett-Teller) analysis of the adsorption isotherms.

[c] Measured by nitrogen adsorption and determined using BJH (Barret–Joyner–Halenda) analysis of the adsorption/desorption isotherms.

[d]Measured with λ_{ex} = 365 nm.

[e]Average size of the luminescent Si features in the sample, estimated from PL spectrum using eq. 1 ($E_{g,Si}$=1.12eV).

[f]Mass percentage. BSA loaded from pH 4 acetate buffer by electrostatic adsorption. Each value represents mean ± standard deviation (n=3).

[g]Mass percentage. BSA loaded from pH 9 tris buffer in the presence of 200 mM $MgCl_{2(aq)}$. Each value represents mean ± standard deviation (n=3).

To experimentally probe and discriminate these two processes, we performed accelerated dissolution experiments in 0.1 M aqueous KOH while monitoring the concentration of free protein released into solution, the concentration of dissolved silicon in solution, and the photoluminescence signal from the remaining particles as a function of time. Immediately after acquisition of each photoluminescence spectrum, the release solution was sampled and assayed for dissolved silicon/silicon dioxide (orthosilicate ion) and protein content using the molybdenum blue[56-57] and bicinchoninic acid (BCA) assays, respectively. The adsorption-loaded, small-pore particles (Figure 3.6a, 3.7a) all displayed an initial burst release of protein, and this was followed by a more steady and slow release with respect to time (Figure 3.8a) and to fraction of silicon dissolved (Figure 3.8b). This result is expected because at the high pH of the dissolution medium both the SiO_2 surface and BSA are negatively charged, resulting in a strong electrostatic repulsion[52, 58] and a relatively rapid release of any surface-adsorbed protein. The rate of BSA release showed no statistically significant difference as a function of thickness of the SiO_2 shell (Figure 3.8a), consistent with the expectation that the protein is predominantly surface bound for the adsorption-loaded material.

In contrast to the observed time dependence of BSA release, luminescence intensity measured from the degrading particles showed a strong dependence on thickness of the SiO_2 shell (Figure 3.9). Photoluminescence from particle samples with the thinnest oxide shell decayed the most rapidly, and those with the thickest shell decayed the most slowly. The wavelength maximum of photoluminescence also tracked with extent of dissolution, with all samples displaying a pronounced blue shift with time (Figure 3.9). This observed blue shift is consistent with the quantum confinement model; as the silicon features become smaller, the emission energy of the quantum-confined semiconductor is expected to increase.[37] The amount of silicon that dissolved

per unit time, measured by molybdenum blue assay, was similar for the thin, medium, and thick shell materials (Figure 3.9c). Whereas the molybdenum blue measurements represent the total amount of silicon that dissolved at a given time, including both the silicon oxide shell and the crystalline silicon cores, the photoluminescence measurements only report on the silicon cores. Thus the data are consistent with the interpretation that the thicker oxide shell takes more time to dissolve, and so it protects the luminescent silicon core for a longer period of time.

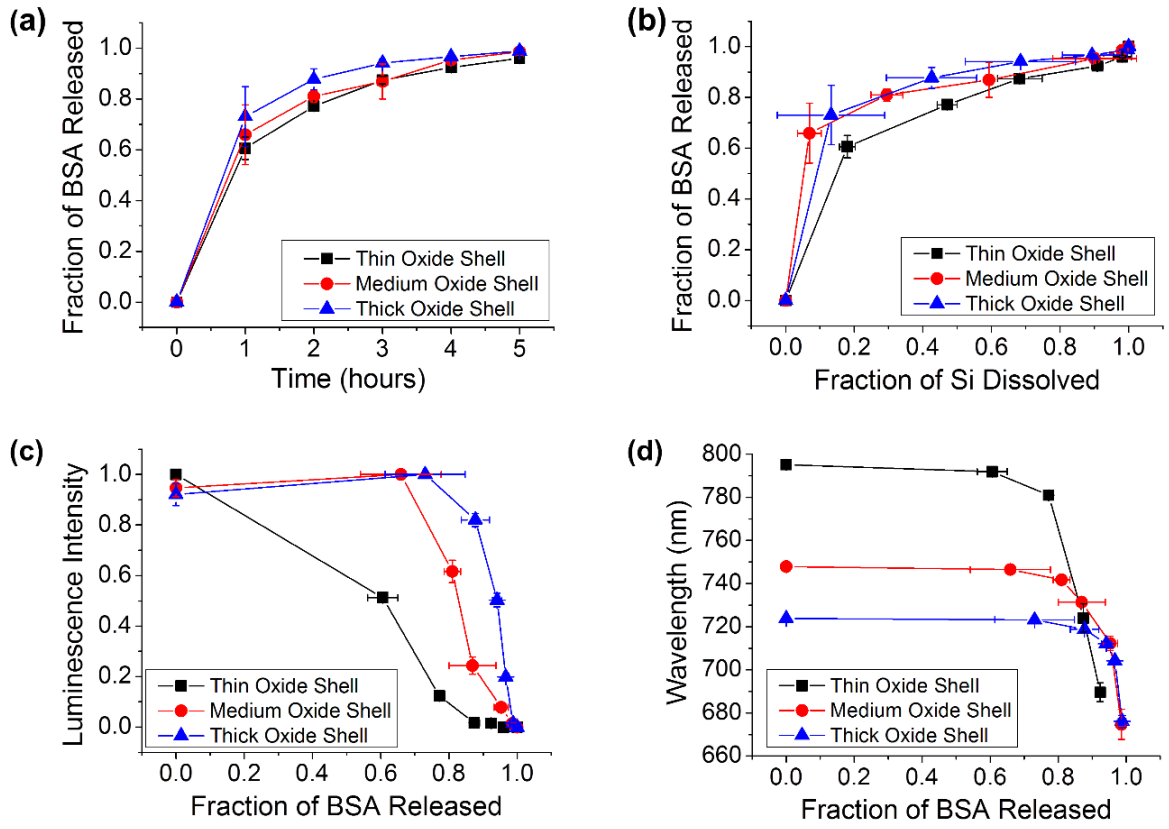

Figure 3.8. Correlations between protein released, silicon dissolved, and photoluminescence from the Si skeletal core for adsorption-loaded core-shell porous Si-SiO_2 particles as they undergo dissolution in aqueous base (0.1 M KOH). Experiments for three core-shell porous Si-SiO_2 structures are displayed in each plot: Traces designated "thin oxide shell", "medium oxide shell", and "thick oxide shell" correspond to pSi particles oxidized at 700 °C for 25 min, 35 min, and 45 min, respectively. (a) Fraction of bovine serum albumin (BSA) released as a function of time. (b) Fraction of BSA released as a function of silicon dissolved. (c) Integrated photoluminescence intensity (in range 650 - 800 nm) from particles as a function of BSA released. (d) Wavelength of maximum photoemission from the Si cores as a function of fraction of BSA released.

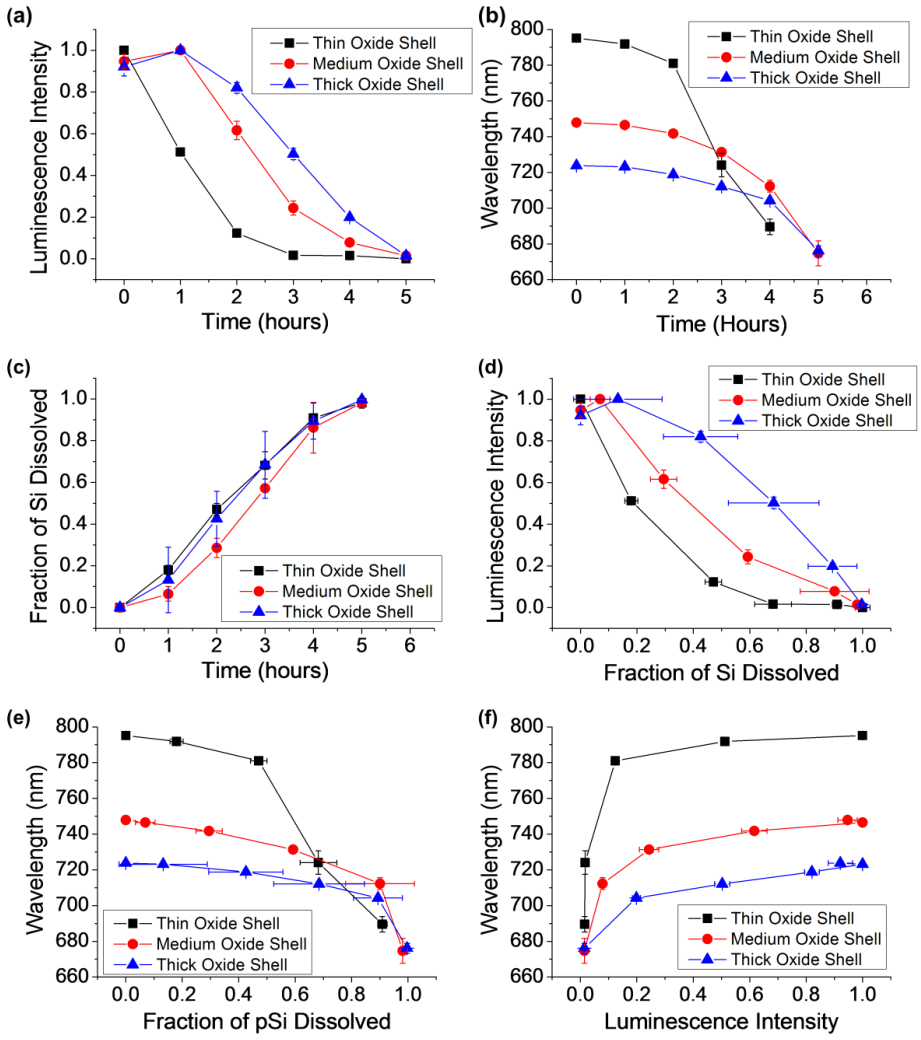

Figure 3.9. Correlations of photoluminescence intensity, photoluminescence wavelength, and fraction of Si dissolved with time exposed to the accelerated dissolution conditions (0.1 M KOH) for three different formulations of core-shell porous Si-SiO_2 particles, loaded with bovine serum albumin (BSA) by the electrostatic adsorption method. The three formulations were prepared with different SiO_2 shell thickness and core size by thermal oxidation at 700 °C for the indicated times. Traces designated "25 min oxidation", "35 min oxidation", and "45 min oxidation" correspond to the "thin oxide shell", "medium oxide shell", and "thick oxide shell" samples, respectively, as discussed in the text. Oxide thickness increased and core diameter decreased with increasing oxidation time. (a) Normalized photoluminescence intensity (λ_{ex} = 365 nm) as a function of time. (b) Wavelength of maximum photoluminescence (λ_{ex} = 365 nm) as a function of time. (c) Fraction of silicon matrix dissolved as a function of time. Mass of dissolved Si was quantified by Molybdenum Blue assay. (d) Normalized photoluminescence intensity as a function of fraction of silicon dissolved. (e) Wavelength of maximum photoluminescence (λ_{ex} = 365 nm) as a function of fraction of silicon dissolved. (f) Wavelength of maximum photoluminescence (λ_{ex} = 365 nm) as a function of normalized photoluminescence intensity. Error bars represent standard deviation (n=3).

The samples with the thin oxide shell displayed photoluminescence signals that most closely matched the release of surface-adsorbed BSA (Figure 3.8c) whereas the loss of photoluminescence was delayed substantially relative to BSA release with samples containing the thicker oxide shells. Luminescence from samples with the thickest oxide shell showed no substantial change in intensity until ~80% of BSA had been released into solution (Figure 3.8c). Because the protein was primarily surface-adsorbed and not entrained in the oxide matrix, this preparation released protein substantially in advance of the degradation of the pSi matrix. This relationship is most apparent in the correlation between dissolved silicon and BSA detected in solution (Figure 3.8b). In contrast to the burst release seen with the adsorption loaded particles, those prepared by physically trapping BSA in the pores generated a more gradual protein release profile. In the physical trapping method, BSA was simultaneously loaded into the pores and trapped by formation of a magnesium silicate precipitate (Figure 3.6b),[53] and so the release of BSA is expected to be more closely tied to the dissolution of this matrix. Accordingly, this preparation displayed near zero-order release kinetics with respect to time (Figure 3.10a), with minimal burst release compared with adsorption-loaded particles (Figure 3.8a). The release of BSA also showed a more linear correlation to the appearance of dissolved silicon (Figure 3.10b) compared with adsorption-loaded particles (Figure 3.8b). The close correspondence of BSA release with appearance of silicon in solution is consistent with the matrix dissolution process depicted in Figure 3.7b. As seen with the adsorption-loaded material, photoluminescence intensity from the magnesium silicate-trapped material degraded as a function of time exposed to the dissolution medium (Figure 3.11). However, degradation was delayed by the presence of the silicate coating. This was particularly apparent in the data from the pSi samples that contained the thinnest oxide shell; whereas photoluminescence intensity began to decay immediately upon immersion in the

aqueous dissolution medium for the adsorption-loaded material (Figure 3.9a), loss of photoluminescence intensity from the magnesium silicate-coated material was not apparent until after 2 h of immersion (Figure 3.11a). As with the adsorption-loaded particles, photoluminescence was more persistent with increasing thickness of the SiO_2 shell. The half-life for loss of photoluminescence intensity, defined as the time at which photoluminescence intensity reached half of its initial value during exposure to the aqueous dissolution solution, also scaled with thickness of the SiO_2 shell for the magnesium silicate-trapped pSi particles: it was ~3, ~4, and ~6h for the thin, medium, and thick SiO_2 shell, respectively (Figure 3.11a). The functional form of the protein release vs photoluminescence intensity relationship differed depending on the particular protein loading method employed and on the thickness of the SiO_2 shell surrounding the Si skeleton of the pSi particles. Although decreases in photoluminescence intensity were related to protein release in all the formulations studied, the trapping-loaded core−shell particles yielded a relationship that could potentially be useful as a predictive tool in a drug-delivery system. Degradation of the photoluminescence signal was a direct result of dissolution of the SiO_2-shell portion of the material, because photoluminescence originates from the quantum-confined silicon skeleton. The magnesium silicate matrix served to delay this process. In addition, the magnesium silicate coating suppressed the burst release of protein, substantially extending its release under the accelerated degradation conditions employed in this portion of the study. The correlation between photoluminescence intensity and BSA detected in solution showed that loss of photoluminescence was delayed relative to release of protein (Figure 3.10c). With the magnesium silicate-trapped particles, the relationship tended to follow a sigmoidal curve with respect to BSA released, where a pronounced drop in photoluminescence intensity was observed after a particular fraction of the BSA payload had been released. The inflection point of the curve scaled with the

thickness of the SiO_2 shell on the Si skeleton. Thus the material that had been prepared with the thin SiO_2 shell had released 40% of its protein payload when the intensity of photoluminescence reached half of its initial value; material with the medium thickness SiO_2 shell had released 50% of the protein at the half intensity point; and material with the thick SiO_2 shell had released 70% of the protein at the half point (Figure 3.10c). The photoluminescence intensity measurement could therefore be used as a surrogate indication of the fraction of protein remaining in the nanomaterial. The emission wavelength also varied systematically with protein release, blue shifting with time (Figure 3.11b) and with fraction of protein released (Figure 3.10d). For the magnesium silicate trapping chemistry, the kinetics of photoluminescence loss and of protein release are almost certainly dictated by separate mechanisms. Whereas the loss of photoluminescence is related to dissolution of the electronically passivating SiO_2 shell, the release of protein is probably more closely tied to the dissolution of the magnesium silicate phase that seals the protein in the pores. This can be inferred from the very rapid release of protein observed in the absence of the magnesium silicate chemistry (with the adsorption-loaded material). However, the SiO_2 shell appears to influence the nature of the magnesium silicate sealant and its ability to load protein. It is noteworthy that, for the small-pore samples, protein loading using the magnesium silicate chemistry was approximately half that of the adsorption-loading process. This suggests that the dissolution of SiO_2 needed to form the magnesium silicate sealant released surface-bound protein, reducing the total amount of protein that was trapped in the pores. In addition, the presence of the magnesium silicate sealant clearly influenced the rate of degradation of the photoluminescence signal. This is to be expected; the SiO_2 shell should dissolve more slowly if it lies underneath an insoluble magnesium silicate coating. Although the photoluminescence decay kinetics depended on the thickness of the SiO_2 shell, the kinetics were also influenced by the presence of the

magnesium silicate sealant. We conclude that the rate of photoluminescence intensity loss from the silicon skeleton comprising the particles relies on multiple factors, although controlling the thickness of the SiO_2 shell appears to be a convenient (if somewhat phenomenological) means to control the correlation between photoluminescence and protein release.

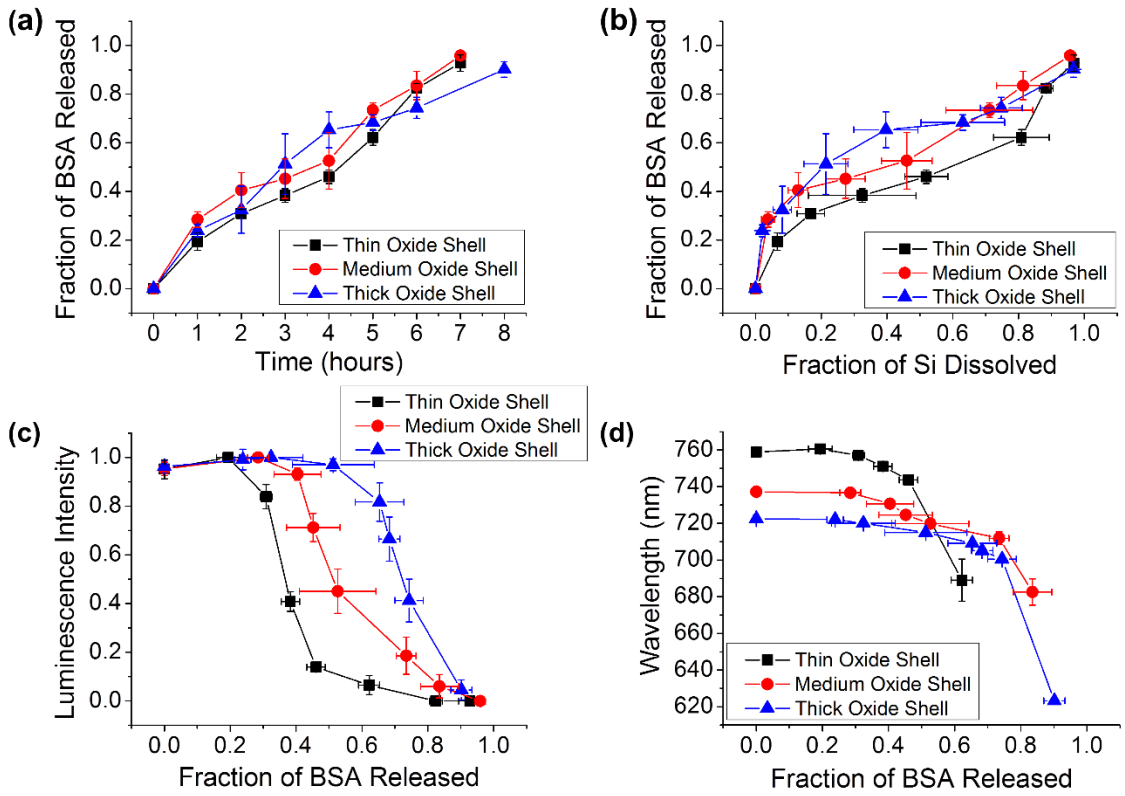

Figure 3.10. Correlations between protein released, silicon dissolved, and photoluminescence from the Si skeletal core for core-shell porous Si-SiO_2 particles loaded with BSA *via* magnesium silicate-trapping chemistry as they undergo dissolution in aqueous base (0.1 M KOH) at room temperature. BSA protein was trapped in the porous Si-SiO_2 particles by means of precipitation of magnesium silicate concommitant with protein loading as described in Figure 3.6b. Traces designated "thin oxide shell", "medium oxide shell", and "thick oxide shell" correspond to pSi particles where the skeletal core was oxidized at 700 °C for 25 min, 35 min, and 45 min, respectively, prior to protein/magnesium silicate loading. (a) Fraction of bovine serum albumin (BSA) released from the particles as a function of time. (b) Fraction of BSA released as a function of silicon dissolved. (c) Integrated photoluminescence intensity (in range 650 - 800 nm) from particles as a function of fraction of BSA released. (d) Wavelength of maximum photoemission from the Si cores as a function of fraction of BSA released. Error bars represent standard deviation (n=3).

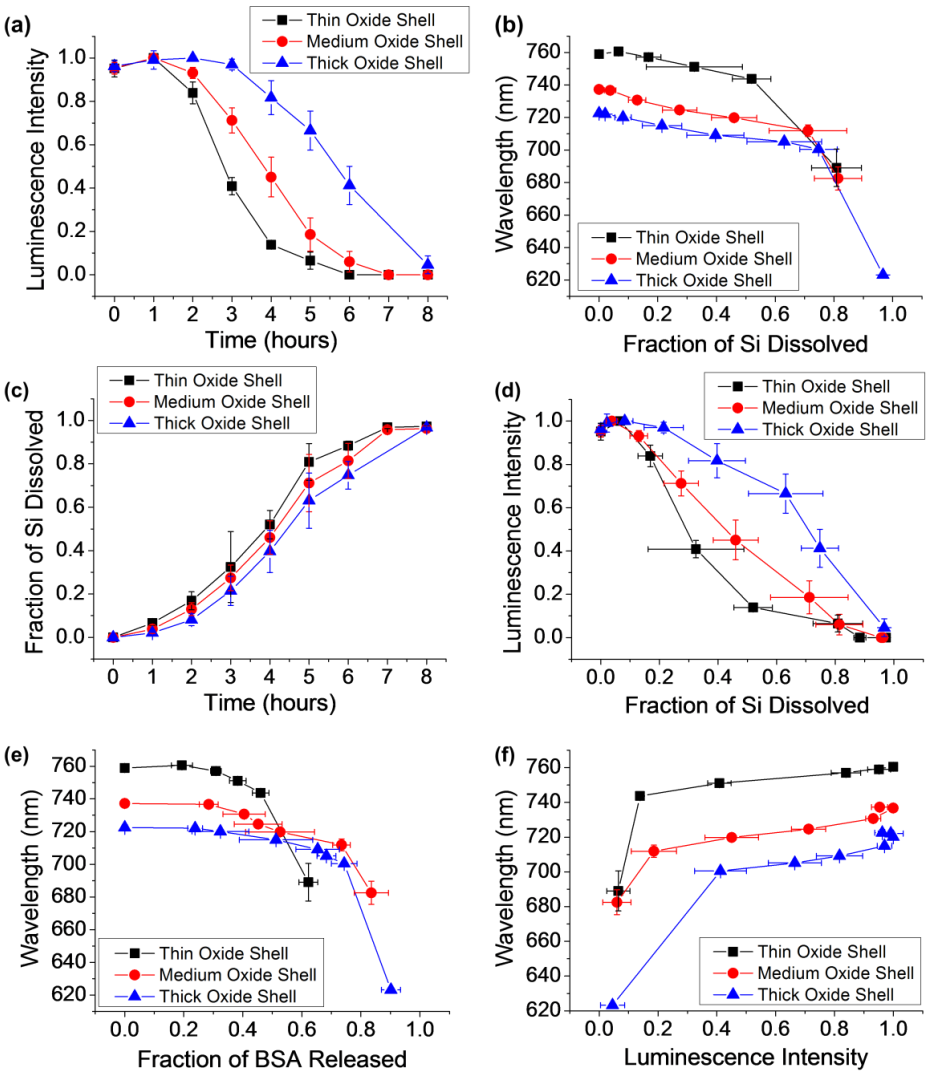

Figure 3.11. Correlations of photoluminescence intensity, photoluminescence wavelength, and fraction of Si dissolved with time exposed to the accelerated dissolution conditions (0.1 M KOH) for three different formulations of core-shell porous Si-SiO_2 particles, loaded with bovine serum albumin (BSA) by the magnesium silicate trapping method. The three formulations were prepared with different SiO_2 shell thickness and core size by thermal oxidation at 700 °C for the indicated times. Traces designated "25 min oxidation", "35 min oxidation", and "45 min oxidation" correspond to the "thin oxide shell", "medium oxide shell", and "thick oxide shell" samples, respectively, as discussed in the text. BSA was trapped in the porous Si-SiO_2 particles by means of precipitation of magnesium silicate concommitant with BSA loading as described in Figure 3.6b. (a) Normalized photoluminescence intensity (λ_{ex} = 365 nm) as a function of time. (b) Wavelength of maximum photoluminescence (λ_{ex} = 365 nm) as a function of time. (c) Fraction of silicon matrix dissolved as a function of time. Mass of dissolved Si was quantified by Molybdenum Blue assay. (d) Normalized photoluminescence intensity as a function of fraction of silicon dissolved. (e) Wavelength of maximum photoluminescence (λ_{ex} = 365 nm) as a function of fraction of silicon dissolved. (f) Wavelength of maximum photoluminescence (λ_{ex} = 365 nm) as a function of normalized photoluminescence intensity. Error bars represent standard deviation (n=3).

3.4.3 BSA Release and Luminescence Correlation in Biologically Relevant *in vitro* Conditions

While the study described up to this point established some design principles that may be useful for self-reporting drug delivery systems, it has several drawbacks that limit its translational relevance: (1) the loading of protein using either of the methods was quite low (2−5%) for most therapeutic applications; (2) the use of very high concentrations (>1 M) of Mg^{2+} in the magnesium silicate trapping method is likely to denature some proteins, reducing their therapeutic efficacy; and (3) the release kinetics measurements were performed under accelerated conditions using a very high pH that is physiologically unrealistic. In order to address these issues, we performed a set of studies using porous Si particles that had been engineered to load more drug under milder conditions, and we performed a longer-term (30 day) release study under more physiologically relevant in vitro conditions. In order to increase the mass loading of protein in the microparticles, the electrochemical conditions for particle preparation were modified1 to approximately double the average pore diameter (Table 3.2, Figure 3.2 and Figure 3.4). These particles are referred to as the "large-pore" samples. The large-pore particles displayed significantly greater mass loading of BSA for both the adsorption and the Mg silicate trapping methods (∼17 and ∼30 wt%, respectively, Table 3.2), compared to the small-pore particles (∼5 and ∼3wt %, respectively, Table 3.1). For the trapping chemistry, the Mg^{2+} ion concentration was lowered to 200 mM. The long-term protein release study was carried out in phosphate-buffered saline (PBS) solution at pH 7.4 and a constant temperature of 37 °C. The data for magnesium silicate-trapped materials are presented in Figure 3.12 and the data for adsorption-loaded material are given in Figure 3.13. Similar to the accelerated release study performed in alkaline solution, photoluminescence decayed more slowly from samples with the thicker oxide shells (Figure 3.12 and Figure 3.13a). The magnesium silicate-trapped material demonstrated minimal burst release of BSA, and release of protein tracked fairly

linearly with dissolution of silicon for all oxide shell thicknesses (Figure 3.12e). By contrast, the adsorption-loaded formulation displayed a pronounced burst that released 20% of the protein within the first 5 days of the 30-day experiment (Figure 3.13e). The long-term release studies showed that the magnesium silicate-trapped samples with a thin oxide shell released protein more rapidly (Figure 3.12b) and dissolved more rapidly (Figure 3.12c) than either of the medium- or thick-oxide shell materials. This difference was not apparent in the accelerated dissolution experiments that were performed in strong KOH solution (Figure 3.10a and Figure 3.11c). Thus particles with a thin oxide shell appear to form the least stable construct with the magnesium silicate-trapping chemistry. By contrast, adsorption-loaded samples dissolved at the same rate under these conditions, regardless of the thickness of their oxide shell (Figure 3.13c). Overall, the long-term release study performed under more physiologically relevant conditions showed more consistent tracking of photoluminescence intensity with BSA release for both loading types and across all oxide thicknesses, compared with the accelerated release study.

3.4.3 Monitoring Photoluminescence by Imaging

To be used as a self-reporting drug-delivery system, the luminescence signature would need to be monitored in vivo. Fluorescence methods in general do not lend themselves to in vivo monitoring due to the low optical transmittance and high optical scattering of live tissues. However, materials administered via subcutaneous, intramuscular, or intraocular injection, or via trans-dermal patch could conceivably be monitored by optical fluorescence. To assess the potential for such remote monitoring, the degradation/dissolution of empty pSi particles was monitored in vitro using a low-cost NIR imaging camera and a UV diode excitation source. Particles were subjected to accelerated dissolution conditions, and luminescence intensity was quantified as integrated intensity as a function of time (Figure 3.14). The decay in luminescence intensity with time

followed a similar trend as was observed with either adsorption loaded (Figure 3.9) or magnesium silicate-sealed (Figure 3.11a) particles.

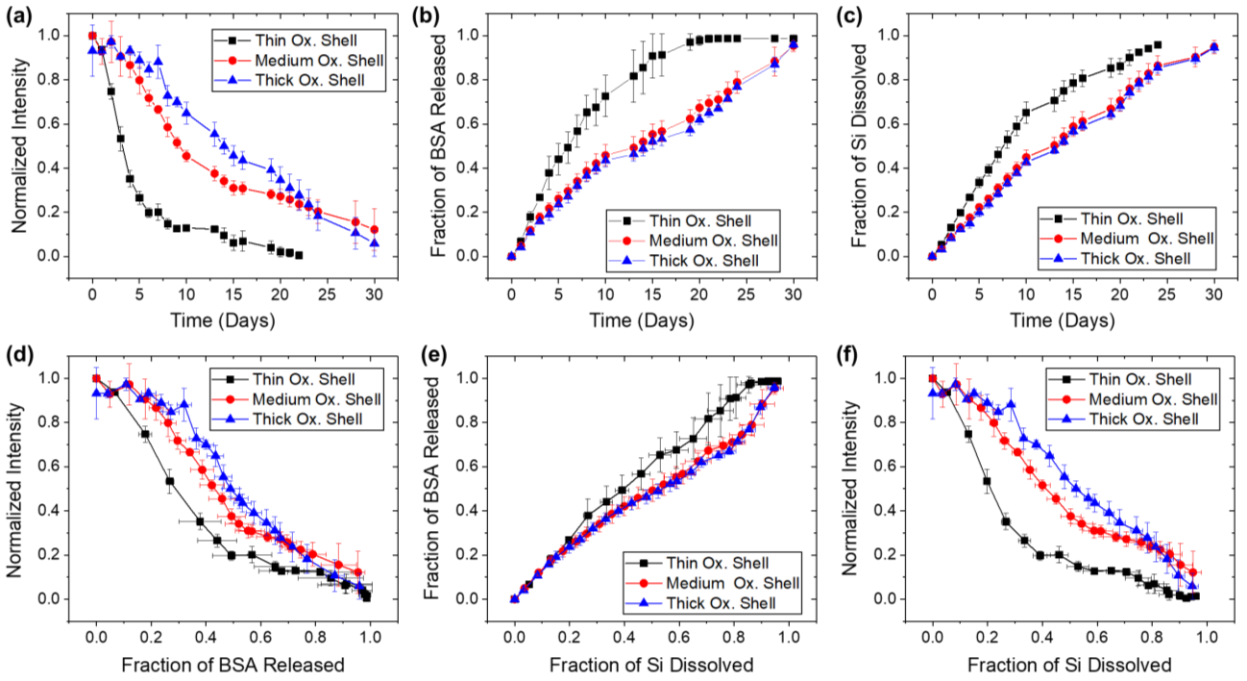

Figure 3.12. Correlations between photoluminescence from the Si skeletal core, protein released, silicon dissolved, and time for trapping-loaded core-shell porous Si-SiO_2 particles as they undergo dissolution in aqueous PBS (pH = 7.4) at 37 °C. The porous Si-SiO_2 particles were prepared with a larger average pore size (20 nm), in contrast to the samples of Fig. 5 (10 nm pores), which resulted in a substantially greater level of protein loaded (see Table 3.2). Protein trapping was achieved by means of precipitation of magnesium silicate as described in Figure 3.6, using 200 mM Mg^{2+}. Traces designated "Thin Ox. Shell", "Medium Ox. Shell", and "Thick Ox. Shell" correspond to pSi particles where the skeletal core was oxidized at 700 °C for 15 min, 20 min, and 30 min, respectively, prior to protein/magnesium silicate loading. (a) Integrated photoluminescence intensity (in wavelength range 600 - 800 nm) from particles as a function of time. (b) Fraction of bovine serum albumin (BSA) released from the particles as a function of time. (c) Fraction of silicon dissolved as a function of time. (d) Integrated photoluminescence intensity from particles as a function of fraction of BSA released. (e) Fraction of BSA released as a function of silicon dissolved. (f) Integrated photoluminescence intensity as a function of fraction of silicon dissolved. Error bars represent standard deviation (n=3).

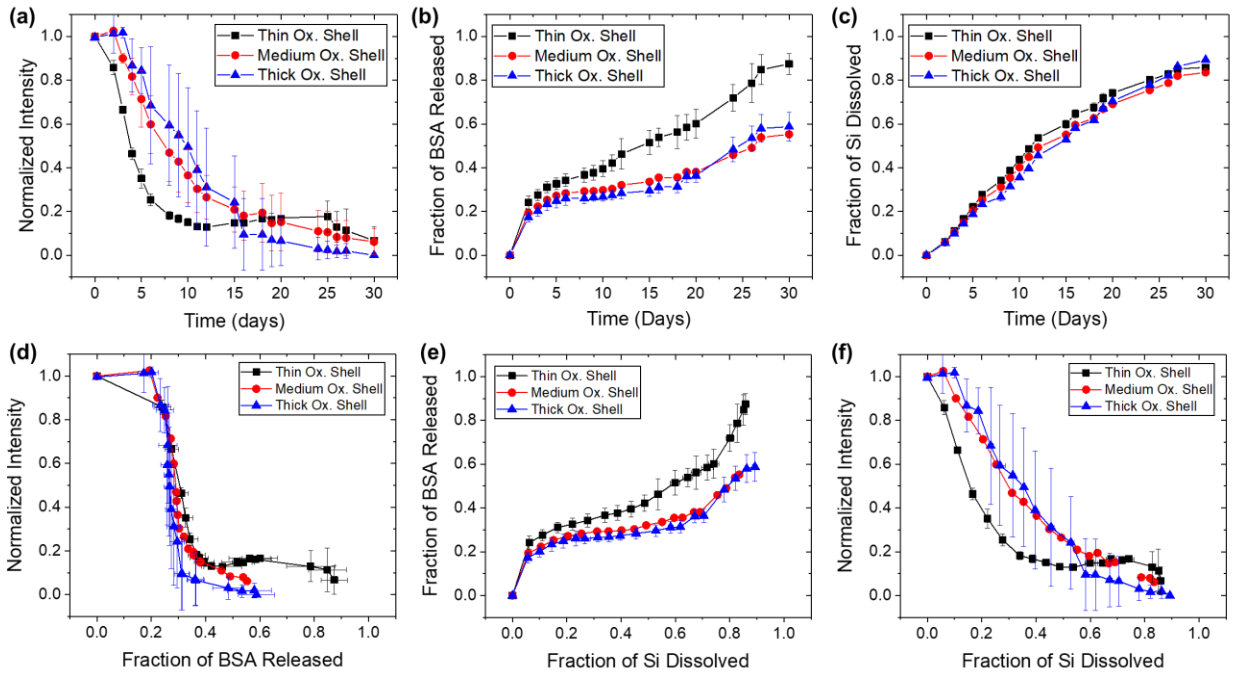

Figure 3.13. Correlations between photoluminescence from the Si skeletal core, protein released, silicon dissolved, and time for adsorption-loaded core-shell porous Si-SiO_2 particles as they undergo dissolution in aqueous PBS (pH = 7.4) at 37 °C. Traces designated "Thin Ox. Shell", "Medium Ox. Shell", and "Thick Ox. Shell" correspond to pSi particles where the skeletal core was oxidized at 700 °C for 15 min, 20 min, and 30 min, respectively, prior to protein loading. (a) Integrated photoluminescence intensity (in wavelength range 600 - 800 nm) from particles as a function of time. (b) Fraction of bovine serum albumin (BSA) released from the particles as a function of time. (c) Fraction of silicon dissolved as a function of time. (d) Integrated photoluminescence intensity from particles as a function of fraction of BSA released. (e) Fraction of BSA released as a function of silicon dissolved. (f) Integrated luminescence intensity as a function of silicon dissolved. Error bars represent standard deviation (n = 2 for the medium oxide shell samples; n = 3 for all other samples).

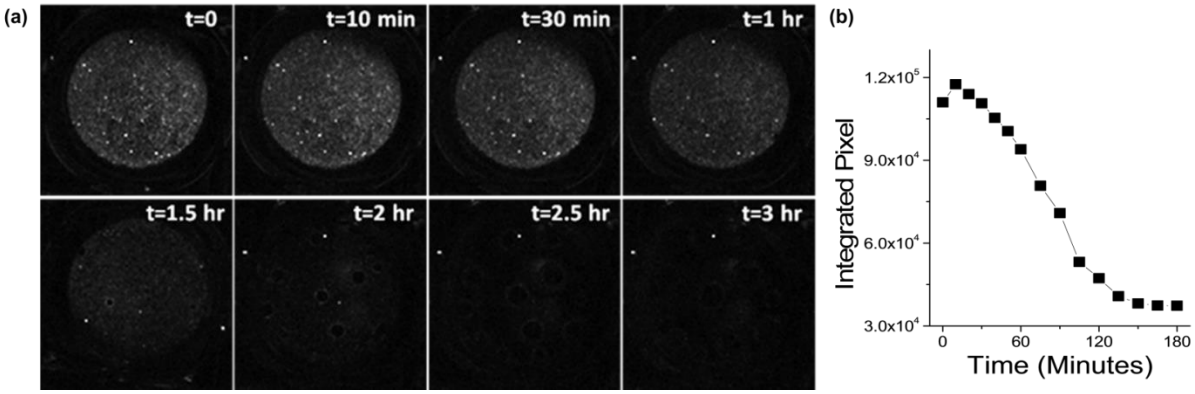

Figure 3.14. Quantification of photoluminescence changes during pSi particle degradation using imaging methods. (a) Photoluminescence images of pSi particles (~ 2mg) dispersed in a microtiter well containing 2M KOH (200 µL), displayed as a time series. Excitation source was a 365 nm light-emitting diode and images were obtained using a NIR camera fitted with a 600 nm long-pass filter. The porous Si particles were prepared by 35-min oxidation at 700 °C, corresponding to the "medium oxide shell" material as discussed in the text. (b) Plot of photoluminescence intensity, integrated as a sum of pixel intensities (ImageJ), as a function of time.

3.5 Conclusion

In conclusion, the present work demonstrated the use of intrinsic photoluminescence of porous silicon microparticles as a self-reporting feature for the degradation of the porous scaffold and the release of a protein payload into aqueous solution. We found that the time at which photoluminescence disappears can be predetermined by controlling the thickness of the protective SiO_2 sheath surrounding the quantum-confined Si features. We compared these temporal profiles for particles that were loaded with protein via two different loading schemes -either by simple adsorption or by physical trapping. For protein that was trapped in the porous particles (via a magnesium silicate precipitation reaction), we found that the temporal profile of the decay in photoluminescence can be used to indicate the time at which the amount of protein remaining in the particles has reached a predetermined level. The magnesium silicate chemistry also suppresses burst release of protein, and it yields a zero-order release kinetic that can be tracked by the photoluminescence signal. We expect that the results of this work will be useful for remote monitoring of payload release for a variety of drug delivery or other controlled release applications.

Chapter 3, in full, is a reprint of the material as it appears Wang, J., Kumeria, T, Bezem, M.T, Wang, J. and Sailor, M.J. Self-reporting Porous Silicon Microparticles for Drug Delivery. Appl. Mater. Interfaces 2017, 10 (4), 3200–3209. The dissertation author was the primary investigator and author of this paper.

3.6 References

1. Allen, T. M.; Cullis, P. R., Drug delivery systems: Entering the mainstream. *Science* **2004,** *303* (5665), 1818-1822.

2. Zhang, L.; Gu, F. X.; Chan, J. M.; Wang, A. Z.; Langer, R. S.; Farokhzad, O. C., Nanoparticles in medicine: Therapeutic applications and developments. *Clin. Pharmacol. Ther.* **2008,** *83* (5), 761-769.

3. Canham, L. T., Bioactive Silicon Structure Fabrication Through Nanoetching Techniques. *Adv. Mater.* **1995,** *7* (12), 1033-1037.

4. Santos, H. A., *Porous Silicon for Biomedical Applications*. Woodhead Publishing, Ltd: Cambridge, UK, 2014.

5. Salonen, J.; Kaukonen, A. M.; Hirvonen, J.; Lehto, V. P., Mesoporous silicon in drug delivery applications. *J. Pharm. Sci.* **2008,** *97* (2), 632-653.

6. Anglin, E. J.; Cheng, L.; Freeman, W. R.; Sailor, M. J., Porous silicon in drug delivery devices and materials. *Adv. Drug Deliv. Rev.* **2008,** *60* (11), 1266–1277.

7. Losic, D.; Simovic, S., Self-ordered nanopore and nanotube platforms for drug delivery applications. *Expert Opin. Drug Deliv.* **2009,** *6* (12), 1363-1381.

8. Liong, M.; Lu, J.; Kovochich, M.; Xia, T.; Ruehm, S. G.; Nel, A. E.; Tamanoi, F.; Zink, J. I., Multifunctional inorganic nanoparticles for imaging, targeting, and drug delivery. *ACS Nano* **2008,** *2* (5), 889-896.

9. Slowing, I. I.; Vivero-Escoto, J. L.; Wu, C. W.; Lin, V. S. Y., Mesoporous silica nanoparticles as controlled release drug delivery and gene transfection carriers. *Adv. Drug Deliv. Rev.* **2008,** *60* (11), 1278-1288.

10. Wang, M. J.; Hartman, P. S.; Loni, A.; Canham, L. T.; Coffer, J. L., Stain Etched Nanostructured Porous Silicon: The Role of Morphology on Antibacterial Drug Loading and Release. *Silicon* **2016,** *8* (4), 525-531.

11. Nieto, A.; Hou, H.; Moon, S. W.; Sailor, M. J.; Freeman, W. R.; Cheng, L., Surface Engineering of Porous Silicon Microparticles for Intravitreal Sustained Delivery of Rapamycin. *Investigative Ophthalmology & Visual Science* **2015,** *56* (2), 1070-1080.

12. Wang, C.; Hou, H.; Nan, K.; Sailor, M. J.; Freeman, W. R.; Cheng, L., Intravitreal controlled release of dexamethasone from engineered microparticles of porous silicon dioxide. *Exp. Eye Res.* **2014,** *129*, 74-82.

13. Zilony, N.; Tzur-Balter, A.; Segal, E.; Shefi, O., Bombarding Cancer: Biolistic Delivery of therapeutics using Porous Si Carriers. *Sci. Rep.* **2013,** *3*.

14. Hartmann, K. I.; Nieto, A.; Wu, E. C.; Freeman, W. R.; Kim, J. S.; Chhablani, J.; Sailor, M. J.; Cheng, L. Y., Hydrosilylated Porous Silicon Particles Function as an Intravitreal Drug Delivery System for Daunorubicin. *J. Ocul. Pharmacol. Ther.* **2013,** *29* (5), 493-500.

15. Godin, B.; Gu, J. H.; Serda, R. E.; Bhavane, R.; Tasciotti, E.; Chiappini, C.; Liu, X. W.; Tanaka, T.; Decuzzi, P.; Ferrari, M., Tailoring the degradation kinetics of mesoporous silicon structures through PEGylation. *J. Biomed. Mater. Res. Part A* **2010,** *94A* (4), 1236-1243.

16. Tzur-Balter, A.; Shatsberg, Z.; Beckerman, M.; Segal, E.; Artzi, N., Mechanism of erosion of nanostructured porous silicon drug carriers in neoplastic tissues. *Nat. Commun.* **2015,** *6*, 6208.

17. Barenholz, Y., Doxil (R) - The first FDA-approved nano-drug: Lessons learned. *J. Control Release* **2012,** *160* (2), 117-134.

18. Hou, H.; Nieto, A.; Belghith, A.; Nan, K.; Li, Y.; Freeman, W. R.; Sailor, M. J.; Cheng, L., A sustained intravitreal drug delivery system with remote real time monitoring capability. *Acta Biomaterialia* **2015,** *24*, 309-321.

19. Horcajada, P.; Chalati, T.; Serre, C.; Gillet, B.; Sebrie, C.; Baati, T.; Eubank, J. F.; Heurtaux, D.; Clayette, P.; Kreuz, C.; Chang, J. S.; Hwang, Y. K.; Marsaud, V.; Bories, P. N.; Cynober, L.; Gil, S.; Ferey, G.; Couvreur, P.; Gref, R., Porous metal-organic-framework nanoscale carriers as a potential platform for drug delivery and imaging. *Nat. Mater.* **2010,** *9* (2), 172-178.

20. McCarthy, J. R.; Weissleder, R., Multifunctional magnetic nanoparticles for targeted imaging and therapy. *Adv. Drug Deliv. Rev.* **2008,** *60* (11), 1241-1251.

21. Janib, S. M.; Moses, A. S.; MacKay, J. A., Imaging and drug delivery using theranostic nanoparticles. *Adv. Drug Deliv. Rev.* **2010,** *62* (11), 1052-1063.

22. Yang, K.; Feng, L.; Shi, X.; Liu, Z., Nano-graphene in biomedicine: theranostic applications. *Chem. Soc. Rev.* **2013,** *42* (2), 530-547.

23. Shubayev, V. I.; Pisanic, T. R.; Jin, S. H., Magnetic nanoparticles for theragnostics. *Adv. Drug Deliv. Rev.* **2009,** *61* (6), 467-477.

24. Zrazhevskiy, P.; Sena, M.; Gao, X. H., Designing multifunctional quantum dots for bioimaging, detection, and drug delivery. *Chem. Soc. Rev.* **2010,** *39* (11), 4326-4354.

25. Weissleder, R.; Schwaiger, M. C.; Gambhir, S. S.; Hricak, H., Imaging approaches to optimize molecular therapies. *Sci. Transl. Med.* **2016,** *8* (355), 355ps16.

26. Lammers, T.; Aime, S.; Hennink, W. E.; Storm, G.; Kiessling, F., Theranostic Nanomedicine. *Accounts Chem. Res.* **2011,** *44* (10), 1029-1038.

27. Nagesha, D. K.; Whitehead, M. A.; Coffer, J. L., Biorelevant calcification and non-cytotoxic behavior in silicon nanowires. *Adv. Mater.* **2005,** *17* (7), 921-+.

28. Low, S. P.; Williams, K. A.; Canham, L. T.; Voelcker, N. H., Evaluation of mammalian cell adhesion on surface-modified porous silicon. *Biomaterials* **2006,** *27* (26), 4538-4546.

29. Coffer, J. L.; Whitehead, M. A.; Nagesha, D. K.; Mukherjee, P.; Akkaraju, G.; Totolici, M.; Saffie, R. S.; Canham, L. T., Porous silicon-based scaffolds for tissue engineering and other biomedical applications. *Phys. Status Solidi A-Appl. Mat.* **2005,** *202* (8), 1451-1455.

30. Park, J.-H.; Gu, L.; Maltzahn, G. v.; Ruoslahti, E.; Bhatia, S. N.; Sailor, M. J., Biodegradable luminescent porous silicon nanoparticles for in vivo applications. *Nat. Mater.* **2009,** *8*, 331-336.

31. Wu, E. C.; Andrew, J. S.; Cheng, L.; Freeman, W. R.; Pearson, L.; Sailor, M. J., Real-time Monitoring of Sustained Drug Release using the Optical Properties of Porous Silicon Photonic Crystal Particles. *Biomaterials* **2011,** *32*, 1957-1966.

32. Xie, Y. H.; Wilson, W. L.; Ross, F. M.; Mucha, J. A.; Fitzgerald, E. A.; Macaulay, J. M.; Harris, T. D., Luminescence and structural study of porous silicon films. *J. Appl. Phys.* **1992,** *71* (5), 2403-2407.

33. Joo, J.; Liu, X.; Kotamraju, V. R.; Ruoslahti, E.; Nam, Y.; Sailor, M. J., Gated Luminescence Imaging of Silicon Nanoparticles. *ACS Nano* **2015,** *9* (6), 6233–6241.

34. Sailor, M. J., *Porous Silicon in Practice: Preparation, Characterization, and Applications*. Wiley-VCH: Weinheim, Germany, 2012; p 249.

35. Segal, E.; Perelman, L. A.; Cunin, F.; Renzo, F. D.; Devoisselle, J.-M.; Li, Y. Y.; Sailor, M. J., Confinement of Thermoresponsive Hydrogels in Nanostructured Porous Silicon Dioxide Templates. *Adv. Funct. Mater.* **2007,** *17*, 1153–1162.

36. Petrova-Koch, V.; Muschik, T.; Kux, A.; Meyer, B. K.; Koch, F.; Lehmann, V., Rapid thermal oxidized porous Si- the superior photoluminescent Si. *Appl. Phys. Lett.* **1992,** *61* (8), 943-945.

37. Cullis, A. G.; Canham, L. T.; Calcott, P. D. J., The structural and luminescence properties of porous silicon. *J. Appl. Phys.* **1997,** *82* (3), 909-965.

38. Gelloz, B.; Koshida, N., Highly enhanced photoluminescence of as-anodized and electrochemically oxidized nanocrystalline p-type porous silicon treated by high-pressure water vapor annealing. *Thin Solid Films* **2006,** *508* (1-2), 406-409.

39. Ray, M.; Sarkar, S.; Bandyopadhyay, N. R.; Hossain, S. M.; Pramanick, A. K., Silicon and silicon oxide core-shell nanoparticles: Structural and photoluminescence characteristics. *J. Appl. Phys.* **2009,** *105* (7).

40. McInnes, S. J. P.; Voelcker, N. H., Silicon-polymer hybrid materials for drug delivery. *Future Med. Chem.* **2009,** *1* (6), 1051-1074.

41. Joo, J.; Cruz, J. F.; Vijayakumar, S.; Grondek, J.; Sailor, M. J., Photoluminescent Porous Si/SiO2 Core/Shell Nanoparticles Prepared by Borate Oxidation. *Adv. Funct. Mater.* **2014,** *24*, 5688-5694.

42. Wolkin, M. V.; Jorne, J.; Fauchet, P. M.; Allan, G.; Delerue, C., Electronic states and luminescence in porous silicon quantum dots: The role of oxygen. *Phys. Rev. Lett.* **1999,** *82* (1), 197-200.

43. Sa'ar, A., Photoluminescence from silicon nanostructures: The mutual role of quantum confinement and surface chemistry. *J. Nanophotonics* **2009,** *3*, 032501.

44. Wilson, W. L.; Szajowski, P. F.; Brus, L. E., Quantum Confinement in Size Selected, Surface-Oxidized Si Nanocrystals. *Science* **1993,** *262*, 1242-1244.

45. Zacharias, M.; Heitmann, J.; Scholz, R.; Kahler, U.; Schmidt, M.; Blasing, J., Size-controlled highly luminescent silicon nanocrystals: A SiO/SiO2 superlattice approach. *Appl. Phys. Lett.* **2002,** *80* (4), 661-663.

46. Ledoux, G.; Guillois, O.; Porterat, D.; Reynaud, C.; Huisken, F.; Kohn, B.; Paillard, V., Photoluminescence properties of silicon nanocrystals as a function of their size. *Physical Review B* **2000,** *62* (23), 15942-15951.

47. Delerue, C.; Allan, G.; Lannoo, M., Theoretical aspects of the luminescence of porous silicon. *Physical Review B* **1993,** *48* (15), 11024-11036.

48. Campbell, I. H.; Fauchet, P. M., The effects of microcrystal size and shape on the one phonon Raman spectra of crystalline semiconductors. *Solid State Communications* **1986,** *58* (10), 739-741.

49. Kanemitsu, Y.; Uto, H.; Masumoto, Y.; Matsumoto, T.; Futagi, T.; Mimura, H., Microstructure and optical properties of free-standing porous silicon films: Size dependence of absorption spectra in Si nanometer-sized crystallites. *Physical Review B* **1993,** *48* (4), 2827-2830.

50. Li, B. B.; Yu, D. P.; Zhang, S. L., Raman spectral study of silicon nanowires. *Phys. Rev. B* **1999,** *59* (3), 1645-1648.

51. Su, T. J.; Lu, J. R.; Thomas, R. K.; Cui, Z. F., Effect of pH on the adsorption of bovine serum albumin at the silica/water interface studied by neutron reflection. *J. Phys. Chem. B* **1999,** *103*, 3727-3736.

52. Perelman, L. A.; Pacholski, C.; Li, Y. Y.; VanNieuwenzhe, M. S.; Sailor, M. J., pH-Triggered Release of Vancomycin from Protein-Capped Porous Silicon Films. *Nanomedicine* **2008,** *3* (1), 31-43.

53. Kang, J.; Joo, J.; Kwon, E. J.; Skalak, M.; Hussain, S.; She, Z.-G.; Ruoslahti, E.; Bhatia, S. N.; Sailor, M. J., Self-Sealing Porous Silicon-Calcium Silicate Core–Shell Nanoparticles for Targeted siRNA Delivery to the Injured Brain. *Adv. Mater.* **2016,** *28*, 7962-7969.

54. Anderson, S. H. C.; Elliott, H.; Wallis, D. J.; Canham, L. T.; Powell, J. J., Dissolution of different forms of partially porous silicon wafers under simulated physiological conditions. *Phys. Status Solidi A-Appl. Res.* **2003,** *197* (2), 331-335.

55. Wang, Y.; Wang, G.; Wang, H.; Liang, C.; Cai, W.; Zhang, L., Chemical-Template Synthesis of Micro/Nanoscale Magnesium Silicate Hollow Spheres for Waste-Water Treatment. *Chem. Eur. J.* **2010,** *16* (11), 3497-3503.

56. Mullin, J. B.; Riley, J. P., The colorimetric determination of silicate with reference to sea and natural waters. *Anal. Chim. Acta* **1955,** *12*, 162-176.

57. Low, S. P.; Voelcker, N. H.; Canham, L. T.; Williams, K. A., The biocompatibility of porous silicon in tissues of the eye. *Biomaterials* **2009,** *30* (15), 2873-2880.

58. Chen, M. Y.; Sailor, M. J., Charge-Gated Transport of Proteins in Nanostructured Optical Films of Mesoporous Silica. *Anal. Chem.* **2011,** *83*, 7186-7193.

CHAPTER FOUR

SELF-REPORTING POROUS SILICON MICROPARTICLES IN THE EYE

4.1 Abstract

The luminescence of porous silicon particles was employed as a self-reporting tool to monitor the release of a small molecule steroid, triamcinolone acetonide for ophthalmic therapeutics. Correlations between the pharmacokinetics and luminescence decay was established in both in vitro and in vivo (rabbit eye) studies. We demonstrate that the luminescence can be tracked over time by imaging using a modified fundus camera that is used in routine clinical practice and without the use of high energy lasers or light sources that may damage the retina. The imaging analysis demonstrate that decay in luminescence can be employed to track the real-time concentration of TA in the vitreous and predict when TA is no longer being released.

4.2 Introduction

Long-lasting formulations in the eye has introduced a new paradigm to chronic ocular therapy.[1-2] Unlike eye drops or gels, therapeutics that are directly injected into the vitreous chamber of the eye allow drug molecules to reach the retina without the need to cross the sclera.[3-4] Due to the invasive nature of injection, high cost and patient discomfort, frequent injection of therapeutic is highly undesirable[5-6] and has led many researchers and companies to develop formulations that are able to maintain therapeutic concentrations of drug (e.g. dexamethasone) within the vitreous for long time scales.[7-9] These exciting advances has led to new FDA approved therapies in the last 10-15 years including Ozurdex (PLGA rod, dexamethasone, Allergan) and Triesence (crystalline particulates, triamcinolone acetonide, Alcon).[10-11]

The pharmacokinetics of long-lasting formulations are determined not only by its form, but also by the turnover rate of liquid in the eye and vitreous rheology.[12] The pharmacokinetic dependence on individual ocular rheological conditions results in high patient to patient variability due to liquefication of the vitreous and aggregation of intraocular hyaluronic acid and collagen

with age and disease condition. Additionally, surgical procedures such as vitrectomy has been well documented to reduce the half-life of intraocular therapeutics.[13-14] While the therapeutic duration of a given drug is approximated by large scale clinical trial, smart formulations that can inform physicians of the real-time pharmacokinetics, such as drug concentration in the vitreous, release rate, or the amount of drug remaining, will enable ophthalmologists to customize treatment plans for individual patients and prevent over/underdosing, which can lead to side effects or faster disease progression.

In this work, we employ luminescent porous silicon particles as a self-reporting probe that can inform the release kinetics of a loaded small molecule drug, triamcinolone acetonide. Because fluorescence imaging in the vitreous is a commonly performed clinical diagnostic, only minor modifications (such as adding appropriate filters to accommodate silicon excitation/emission) are necessary to allow existing fundus imaging systems to image silicon particles in vivo. Porous silicon particles have already been shown by us and others to be biocompatible/biodegradable in the eye and other tissues.[15-16] Additionally, it has been employed as a drug delivery carrier for many different types of therapeutics such as oligonucleotides,[17-19] antibodies[20] and small molecules.[21-22] The beauty of porous silicon self-reporting systems is that no additional chemical modification or additive is required provide a sensing output.[23] Instead, the silicon skeleton itself can be quantum confined by oxidation into a 1D wire and display luminescence in the visible-near IR wavelengths.[24-26] Additionally, the luminescence signature is dependent on the size and number of crystalline silicon emission centers.[27] During degradation, 1D wire becomes narrower and silicon oxidizes and dissolves into silicic acid. These structural changes cause the luminescent signature to blue shift in wavelength and decrease in intensity.[28-29] These properties allow us to conveniently track particle degradation in vivo and indirectly probe the release of drug. While

previous work has demonstrated the self-reporting concept using bovine serum albumin as a model drug,[30] this work seeks to use a therapeutic, triamcinolone acetonide, and test the luminescent correlation in vivo.

4.3 Materials and Experimental Methods

4.3.1 Materials

Silicon wafers, polished on the (100) face, boron-doped (p-type), resistivity <1.5 mΩ·cm were obtained from Virginia Semiconductor, Inc. or from Siltronix. Absolute ethanol (200 proof) was obtained from Rossville Gold Shield Chemicals.

4.3.2 Synthesis of Porous Silicon (pSi) Microparticles

Porous silicon particles were synthesized by electrochemical etching of single crystalline silicon wafers (highly boron doped) in ethanolic HF (3:2 49% HF to EtOH). A 3-layer perforated etch was applied using a three-step waveform at 80 mA/cm^2 for 720 s, 167 mA/cm^2 for 1 s and 0 mA/cm^2 for 1 s. The high current step generated high porosity layers to facilitate pSi fracture at the desired film depth during sonication. The last step was applied to allow HF diffusion and prevent local depletion of HF near the Si interface. The three-step waveform was repeated three times and followed by an electropolishing step using 3.33% HF (49% HF diluted in ethanol) and a current of 4.2 mA/cm^2 for 550 s. The electropolishing step allowed removal of the porous film from the bulk wafer and the films were ultrasonicated (VWR Ultrasonic Cleaner) in ethanol at 90-minute intervals. Between each interval, the particles were settled and separated three times to remove large and nano- particles. The particles were stored in ethanol to prevent oxidation in air.

4.3.3 Luminescence Activation of Porous Silicon Microparticles

Porous silicon particles (1 mg/mL) were soaked in ethanol and either Tris buffered saline (TBS) (pH 7.4, 1X, Fisher Scientific), borate buffer (pH 9, Sigma Aldrich), or phosphate buffered saline (PBS) (pH 7.4, 1X, Life Technologies) at a ratio of 100:4 buffer to EtOH. The particles were stirred gently in a cuvette, illuminated with a 365 nm LED (Ocean Optics) and a spectrum was collected every 2-10 minutes. The optimal luminescence activation time was determined as the time for the largest integrated intensity over 500-1100 nm respectively.

To calculate the quantum yield, particles were agitated on a rotating wheel in the same respective ethanolic buffers mentioned above. The buffer was removed and the particles were washed 3 times in water and 3 times in ethanol (1 mg/mL) at the predetermined optimal activation time. The particles were dried in an oven at 80ºC and placed on double sided tape on a glass slide. The quantum yield was collected using a 365 nm LED in an integrating sphere connected to an Ocean Optics Pro spectrometer. A clean glass slide with double sided tape was employed as a blank control.

Prior to drug loading, pSi particles were soaked in TBS buffer for eight hours and agitated on a spinning wheel. After luminescence activation, the particles were settled and washed twice in water (1 mg/mL) and three times in ethanol (1 mg/mL). The particles were heated in a tube furnace at 200ºC for 2 hrs.

4.3.4 Surface Modification, Triamcinolone Acetonide Loading and Pluronic Coating in Porous Silicon Microparticles

After TBS activation and thermal annealing, particles were functionalized with octyl trimethoxy silane (sigma Aldrich) by soaking in 5 vol% silane in non-anhydrous toluene (10 mg of pSi to 1 mL of silane solution). The reaction was agitated by gentle stirring and heating in a

sand bath at 70ºC for 18 hrs. After the reaction, the particles were washed three times with toluene and twice with ethanol (10 mg/mL). The particles were dried in an oven at 80ºC for 30 min.

For drug loading, particles (50 mg/mL) were soaked in a solution of triamcinolone acetonide dissolved in dimethyl sulfoxide (DMSO) (90 mg/mL) for 18 hrs. After loading, particles were washed once in 30 vol% ethanol water followed by 10 vol% ethanol in water (50 mg/mL). To thoroughly remove the solvent, the particles were placed in a vacuum oven and, under vacuum, heated to 180ºC and maintained for 1 hr. The oven was allowed to cool back to room temperature under vacuum before the particles were removed.

For better dispersibility in aqueous buffers, TA loaded particles (50 mg/mL) were soaked in a 0.5 wt% pluronic solution in MilliQ water for 30 min and agitated on a rotating wheel. The particles were washed with MilliQ water (50 mg/mL) three times and dried in a vacuum desiccator at room temperature.

4.3.5 Particle Imaging with SEM Microscopy

Particles were imaged using a Zeiss Sigma 500 scanning electron microscope (SEM). The SEM was set to an acceleration voltage of 3kV, InLens secondary electron detector, working distance of 3-4 mm and an aperture of 30μm.

4.3.6 Nitrogen Adsorption Measurements for Porosity, FTIR Spectroscopy and TGA

Nitrogen adsorption/desorption isotherms were recorded with a Micromeritics ASAP2020 and set to collect as 5 point analysis mode at 77K. The particles were degassed at 150°C prior to analysis.

Attenuated total reflectance Fourier transform infrared (ATR-FTIR) spectra were collected using a Thermo Scientific Nicolet 6700 FTIR instrument with a Smart iTR diamond ATR fixture (128 averages).

Thermal gravimetric analysis (STA 6000, Perkin Elmer) was employed to quantify silane grafting, TA loading, and pluronic coating efficiency. Particles (5-10 mg) were placed on ceramic pan (pre-burned to remove contaminates) and heated to 800ºC at10ºC/min, held at 800 ºC for 1 min, and cooled to 30ºC at 10ºC/min. Oxygen flowed through the chamber at 20 mL/min.

4.3.7 In Vitro Study

Porous silicon particles (3 mg) were placed in each of a 3 chamber custom machined flow cell following the addition of 1.5 mL of Hank's balanced salt solution (HBSS). The HBSS was pulled through custom designed flow cell at 5 µL/min and into 15 mL falcon tubes using an Ismatec 12 channel peristaltic pump (IPC-N) and tubing (2-Stop LMT-55 Tubing, length - 16") with an inner diameter (ID) of 0.13mm. The falcon tubes were changed daily. The flow cell had a quartz window on each chamber lid and particles were imaged at each time point.

Particle imaging was performed using a point grey camera and excited with a 385 nm light source. The excitation light reached the sample by reflecting from a dichroic mirror (530 nm, 45°) and the image was collected after passing through a 700 nm longpass filter. A rhodamine B standard in a flat cuvette was employed to correct for any differences in excitation light intensities during the release study.

4.3.8 In Vivo Study

The eyes of 4 pigmented New Zealand rabbits were injected with of C3F8 gas to liquify the vitreous three weeks prior to the study. Before injection, particles were rinsed once with 200 uL of sterile balanced salt solution (BSS). All animal studies were performed according to the ARVO statement for the Use of Animals in Ophthalmic and Vision Research, and were approved by The Institutional Animal Care and Use Committee of University of California, San Diego. For the intravitreal injection procedure, the rabbits were anesthetized with subcutaneous injections of

25 mg/kg ketamine (Fort Dodge Animal Health) and 4 mg/kg xylazine (Akorn Inc.). Slit lamp and indirect ophthalmoscopy were performed on all animal eyes before injection. The rabbits eyes were dilated using 1-2 drops of 1% tropicamide (Akorn) and 2.5% phenylephrine hydrochloride (Akorn) and locally anesthesia was given using 0.5% proparacaine (Akorn) eye drops. Particles (3 mg) dispersed in sterile BSS were injected into the midvitreous cavity of the right eye under direct view of a surgical microscope and using a 27 1/2 gauge insulin syringe (BD). As a toxicity control, BSS was injected into the left eye following the same procedure. Color fundus photographs using a Cannon T2i were taken at each exam.

For all time points, the eyes were examined using slit lamp biomicroscopy, a handheld tonometer (Tonopen, Medtronic) for intraocular pressure (IOP), and indirect ophthalmoscopy. Anterior chamber inflammatory cells, local vitreous opacities, and general vitreous clarity were scored during fundus exams to monitor toxicity. The luminesce of the particles were imaged using a modified fundus imaging system (Canon C60-U) and connected to a CoolSnap HQ2 (Photometrics) black and white cooled CCD. The white flash of the imaging system was filtered using a 532 nm shortpass. At each flash, the image was split on a dichroic mirror (600 nm) and passed through a 700 nm longpass filter before reaching the CCD. Vitreous taps (<50 μL) were performed using the same animal protocol described above and using a 27 1/2-gauge syringe. At the end of the study, rabbits were sacrificed using a standard procedure previously published.[31] Eyes were enucleated and dissected for histology and other analysis.

4.3.9 High performance liquid chromatography (HPLC) – UV-Vis

To quantify the concentration of TA for the in vitro study, 0.5-1 mL of the release solution was placed into glass HPLC sampling vials (2 mL - 9 mm clear glass screw thread vials, Thermo Fisher). The samples were then analyzed with an UltiMate™ 3000 Rapid Quaternary System

UHPLC (Thermo Fisher) equipped with a C18 reverse phase column (silica 5 µm particle, 150 mm, max pressure: 4500 psi, Thermo Fisher). The triamcinolone concentration in each sample was determined by comparison to a standard calibration curve (freshly prepared for each run).

4.3.10 HPLC – Mass Spectroscopy

The vitreous taps were stored at -20 °C until analysis. The fluid from each tap (20 µL) was mixed with 100 µL acetonitrile (HPLC grade, Fisher Chemicals) and allowed to sit for 2 hr. The sample was then centrifuged at 12,500 rpm for 20 min. and 110 µL of the supernatant was removed to a separate tube. As an internal standard, 10 µL of 200 ng/mL of ketorolac (Cayman Chemical, purity >95%) dissolved in ethanol was added to the mixture. As a control and using the same internal standard, triamcinolone acetonide and blank (internal standard only) samples were prepared using the same method. The samples were placed under vacuum until all the solvent had evaporated, and the solids were resuspended in 100 µL of HPLC grade acetonitrile and placed in glass autosampler tubes. The samples were analyzed with an Agilent 1260 liquid chromatograph (LC) system coupled with a Thermo LCQdeca mass spectrometer using positive ion mode electrospray ionization (ESI) as the ion source. The ESI voltage was set at 5 kV with sheath gas flow rate of 80 units, auxiliary gas flow rate of 20 units and capillary temperature of 250 °C. The concentration of triamcinolone (ng/mL) in each sample was calculated by normalization to the internal standard and comparison to the standard curve.

4.3.11 Rabbit Eye Histology

Rabbit eye histology was performed on eyecups that were fixed (immediately after sacrifice) in Davidson's for 24 hours before being processed for paraffin embedding. The paraffin sections were stained with hematoxylin and eosin (H&E).

4.4 Results and Discussion

4.4.1 Luminescence Activation of Porous Silicon Microparticles

In order to track the decay luminescence of particles overtime, the luminescence signature of the particles must have as strong quantum yield (QY) to enable signal capture and quantification in vivo and with the fundus camera or respective imaging device. Previous methods of activating luminescence include borate solution aging[29] and thermal oxidation[32]. While thermal oxidation provides a stable and robust shell around the crystalline Si core[33], the typical quantum yield is <10% and cannot be captured using the fundus setup employed in this work. While the quantum yield of borate oxidation can reach up to ~20-25% QY,[29] the oxidation conditions are typically carried out in high pH which may cause significant particle degradation and thus shortening the luminescence stability and drug elution time. In order to synthesize long lasting particles with high quantum yield, we compared three commercially available and commonly used buffers as the aging solution for activating the luminescence of porous silicon. Borate buffer (pH 9), Tris buffered saline (TBS) (pH 7.4) and phosphate buffered saline (PBS) (pH 7.4) were selected for ease of experimentation and reproducibility.

Porous silicon films were synthesized by electrochemical etching of single crystalline wafers using ethanolic HF (3:2 49% HF to ethanol). A perforated waveform was employed to create three layers of ~38 μm thick films and separated by high porosity layers (Figure 4.1).[34] Nitrogen adsorption measurements (Figure 4.2) and scanning electron imaging (Figure 4.3) revealed that the etch generated an average pore diameter of 19 nm. Porous silicon films were removed from the wafer by an electropolishing etch. The films were ultrasonicated and nanoparticles suspended in supernatant were removed after microparticle sedimentation. The sonication process yielded porous silicon microparticles of ~65 μm (Figure 4.4). Particles were

kept in ethanol after the etch and was never allowed to dry to maintain the scaffold structural integrity and prevent pore collapsing, which has been reported to reduce the quantum yield[35]. To activate the luminescence, particles were soaked in 100:4 ratio of buffer to ethanol at a concentration of 1 mg/mL in a cuvette and stirred. Spectroscopic measurements (λ_{ex}=365 nm) were employed to measure the luminescence activation of the particles over time and to determine the optimal luminescence activation time (Figure 4.5).

Not surprisingly, the wavelength and peak shift kinetics appear to have similar shape but occur over different time scales indicating that the luminescence activation mechanism is the same for all three buffers. While the wavelength redshifted initially, it occurs over low intensity regions suggesting that small regions of the particle (such as the edges), that has presumably finer features, activate at shorter time scales and at lower wavelengths. Overtime, the skeleton with larger features starts to oxidize and is attributed to the red shift of the signal. Once the majority of the skeleton has oxidized, the wavelength begins to uniformly blue shift. At this wavelength transition, the intensity of the luminescence began to grow more rapidly and validates previous work that suggest the oxide layer caps off surface states and shields the silicon from significant quenching in water.

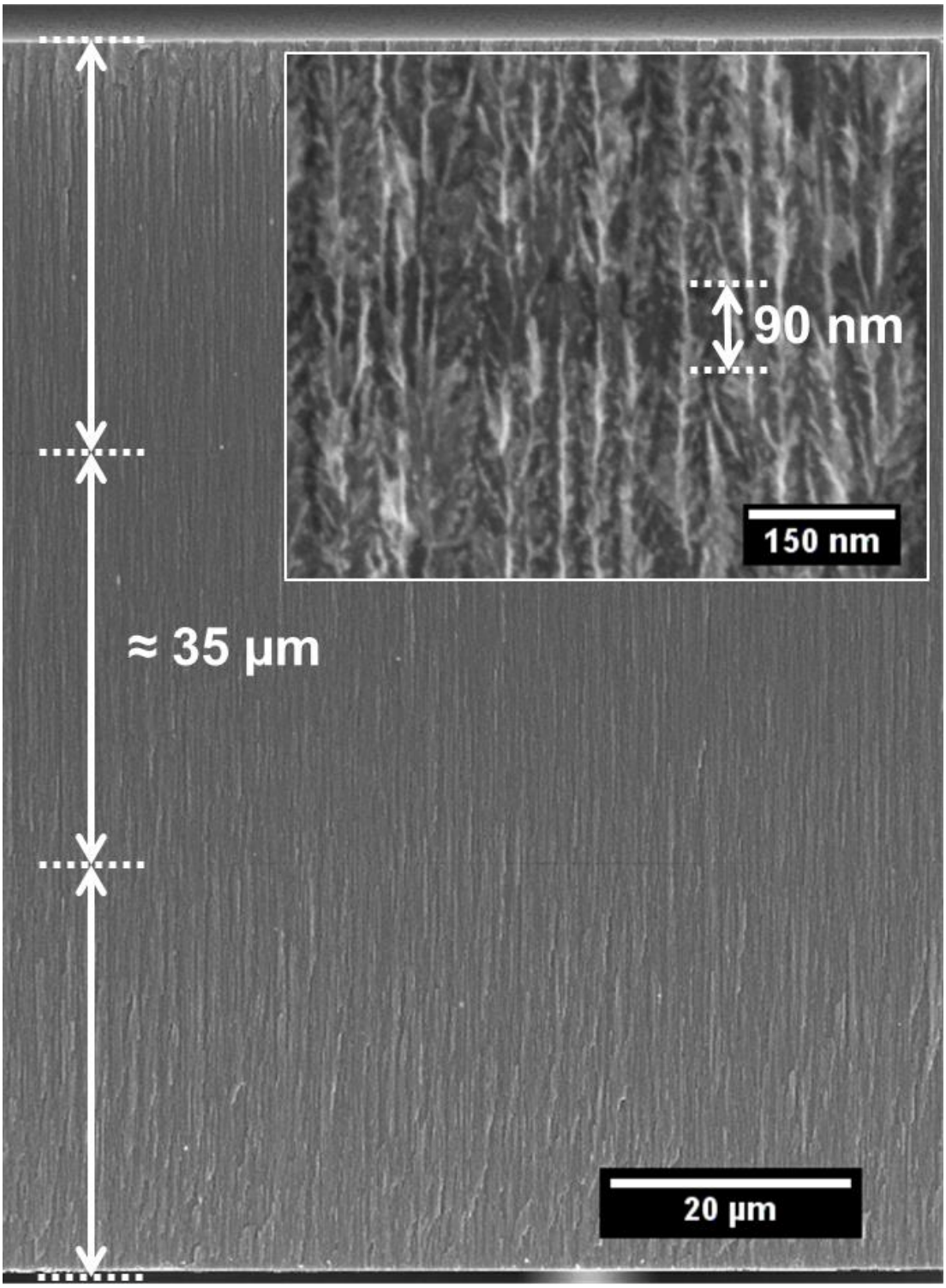

Figure 4.1. Cross sectional scanning electron microscope images of a typical porous silicon layer showing three layers, each ~34 µm, and segregated by ~90 nm high porosity layers.

(a)

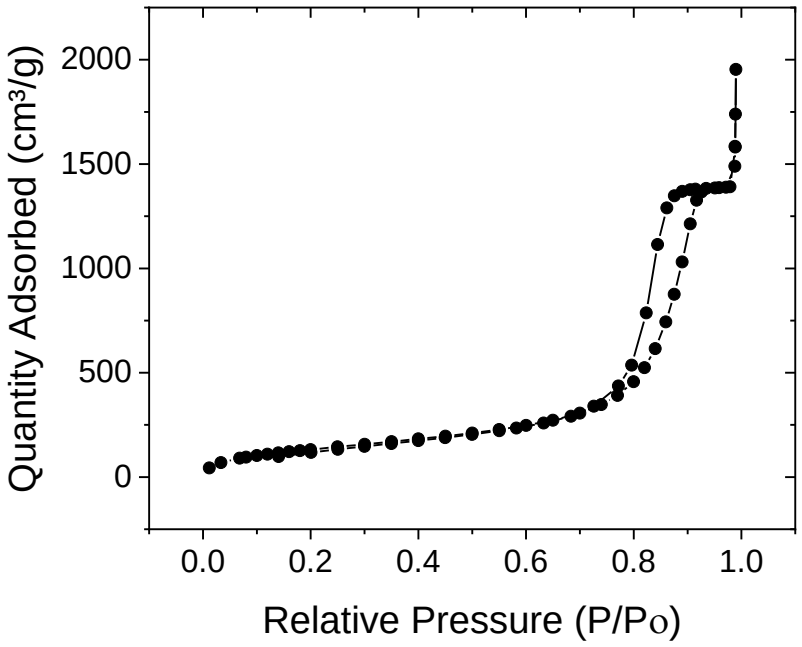

(b)

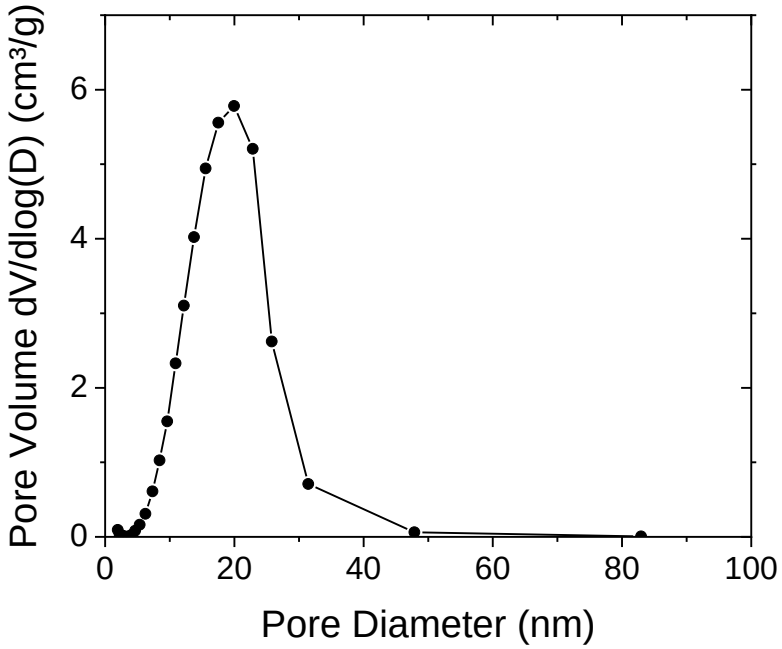

Figure 4.2. The (a) nitrogen adsorption isotherm and (b) the BJH adsorption approximation for pore volume versus pore diameter.

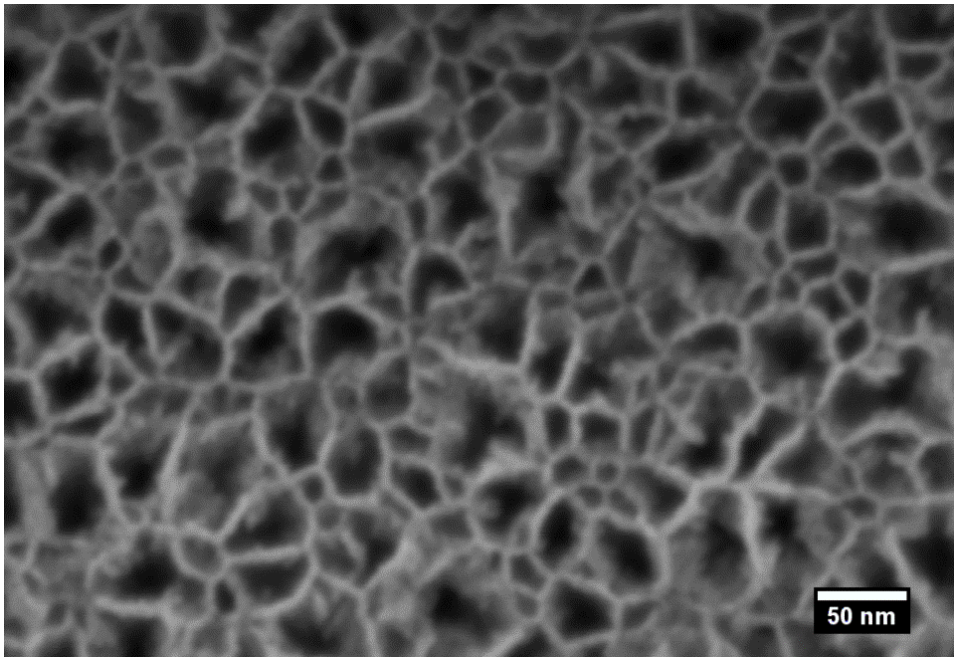

Figure 4.3. Scanning electron microscope image of the pore morphology of typical porous silicon films that were employed to fabricate the particles prior to oxidation and TA loading.

Figure 4.4. Microscope images of porous silicon particles after sonication.

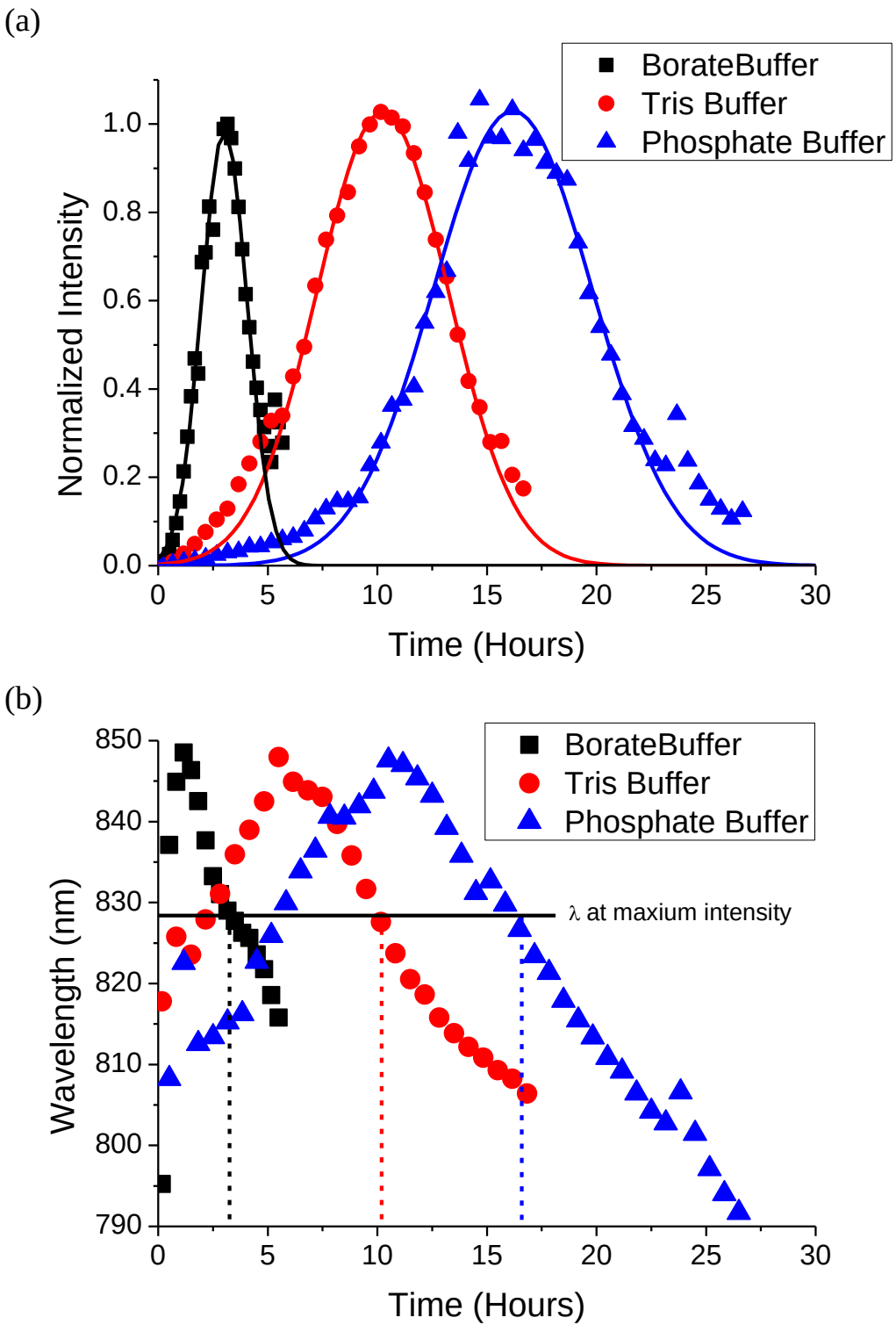

Figure 4.5. Spectral characterization of luminescence activation in borate, tris, of phosphate buffer. The changes in (a) integrated intensity and (b) wavelength over time appears to follow similar trends but at different time scales. The time at which the luminescence intensity is the highest was noted for particle stability studies.

After finding the optimal activation time for the brightest luminescence, particles were soaked in the respective buffers for the predetermined duration and concentration. Particles were washed three times in water and ethanol, dried, and imaged with a microscope. The microscope images revealed severe cracking of borate-soaked particles suggesting the skeleton has degraded more extensively relative to the other buffers (Figure 4.6). Particles treated with TBS exhibited mild cracking and, with PBS, no cracking at all. These results are expected as the high pH of borate may be more corrosive to the silicon than the near neutral pH of the other buffers. Compared to PBS, Tris contains amine groups that may facilitate faster degradation of the matrix and more extensive reprecipitation of silica onto the particle surface. We selected Tris as our activating buffer because of the shorter activation time and does not significantly compromise particle stability.

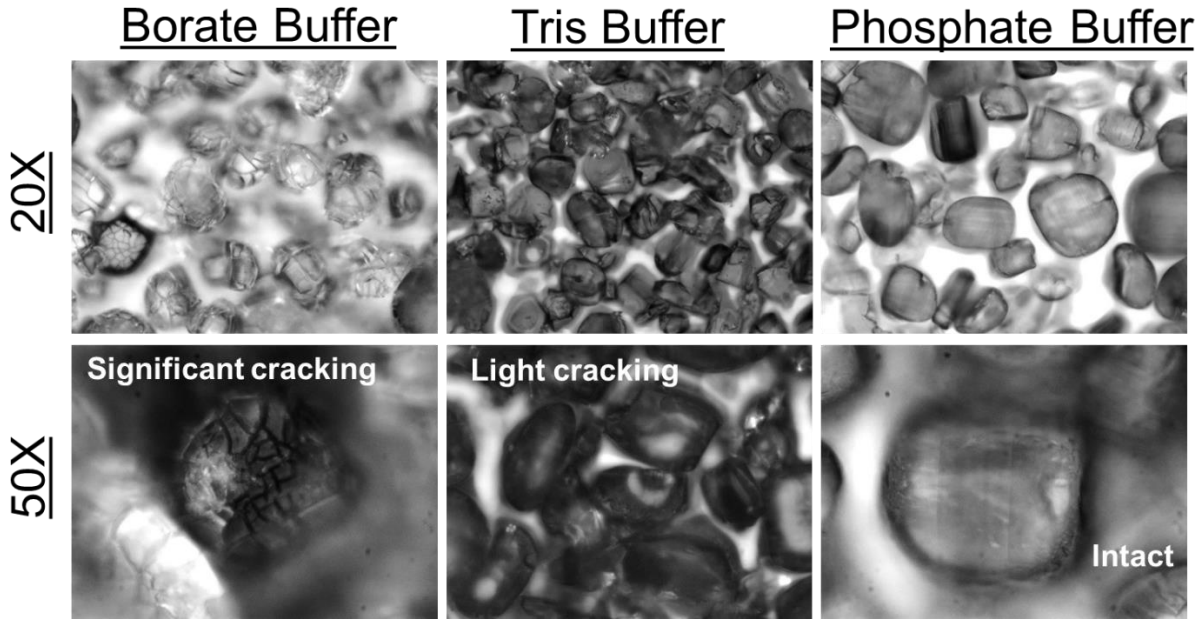

Figure 4.6. Microscope images collected using a 20X and 50X objective lens of particles soaked in borate, tris, or phosphate buffer to the predetermined time for optimal luminescence intensity. Due to the high pH, borate particles displayed significant cracking indicating that the particles were the least stable. Particles soaked in tris buffered had mild cracking and particles in phosphate buffer, or the mildest buffer employed in this study, had minimal cracking.

4.4.2 Surface Modification for Loading of Triamcinolone Acetonide

Surface modification of particles were selected to improve drug adhesion to the particle and injectability of the particles in the eye (Figure 4.7). After selecting Tris buffer, particles were thermally annealed in a tube furnace at 200°C for two hours (higher temperatures would cause significant changes in the particle oxidation and luminescence properties). Particles were functionalized with octyl groups so that it will have stronger electrostatic interactions with triamcinolone acetonide (TA), a hydrophobic steroid for treating chronic uveitis. TA was adsorption loaded into the functionalized particles by soaking in concentrated drug solution in DMSO. After washing, residue DMSO was found by thermal gravimetric analysis (TGA) (not shown) in the samples due to mass loss starting at ~180-190°C. To thoroughly remove DMSO, particles were heated to 180°C for 1 hr under vacuum. Following loading, particles were coated with pluronic so to improve dispersity of the particles in buffer for injection. Successful C8 grafting, TA loading, and pluronic coating was characterized by TGA (Table 4.1) and Fourier transform infrared spectroscopy (FTIR) (Figure 4.8).

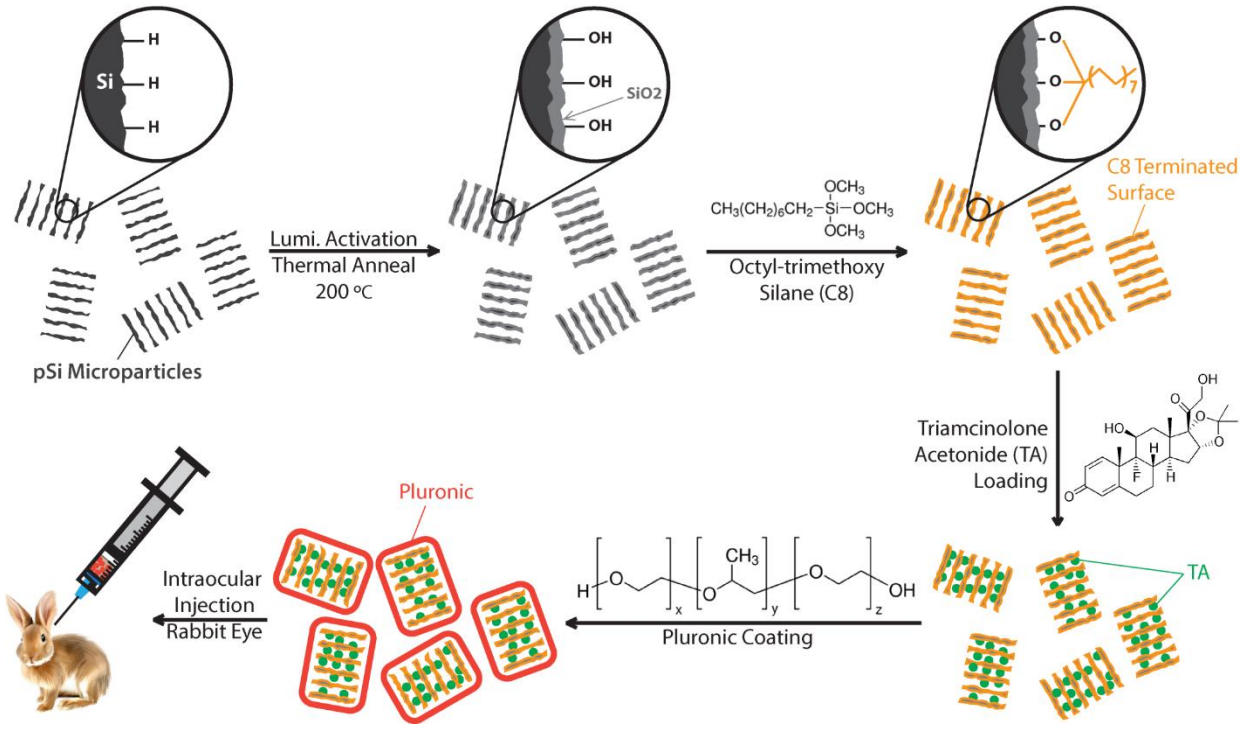

Figure 4.7. The schematic of the surface modifications and chemistries performed on porous silicon particles to enable stable luminescence, TA loading and dispersity in aqueous solutions.

Table 4.1. The summary of weight percent of each formulation following thermal gravimetric analysis. A control with luminescent silicon particles was performed to confirm minimal changes in mass after despite the likely oxidation of the silicon skeleton under the heating conditions.

	C8 Grafting	**Triamcinolone Acetonide**	**Pluronic Coating**
Weight Percent	9%	7%	3%

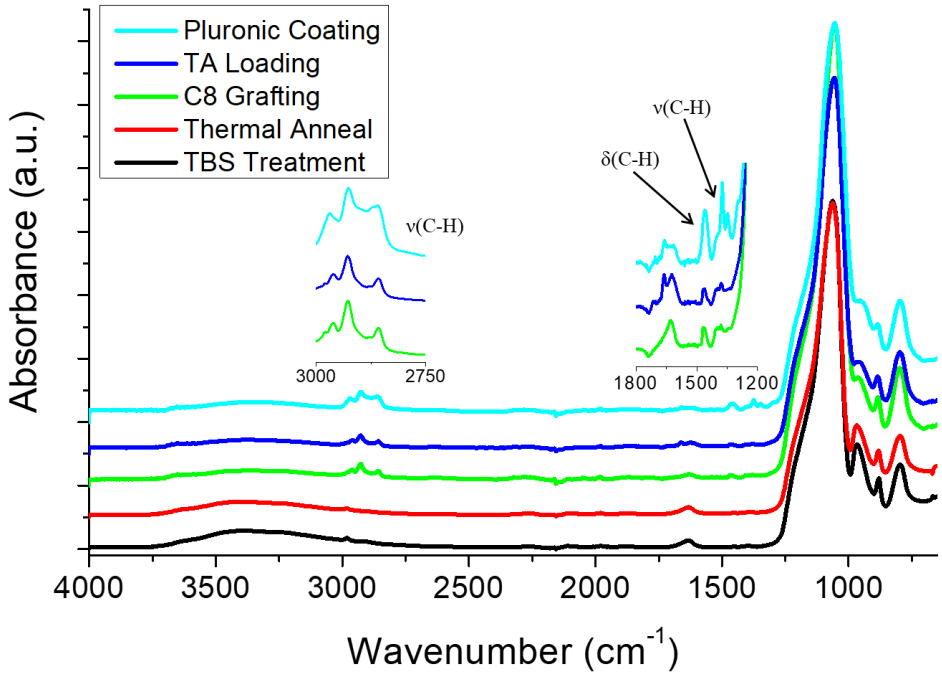

Figure 4.8. Fourier transform infrared spectroscopy of particles following luminescence activation, thermal treatment, C8 grafting, TA loading, and pluronic coating. The luminescence activation process creates an oxide shell around the silicon skeleton so that characteristic Si-H peaks, 2200 cm^{-1}, were not observed. Following thermal anneal, water residue within the pores were reduced although trace amounts was still observed by peaks ~1600 cm^{-1} and the broad peak between 3000-3750 cm^{-1}. Successful functionalization was observed by C-H peaks between 2750-3000 cm^{-1} and 1200-1500 cm^{-1}. Following loading, the peak at ~1700 cm^{-1} represents the C=O bond on TA and an increase in all of the C-H peaks after pluronic coating suggests its presence.

4.4.3 In Vitro Luminescence and Release Study

To test the correlation between the pharmacokinetics and luminescence, a release study was performed in a custom-made setup (Figure 4.9). The setup is composed of a custom machined three chamber Teflon flow cell and enclosed with a quartz window on the lid to allow imaging. Particles settled to the bottom of the chamber and Hank's balanced salt solution was continuously pulled through the flow cell using a low flow 12-chamber peristaltic pump (Ismatec, IPC-N) at 5 μL/min into falcon tubes, which was changed daily. Each day, particles were imaged using an IR black and white Point Grey camera, illuminated using a 385 nm light source, and passed through a 700 nm longpass filter. Images were analyzed using ImageJ and a MATLAB code to determine the location and intensity of the particles. The image was first background corrected to remove any artifacts of a gradient background. The canny edge detection method was employed for automatic thresholding and to define a mask that represents the particles. The intensity was determined by integrating regions within the mask and dividing by the number of pixels within the region.

The cumulative drug release and intensity at wavelengths >700 nm with respect to time is shown in Figure 4.10a. Particles displayed a typical burst release profile followed by slow release. While this is consistent with previous findings, the pluronic coating allows wetting of the porous silicon particles that may exacerbate the burst release. However, without the coating, the formulation would be difficult to inject due to clogging within the syringe. To ensure that both the C8 functionalization and pluronic coating was necessary, another release study was performed with particles loaded without the two steps. The particles with the additional functionalization and coating demonstrated more long-lasting release.

The luminescence of the particles >700 nm decreased rapidly due to blue shift in the wavelength and decrease in luminescence intensity due to oxidation and degradation of quantum confined silicon crystals. Correlations between luminescence intensity and drug release was observed in Figure 4.9b. Although not completely linear, each normalized intensity value corresponds to a unique release amount and, as the intensity decrease, more TA was released. When the intensity has decayed to ~20% (day 10), most of the drug has been released indicating the need for another injection. While the drug release profile is not near 0-order and long (~months), we decided to test the luminescence correlation in vivo to determine viability of luminescence monitoring in the eye.

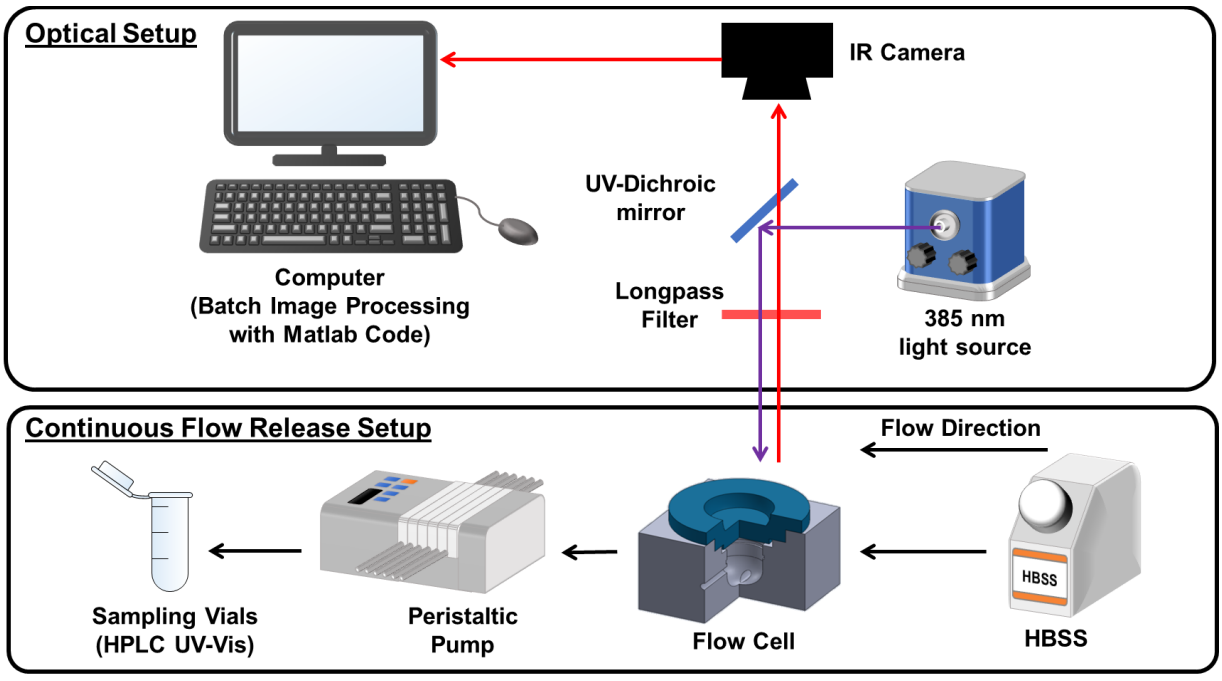

Figure 4.9. The schematic of the in vitro setup employed to image the particles and turnover buffer medium for sampling the TA concentration.

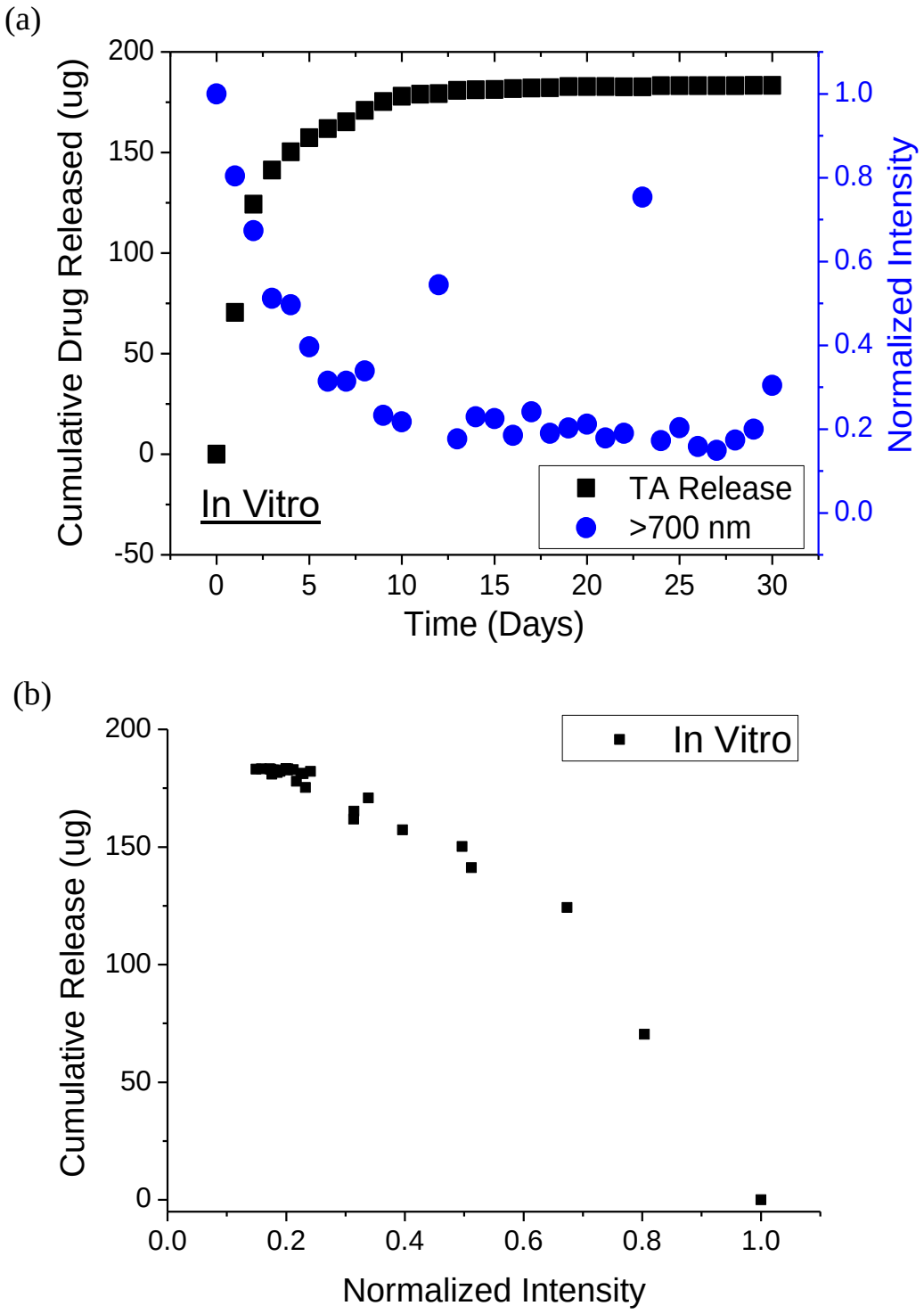

Figure 4.10. (a) Cumulative release of TA and changes in luminescence intensity over 30 days from the in vitro study. (b) The cumulative release versus normalized intensity from (a) to demonstrate self-reporting capabilities of the particles.

4.4.5 In vivo Testing of Self Reporting Microparticles

To test the self-reporting capabilities of the particles, ~3 mg of particles was injected into the right eye of four pigmented New Zealand rabbits. The vitreous of the rabbits were liquefied by injecting octafluoropropane (C3F8) gas into the eye at least three weeks prior to injection to enable vitreous sampling. Rabbits were imaged using a modified Canon fundus imaging setup and black and white Photometrics cooled CCD (Figure 4.11). At each time point, vitreous solution (<50µL) was collected to quantify the TA concentration. A similar MATLAB imaging code was employed to quantify the intensity of particles in vivo.

Both the luminescence intensity and the pharmacokinetics of TA in the eye (Figure 4.12) follows a similar trend that was observed in vitro. As demonstrated with the in vitro study, the luminescence correlates well with the release kinetics showing, for the first time, a feasible self-reporting system in vivo using porous silicon particles. Additionally, the image collected from the in vivo experiment were analyzed using automatic thresholding to obtain intensity values for monitoring the drug release. The imaging method was performed using an existing fundus system and demonstrates that the particles could be visualized in the eye during a routine clinical exam and does not require high intensity light sources that may cause retinal damage.

The eye was closely monitored during the study to monitor the safety of the luminescent formulation and imaging method. No toxicity was observed during the routine exams during the release study and the histology slides collected from eye cups after the rabbits were sacrificed (Figure 4.13).

While these results are exciting, more studies and optimization is required for translation of these formulations. New loading methods, such as melt-casting, for hydrophobic small molecules that enable near 0-order release is required for more optimal release times and to prevent

toxicity that may be experienced from burst release and the long tail (below therapeutic concentrations). The injectability could be improved by dispersing the particles in a gel (such as hyaluronic acid, which is already found in the eye) instead of pluronic coatings, which may accelerate the drug release due to improved wetting of the particles. Additionally, the imaging system could be improved for fast auto-focus and capture the fundus in its entirety. Due to the size of the CCD, the images collected only represents a section of a typical fundus photo. An ideal imaging system would be able to reconstruct a 3D fluorescent image of the eye so that the particle intensity could be related to its volume rather than area in an image. In 2D setups, some portion of particles will inevitably be out of focus and particles stacked out of plane in the image will create hotspots making the image analysis challenging. Because intraocular imaging is critical for diagnosis of many ophthalmic diseases, better imaging systems (including 3D imaging) are being developed that will aid in the translation of self-reporting systems.

Self-reporting systems are exciting technologies for the eye and a much-needed functionality for long-lasting ophthalmic therapeutics because, for many chronic eye diseases, re-dosing is evaluated based on vision deterioration, which irreversible and can significantly lower the quality of life. The transparent nature of the eye allows direct fluorescence imaging of the self-reporting system without significant autofluorescence or interference. In addition to the ophthalmic therapeutics, self-reporting systems can also be employed in other types of therapeutic applications that are accessible for fluorescence imaging such as subcutaneous, intramuscular and gastro-intestinal drug delivery. Because the excited lifetime of porous silicon emission is on the scale of microseconds, background autofluorescence could be excluded from imaging by time resolved imaging, where signal collection from the CCD does not begin until the 100-1μs after the pulsed light is off.[36-37]

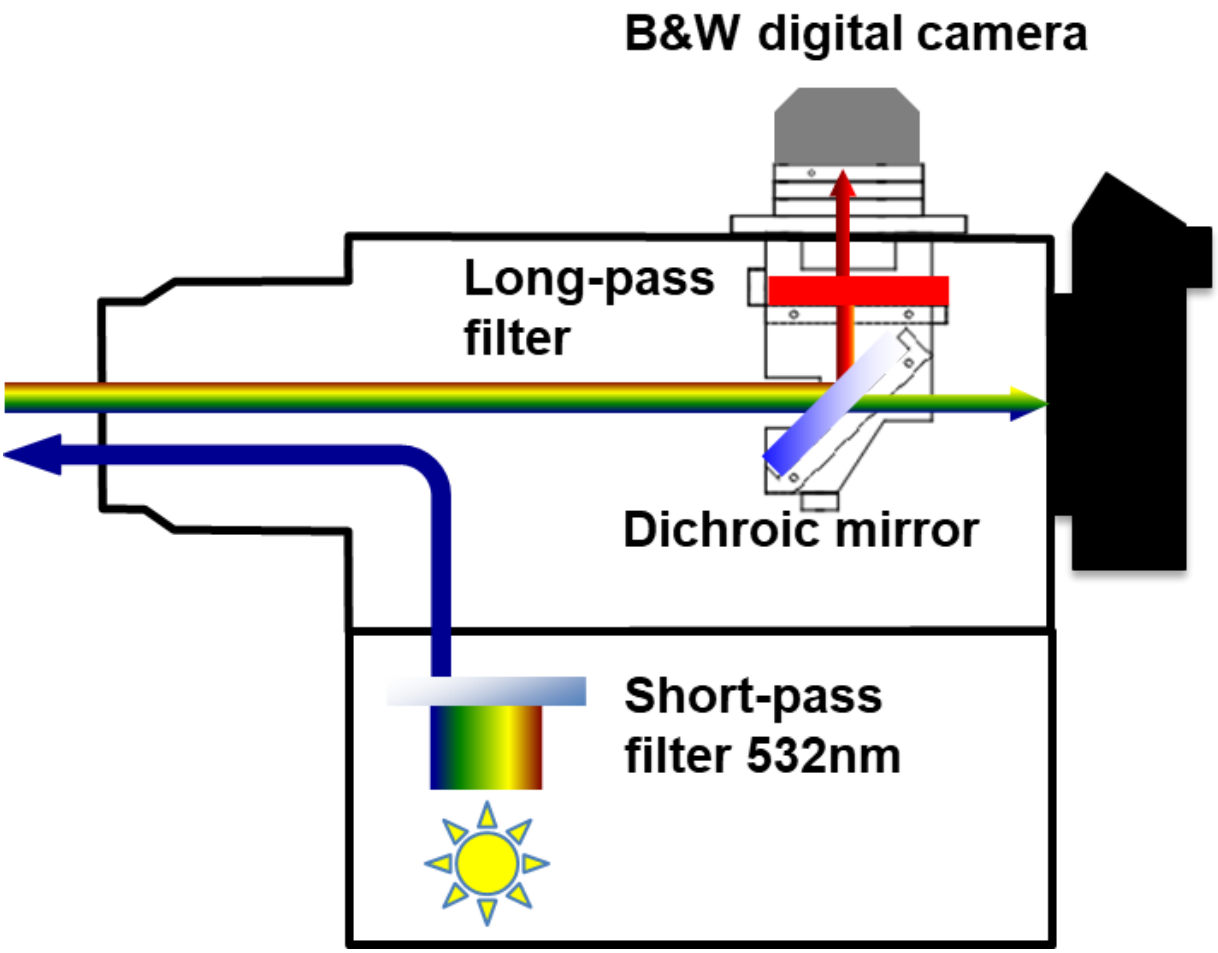

Figure 4.11. The schematic of the optical filters added to the fundus imaging camera. The dichroic mirror reflected light >650 nm and a 700 nm longpass filter was added. The flash from the original setup (xenon tube) was not modified or changed to prevent any retinal damage from high energy light sources.

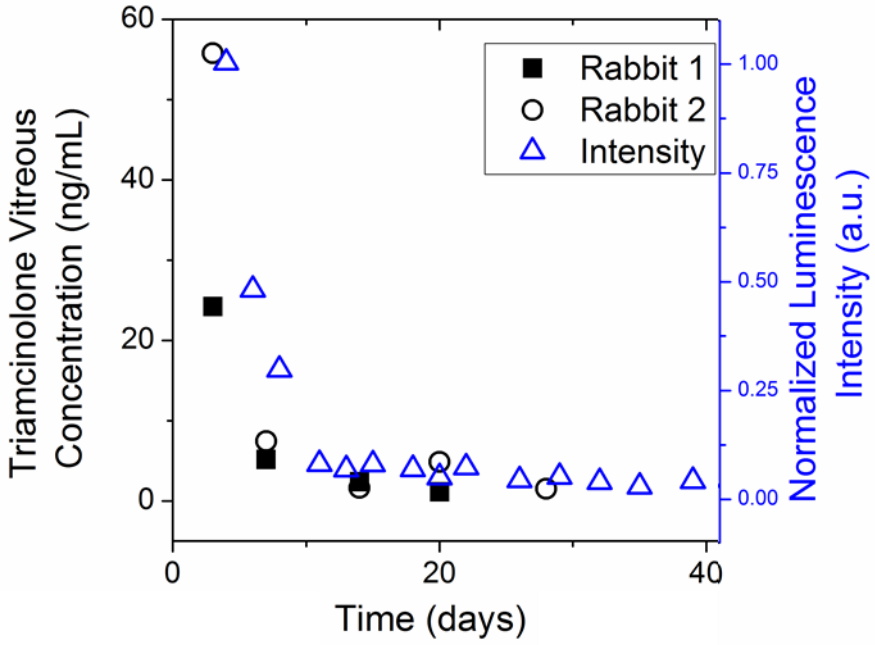

Figure 4.12. The in vivo concentration of TA and normalized intensity of porous silicon particles. The TA concentration was determined by vitreous taps at each time point following extraction of TA in acetonitrile and analysis in HPLC-M/S. Intensity values were extracted from the images following image analysis with a MATLAB code using canny edge detection function.

(a)

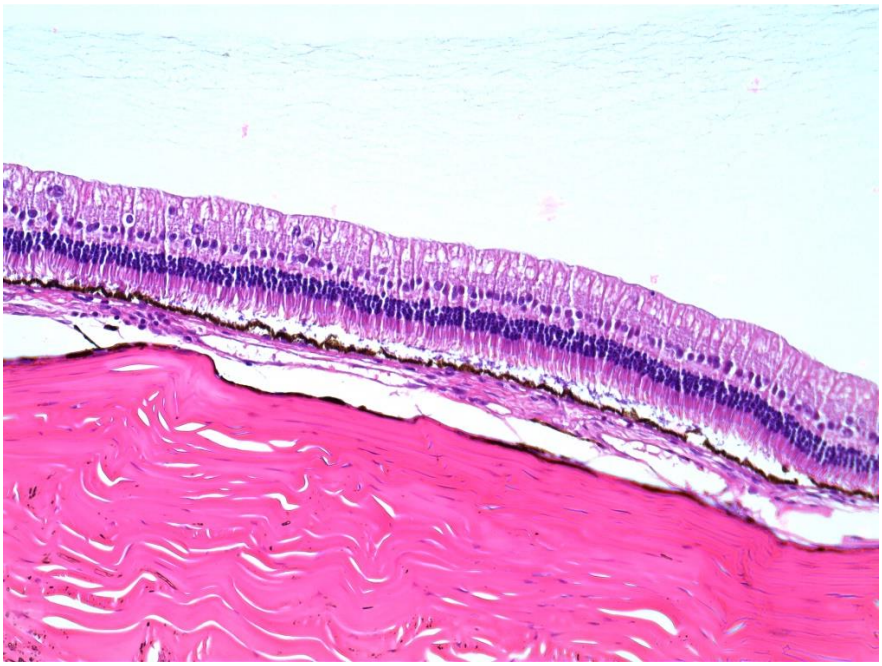

(b)

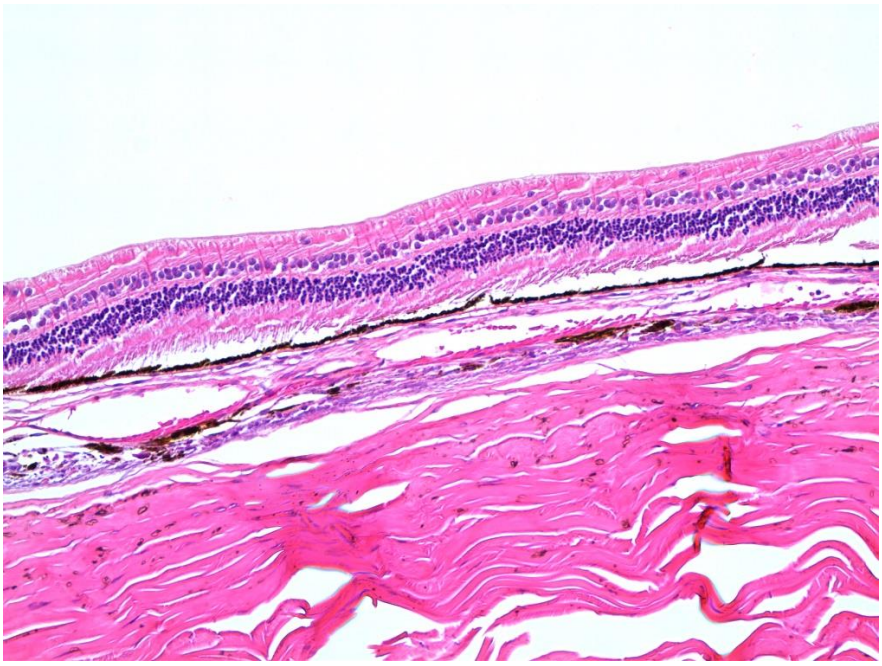

Figure 4.13. Representative histology images of the rabbit eye cup where (a) the right eye was injected with particles and (b) the left eye, or the control, was injected with sterile BSS. Histology samples were collected from the same rabbits in the pharmacokinetic/imaging study to observe long-term side effects of the particles and the imaging method. The paraffin sections were stained with both hematoxylin and eosin. No toxicity was observed by light microscopy of stained sections for both eyes of all the rabbits.

4.5 Conclusions

The self-reporting capabilities of drug loaded porous silicon particles were demonstrated in vitro and, for the first time, in vivo. The fluorescence of the particles decayed over time and tracked with the release of triamcinolone acetonide. These results suggest the potential for using porous silicon as a theranostic platform system for personalized therapeutics in the eye and can be reconfigured and translated to other diseases and routs of delivery.

Chapter 4, in part is currently being prepared for submission for publication of the material. Wang, J., Warther, D., Kumeria, T., Ying, X., Huffman, K., Cheng, L., Freeman, W.R. and Sailor, M.J. Self-Reporting Porous Silicon Microparticles for Sustained Delivery of Intraocular Therapeutics. The dissertation/thesis author was the primary investigator and author of this material.

4.6 References

1. Bourges, J. L.; Bloquel, C.; Thomas, A.; Froussart, F.; Bochot, A.; Azan, F.; Gurny, R.; BenEzra, D.; Behar-Cohen, F., Intraocular implants for extended drug delivery: Therapeutic applications. *Advanced Drug Delivery Reviews* **2006,** *58* (11), 1182-1202.

2. Short, B. G., Safety Evaluation of Ocular Drug Delivery Formulations: Techniques and Practical Considerations. *Toxicologic Pathology* **2008,** *36* (1), 49-62.

3. Agrahari, V.; Mandal, A.; Agrahari, V.; Trinh, H. M.; Joseph, M.; Ray, A.; Hadji, H.; Mitra, R.; Pal, D.; Mitra, A. K., A comprehensive insight on ocular pharmacokinetics. *Drug Deliv Transl Res* **2016,** *6* (6), 735-754.

4. Urtti, A., Challenges and obstacles of ocular pharmacokinetics and drug delivery. *Advanced Drug Delivery Reviews* **2006,** *58* (11), 1131-1135.

5. Lanzetta, P.; Holz, F.; Mones, J.; Querques, G.; Stanga, P.; Veritti, D.; Barbone, F.; Brusaferro, S.; Isola, M., Intravitreal injections: a healthcare failure modes and effects analysis. *Ophthalmologica. Journal international d'ophtalmologie. International journal of ophthalmology. Zeitschrift fur Augenheilkunde* **2013,** *230* (3), 151-64.

6. Aiello, L. P.; Brucker, A. J.; Chang, S.; Cunningham, E. T., Jr.; D'Amico, D. J.; Flynn, H. W., Jr.; Grillone, L. R.; Hutcherson, S.; Liebmann, J. M.; O'Brien, T. P.; Scott, I. U.; Spaide, R. F.; Ta, C.; Trese, M. T., Evolving guidelines for intravitreous injections. *Retina* **2004,** *24* (5 Suppl), S3-19.

7. Campbell, R. J.; Bronskill, S. E.; Bell, C. M.; Paterson, J. M.; Whitehead, M.; Gill, S. S., Rapid Expansion of Intravitreal Drug Injection Procedures, 2000 to 2008: A Population-Based AnalysisIncreased Intravitreous Injections, 2000-2008. *JAMA Ophthalmology* **2010,** *128* (3), 359-362.

8. Choonara, Y. E.; Pillay, V.; Danckwerts, M. P.; Carmichael, T. R.; du Toit, L. C., A review of implantable intravitreal drug delivery technologies for the treatment of posterior segment eye diseases. *J Pharm Sci* **2010,** *99* (5), 2219-39.

9. Peyman, G. A.; Lad, E. M.; Moshfeghi, D. M., Intravitreal injection of therapeutic agents. *Retina* **2009,** *29* (7), 875-912.

10. Pearce, W.; Hsu, J.; Yeh, S., Advances in drug delivery to the posterior segment. *Curr Opin Ophthalmol* **2015,** *26* (3), 233-239.

11. FDA approves novel gene therapy to treat patients with a rare form of inherited vision loss. Fischer, A., Ed. FDA News Release, 2017.

12. del Amo, E. M.; Rimpelä, A.-K.; Heikkinen, E.; Kari, O. K.; Ramsay, E.; Lajunen, T.; Schmitt, M.; Pelkonen, L.; Bhattacharya, M.; Richardson, D.; Subrizi, A.; Turunen, T.; Reinisalo, M.; Itkonen, J.; Toropainen, E.; Casteleijn, M.; Kidron, H.; Antopolsky, M.; Vellonen, K.-S.; Ruponen, M.; Urtti, A., Pharmacokinetic aspects of retinal drug delivery. *Progress in Retinal and Eye Research* **2017,** *57*, 134-185.

13. Chin, H. S.; Park, T. S.; Moon, Y. S.; Oh, J. H., Difference in clearance of intravitreal triamcinolone acetonide between vitrectomized and nonvitrectomized eyes. *Retina* **2005,** *25* (5), 556-60.

14. Edington, M.; Connolly, J.; Chong, N. V., Pharmacokinetics of intravitreal anti-VEGF drugs in vitrectomized versus non-vitrectomized eyes. *Expert Opinion on Drug Metabolism & Toxicology* **2017,** *13* (12), 1217-1224.

15. Low, S. P.; Voelcker, N. H.; Canham, L. T.; Williams, K. A., The biocompatibility of porous silicon in tissues of the eye. *Biomaterials* **2009,** *30* (15), 2873-80.

16. Nieto, A.; Hou, H.; Sailor, M. J.; Freeman, W. R.; Cheng, L., Ocular silicon distribution and clearance following intravitreal injection of porous silicon microparticles. *Experimental eye research* **2013,** *116*, 161-168.

17. Kim, B.; Pang, H.-B.; Kang, J.; Park, J.-H.; Ruoslahti, E.; Sailor, M. J., Immunogene therapy with fusogenic nanoparticles modulates macrophage response to Staphylococcus aureus. *Nature communications* **2018,** *9* (1), 1969-1969.

18. Wan, Y.; Apostolou, S.; Dronov, R.; Kuss, B.; Voelcker, N. H., Cancer-targeting siRNA delivery from porous silicon nanoparticles. *Nanomedicine (London, England)* **2014,** *9* (15), 2309-21.

19. Tanaka, T.; Mangala, L. S.; Vivas-Mejia, P. E.; Nieves-Alicea, R.; Mann, A. P.; Mora, E.; Han, H.-D.; Shahzad, M. M. K.; Liu, X.; Bhavane, R.; Gu, J.; Fakhoury, J. R.; Chiappini, C.; Lu, C.; Matsuo, K.; Godin, B.; Stone, R. L.; Nick, A. M.; Lopez-Berestein, G.; Sood, A. K.; Ferrari, M., Sustained small interfering RNA delivery by mesoporous silicon particles. *Cancer Res* **2010,** *70* (9), 3687-3696.

20. Andrew, J. S.; Anglin, E. J.; Wu, E. C.; Chen, M. Y.; Cheng, L.; Freeman, W. R.; Sailor, M. J., Sustained Release of a Monoclonal Antibody from Electrochemically Prepared Mesoporous Silicon Oxide. *Advanced Functional Materials* **2010,** *20* (23), 4168-4174.

21. Liu, D.; Bimbo, L. M.; Mäkilä, E.; Villanova, F.; Kaasalainen, M.; Herranz-Blanco, B.; Caramella, C. M.; Lehto, V.-P.; Salonen, J.; Herzig, K.-H.; Hirvonen, J.; Santos, H. A., Co-delivery of a hydrophobic small molecule and a hydrophilic peptide by porous silicon nanoparticles. *Journal of Controlled Release* **2013,** *170* (2), 268-278.

22. Wang, M.; Coffer, J. L.; Dorraj, K.; Hartman, P. S.; Loni, A.; Canham, L. T., Sustained Antibacterial Activity from Triclosan-Loaded Nanostructured Mesoporous Silicon. *Molecular Pharmaceutics* **2010,** *7* (6), 2232-2239.

23. Park, J.-H.; Gu, L.; von Maltzahn, G.; Ruoslahti, E.; Bhatia, S. N.; Sailor, M. J., Biodegradable luminescent porous silicon nanoparticles for in vivo applications. *Nature Materials* **2009,** *8*, 331.

24. Cullis, A. G.; Canham, L. T.; Calcott, P. D. J., The structural and luminescence properties of porous silicon. *Journal of Applied Physics* **1997,** *82* (3), 909-965.

25. Canham, L. T., Silicon quantum wire array fabrication by electrochemical and chemical dissolution of wafers. *Applied Physics Letters* **1990,** *57* (10), 1046-1048.

26. Lehmann, V.; Gösele, U., Porous silicon formation: A quantum wire effect. *Applied Physics Letters* **1991,** *58* (8), 856-858.

27. Wolkin, M. V.; Jorne, J.; Fauchet, P. M.; Allan, G.; Delerue, C., Electronic States and Luminescence in Porous Silicon Quantum Dots: The Role of Oxygen. *Physical Review Letters* **1999,** *82* (1), 197-200.

28. Bsiesy, A.; Vial, J. C.; Gaspard, F.; Herino, R.; Ligeon, M.; Muller, F.; Romestain, R.; Wasiela, A.; Halimaoui, A.; Bomchil, G., Photoluminescence of high porosity and of electrochemically oxidized porous silicon layers. *Surface Science* **1991,** *254* (1), 195-200.

29. Joo, J.; Cruz, J. F.; Vijayakumar, S.; Grondek, J.; Sailor, M. J., Photoluminescent Porous Si/SiO2 Core/Shell Nanoparticles Prepared by Borate Oxidation. *Advanced Functional Materials* **2014,** *24* (36), 5688-5694.

30. Wang, J.; Kumeria, T.; Bezem, M. T.; Wang, J.; Sailor, M. J., Self-Reporting Photoluminescent Porous Silicon Microparticles for Drug Delivery. *ACS applied materials & interfaces* **2018,** *10* (4), 3200-3209.

31. Cheng, L.; Hostetler, K. Y.; Chaidhawangul, S.; Gardner, M. F.; Beadle, J. R.; Toyoguchi, M.; Bergeron-Lynn, G.; Freeman, W. R., Treatment or prevention of herpes simplex virus retinitis with intravitreally injectable crystalline 1-O-hexadecylpropanediol-3-phospho-ganciclovir. *Invest Ophthalmol Vis Sci* **2002,** *43* (2), 515-21.

32. Wang, J.; Kumeria, T.; Bezem, M. T.; Wang, J.; Sailor, M. J., Self-Reporting Photoluminescent Porous Silicon Microparticles for Drug Delivery. *ACS Appl Mater Interfaces* **2018,** *10* (4), 3200-3209.

33. Petrova-Koch, V.; Muschik, T.; Kux, A.; Meyer, B. K.; Koch, F.; Lehmann, V., Rapid-thermal-oxidized porous Si−The superior photoluminescent Si. *Applied Physics Letters* **1992,** *61* (8), 943-945.

34. Qin, Z.; Joo, J.; Gu, L.; Sailor, M. J., Size Control of Porous Silicon Nanoparticles by Electrochemical Perforation Etching. *Particle & Particle Systems Characterization* **2014,** *31* (2), 252-256.

35. Joo, J.; Defforge, T.; Loni, A.; Kim, D.; Li, Z.; Sailor, M. J.; Gautier, G.; Canham, L. T., Enhanced quantum yield of photoluminescent porous silicon prepared by supercritical drying. *Applied Physics Letters* **2016,** *108* (15), 153111.

36. Gu, L.; Hall, D. J.; Qin, Z.; Anglin, E.; Joo, J.; Mooney, D. J.; Howell, S. B.; Sailor, M. J., In vivo time-gated fluorescence imaging with biodegradable luminescent porous silicon nanoparticles. *Nat Commun* **2013,** *4*, 2326.

37. Joo, J.; Liu, X.; Kotamraju, V. R.; Ruoslahti, E.; Nam, Y.; Sailor, M. J., Gated Luminescence Imaging of Silicon Nanoparticles. *ACS Nano* **2015,** *9* (6), 6233-6241.

CHAPTER FIVE

Molecular Weight Dependence on Polymer Flow into Mesoporous Silicon Templates

5.1 Abstract

The effect of molecular weight on the rate and extent of melt-infiltration of polystyrene into mesoporous silicon-based photonic crystals is investigated as a function of polymer molecular weight (Figure 5.1). Polymer viscosity and chain end-to-end (R_{ee}) distance correlate with the rate and extent of infiltration. High molecular weight (M_w) polystyrene (200 or 400 kDa) infiltrates the mesoporous material in two distinct phases: a rapid phase where the larger pores of the template are filled, followed by a slower phase during which the smaller pores fill. Low molecular weight polystyrene (20 and 35 kDa) fills the pores more uniformly, progressing into the film as a single, relatively distinct front of liquid polymer. Scanning electron microscope (SEM) analyses of cross sections of the films are consistent with the optical measurements, showing a lower extent of infiltration for the higher molecular weight polymers. Removal of the porous Si templates by soaking in a chemical etchant generates free-standing films of nanostructured polymer. The low molecular weight samples display better replication.

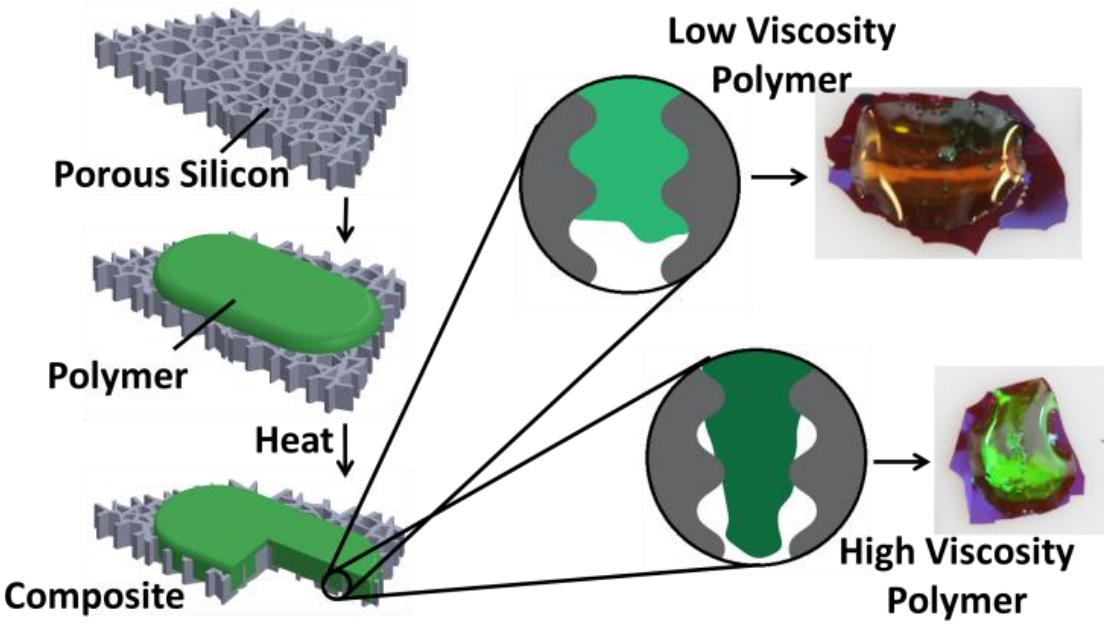

Figure 5.1 Porous silicon was employed as a template to fabricate composite and free standing polymer photonic crystals. As the molecular weight increased, the viscosity and end to end distance increased so that the polymer flowed into the template without filling the voids.

5.2 Introduction

Porous silicon (pSi) is a useful template for the formation of composite materials because the electrochemical means of preparation provides a high degree of systematic control over the porosity and pore size of the template. Such structures are of interest for a variety of biomedical,[1-6] sensing,[7-13] and energy[14-20] applications. Composites have been prepared using a wide range of guest materials,[10] including metals,[21-24] refractory oxides,[9, 25-30] carbon,[31-32] and polymers.[1-2]

For polymers, the nanoscale confines of porous media can exert a strong influence on polymer properties, such as the volume phase transition, viscosity, and morphology.[10, 12, 33-39] The operative mechanism for pore filling is also dependent on pore size. For example, the viscosity of the polymer and radius of gyration of the individual chains may inhibit its infiltration into nanometer-scale pores while allowing more rapid infiltration into larger meso- or macropores.[40] Although the average pore dimensions in the porous Si system can be tuned over a wide range (nanometers to micrometers), an individual sample typically displays a relatively large distribution of pore sizes, and so the pore filling dynamics can be expected to be complex. Thus, a viscous polymer might be expected to infiltrate larger macro- or mesopores relatively quickly but be excluded from smaller mesopores or micropores in a given sample.

In this work, we study the mechanism of filling of mesoporous silicon using molten polystyrene as a test system. We employ optical reflectance spectroscopy to measure rate and extent of infiltration as a function of polymer molecular weight, using porous Si samples optically structured in the form of rugate filters. We then selectively remove the porous silicon template by chemical dissolution, creating free-standing polymer replicas.

5.3 Materials and Experimental Methods

5.3.1 Materials

Silicon wafers, highly boron-doped (resistivity < 0.0015 Ω·cm), polished on the (100) face, and 525 ± 25 μm thick, were purchased from Virginia Semiconductors. Absolute ethanol (200 proof) was obtained from Rossville Gold Shield Chemicals. Hydrofluoric acid (48% aqueous, ACS grade) was obtained from Macron Chemicals. Polystyrene (analytical standard, for GPC, molecular weight 20,000, 35,000, 200,000, and 400,000 g/mol M_w) and poly(vinylidene fluoride) beads (analytical standard for GPC, with average 180,000 g/mol M_w) were purchased from Sigma-Aldrich Chemicals.

5.3.2 Preparation of Porous Silicon Templates.

The porous Si photonic crystal templates were prepared by electrochemical etch using a 3:1 (v:v) solution of 48% aqueous hydrofluoric acid:ethanol electrolyte and a platinum coil counter electrode (Caution: HF is highly corrosive and toxic. Proper protective equipment should be employed to avoid contact with skin or lungs). Photonic crystal (rugate) structures were etched using a sinusoidal current density− time waveform, modulated between 10 and 90 mA/cm^2 for 200 repeats and a period of ∼6 s for the polystyrene studies and 25−100 mA/cm^2 for 240 repeats and a period of ∼5 s for the poly(vinylidene fluoride) studies. The porous films were removed from the substrate by application of a constant current density of 6.25 mA/cm^2 for 300 s in a 1:15 (v:v) solution of 48% aqueous hydrofluoric acid and ethanol electrolyte, generating freestanding films of 40 μm approximate thickness. Samples were then thermally oxidized at 500 °C for 2 h in air.

5.3.3 Fabrication of Polystyrene Photonic Crystals.

The procedure to prepare polystyrene photonic crystals is outlined in Figure 5.2. Powdered polystyrene was melted into sheets and fractured into small pieces for ease of use. The polymer

was placed on top of a freestanding porous Si film (removed from the Si substrate), and the assembly was heated at 155 °C on a hot plate for 1 h. Infiltration of the melt-cast polymer was verified qualitatively by a change in color of the composite film. To remove the porous Si template, the composite was placed in a solution of 3:1:1 48% aqueous HF:ethanol:dimethyl sulfoxide for 16 h, following a previously reported procedure.[31]

6.3.4 Characterization using Fourier Transform Infrared Spectroscopy.

Attenuated total reflectance (ATR) Fourier transform infrared (FTIR) spectra were obtained using a Thermo Scientific Nicolet 6700 FTIR spectrometer fitted with a Smart iTR sampling accessory. Each spectrum was acquired in the range 600−4000 cm^{-1}, at a resolution of 4 cm^{-1}, and average of 128 scans.

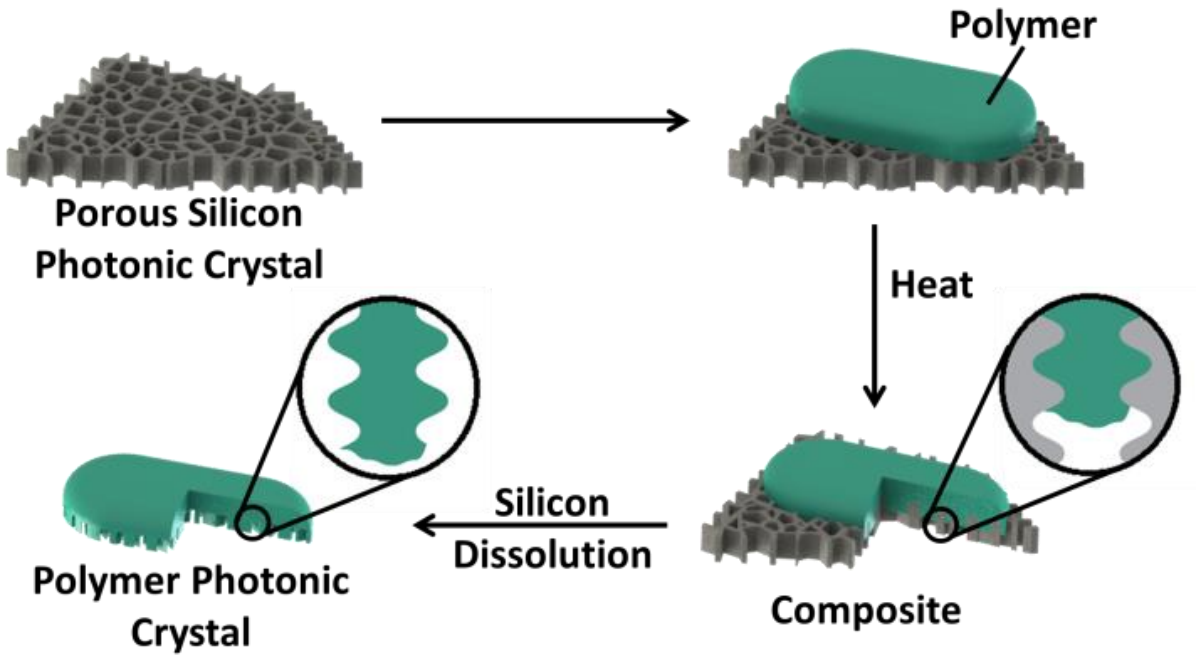

Figure 5.2. Schematic of method used to prepare composite and free-standing replicas from a porous Si photonic crystal template by melt-casting.

5.3.5 Imaging using Scanning Electron Microscopy.

The samples were first sputtercoated with iridium (Emitech K575X Sputter Coater). A FEI XL30 scanning electron microscope (SEM) was used to image the surface and cross-section of the porous Si, porous Si−polymer composites, and polymer replicas. The SEM was set to an accelerating voltage of 5 kV and spot size of 3 μm. Semiquantitative pore size determination was derived from the SEM images using the image analysis program ImageJ (National Institutes of Health). Energy dispersive X-ray (EDX) analysis was performed on the same instrument, using an accelerating voltage of 20 kV and a spot size of 4 μm.

5.3.6 Polystyrene Characterization Using Differential Scanning Calorimetry (PerkinElmer Pyris Diamond DSC).

The polystyrene samples were sealed in 10 μL aluminum samples pans (PerkinElmer, BO14-6650, BO14-6117). An identical aluminum pan/lid was employed as a reference. The samples (5−10 mg) were heated at 10 °C/min from 30 to 200 °C and held at 200 °C for 1 min under nitrogen gas (20 mL/min). The samples were then cooled to 30 °C at 10 °C/min. The DSC results were analyzed with Origin Pro (OriginLab, Inc.).

5.3.7 Optical Spectroscopy and Analysis.

Reflectance spectra were acquired using a CCD spectrometer (Ocean Optics USB-4000) fitted to a bifurcated fiber optic cable as previously described.41 One arm of the optical fiber was connected to the spectrometer, while the other arm was connected to a tungsten light source (Ocean Optics LS-1). The distal end of the combined fiber was attached to an objective lens to allow acquisition of 180° reflectance spectra from the sample surface, with a spot size of approximately 1−2 mm^2. The spectra were smoothed and processed with Origin Pro (OriginLab, inc) to determine the maximum peak position. The experimental setup for real-time optical monitoring of the

polymer infiltration process is shown in Figure 5.3. Polystyrene was pre-melted on a glass slide at 155 °C for 20 min. The porous Si film was preheated at the same time, and the reflectance spectrum (time = 0) was acquired. The molten polymer (still in contact with the glass slide) was then placed into contact with the porous Si film, and the glass slide was positioned such that polymer was directly on top the film. This contacting process was accomplished within 30 s, between collection of the initial and the second spectrum. A time series of spectra were then acquired to monitor the melt infiltration process. The percent polymer infiltration was approximated using the following equation:

$$\% \text{ Infiltration } = \frac{\Delta\lambda_{obs}}{\Delta\lambda_{calc}} \times 100\% \tag{5.1}$$

where $\Delta\lambda_{obs}$ is the observed spectral shift of the stop band at the particular point in time during polymer infiltration that the spectrum was acquired, and $\Delta\lambda_{calc}$ is the spectral shift calculated assuming complete filling of the pores by polymer. The spectral shift for "complete filling" was calculated by application of a two-component Bruggeman model for the composite index of the porous Si film, assuming a polystyrene refractive index of 1.61. The average porosity of the porous layer and index of the porous Si skeleton was calculated in a separate experiment using a combination of the Bruggeman model and the spectral shift of the porous Si film when infiltrated with ethanol using the following equation:

$$\Delta\lambda_{SB} = 2n_{ave}d_p \tag{5.2}$$

where λ_{SB} is the wavelength of the stop band, n_{avg} is the average refractive index of the film, and d_p is the spatial periodicity of the layers in the multilayered nanostructure (typically 190 nm in this work).[41] The number of repeat units in the film was 200, and the total film thickness was 38 μm.

Transmission spectra were acquired using a CCD spectrometer (Ocean Optics USB-4000), a tungsten white light source (Ocean Optics LS-1), and two fiber optic cables. One fiber optic cable connected the light source to a lens which focused the light to a spot size of ~1 mm^2 on the sample. The sample was held on a transparent microscope slide. The second fiber optic cable was connected to a collimator collection lens on the opposite side of the sample so as to send the transmitted light to the spectrometer.

5.4 Results and Discussion

5.4.1 Preparation of Porous Si Templates and Polystyrene Polymer Composites

Historically two main methods have been employed to introduce polymers into porous Si templates: (1) in situ polymerization, where a monomer is introduced into the porous matrix in the presence of an appropriate catalyst and polymerization occurs in situ;[2, 10, 31, 42-48] and (2) casting of an already formed polymer into the porous film via melt or solution infiltration routes.[1, 4-5, 11, 49-56] The in situ polymerization route is limited to compatible polymer−catalyst systems, but it holds an advantage over casting methods in that the much smaller monomer units can in principle more effectively infiltrate the smallest pores of the porous Si template. The purpose of the present study was to investigate diffusion of preformed polymers into a porous Si template and identify the limitations of the melt-casting route as a means of preparing porous Si−polymer composites and replicas.

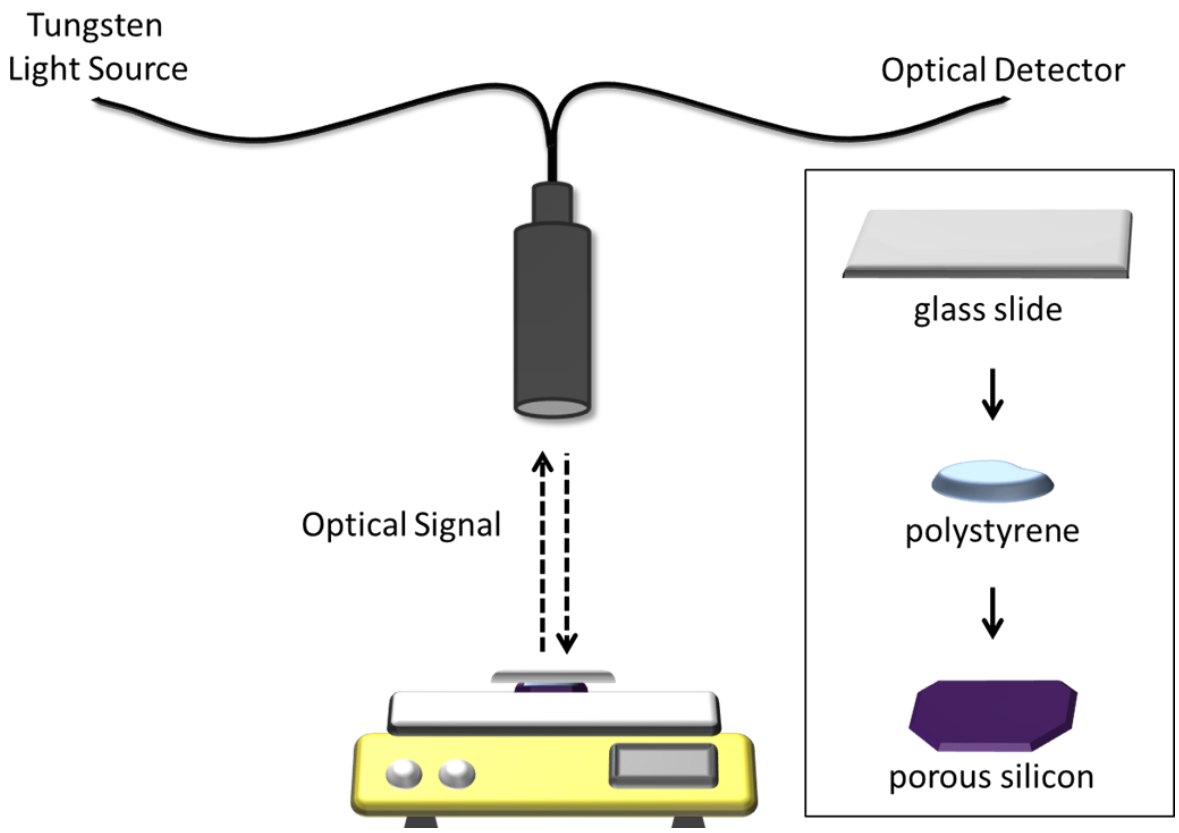

Figure 5.3. Schematic of the experimental setup for real-time optical monitoring of polystyrene infiltration during melt-casting. The free-standing porous Si film was placed on a laboratory hot plate and pre-heated. The polymer was placed on top of a microscope slide, which was heated separately until the polymer melted and spread on the slide (155°C for 20 min). The molten polymer on the glass slide was then placed into contact with the porous Si film. The glass slide containing the molten polymer served as an optical window to monitor the infiltration process. The hot plate was maintained at the desired temperature and a series of spectra were obtained as the polymer infiltrated into the porous Si substrate. The optical probe, light source, and spectrometer details are given in the experimental section.

The approach used to prepare polymer−porous Si composites and then remove the porous Si template to generate polymer replicas is outlined in Figure 5.2. In this study all the porous Si templates were prepared as rugate optical filters. First described by Vincent in 1994,[57] a porous Si rugate filter is a one-dimensional photonic crystal consisting of alternating layers of high and low porosity, prepared by modulating the current during electrochemical etch of the silicon wafer. The pores in this type of etch propagate predominantly in the ⟨100⟩ direction of the crystal, and the porosity modulation was apparent in the cross-sectional scanning electron microscope (SEM) images as a series of horizontal bands of alternating contrast (Figure 5.4a). These bands correspond to a variation in the bulk density of the nanostructure that was generated by the periodic etching waveform. Higher magnification revealed a periodic change in average pore size as a function of depth in the film (Figure 5.4a). The variation of pore size between high and low porosity layers was estimated to be less than a factor of 2 based on the cross-sectional SEM images. The plan-view SEM image (Figure 5.4b) showed a distribution of pore diameters ranging from 1 to 50 nm, with a median pore size of ∼10 nm. An advantage of the rugate nanostructure is that it displays intense structural color, and the color is controlled by the layer spacing and the refractive index of the porous matrix.58 In this work the porous Si rugate filter templates exhibited a stop band at ∼490 nm (Figure 5.5).

The porous Si templates were removed from the Si substrate by a lift-off procedure and then thermally oxidized to improve their stability and the reproducibility of the templating procedure. Polymers were then infiltrated via a melt-casting procedure as outlined in Figure 5.3.

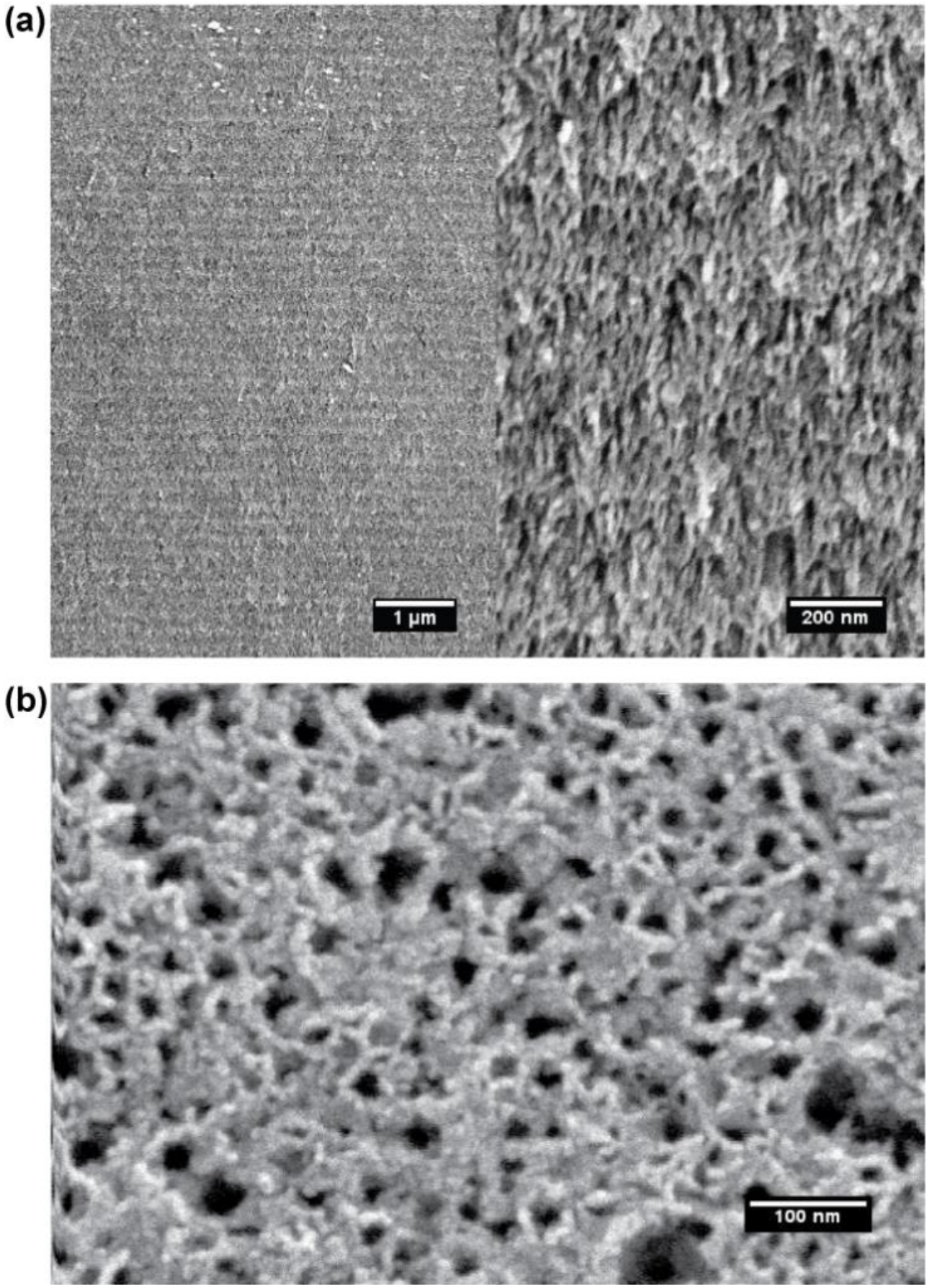

Figure 5.4. Scanning electron microscope (SEM) images of a representative porous Si template used in this work. (a) Cross-sectional views, obtained at two magnifications, showing the sinusoidal porosity modulation running parallel to the front face of the wafer. (b) Plan-view image, showing the pore texture.

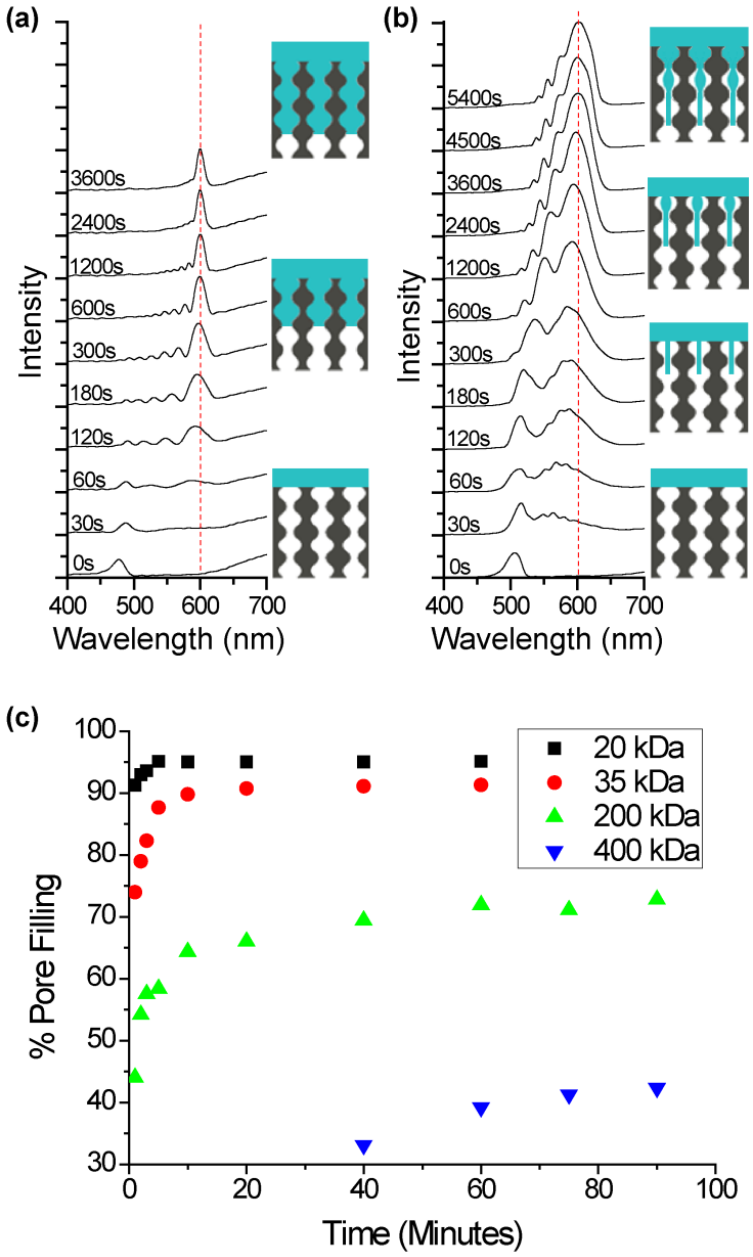

Figure 5.5. Time series of optical reflectance spectra obtained during melt infiltration of (a) Mw = 20 kDa and (b) Mw = 200 kDa polystyrene into porous Si photonic crystal templates. Based on an ethanol infiltration measurement on each of the samples, the completely filled sample in (a) should display a λ_{SB} = 608 nm. The completely filled sample in (b) should display a λ_{SB} = 629 nm. (c) Percent filling of polystyrene into the pores of the porous Si template as a function of time for the four types of polystyrene used in this work. Polymer molecular weight as indicated. Percent pore filling as defined in eq 5.1 as percent infiltration. Time = 0 corresponds to the spectrum obtained immediately prior to application of the molten polymer. Nominal temperature maintained at 155 °C throughout the experiment.

5.4.2 Optical Monitoring of the Polystyrene Infiltration Process.

Introduction of a liquid into a porous Si photonic crystal results in a change in refractive index that induces a shift in the photonic stop band of the material, and this spectral shift is readily monitored in real time.[1, 58-59] We used this phenomenon in the present work to quantify the rate and extent of pore filling by the molten polymer. Infiltration of polymer into the porous Si templates was apparent in the temporal evolution of the optical reflectance spectra (Figure 5.5). Prior to polymer infiltration, the wavelength of the stop band (λ_{SB}) of the porous Si template appeared at ~490 nm, with about ±15 nm variability from sample to sample. The average porosity of the template was typically 55%. The value of λ_{SB} corresponds to a value of n_{avg} (the average refractive index of the porous silicon skeleton and the air in the voids) of 1.2−1.3 (eq 5.2). The porous Si film and polymer were preheated at 155 °C, a temperature well above the glass transition temperature of the polymer (determined by differential scanning calorimetry, Figure 5.6, so the polymer was molten when in contact with the template. As liquid polystyrene flowed into the template, the reflectance spectrum evolved in one of two distinctive patterns, depending on molecular weight (weight-average, M_w) of the polymer.

For the low molecular weight polystyrene materials (M_w = 20 and 35 kDa), a second peak appeared at λ_{SB} ~ 600 nm, and this peak increased in intensity with time while the original λ_{SB} ~ 480 nm peak diminished in intensity (Figure 5.5a). The value of λ_{SB} of the second peak did not shift appreciably from ~600 nm during infiltration. For the higher molecular weight polystyrenes (200 and 400 kDa), a second peak also appeared, but it displayed a distinct shift in wavelength with time (Figure 5.5b). At early stages of infiltration, this new peak appeared as a broad shoulder on the original (air-filled) stop band (λ_{SB} ~ 500 nm), and the value of λ_{SB} of the new peak gradually red-shifted until finally reaching a value of λ_{SB} ~ 600 nm.

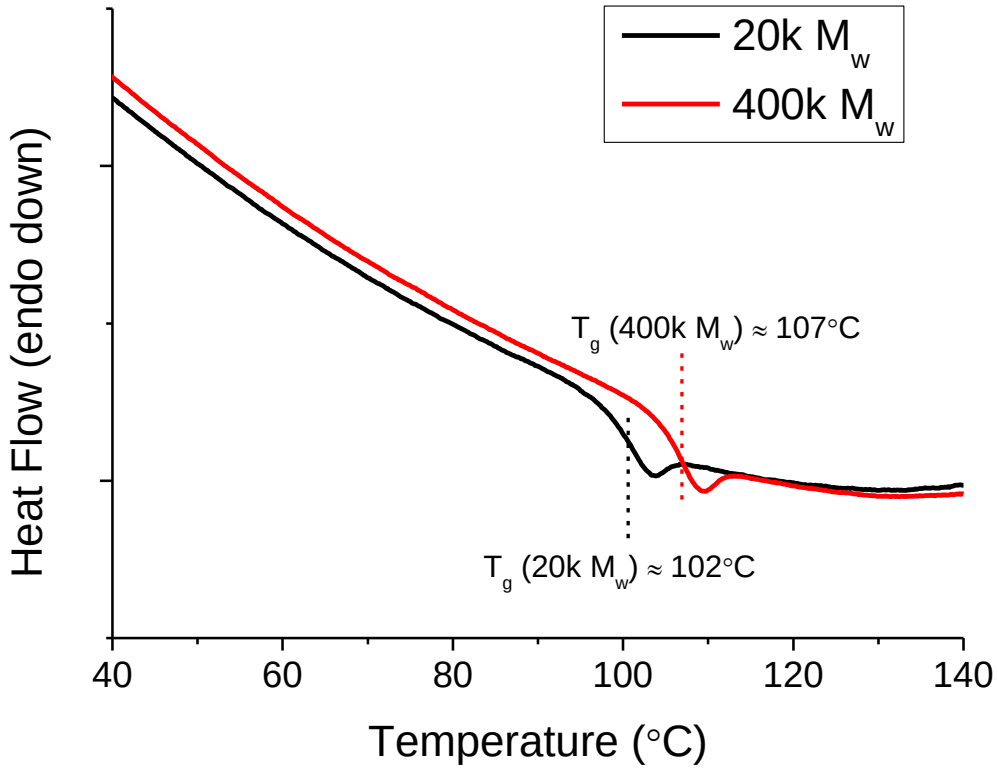

Figure 5.6. Differential scanning calorimetry (DSC) curves of 20,000 and 400,000 Mw polystyrene used in this study. The glass transition temperature was determined (T_g) by taking the maxima of the 1st derivative.

The percent infiltration of each of the polystyrene polymers as a function of infiltration time was calculated from the optical spectra, based on the measured porosity of the porous Si films and assuming a refractive index for the polystyrene component (independent of molecular weight) of 1.61 (Figure 5.5c). The rate at which the molten polymer infiltrated was directly related to polymer molecular weight, with the shortest polymer reaching a constant value of percent infiltration in the shortest time (within 10 min) and the longest polymer not quite reaching steady-state infiltration even after 1 h at 155 °C. The percent infiltration of polymer into the porous template was inversely related to polymer molecular weight, with 400, 200, 35, and 20 kDa polystyrene filling 40, 70, 88, and 95% of the pores, respectively. Thus, the data are consistent with the interpretation that the higher the polymer molecular weight, the slower and less efficiently it can fill the mesoporous matrix. For all conditions studied, molten polystyrene was never found to completely displace the air in the porous Si matrix.

5.4.3 Mechanism of Polymer Infiltration.

The difference in infiltration behavior between the low and the high molecular weight polymers noted above is interpreted as arising from two separate filling phenomena. The first process involves simple filling of the pores from top to bottom, where polymer enters the porous film as a single wave of material as depicted in Figure 5.5a. The second process involves filling of the larger pores first, followed by a slower infiltration of polymer into the smaller branching voids of the material as shown in Figure 5.5b. The first process is expected to be more important for low molecular weight, low viscosity polymers while the second process should be more dominant with the larger, higher viscosity polymers.

The low molecular weight (20 and 35 kDa) polystyrene used in these experiments has relatively low viscosity at the infiltration temperature used, and the data suggest that it readily

flowed into the porous nanostructure and all of its voids as a single slab of polymer. Thus, at a given point in time during polymer infiltration, the porous Si multilayer consisted of a polymer-filled top layer and an air-filled bottom layer. The evolution of the optical spectrum is consistent with this interpretation; the polymer-filled layers displayed a λ_{SB} corresponding to a porous Si rugate filter completely filled with polymer (600 nm for these samples), and the air-filled layers displayed the original λ_{SB} of ~485 nm (Figure 5.5a). As the polymer front propagated into the film, it filled more layers of the rugate filter, and the intensity of the stop band peak for the polymer-filled layers increased. At the same time, the number of layers of the porous Si sample filled with air decreased, and the intensity of the stop band peak associated with the air filled layers decreased correspondingly.

The observed spectral changes in the wavelength and line shape of the stop band are in good agreement with transfer matrix calculations performed to simulate the polymer infiltration process. The simulated results (Figure 5.7) show a gradual reduction in intensity and broadening of the original stop band feature at 485 nm, while a new, broad stop band feature grows and sharpens at 600 nm. The simulations indicate that the 600 nm stop band should become observable when 25−50 periods, or 12.5−25% of the film is infiltrated with polystyrene.

The distinctively different infiltration behavior observed with the high molecular weight (200 and 400 kDa) polystyrenes can be interpreted in terms of a different pore filling mechanism. The high molecular weight polystyrenes possess relatively high viscosity at the infiltration temperature used and likely could not flow into the smaller branching pores of the nanostructure as effectively as low molecular weight polystyrene. Thus, the polymer flowed into the larger pores of the template first, filling the entire film from top to bottom, and the smaller voids filled on a longer time scale. Such a process is expected to change the refractive index of the entire film

gradually, resulting in a successive red shift of the stop band of the photonic crystal. Additionally, the smaller voids can be expected to fill sequentially from the top to the bottom of the porous film, following the flow of polymer into the larger pores in a given region of the film. This would generate a gradient of refractive index and the observed dispersion in wavelength of the stopband during polymer infiltration. As was observed with the high molecular weight polystyrene, a large, broad shoulder on the main stop band appeared relatively early in the polymer filling process, and this shoulder gradually red-shifted, evolving into a broad but distinct peak at 600 nm (Figure 5.5b). The peak never reached its maximum theoretical wavelength, indicating that polymer was excluded from the smallest pores in the material, which never completely filled.

The line width of the photonic stop band observed from the high molecular weight polystyrene samples is consistent with the above interpretation. The line width of a rugate filter is related to the uniformity of the periodic index contrast gradient in the layers. The high viscosity and low diffusivity of the polymer resulted in uneven filling of the pores, which is expected to lead to deviations from the ideal sinusoidal periodicity of refractive index in the filter. This would yield a dispersion of stop band λ_{SB} values and broadening of the band. By contrast, if the polymer had infiltrated the template as a front (as with the low molecular weight polymers), transfer matrix calculations showed that the stop band would have retained a narrow bandwidth through the process. Although both sample types (high and low molecular weight) displayed broadening of the stop band during polystyrene infiltration (Figure 5.5), the line broadening was more pronounced for the high molecular weight samples. Consistent with the observed inability of the higher molecular weight polymers to completely infiltrate the nanostructure (Figure 5.5c), the final line width observed from the high molecular weight samples was substantially larger than for the low molecular weight samples.

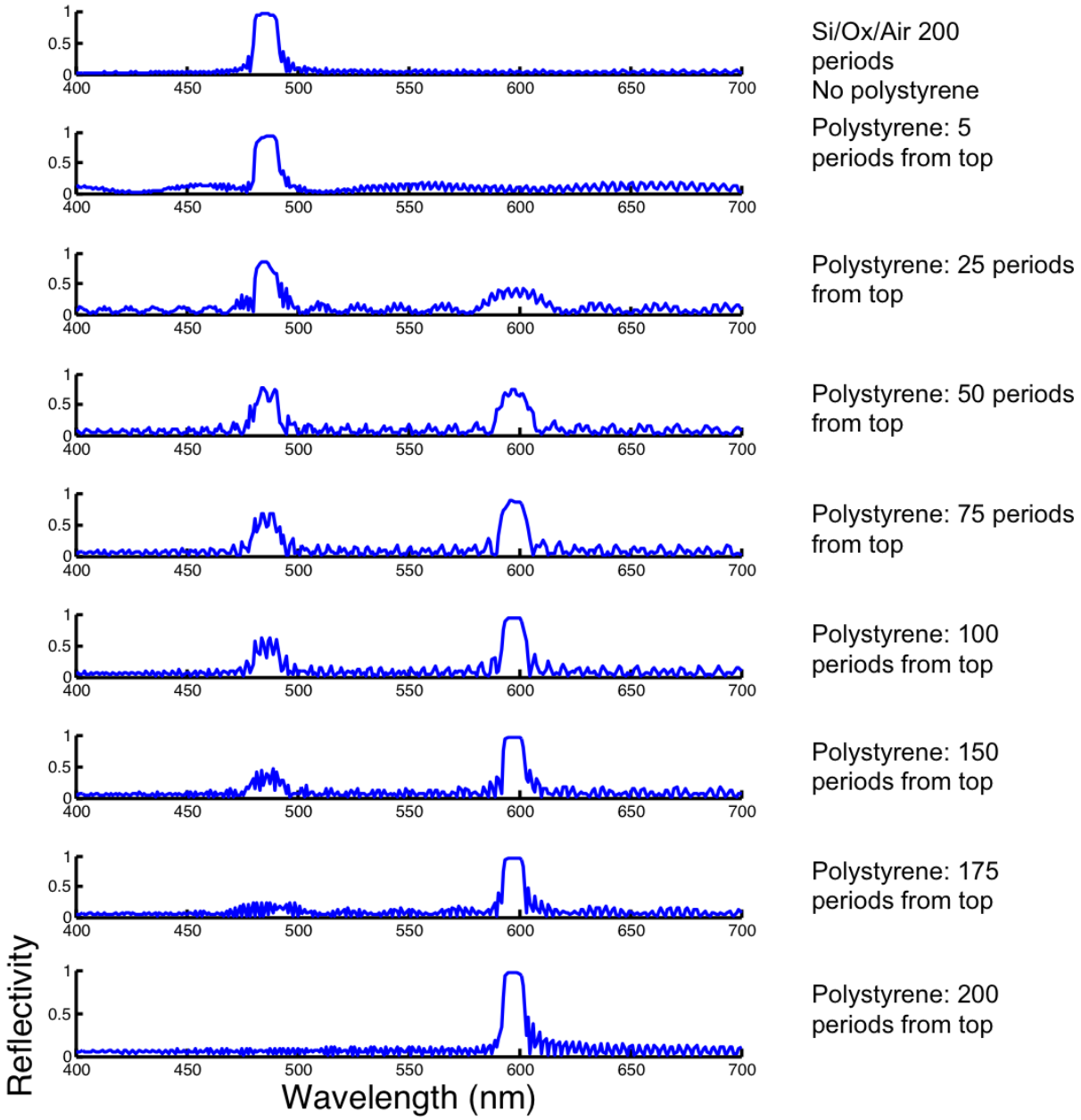

Figure 5.7 Calculated reflectivity spectra of oxidized porous Si rugate filter (λ_{SB} = 485 nm) before (top) and at various stages of polystyrene (n=1.6) infiltration, assuming that the polymer infiltrates as a single front, as described in the text. Calculations use the transfer matrix method, assuming a spatial period of 190 nm and a partially oxidized porous Si matrix. The refractive index of the porous Si skeleton was calculated by assuming an original as-etched sample with average porosity of 75%, which then underwent oxidation wherein 50% of the silicon skeleton was converted to silicon dioxide. A sinusoidal porosity contrast value of ±1.5% was superimposed on the average value of 75%, the number of repeats for the entire structure was 200, and a sampling wavelength of 1 nm was used for all the calculations. Final wavelength value of the stopband after complete polystyrene infiltration is λ_{SB} = 600 nm.

A simple interpretation of the low degree of infiltration observed for the composite samples is that polymer was excluded from the smallest voids in the porous Si template. This exclusion could be a kinetic or a physical phenomenon. Polymer diffusion is a complex process involving the end-to-end distance of the polymer, its degree of entanglement, and its local and bulk viscosity. Furthermore, diffusion rates for polymers in confined media can deviate substantially from the bulk values. For example, Russell and co-workers observed unusually high mobility and only a weak dependence on molecular weight for diffusion of polystyrene in the confined geometry of a nanoporous alumina template.[40]

In order to discern the relationship between pore size, polymer size, and the infiltration phenomena observed, we calculated the end-to-end distance for the polystyrene samples used in the present study. We used the freely rotating chain model developed by Flory[60] where r is the average chain length, C_∞ is the characteristic ratio, N is the number of chains, and l is the bond length in the styrene monomer, taken as the C−C bond distance of 1.54 Å:

$$\langle r\ CN \rangle = \infty\ l\ 2\ 1/2\ 1/2\ 1/2 \qquad (5.3)$$

The ideal model was employed for the calculations by assuming the Flory theorem,[61] which states that the polymer melt behaves in theta or ideal conditions where the chains are “unperturbed” and “phantom-like”. The characteristic ratio for polystyrene was taken as 10.3 based on the calculations of Graessley and Edwards.[62] The entanglement molecular weight (M_e) value for polystyrene used in this study, obtained from Fetters et al.,[63] was 18.1 kDa. The results are summarized in Table 5.1.

Table 5.1. The molecular weight, number of repeat units, root mean square end to end distance, and ratio with respect to the entanglement molecular weight. Repeat units, end to end distance, and entanglement ratio are based on calculations outlined in the text.

Molecular Weight (M_w)	**Number of Repeat Units**	**End to End Distance (nm)**	**Entanglement Ratio**
20,000	**182**	**6.6**	**1.3**
35,000	**318**	**8.8**	**1.9**
200,000	**1818**	**21.1**	**11.0**
400,000	**3636**	**29.8**	**22.1**

The calculations indicate that the end-to-end distance of the two low molecular weight polymers is less than 2 nm, smaller than the diameter of pores typically generated by electrochemical etch of silicon. Thus, the low molecular weight (20 and 35 kDa) polystyrene is expected to display more of a bulklike behavior in the confines of the porous Si template, consistent with the uniform pore infiltration observed. The low molecular weight polystyrene effectively replicated the porous Si nanostructure by simultaneously filling the larger pores and a substantial portion of the smallest voids. For higher molecular weight (200 and 400 kDa) polystyrene, the polymer end-to-end distance is calculated to be >10 nm, larger than many of the pores in the template. The observed evolution of the reflection spectra for the high molecular weight composite samples is consistent with the calculations and supports the hypothesis that the high molecular weight polymers infiltrated the larger pores first and then slowly and incompletely filled the smaller voids.

5.4.4 Polystyrene Replicas.

To further investigate the polymer dynamics described above, the melt-cast polymer was separated from the porous Si template by selective chemical etching, which generated freestanding polystyrene replicas. The porous Si templates were prepared as photonic crystals as in the above experiments, and polystyrene (either 35 or 400 kDa) was melt infiltrated (155 °C) for 1 h. At this point the relative extent of polymer infiltration was readily discerned as a visual color difference (Figure 5.8a). Whereas the original, empty templates displayed a green color, the low molecular weight composites displayed a uniform orange-red color while the high molecular weight composites displayed a range of colors across the film, from orange to green. As discussed above, this dispersion in λ_{SB} for the high molecular weight composite is attributed to heterogeneous filling of the nanostructure in the porous template. The larger red shift in λ_{SB} of the low molecular weight

composite is indicative of the greater extent of polymer infiltration, corresponding to approximately 90% of the porous Si voids filled. The high molecular weight polymer only infiltrated its porous Si template by approximately 40%.

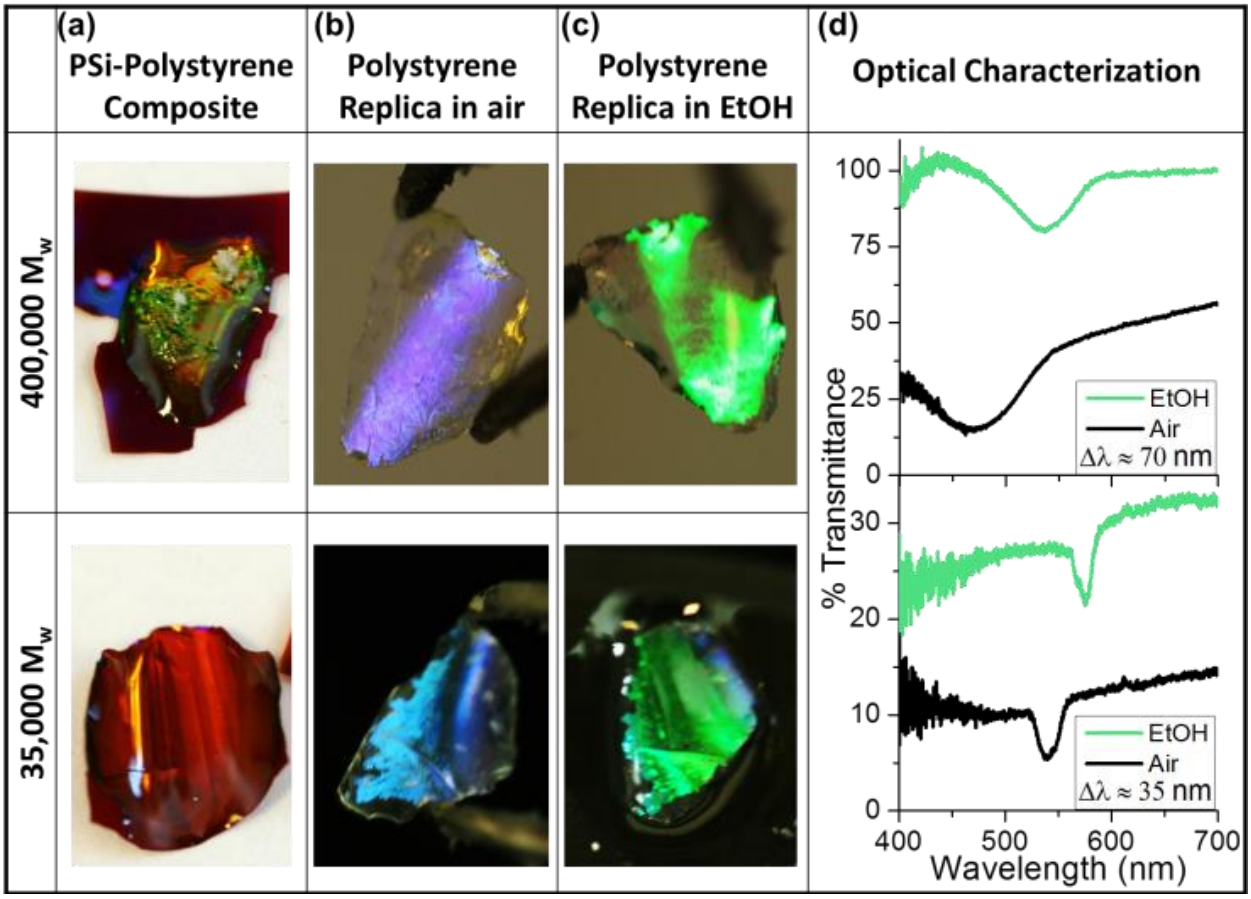

Figure 5.8 Comparison of replicas prepared from Mw = 400 kDa (top row) and 35 kDa (bottom row) polystyrene. Photographs of (a) polystyrene−porous Si composites, (b) polystyrene replicas with the template removed by selective etching, and (c) the same polystyrene replica from (b), wetted with ethanol. All samples were prepared using a porous Si template in the form of a rugate filter photonic crystal with λ_{SB} = 520 nm (in air). (d) Optical transmission spectra of the polystyrene replicas, obtained with air or ethanol (EtOH) filling the pores, as indicated.

The porous Si template was selectively removed from the composites by soaking in a solution containing aqueous HF and dimethyl sulfoxide (DMSO). The DMSO acts as a mild oxidant for Si, and the HF dissolves and removes SiO_2.[31, 64] Removal of the template was confirmed by Fourier transform infrared (FTIR) spectroscopy (Figure 5.9); the strong Si−O stretching mode at 1030 cm^{-1} that was apparent in the template and in the polystyrene-infiltrated template was completely absent in the replica after the chemical etching procedure.

The freestanding polymer-only films retained the nanostructure of the template, as indicated most obviously by the intense color in their visual appearance (Figure 5.8b) but also by cross-sectional SEM images and by spectral measurements. The SEM images of the replicas (Figure 5.10) revealed that the nanostructure was replicated in both of the polymer castings (using either high or low molecular weight polystyrene), although polymer infiltration appeared more complete and uniform with the low molecular weight polymer. The high molecular weight polymer replica displayed a pronounced porosity gradient from top to bottom of the structure, and distinct string-like features were apparent at the bottom edge of the film (Figure 5.8b). As each layer displays roughly the same porosity, the lag in pore filling of smaller voids (as opposed to heterogeneous filling due to the diversity of pore morphologies) presents the dominate reason for the broad and shifting stop band. Here the "top" of the film refers to the face where molten polymer initially encountered the porous Si template during melt-casting. The string-like features near the bottom of the film are suggestive of the proposed infiltration mechanism, where the end-to-end distance of high molecular weight polystyrene is comparable to or larger than the average pore diameter in the porous Si template, and the highly entangled polymer segments must align to permit more rapid flow as they traverse the narrow pore structure.

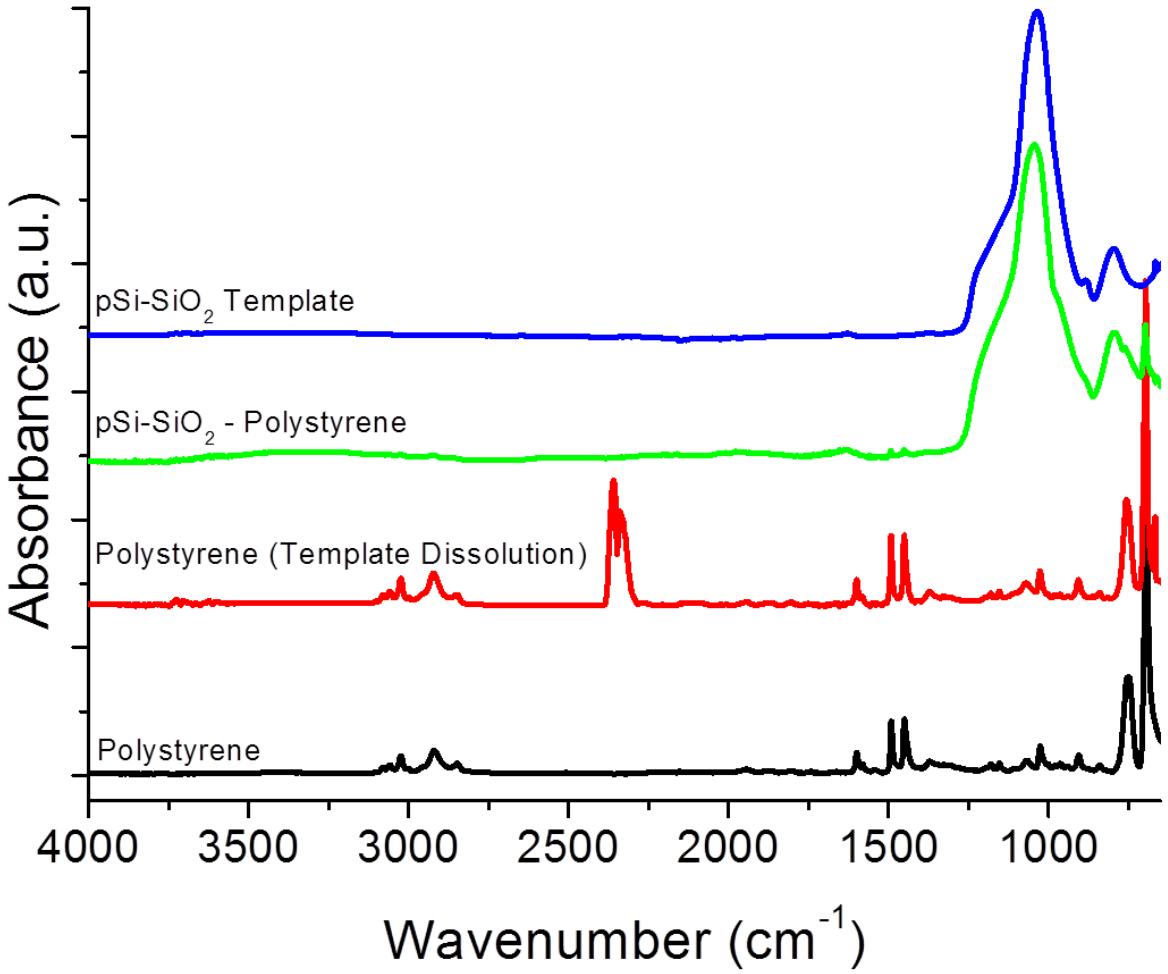

Figure 5.9 FTIR spectra of (top to bottom) the porous Si template, the polystyrene-silicon composite, the free standing polystyrene replica, and pristine polystyrene as a reference. The porous Si templates contain a sheath of SiO_2 surrounding the Si skeleton, whose characteristic vibrational mode is apparent in the FTIR spectrum: $\upsilon(Si\text{-}O_2)$ stretching vibration at 1030 cm^{-1}. After dissolution of the template, the characteristic Si-O vibrations are no longer observed in the spectrum, indicating complete removal of Si/SiO_2. The two bands centered at 2350 cm^{-1} in the replica are attributed to atmospheric CO_2.

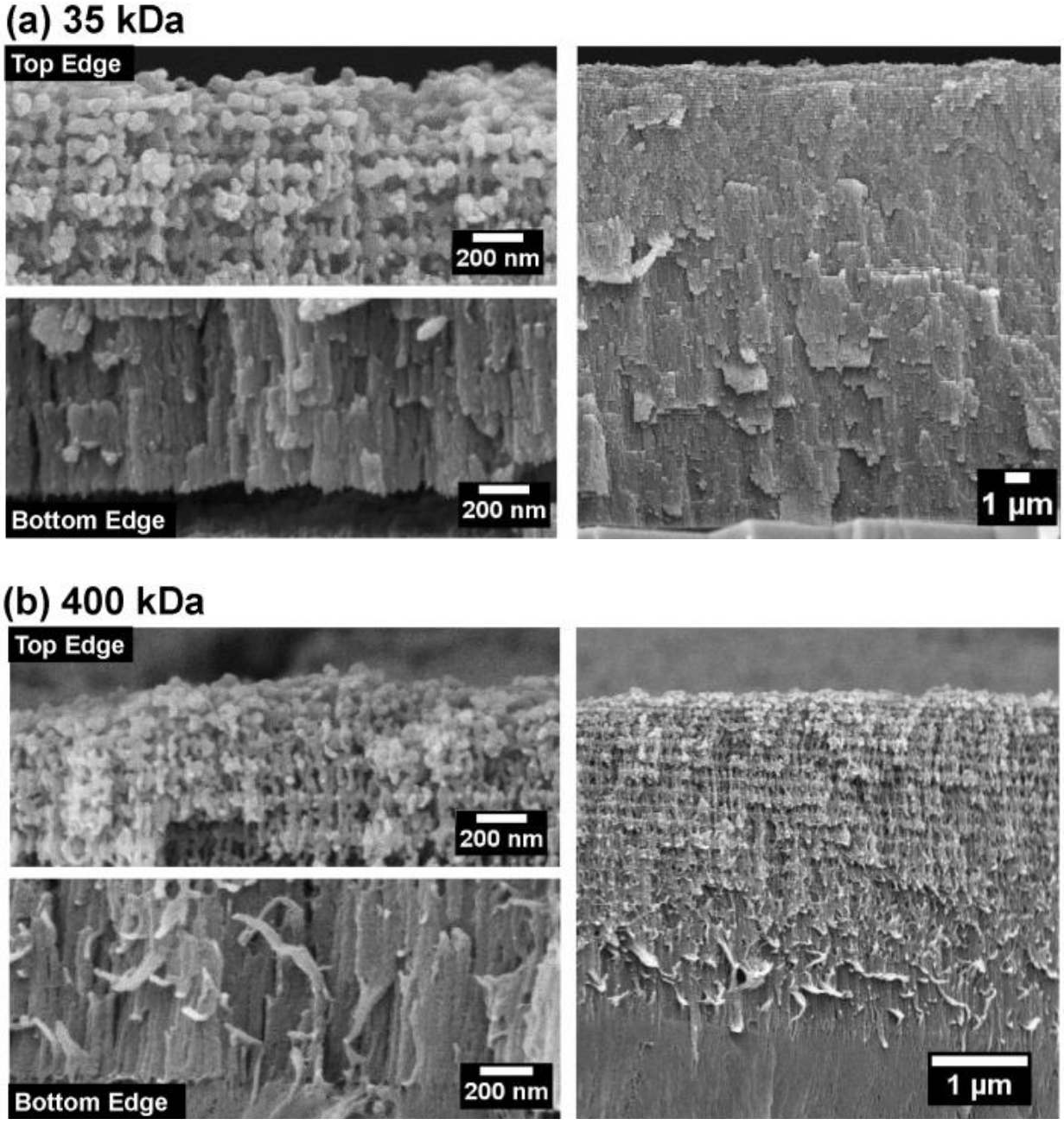

Figure 5.10 Cross-sectional SEM images of the top edge, bottom edge, and entire layer of photonic crystal replicas made using polystyrene of Mw 35 kDa (a) and 400 kDa (b). Here "top edge" refers to the side of the porous Si template that was originally in contact with molten polystyrene during the infiltration process. Both samples were prepared by melt infiltration into a porous Si rugate filter template followed by dissolution of the silicon template using a DMSO/HF(aq) etchant as described in the text.

Both high and low molecular weight polystyrene replicas displayed photonic stop bands, and the porosity of each replica was determined by the characteristic red shift of the stop band upon introduction of ethanol (Figure 5.8b−d). The SLIM technique41 was used to calculate the porosity of the film from the shift in the stop band, assuming appropriate refractive index values for polystyrene (n = 1.61) and ethanol (n = 1.36). Porosity of the high molecular weight (400 kDa) polystyrene replica was 49% and porosity of the low molecular weight (35 kDa) replica was 24%. The measured lower porosity of the replica made from low molecular weight polystyrene is consistent with its ability to more fully infiltrate the template.

5.5 Conclusion

In this work we fabricated polymer and polymer composite photonic crystals by melt-casting into porous Si photonic crystal templates. Using polystyrene as a test case, we demonstrated that the molecular weight of the polymer significantly impacts its infiltration dynamics and the final structure of the polymer photonic crystal. Lower molecular weight polystyrene displayed greater uniformity and higher fidelity of the nanostructure during infiltration because of its lower viscosity and the smaller end-to-end chain distances. Due to size exclusion and polymer entanglement effects, higher molecular weight polystyrene photonic crystals displayed string-like defects and incomplete filling of the template due to restricted polymer flow into the smaller voids. We then studied template dissolution from polymer composites using chemical etchants that dissolve both Si and SiO_2.

Chapter 5, in full, is a reprint of the material as it appears Wang, J., Lee, G.Y., Kennard, R.M, Bisiewicz, R.H., Barillaro, G., Cortez Lemus, N.A., Cao, X.C., Anglin, E.J., Park, J.S., Potocny, A., Bernhard, D. Li, J., and Sailor, M.J. Engineering the Properties of Polymer Photonic

Crystals with Mesoporous Silicon Templates. Chem. Mater. 2017, 29 (3), 1263-1272. The dissertation author was the primary investigator and author of this paper.

5.6 References

1. Li, Y. Y.; Cunin, F.; Link, J. R.; Gao, T.; Betts, R. E.; Reiver, S. H.; Chin, V.; Bhatia, S. N.; Sailor, M. J., Polymer Replicas of Photonic Porous Silicon For Sensing and Drug Delivery Applications. *Science* **2003,** *299* (5615), 2045-2047.

2. Yoon, M. S.; Ahn, K. H.; Cheung, R. W.; Sohn, H.; Link, J. R.; Cunin, F.; Sailor, M. J., Covalent Crosslinking of 1-D Photonic Crystals of Microporous Si by Hydrosilylation and Ring-Opening Metathesis Polymerization. *Chem. Commun.* **2003**, 680-681.

3. Coffer, J. L.; Whitehead, M. A.; Nagesha, D. K.; Mukherjee, P.; Akkaraju, G.; Totolici, M.; Saffie, R. S.; Canham, L. T., Porous silicon-based scaffolds for tissue engineering and other biomedical applications. *Phys. Status Solidi A-Appl. Mat.* **2005,** *202* (8), 1451-1455.

4. Mukherjee, P.; Whitehead, M. A.; Senter, R. A.; Fan, D. M.; Coffer, J. L.; Canham, L. T., Biorelevant mesoporous silicon/polymer composites: directed assembly, disassembly, and controlled release. *Biomed. Microdevices* **2006,** *8* (1), 9-15.

5. Nan, K.; Ma, F.; Hou, H.; Freeman, W. R.; Sailor, M. J.; Cheng, L., Porous silicon oxide-PLGA composite microspheres for sustained ocular delivery of daunorubicin. *Acta Biomaterialia* **2014,** *10* (8), 3505-3512.

6. Henstock, J. R.; Ruktanonchai, U. R.; Canham, L. T.; Anderson, S. I., Porous silicon confers bioactivity to polycaprolactone composites in vitro. *Journal of Materials Science-Materials in Medicine* **2014,** *25* (4), 1087-1097.

7. Lin, H.; Gao, T.; Fantini, J.; Sailor, M. J., A Porous Silicon-Palladium Composite Film for Optical Interferometric Sensing of Hydrogen. *Langmuir* **2004,** *20*, 5104-5108.

8. Chan, D. Y.; Sega, A. G.; Lee, J. Y.; Gao, T.; Cunin, F.; Renzo, F. D.; Sailor, M. J., Optical detection of C2 hydrocarbons ethane, ethylene, and acetylene with a photonic crystal made from carbonized porous silicon. *Inorg. Chim. Acta* **2014,** *422*, 21–29.

9. Tsang, C. K.; Kelly, T. L.; Sailor, M. J.; Li, Y. Y., Highly Stable Porous Silicon Carbon Composites as Label-Free Optical Biosensors. *ACS Nano* **2012,** *6* (12), 10546-10554.

10. Bonanno, L. M.; Segal, E., Nanostructured porous silicon-polymer-based hybrids: from biosensing to drug delivery. *Nanomedicine* **2011,** *6* (10), 1755-1770.

11. De Stefano, L.; Rotiroti, L.; De Tommasi, E.; Rea, I.; Rendina, I.; Canciello, M.; Maglio, G.; Palumbo, R., Hybrid polymer-porous silicon photonic crystals for optical sensing. *J. Appl. Phys.* **2009,** *106* (2).

12. Segal, E.; Perelman, L. A.; Cunin, F.; Renzo, F. D.; Devoisselle, J.-M.; Li, Y. Y.; Sailor, M. J., Confinement of Thermoresponsive Hydrogels in Nanostructured Porous Silicon Dioxide Templates. *Adv. Funct. Mater.* **2007,** *17*, 1153–1162.

13. Jang, S.; Kim, J.; Koh, Y.; Ko, Y. C.; Woo, H. G.; Sohn, H., Multi-encoded rugate porous silicon as nerve agents sensors. *J. Nanosci. Nanotechnol.* **2007,** *7* (11), 4049-4052.

14. Xiao, J.; Xu, W.; Wang, D. Y.; Choi, D. W.; Wang, W.; Li, X. L.; Graff, G. L.; Liu, J.; Zhang, J. G., Stabilization of Silicon Anode for Li-Ion Batteries. *J. Electrochem. Soc.* **2010,** *157* (10), A1047-A1051.

15. Li, X.; Gu, M.; Hu, S.; Kennard, R.; Yan, P.; Chen, X.; Wang, C.; Sailor, M. J.; Zhang, J.-G.; Liu, J., Mesoporous silicon sponge as an anti-pulverization structure for high-performance lithium-ion battery anodes. *Nat. Commun.* **2014,** *5*, 4105.

16. Wang, X. L.; Han, W. Q., Graphene Enhances Li Storage Capacity of Porous Single-Crystalline Silicon Nanowires. *ACS Appl. Mater. Interfaces* **2010,** *2* (12), 3709-3713.

17. Chouket, A.; Elhouichet, H.; Oueslati, M.; Koyama, H.; Gelloz, B.; Koshida, N., Energy transfer in porous-silicon/laser-dye composite evidenced by polarization memory of photoluminescence. *Appl. Phys. Lett.* **2007,** *91* (21), 211902.

18. Churaman, W.; Currano, L.; Singh, A. K.; Rai, U. S.; Dubey, M.; Amirtharaj, P.; Ray, P. C., Understanding the high energetic behavior of nano-energetic porous silicon. *Chem. Phys. Lett.* **2008,** *464* (4-6), 198-201.

19. Betty, C. A.; Sasikala, R.; Jayakumar, O. D.; Sakuntala, T.; Tyagi, A. K., Photoelectrochemical properties of porous silicon based novel photoelectrodes. *Prog Photovoltaics* **2011,** *19* (3), 266-274.

20. Becker, C. R.; Apperson, S.; Morris, C. J.; Gangopadhyay, S.; Currano, L. J.; Churaman, W. A.; Stoldt, C. R., Galvanic Porous Silicon Composites for High-Velocity Nanoenergetics. *Nano Lett.* **2011,** *11* (2), 803-807.

21. Tsuboi, T.; Sakka, T.; Ogata, Y. H., Metal deposition into a porous silicon layer by immersion plating: Influence of halogen ions. *J. Appl. Phys.* **1998,** *83* (8), 4501-4506.

22. Jeske, M.; Schultze, J. W.; Thonissen, M.; Munder, H., Electrodeposition of metals into porous si. *Thin Solid Films* **1995,** *255*, 63-66.

23. Andsager, D.; Hillard, J.; Hetrick, J. M.; AbuHassan, L. H.; Plisch, M.; Nayfeh, M. H., Quenching of porous silicon photoluminescence by deposition of metal adsorbates. *J. Appl. Phys.* **1993,** *74* (7), 4783-4785.

24. Anderson, D. G.; Anwar, N.; Aylett, B. J.; Earwaker, L. G.; Nasir, M. I.; Farr, J. P. G.; Stiebahl, K.; Keen, J. M., Chemical vapor deposition of metals and metal silicides on the internal surfaces of porous si. *J. Organomet. Chem.* **1992,** *437*, C7-C12.

25. Song, Y.-Y.; Schmuki, P., Modulated TiO2 nanotube stacks and their use in interference sensors. *Electrochem. Commun.* **2010,** *12* (4), 579-582.

26. Mun, K.-S.; Alvarez, S. D.; Choi, W.-Y.; Sailor, M. J., A Stable, Label-free Optical Interferometric Biosensor Based on TiO2 Nanotube Arrays. *ACS Nano* **2010,** *4* (4), 2070-2076.

27. Granitzer, P.; Rumpf, K.; Tian, Y.; Akkaraju, G.; Coffer, J.; Poelt, P.; Reissner, M., Fe3O4-nanoparticles within porous silicon: Magnetic and cytotoxicity characterization. *Applied Physics Letters* **2013,** *102* (19), 193110.

28. Kinsella, J. M.; Ananda, S.; Andrew, J. S.; Grondek, J. F.; Chien, M.-P.; Scadeng, M.; Gianneschi, N. C.; Ruoslahti, E.; Sailor, M. J., Enhanced Magnetic Resonance Contrast of Fe3O4 Nanoparticles Trapped in a Porous Silicon Nanoparticle Host. *Adv. Mater.* **2011,** *23*, H248–H253.

29. Balakrishnan, S.; Gun'ko, Y. K.; Perova, T. S.; Rafferty, A.; Astrova, E. V.; Moore, R. A., Porous silicon - rare earth doped xerogel and glass composites. *Physica Status Solidi a-Applications and Materials Science* **2005,** *202* (8), 1693-1697.

30. Amato, G.; Borini, S.; Rossi, A. M.; Boarino, L.; Rocchia, M., Si/SiO2 nanocomposite by CVD infiltration of porous SiO2. *Physica Status Solidi a-Applications and Materials Science* **2005,** *202* (8), 1529-1532.

31. Kelly, T. L.; Gao, T.; Sailor, M. J., Carbon and Carbon/Silicon Composites Templated in Microporous Silicon Rugate Filters for the Adsorption and Detection of Organic Vapors. *Adv. Mater.* **2011,** *23*, 1776–1781.

32. Du, C. Y.; Chen, M.; Wang, L.; Yin, G. P., Covalently-functionalizing synthesis of Si@C core-shell nanocomposites as high-capacity anode materials for lithium-ion batteries. *J. Mater. Chem.* **2011,** *21* (39), 15692-15697.

33. Martin, J.; Nogales, A.; Martin-Gonzalez, M., The Smectic-Isotropic Transition of P3HT Determines the Formation of Nanowires or Nanotubes into Porous Templates. *Macromolecules* **2013,** *46* (4), 1477-1483.

34. Liu, S.; Guo, D.; Xie, G., Nanoscale lubricating film formation by linear polymer in aqueous solution. *J. Appl. Phys.* **2012,** *112* (10).

35. Koga, T.; Jiang, N.; Gin, P.; Endoh, M. K.; Narayanan, S.; Lurio, L. B.; Sinha, S. K., Impact of an Irreversibly Adsorbed Layer on Local Viscosity of Nanoconfined Polymer Melts. *Phys. Rev. Lett.* **2011,** *107* (22).

36. Mackay, M. E.; Dao, T. T.; Tuteja, A.; Ho, D. L.; Van Horn, B.; Kim, H. C.; Hawker, C. J., Nanoscale effects leading to non-Einstein-like decrease in viscosity. *Nat. Mater.* **2003,** *2* (11), 762-766.

37. Overney, R. M.; Buenviaje, C.; Luginbuhl, R.; Dinelli, F., Glass and structural transitions measured at polymer surfaces on the nanoscale. *J. Therm. Anal. Calorim.* **2000,** *59* (1-2), 205-225.

38. Perelman, L. A.; Moore, T.; Singelyn, J.; Sailor, M. J.; Segal, E., Preparation and Characterization of a pH- and Thermally Responsive Poly(N-isopropylacrylamide-co-acrylic acid)/Porous SiO(2) Hybrid. *Adv. Funct. Mater.* **2010,** *20* (5), 826-833.

39. Massad-Ivanir, N.; Shtenberg, G.; Zeidman, T.; Segal, E., Construction and Characterization of Porous SiO(2)/Hydrogel Hybrids as Optical Biosensors for Rapid Detection of Bacteria. *Adv. Funct. Mater.* **2010,** *20* (14), 2269-2277.

40. Shin, K.; Obukhov, S.; Chen, J.-T.; Huh, J.; Hwang, Y.; Mok, S.; Dobriyal, P.; Thiyagarajan, P.; Russell, T. P., Enhanced mobility of confined polymers. *Nature materials* **2007,** *6* (12), 961-965.

41. Sailor, M. J., *Porous Silicon in Practice: Preparation, Characterization, and Applications*. Wiley-VCH: Weinheim, Germany, 2012; p 249.

42. Soeriyadi, A. H.; Gupta, B.; Reece, P. J.; Gooding, J. J., Optimising the enzyme response of a porous silicon photonic crystal via the modular design of enzyme sensitive polymers. *Polymer Chemistry* **2014,** *5* (7), 2333-2341.

43. McInnes, S. J. P.; Thissen, H.; Choudhury, N. R.; Voelcker, N. H., New biodegradable materials produced by ring opening polymerisation of poly(L-lactide) on porous silicon substrates. *J. Colloid Interface Sci.* **2009,** *332* (2), 336-344.

44. Fukami, K.; Sakka, T.; Ogata, Y. H.; Yamauchi, T.; Tsubokawa, N., Multistep filling of porous silicon with conductive polymer by electropolymerization. *Physica Status Solidi a-Applications and Materials Science* **2009,** *206* (6), 1259-1263.

45. Harraz, F. A.; Salem, M. S.; Sakka, T.; Ogata, Y. H., Hybrid nanostructure of polypyrrole and porous silicon prepared by galvanostatic technique. *Electrochim. Acta* **2008,** *53* (10), 3734-3740.

46. Ciampi, S.; Bocking, T.; Kilian, K. A.; Harper, J. B.; Gooding, J. J., Click chemistry in mesoporous materials: Functionalization of porous silicon rugate filters. *Langmuir* **2008,** *24* (11), 5888-5892.

47. Lie, L. H.; Patole, S. N.; Hart, E. R.; Houlton, A.; Horrocks, B. R., Photochemical Reaction of Diazomethane with Hydrogen-Terminated Silicon Surfaces. *J. Phys. Chem. B* **2002,** *106* (1), 113 -120.

48. Heinrich, J. L.; Lee, A.; Sailor, M. J., Porous Silicon Used as an Initiator in Polymerization Reactions. *Mat. Res. Soc. Symp. Proc.* **1995,** *358*, 605-610.

49. Yersak, T. A.; Shin, J.; Wang, Z.; Estrada, D.; Whiteley, J.; Lee, S.-H.; Sailor, M. J.; Meng, Y. S., Preparation of Mesoporous Si@PAN Electrodes for Li-Ion Batteries via the In-Situ Polymerization of PAN. *ECS Electrochem. Lett.* **2015,** *4* (3), A33-A36.

50. Li, Y. Y.; Cunin, F.; Sailor, M. J.; Link, J. R.; Gao, T. Nanostructured casting of organic and bio-polymers in porous silicon templates. U.S. Patent #7,713,778, May 11, 2010, 2010.

51. Kashanian, S.; Harding, F.; Irani, Y.; Klebe, S.; Marshall, K.; Loni, A.; Canham, L.; Fan, D. M.; Williams, K. A.; Voelcker, N. H.; Coffer, J. L., Evaluation of mesoporous silicon/polycaprolactone composites as ophthalmic implants. *Acta Biomater.* **2010,** *6* (9), 3566-3572.

52. Bonanno, L. M.; DeLouise, L. A., Integration of a Chemical-Responsive Hydrogel into a Porous Silicon Photonic Sensor for Visual Colorimetric Readout. *Adv. Funct. Mater.* **2010,** *20* (4), 573-578.

53. Xia, T. A.; Kovochich, M.; Liong, M.; Meng, H.; Kabehie, S.; George, S.; Zink, J. I.; Nel, A. E., Polyethyleneimine Coating Enhances the Cellular Uptake of Mesoporous Silica Nanoparticles and Allows Safe Delivery of siRNA and DNA Constructs. *ACS Nano* **2009,** *3* (10), 3273-3286.

54. Wu, J.; Sailor, M. J., Chitosan Hydrogel-Capped Porous SiO2 as a pH-Responsive Nano-Valve for Triggered Release of Insulin. *Adv. Funct. Mater.* **2009,** *19*, 733–741.

55. McInnes, S. J. P.; Voelcker, N. H., Silicon-polymer hybrid materials for drug delivery. *Future Med. Chem.* **2009,** *1* (6), 1051-1074.

56. Li, Y. Y.; Kollengode, V. S.; Sailor, M. J., Porous silicon/polymer nanocomposite photonic crystals by microdroplet patterning. *Adv. Mater.* **2005,** *17* (10), 1249-1251.

57. Vincent, G., Optical properties of porous silicon superlattices. *Appl. Phys. Lett.* **1994,** *64* (18), 2367-9.

58. Snow, P.; Squire, E.; Russell, P. S. J.; Canham, L., Vapor sensing using the optical properties of porous silicon Bragg mirrors. *Journal of Applied Physics* **1999,** *86* (4), 1781-1784.

59. Allcock, P.; Snow, P., Time-resolved sensing of organic vapors in low modulating porous silicon dielectric mirrors. *Journal of Applied Physics* **2001,** *90* (10), 5052-5057.

60. Flory, P. J., The configuration of real polymer chains. *The Journal of Chemical Physics* **1949,** *17* (3), 303-310.

61. Colby, R.; Rubinstein, M., Polymer physics. *New-York: Oxford University* **2003**, 274-281.

62. Graessley, W.; Edwards, S., Entanglement interactions in polymers and the chain contour concentration. *Polymer* **1981,** *22* (10), 1329-1334.

63. Fetters, L. J.; Lohse, D. J.; Milner, S. T.; Graessley, W. W., Packing length influence in linear polymer melts on the entanglement, critical, and reptation molecular weights. *Macromolecules* **1999,** *32* (20), 6847-6851.

64. Anglin, E. J.; Schwartz, M. P.; Ng, V. P.; Perelman, L. A.; Sailor, M. J., Engineering the chemistry and nanostructure of porous silicon Fabry-Pérot films for loading and release of a steroid. *Langmuir* **2004,** *20* (25), 11264-11269.

CHAPTER SIX

A Visual Sensor for Sterilization of Polymer Fixtures Using Embedded Mesoporous Silicon Photonic Crystals

6.1 Abstract

A porous photonic crystal is integrated with a plastic medical fixture (IV connector hub) to provide a visual colorimetric sensor to indicate the presence or absence of alcohol used to sterilize the fixture. The photonic crystal is prepared in porous silicon (pSi) by electrochemical anodization of single crystal silicon, and the porosity and the stop band of the material is engineered such that the integrated device visibly changes color (green to red or blue to green) when infiltrated with alcohol. Two types of self-reporting devices are prepared and their performance compared: the first type involves heat-assisted fusion of a freestanding pSi photonic crystal to the connector end of a preformed polycarbonate hub, forming a composite where the unfilled portion of the pSi film acts as the sensor; the second involves generation of an all polymer replica of the pSi photonic crystal by complete thermal infiltration of the pSi film and subsequent chemical dissolution of the pSi portion. Both types of sensors visibly change color when wetted with alcohol, and the color reverts to the original upon evaporation of the liquid. The sensor performance is verified using E. coli-infected samples.

6.2 Introduction

Intravascular (IV) catheters are among the most commonly used means of delivering therapeutics or for aspirating blood samples in hospitals and clinics worldwide. Despite widespread use, these devices are prone to bacterial colonization that puts patients at risk of local and systemic infections such as injection-site infection, catheter related-bloodstream infection, phlebitis, septic thrombophlebitis, endocarditis, and other complications. In the United States alone, more than 80,000 intravascular catheter-related complications are reported every year for patients in intensive care units, with an estimated 9600 to 20,000 deaths and an expense ranging from $296 million to $2.3 billion US annually.[1-4] Needle-less systems, where an IV line is placed in the patient

and reused multiple times via a port or hub, are now common in healthcare settings, and they have led to substantial reductions in needle-stick injuries. Failure to properly disinfect the reusable injection port on such IV catheters is considered one of the more pervasive errors made by staff and health care professionals.[5] When not disinfected between administration sets, an IV connector hub can provide a source of infection, and when disinfected improperly, the infusion of residual disinfectants into the bloodstream can lead to phlebitis.[6-9] Phlebitis is an inflammation of the cannulated vein, and it is the most frequent complication associated with peripheral IV catheters, occurring in 27−70% of all the catheters deployed.[10-14] IV-related phlebitis is recognized as a problem by manufacturers, the Center for Disease Control (CDC), and the Infusion Nurses Society (INS).[15-22] This study was motivated by the desire to incorporate a sensor on an IV catheter connector hub that could provide a visual cue to the healthcare worker that the device has been disinfected, and furthermore indicate when the liquid sterilizing agent has been completely removed.

The approach used in this work is based on embedding a mesoporous photonic crystal into the surface of a plastic fixture.[23-25] Our group and others have shown that porous silicon (pSi) can be used as a template for solution-cast or heat cast polymers,[26-31] and the resulting polymer-pSi composites or polymer replicas can retain the porous nanostructure of the template. By using a porous photonic crystal as the template, the polymer takes on the spectral characteristics of the template, in particular, its ability to display a stop band in the reflectance spectrum, and the ability of this stop band to shift when infiltrated with a liquid - resulting in a color change that is readily observed with the unaided eye. For the present work, we employed thermal infiltration to either partially or completely infiltrate the template, and used an IV connector (BD-MaxPlus® Clear) made of polycarbonate, which formed a viscous liquid that infiltrated the pores of the pSi host.

Two types of sensors were prepared (Figure 6.1): (a) a composite sensor, where the pSi template was fused to the polycarbonate surface, partially infiltrating the pSi film but leaving the majority of the pore structure open and available for sensing; and (b) an all-polymer sensor, where the pSi template was completely infiltrated with polymer and then removed by chemical dissolution. The sensor devices were tested for their ability to indicate the presence of disinfectant delivered by a commercial alcohol swab (70% isopropyl alcohol), and sterilization was confirmed using a nonpathogenic E. coli strain and a standard culturing assay.

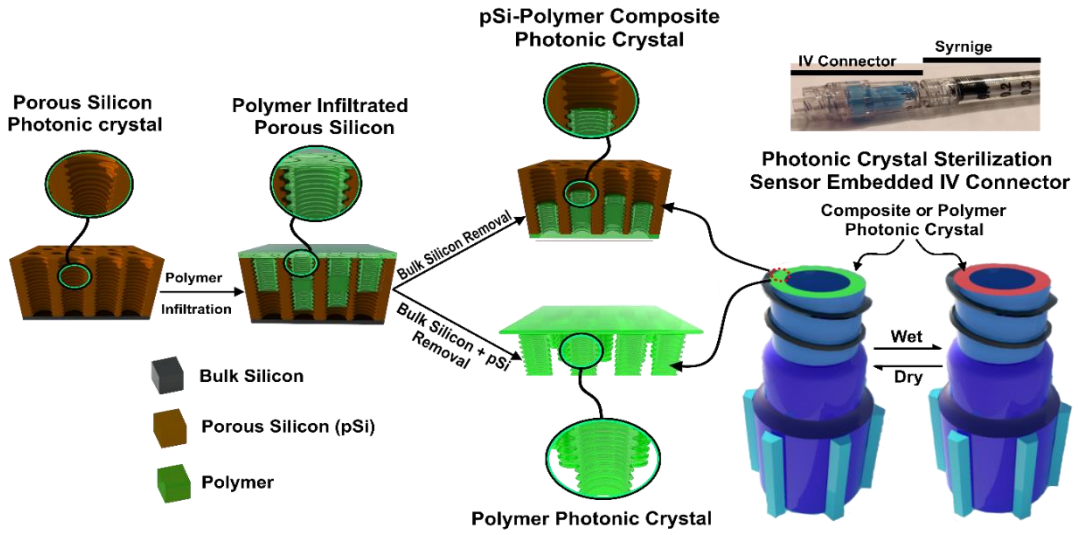

Figure 6.1. Schematic of the Steps Used to Prepare pSi−polymer Composites and All-Polymer Photonic Crystals Used as Sterilization Sensors. First, a pSi template is prepared by electrochemical etching using a sinusoidal current density-time waveform, such that it possesses a layered porous nanostructure that acts as a 1-dimensional photonic crystal. Then the polymer (in this work, a test article or a commercial IV connector hub) is thermally infiltrated into the pores of the pSi template by raising its temperature above the glass transition temperature of the polymer (230 °C for the polycarbonate used in this work). To prepare the pSi-polymer composite photonic crystal, the polymer is only partially infiltrated into the pSi nanostructure, and the thermally infiltrated structure separates from the silicon wafer substrate upon cooling. For the all-polymer photonic crystal, the composite is removed by freeze-fracture, and then the nanostructured pSi template is removed by chemical dissolution using a mixture of dimethyl sulfoxide, aqueous HF, and ethanol. A photograph of a sensor-embedded IV connector hub mated to a syringe is shown on the upper right. The tip of the hub where the photonic sensor is located attaches to the syringe through a luer lock fitting, and the opposite end of the hub connects to an IV line. Under normal operation, the luer lock isolates the sensor element from the fluid being delivered and there is no contact between the IV fluid and the sensor.

6.3 Materials and Experimental Methods

6.3.1 Materials

Single-crystal silicon wafers, highly boron-doped (ptype), of resistivity 1 mΩ·cm, and thickness 525 ± 25 μm and polished on the (100) face were purchased from Virginia Semiconductor. Absolute ethanol (200 proof) was obtained from VWR International Corp. Hydrofluoric acid (48% aqueous, ACS grade) was obtained from Macron Chemicals. Potassium hydroxide (ACS grade, 85%) was purchased from Fisher Scientific Chemicals, Inc. Phosphate buffered saline (PBS) solution and Hank's buffered saline solution (HBSS) was purchased from Gibco, Inc. Aqueous solutions were prepared from 18 MΩ deionized water (DI). Clear polycarbonate sheets were purchased from eplastic, inc. (HYGARD MS1250 CLEAR-A00, 040 in. thick). BD MaxPlus Clear IV connectors were purchased from the manufacturer. Identity of the polymers was confirmed by FTIR (strong bands at 1769, 1503, 1219, 1187, and 1158 cm−1 characteristic of polycarbonate).

6.3.2 Preparation of pSi Photonic Crystal Templates.

Different pSi rugate filter templates were used for the pSi-polymer composite and the all-polymer sensors. Both types of pSi photonic crystals were etched into the highly doped silicon samples by electrochemical anodization (Keithley Sourcemeter model 2651, Tektronix, USA) in aqueous ethanolic hydrofluoric acid (3:1 v:v 48% aqueous HF:ethanol) electrolytes following published procedures.23 Caution: HF is highly toxic and contact with skin should be avoided. Anodization of the wafers was preceded by a "sacrificial etch" step to prepare clean and reproducible silicon surfaces. The sacrificial etch was carried out at constant current density (100 mA cm−2) for 30 s, which generated a thin porous silicon layer. This layer was then completely removed by immersion in a 2 M aqueous solution of potassium hydroxide (KOH). The pSi photonic crystal templates for the pSi-polymer compsite sensor were prepared by application of a

sinusoidal current densitytime profile (minimum current density: 100 mA cm−2, maximum current density: 200 mA cm−2, period: 2.6 s, 300 cycles). The templates were then thermally oxidized in a muffle furnace (Thermolyne, Thermo Fisher, USA) at 500 °C for 4 h (including the time for temperature ramp of 10 °C/min from/to ambient for both the heating and cooling phases). For the pSi photonic crystal templates used to prepare the all-polymer sensors, the current density limits and the period of the waveform were the same as for the pSi polymer composite devices, but the number of cycles was 250, resulting in a thinner pSi template. The thermal oxidation (500 °C) was carried out for 2 h.

6.3.3 Polymer Infiltration into pSi Photonic Crystal Templates.

All polymers were thermally infiltrated into the pSi templates by placing the polymer onto the template and heating it above the glass transition temperature of the polymer (210 °C). To prepare the pSi-polymer composite and the all-polymer photonic disks, a polycarbonate sheet (∼1.5 cm × 1 cm) was placed on top of the pSi template and preheated to 185 °C on a hotplate (in air). After 2 h at 185 °C, the temperature was raised to 210 °C and infiltration was allowed to proceed for 16−18 h. The samples were allowed to cool to room temperature, and they were then immersed in liquid nitrogen. The rapid cooling usually resulted in fracture at the polymer/silicon substrate interface, generating freestanding pSi-polymer composites. The resulting pSi-composite sensors were then cut into disks with a diameter of 5 mm using a metal hole punch and used as-is. The allpolymer sensor disks were prepared from these pSi-composites by soaking in a solution consisting of 1 part dimethyl sulfoxide (DMSO), 3 parts 48% aqueous HF, and 1 part ethanol for 18 h. This solution has been shown to effectively remove Si and SiO_2 from composite pSi structures.[39]

Polymer infiltration of IV connector hub units (BDMaxPlus® Clear) was carried out using the above thermal infiltration process, where the IV connectors were placed onto the pSi substrate and heated to 185 °C for 2 h. The connectors were pressed to the surface to ensure contact of the sensor to the silicon. The temperature was then increased to 210 °C for 10−18 h. To prepare the all-polymer IV connector hub sensors, the pSi template was removed by soaking in DMSO/HF/EtOH (1:3:1) for 8 h.

6.3.4 Scanning Electron Microscopy and EDS Analysis

Samples were imaged using a Zeiss Sigma 500 scanning electron microscope (SEM) with at an accelerating voltage of 1 kV. The samples were coated with iridium using a sputter coater prior to imaging to prevent charging. The energy dispersive X-ray spectra (EDS) were obtained using a Philips XL30 field emisson SEM fitted with an EDS detector (iXRF Systems, inc), operating at an accelerating voltage of 20 kV and using integration times of 50 s. Images were processed and analyzed using ImageJ software (public domain program, NIH). SEM images of bacteria were obtained ater sequential dehydration in decreasing concentrations of ethanol (100% v/v to 0% v/v).

6.3.5 Optical Characterization

Reflectance spectra were acquired using a CCD spectrometer (Ocean Optics USB-4000) fitted to a bifurcated fiber optic cable as previously described.[23] One arm of the optical fiber was connected to the spectrometer, while the other arm was connected to a tungsten light source (Ocean Optics LS-1). The distal end of the combined fiber was attached to a focusing lens to allow acquisition of 180° reflectance spectra from the sample surface, with a spot size of approximately 2 mm in diameter. The porosity and thickness of the samples was calculated using the spectroscopic liquid infiltration method (SLIM) described previously.[23, 32] For the measurements

involving repeated wetting/drying cycles, the sensor sample was firmly clamped to an optical table and the spectrometer was configured to acquire a spectrum every minute for a period of 2 h. A baseline signal was acquired for 10 min and then an aliquot (10 μL) of 70% isopropyl alcohol was applied to the surface of the sensor. After approximately 3 min the sample was dried in a stream of compressed air. The sample was then allowed to sit in air for an additional 3 min and the next aliquot of alcohol was applied, up to a total of 10 applications. Refractive index of liquids was measured with a Refracto 30GS (Mettler Toledo). Digital photographs were obtained using a Canon Rebel XT1 digital camera fitted with a macro lens.

6.3.6 Bacteria Culture and Sterilization Procedures

A nonpathogenic E. coli strain, FDA strain Seattle 1946, was obtained from American Type Culture Collection (ATCC). A single colony of E. coli was inoculated into Luria−Bertani (LB) media (COR Biosciences, USA) and incubated overnight at 37 °C. The culture was then washed three times with PBS (pH 7.4) by centrifugation (Centrifuge 5804, Eppendorf, 4200×g, 5 min) and resuspended in 10 mL of buffer. The culture was diluted to an optical density (OD) of 0.1 (measured at 600 nm), corresponding to 108 CFU/mL.[33-34] In order to assess the efficiency of sterilization of infected sensors, the culture was diluted to 2 × 106 CFU/mL and the devices were incubated in the mixture for 4 h. The samples were then rinsed briefly with water and scrubbed with a 70% isopropyl alcohol saturated swab (Webcol alcohol pads, Covidien) for 30−60 s, following the published protocol.[22] In order to assay for remaining live bacteria, the sample surface was thoroughly scraped with a heat sterilized inoculation loop and the bacteria collected in 200 μL of sterile water. For each sample, four dilutions of bacteria were prepared 0×, 100×, 1000×, and 10000× in sterile water and streaked onto an agar plate (Prepoured Agar BioRad). The plate was incubated at 37 °C for 16 h and the number of CFUs was determined by counting the colonies and

accounting for appropriate dilution. Only the agar plates that contained 25−250 colonies per plate were considered in the CFU/mL calculation.

6.3.7 Si Leaching Tests

The IV connector-sensor device was attached to a 1 mL syringe filled with 1 mL HBSS that was pushed through the IV connector into a glass vial. The delivered volume was measured taking into account the dead volume in the syringe and IV connector hub to test for gross leakage. The delivered solution was tested for traces of dissolved silicon using the molybdenum blue (MB) assay. The MB assay reagents were prepared following the literature protocol:46 Solution A was prepared by adding ammonium molybdate tetrahydrate (1 g) and concentrated hydrochloric acid (3 mL) to 25 mL DI water, mixing, and then diluting in a volumetric flask with additional DI water to a total volume of 50 mL. For solution B, oxalic acid (4 g), 4-(methylamino)phenol hemisulfate (1.33 g), and anhydrous sodium sulfite (0.8 g) were added to 100 mL of DI water and mixed well. The solution was diluted in a volumetric flask with additional DI water to a total volume of 200 mL. For assaying, the test solution, solution A, and solution B were mixed in a volume ratio of 4:1:5 in an Eppendorf tube and incubated at room temperature for 1 h. The silicon content was quantified by measuring the absorbance at 810 nm and comparing to a standardized curve prepared from ICP standard of Si (TraceCERT, 1000 mg/L Si in nitric acid, SigmaAldrich).

6.4 Results and Discussion

6.4.1 Fabrication of pSi Templates for the Photonic Sensors.

The pSi templates for both types of sensors (polymer composite and all-polymer) were synthesized by electrochemical anodization of single-crystal silicon wafers in an aqueous ethanolic hydrofluoric acid electrolyte using a sinusoidal current−time profile as previously described.[23, 35] Cross-sectional scanning electron microscope (SEM) images revealed the modulation in porosity

as a series of light and dark bands spaced at approximately 150 nm and running parallel to the surface of the porous layer (Figure 6.2 and Figure 6.3). The evenly spaced layers generate an optical rugate filter, displaying a stop-band in the reflection spectrum with a wavelength of maximum reflectance directly proportional to the spacing in the layers (Figure 6.4).[36-37] Thus, the apparent color of the pSi template (and thus the resulting templated sensors) was readily engineered by adjusting the period of the sine wave that served as the current density−time waveform used in electrochemical anodization of the silicon wafer. Digital analysis of the planeview SEM images (Figure 6.2a) indicated a mean pore diameter of 19 ± 7 nm. Average porosity of the pSi template, measured by means of gravimetry and by the spectroscopic liquid infiltration method (SLIM),[23] was ~60% for both sensor types (Figure 6.4 and Table 6.1). For the pSi-polymer composite sensors, the pSi templates were designed to be thicker, containing more porous layers than the templates used for the all-polymer sensors. The thickness of the templates was measured by cross-sectional SEM, by SLIM, and by gravimetry, and they were on the order of ~60 μm thick for the pSi-polymer composite sensor templates and ~40 μm thick for the all-polymer sensor templates (Table 6.1).

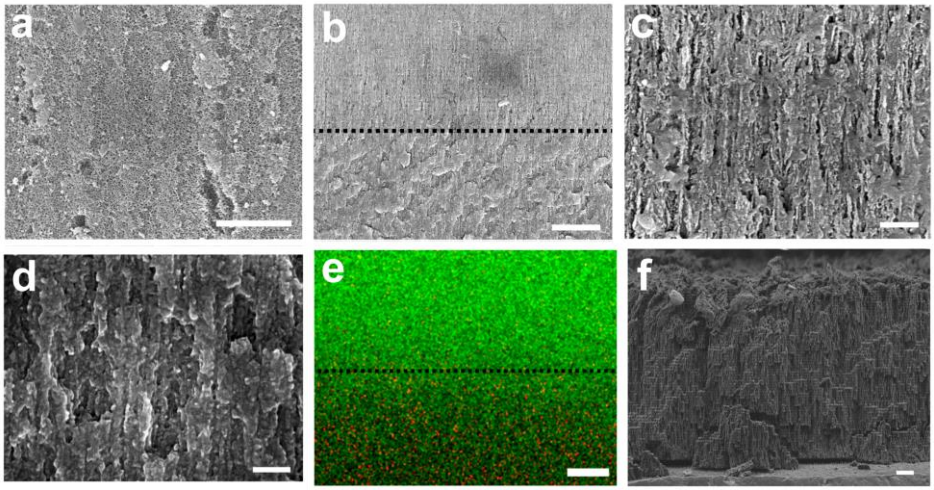

Figure 6.2. SEM images of pSi-polymer composite photonic sensor element consisting of a pSi template partially infiltrated with polycarbonate. (a) Plan view of the pSi template on the side opposite the polymer layer, showing the open pore structure of the template with no detectable polymer. Scale bar: 1 μm. (b) Cross-sectional image showing the interface between the polymer-infiltrated region of the pSi film and the empty region of the pSi film. The layered nanostructure corresponding to the periodic porosity gradient that was generated during electrochemical preparation of the pSi template is apparent. The dashed line indicates the demarcation between polymer-filled and empty pSi regions. Scale bar: 2 μm. (c) Higher magnification crosssectional image of the empty region of the pSi film (above the dashed line in (b)), representing ~6 cycles of the repeating rugate nanostructure in the porous film. Scale bar: 200 nm. At this magnification, the gradual oscillations in porosity that occurs in the nanostructure to generate the optical rugate filter are not readily apparent. (d) Cross-sectional image obtained at the same magnification as in (c), but of the polycarbonate-filled region of the pSi film (below the dashed line in (b)). Scale bar: 200 nm. (e) EDS element map of approximately the same region as represented in (b), showing the boundary and depth of polymer infiltration (green represents silicon and red represents carbon). Scale bar: 2.5 μm. (f) Cross-sectional image of the all-polymer photonic sensor for comparison. This sample was prepared by thermal infiltration of a pSi template with polycarbonate as in the other images, but the silicon nanostructure has been removed by selective dissolution using dimethyl sulfoxide/ HF(aq) as described in the text. Scale bar: 1 μm.

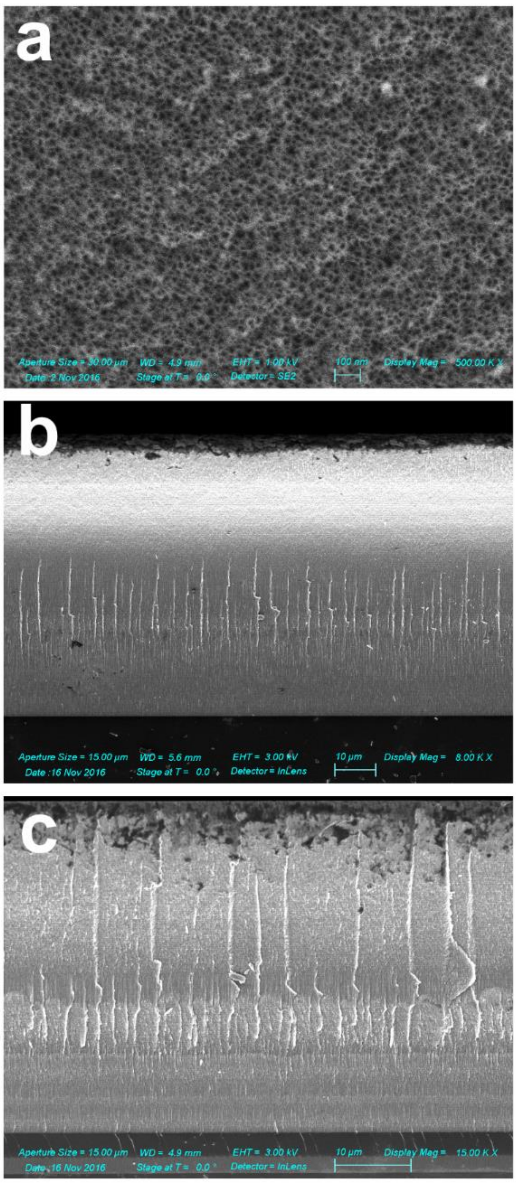

Figure 6.3. Scanning electron microscope (SEM) Images of Porous Silicon Photonic Crystal Templates. (a) Plan-view image representative of all the pSi templates used in this study, revealing the pore morphology. The mean pore diameter of the porous layer was 19 ± 7 nm, determined from the planview image using the ImageJ image processing software package (NIH). (b) Cross-sectional SEM image of the pSi template used to prepare the all-polymer photonic sensors (thickness 43.0 ± 0.2 μm). (c) Crosssectional SEM image of the pSi template used to prepare the composite photonic sensor (thickness 67.3 ± 0.3 μm). These images were acquired in secondary electron imaging mode, using a Zeiss Sigma 500 SEM operating at an accelerating voltage of 1 kV (a) or 3 kV (b and c). The all-polymer and composite sensors that resulted from these templates displayed thicknesses of 37 ± 2 μm and 61 ± 4 μm, respectively (images not shown).

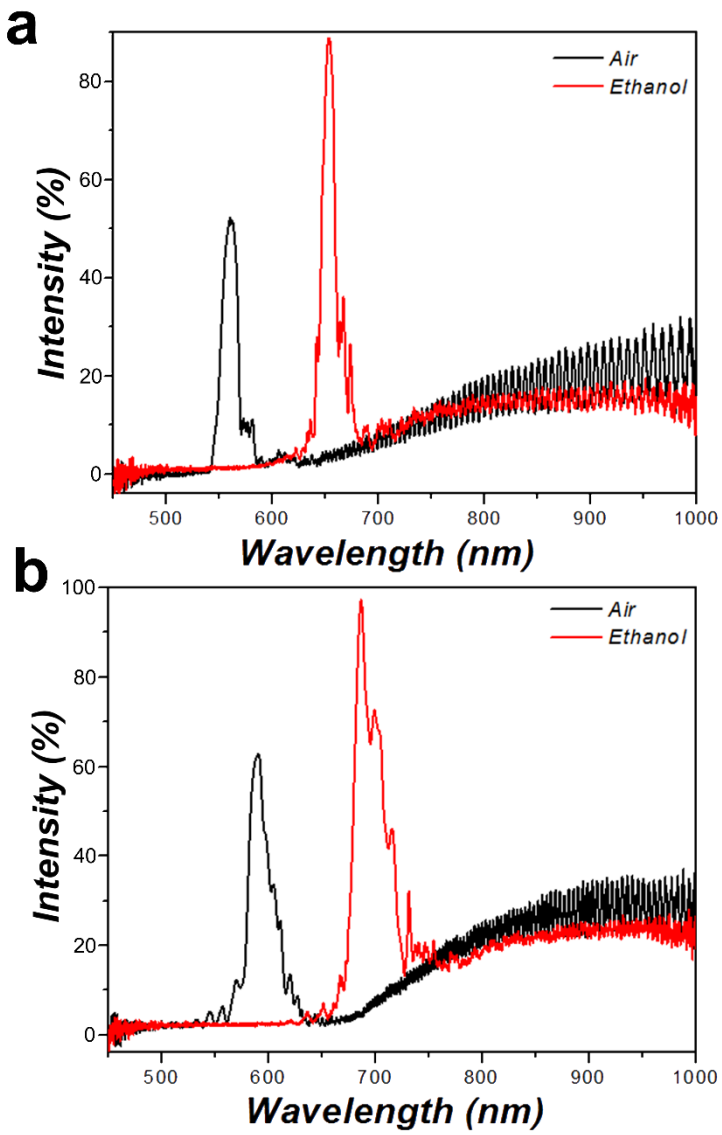

Figure 6.4. Optical reflection spectra of pSi templates used to prepare (a) the all-polymer sensor and (b) the pSi-polymer composite sensor. Both panels present reflectance spectra measured on the samples in air (black trace) and immersed in ethanol (red trace). These spectra, acquired before and after wetting of the porous nanostructure with ethanol, are used to determine the thickness and porosity of the pSi template. The red shift in the spectrum derives from the increase in average refractive index of the film when the air (n = 1.000) in the porous nanostructure is replaced with ethanol (n = 1.361). The degree of spectral shift is related to the average refractive index of the pSi skeleton and the average porosity of the film.1 To obtain open porosity and thickness, measured values of effective optical thickness were fit to a two-component Bruggeman effective medium approximation. For the template used to prepare the all-polymer sensor, the porosity and thickness of the pSi template were 61 ± 1 % and 38 ± 2 μm, respectively. For the template used to prepare the composite sensor, the porosity was 60 ± 2 % and the thickness was 61 ± 4 μm. These spectra were obtained on the as-etched pSi templates, prior to thermal oxidation.

Table 6.1. Porosity, thickness, and color of sensors. Porosity and thickness values determined using the indicated methods[a] for the templates used to prepare the pSi-polymer composite and the all-polymer photonic sensors.

Sensor Type	Thickness (μm)			Porosity (%)		λ_{sb}, pSi as-etched[b]	λ_{sb}, pSi post-ox[c]	λ_{sb}, final device[d]
	SEM	SLIM	Grav.	SLIM	Grav.			
pSi-polymer composite sensor	67.3 ± 0.3	61 ± 4	57 ± 1	60 ± 2	65 ± 2	560 nm	525 nm	550 nm
All-polymer sensor	43.0 ± 0.2	38 ± 2	42 ± 1	61 ± 1	62 ± 2	592 nm	538 nm	447 nm

[a] SEM is thickness of pSi photonic crystals before oxidation measured from cross-sectional scanning electron microscope images; SLIM refers to the Spectroscopic Liquid Infiltration Method, a nondestructive optical measurement that determines film thickness and porosity from the optical constants and the Fabry-Perot interference spectrum;1 Grav. is a gravimetric measurement based on mass changes as described in reference (1).

[b] Wavelength of the maximum in the stop band reflection measured on the pSi template, as-etched but prior to oxidation or polymer infiltration.

[c] Wavelength of the maximum in the stop band reflection measured on the pSi template, after oxidation but prior to polymer infiltration. Oxidation was performed in air at 500 °C for 2 hrs.

[d] Wavelength of the maximum in the stop band reflection measured on the final sensor fixture. For the pSi-polymer device, this corresponds to the pSi template after partial thermal infiltration of polycarbonate. For the all-polymer device, this corresponds to the pSi template that had been thermally infiltrated with polycarbonate and then treated with DMSO/HF(aq) etchant to remove residual pSi from the device.

6.4.2 Fabrication of pSi-Polymer Composite Photonic Sensors

One of the key motivations for constructing the composite sensors was to capitalize on the high refractive index contrast afforded by silicon. This can be expected to give a strong reflectance spectrum that is more readily seen by eye when the sensor is wetted with the disinfectant solution; for example, if the porous skeleton possesses a refractive index closely matching the value of the liquid disinfectant filling the pores, then the intensity of the stop band reflectance will be near zero. The index of refraction of crystalline silicon in the wavelength range of interest is 3.8[36] while the index of polycarbonate (1.58)[38] is closer to the index of 70% aqueous isopropanol (1.372 ± 0.001 at 22.6 °C, measured at λ = 589.3 nm) used as a disinfectant. Thus, we attempted to build a sensor element where only a small portion of the pSi film was infiltrated with polymer, in order to serve as an anchoring point, while the majority of the pSi layer remained open and exposed on the fixture surface to act as the sensor (Figure 6.1). The thermal infiltration process used to fabricate the pSi-polycarbonate composites was first optimized using hard polycarbonate disks and a range of temperatures and infiltration times was explored. To improve polymer infiltration and avoid drift of the optical spectrum during processing, the pSi templates were partially oxidized by heating at 500 °C for 2 h in air prior to polymer infiltration. This treatment generated a thin oxide shell on the pSi skeleton. Filling of pores by polymers is a complex process that is highly dependent on the pore size of the host and the viscosity of the polymer.[26, 39] In the present case, the optimal thermal infiltration procedure was determined to be as follows: the polycarbonate disk was placed on top of the pSi photonic crystal template, the assembly was heated at 185 °C for 2 h, and then the temperature was increased to 230 °C and the device was maintained at that temperature for an additional 12 h. We found that the first step of heating at 185 °C was effective in avoiding the formation of air bubbles in the polymer. The second heating step yielded relatively complete

infiltration of the pores. Upon cooling, the polymer-infiltrated pSi layer spontaneously detached from the underlying bulk silicon wafer due to stresses associated with solidification of the polymer and differences in the thermal expansion coefficients of silicon and polycarbonate, resulting in a freestanding pSi-polymer composite. The open pore structure of the pSi template was readily observed on the detached side of the film (Figure 6.2a), indicating that the polymer did not fully infiltrate the nanostructure. This was confirmed by optical reflectance measurements (Figure 6.5) and with cross-sectional SEM measurements (Figure 6.2b). Energy dispersive X-ray spectroscopy (EDS) was employed in the SEM to confirm the infiltration of polymer into the pSi template, and it indicated that the polymer penetrated to depths of between 7 and 10 μm into the 60-μm-thick pSi templates (Figure 6.2b,e). This is consistent with the optical measurements; the reflection spectrum from the composite film displayed two distinct stop bands, one at the wavelength corresponding to the air-filled pSi template (λ_{sb} = 520 nm) and another, weaker band (λ_{sb} = 660 nm) arising from the polycarbonate-filled region of the pSi template (Figure 6.5, Supporting Information). The imprinting process (i.e., infiltration of polymer into the pSi master to replicate its nanostructure) yielded comparable morphological and spectral characteristics when commercial polycarbonate IV connector hubs were used in place of the polycarbonate disks (Figure 6.6).

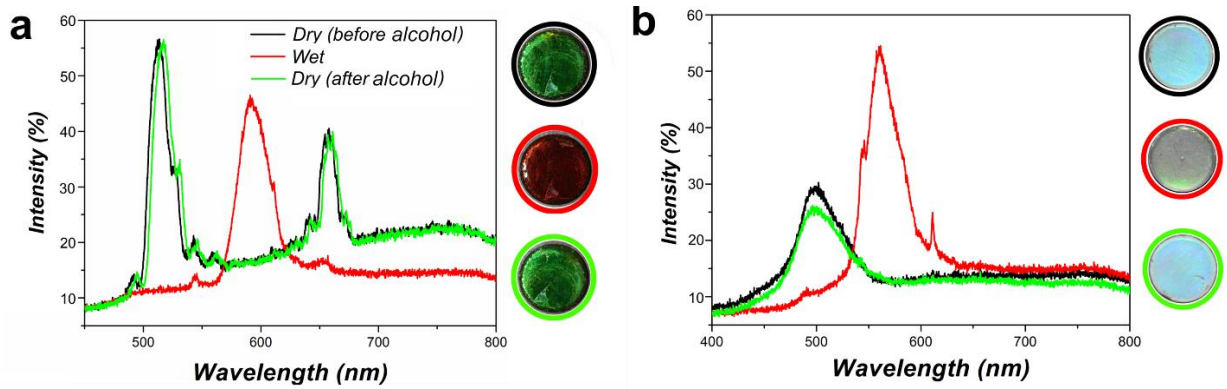

Figure 6.5. Optical reflection spectra and photographs of pSi-polycarbonate composite (a) and all-polymer (b) samples used to characterize the templating and alcohol sensing properties. (a) Optical reflection spectra of the dry pSi-polymer composite (black trace), the pSi-polymer composite wetted with 70 % isopropyl alcohol (red trace), and the pSi-polymer composite after the alcohol solution has dried for ~ 2 min in air (green trace). The pSi-polymer composite was prepared by partial infiltration (melt-casting) of a polycarbonate sheet as described in the text. Because the pSi film is only partially infiltrated with polycarbonate, the sample displays two stop bands. The stop band at 520 nm corresponds to the empty portion of the pSi layer (not filled with polycarbonate) and the band at 660 nm corresponds to the portion of the pSi layer that is filled with polycarbonate. Upon wetting with alcohol, the stop band at 520 nm (the empty portion of the pSi film) shifts to 600 nm and the stop band at 660 nm displays a negligible shift. The 660 nm band appears weak in the wetted sample relative to the 600 nm band because the spectra are not corrected for the instrument response function or the tungsten halogen lamp intensity distribution. The tungsten halogen light source has relatively low intensity in the blue-green region of the spectrum. Photographs of the sensor samples at the various stages of the experiment (before wetting, wet, and after drying in air) are shown at the right. (b) Optical reflection spectra of the dry all-polymer film (black trace), the all-polymer film wetted with 70 % isopropyl alcohol (red trace), and the all-polymer film after the alcohol solution has dried for ~ 2 min in air (green trace). The all-polymer sensor film was prepared by melt-casting of a polycarbonate sheet and dissolution and removal of the pSi template as described in the text. Because this film no longer contains a pSi component, the sample displays a single stop band, which is associated with the photonic nanostructure in the polymer replica. A distinct red shift is observed for both types of photonic disks when they are infiltrated with liquid.

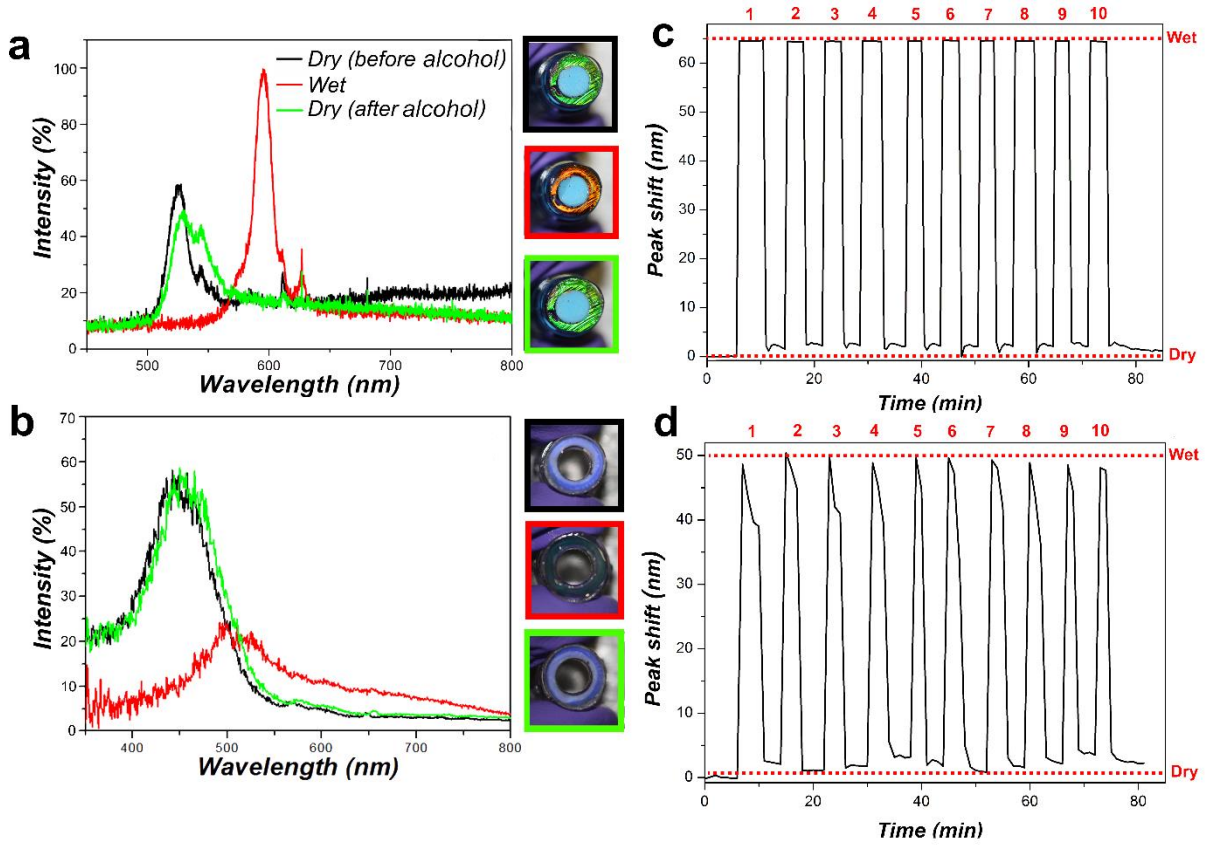

Figure 6.6. Spectral shifts and reproducibility of pSi-polymer composite and all-polymer photonic sensors embedded in IV connector hub units. Reflected light spectra quantify the shift in the photonic stop-band when 70% isopropyl alcohol sterilization solution is applied: (a) pSi-polymer composite photonic sensor; (b) all-polymer photonic sensor. Images at the right of each plot show digital photographs of the IV connector hub units corresponding to the traces: top, dry sensor prior to alcohol; middle, sensor wetted with alcohol; bottom, sensor after a few minutes of air-drying. Border color of each photograph corresponds to the color of each representative trace in the plots. (c-d) Changes in the wavelength of the reflection stop-band, recorded during repeated exposure of (c) composite IV connector hub unit and (d) all-polymer IV connector hub unit to 70 % isopropyl alcohol solution. Peak shift values correspond to the increase in wavelength (red shift) of the stop band when the porous nanostructure is fully wetted with 70 % isopropyl alcohol solution ("Wet") relative to the dry, air-filled sensor ("Dry"). The number of sterilization cycles is indicated on the top.

6.4.3 Fabrication of All-Polymer Photonic Sensors

Whereas the pSi-polymer composite sensors displayed strong, readily observable colors due to the high refractive index of the silicon skeleton, the presence of silicon, or any material other than the medical-grade polycarbonate of the fixture raises concerns about potential contamination or adverse reactions of fluids contacting the device. Therefore, we also explored an alternative device design where the photonic sensor was composed completely of polycarbonate. This approach relied on the ability of the pSi material to serve as a removable template for polymer casting that can be selectively removed by a chemical etchant.[27] There are a few chemical systems that can selectively remove silicon: the well-known xenon difluoride etchant used in the manufacture of silicon MEMS,[40] strongly alkaline solutions such as aqueous KOH,[23] and mixtures of dimethyl sulfoxide and aqueous HF.[41] In this work we chose to use the dimethyl sulfoxide/aqueous HF etchant due to its low reactivity with polycarbonate.

The dimethyl sulfoxide (DMSO) in the dimethyl sulfoxide/ aqueous HF system acts as a mild chemical oxidant, converting silicon to silicon dioxide. In the presence of aqueous HF, the oxide product then dissolves. The relatively low surface tension of DMSO allows the etchant solution to penetrate the mesoporous structure, allowing efficient removal of the pSi skeleton.[41-42] In the present case, the procedure was sufficiently mild that the polymer retained a replica of the nanostructure of the original pSi template (Figure 6.2f), and the resulting all polymer nanostructure displayed the optical properties of a photonic crystal (Figure 6.5). However, because the wavelength of the stop band depends on the volume fraction and the index of refraction of the skeleton, the stop band of the resulting polycarbonate replicas was substantially blue-shifted from the stop band of the original pSi templates. Thus, the stop band of the pSi template used for the all-polymer photonic sensors was engineered with a periodicity appropriate to yield the desired

color in the final system (Table 6.1). The imprinting process yielded similar results with commercial polycarbonate IV connector hubs as it did with polycarbonate disks (Figure 6.6).

6.4.4 Sensing of Alcohol Sterilization Solutions Using the Photonic Devices

The ability of the pSi-polymer composite and the all-polymer photonic devices to detect the presence of 70% isopropyl alcohol disinfecting solutions was then assessed by optical reflectance spectroscopy and by visual inspection. A distinctive red shift in the stop-band of >60 nm was observed for either the pSi-polymer or the all-polymer photonic sensor disks. The visual appearance of the pSi-polymer composite changed from green to red upon addition of the alcohol disinfectant (Figure 6.5a and Figure 6.6a), and for the all-polymer photonic structure the color changed from blue to light green (Figure 6.5b and Figure 6.6b). The spectral observations for the imprinted commercial polycarbonate IV connector hubs were similar to those of the polycarbonate disk test articles, although the net spectral shifts upon alcohol infiltration were somewhat smaller for the IV connector hub devices (65 nm vs 80 nm for the composite sensors and 40 vs 60 nm for the all-polymer sensors). This implies that the porosity of the photonic crystal was somewhat lower for the IV connector hubs relative to the polycarbonate disk test articles and suggests that the polycarbonate comprising the IV connector hubs did not infiltrate the pSi templates as fully as the polycarbonate comprising the test disks. The difference in flow behavior is not surprising, as the hubs and the disks derived from different manufacturers, and it is unlikely that the viscosity, molecular weight, and other fundamental properties of the two types of polycarbonate test articles used in this study were the same. Although we confirmed that both comprised polycarbonate by FTIR measurements, we did not measure viscosity, average molecular weight, or other properties of the polymer samples. The photonic stop-band for both the photonic sensors returned to their original values after evaporation of the disinfectant. Both types of devices were able to visually

report complete evaporation of the disinfectant, although the intensity of the stop band displayed by the all-polymer devices was distinctively weaker and more difficult to discern than for the pSi-polymer composites. The weaker reflection from the all-polymer rugate filters is consistent with the lower refractive index contrast between polycarbonate and the medium filling the pores (either air or alcohol) relative to the index contrast between silicon and these same media, as discussed above and elsewhere.[24, 37, 43] The color changes were stable and reproducible over repeated wetting and air-drying cycles (Figure 6.6c,d). Direct addition of 70% isopropyl alcohol (20 μL) into these devices required 2−3 min to completely evaporate and for the original color to return. A concern with colorimetric sensors is that a fraction of the human population is color-blind and so may not readily be able to distinguish blue-to-green or green-to-red color changes. For this reason we explored the possibility of tuning the spectral band of the photonic sensor to the red, such that liquid infiltration shifted the stop band into the near-infrared region of the spectrum (Figure 6.7). The visual perception to a completely color-blind person (or in a grayscale image) in this case was a distinctive change from light to dark upon liquid infiltration.

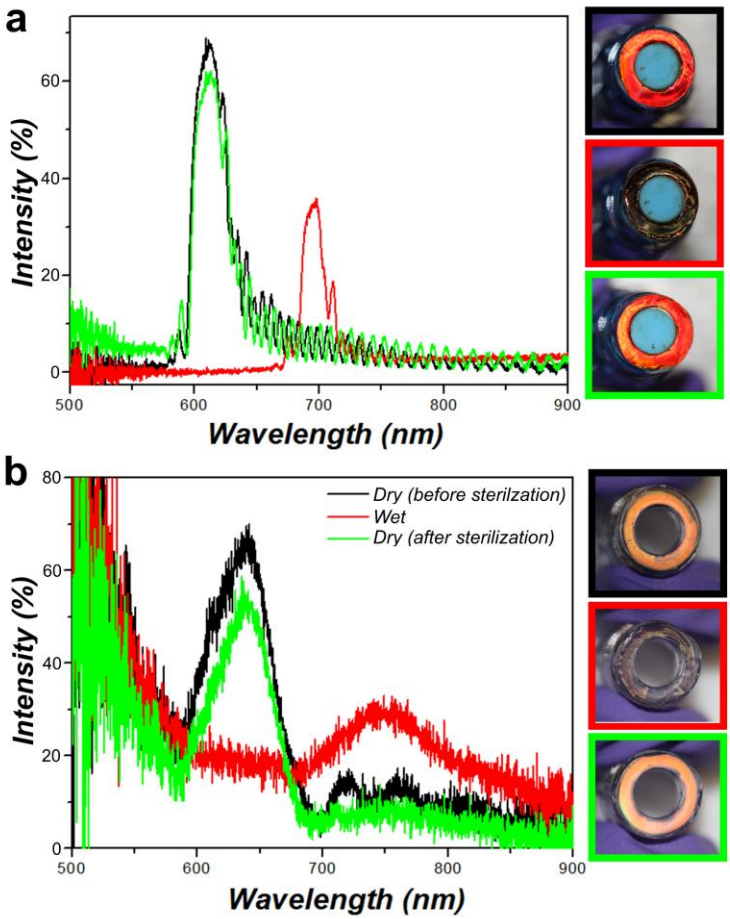

Figure 6.7. Optical reflection spectra of red colored pSi-polycarbonate composite (a) and all-polymer (b) samples integrated into IV connector hub units. The pSi templates in these experiments were engineered such that they appeared red when dry. Upon infiltration of ethanol, the sensor appears black as the reflection stop-band shifts to the NIR region of the spectrum, which is not visible to the human eye. Thus the these fixtures would appear to undergo a white to black transition to a color-blind individual. Optical reflection spectra and digital photographs of the pSi-polymer composite and polymer sterilization sensor embedded in IV connector hubs were obtained using the same measurement conditions as given in Figure S3, except the spectra here were corrected for instrument spectral response by ratioing to the spectrum of a silver mirror. The sinusoidal waveform used to prepare the pSi templates for these devices were etched by varying the current density between 100 to 200 mA cm^{-2} for 300 and 250 repeats for the pSi-polymer composite and the all-polymer sensors, respectively. The period of the sinusoidal waveform for the pSi-polymer composite device was 2.2 sec and for the all-polymer device it was 1.9 sec. Reflection spectra and digital photographs of samples correspond to dry (black trace or outline), wetted with 70 % isopropyl alcohol (red trace or outline), and after the alcohol solution has dried for ~ 2 min in air (green trace or outline).

6.4.5 Sensor Performance under a Bacterial Challenge.

In order to validate the sensors in a realistic complex matrix, we exposed the photonic sensors embedded in IV connectors to growth media containing bacteria. There were two main goals of these experiments: first, we wanted to evaluate if contaminants would collect in the nanoporous matrix of the sensors, fouling the optical response. Second, it is known that bacteria can accumulate on porous media, and there is a potential that such surfaces may enhance bacterial colonization and growth and thus be more difficult to sterilize.[44-47] The sensors were incubated in 2 × 106 CFU/mL of nonpathogenic E. coli (FDA strain Seattle 1946) in Luria−Bertani (LB) media for 4 h. Subsequently, the sensors were thoroughly rinsed with DI water and then scraped with an inoculation loop to collect the adhered bacteria, which were then cultured on agar plates to determine the number of colony-forming units (CFUs). We detected (1.5 ± 0.4) × 105 CFU/mL on the pSi-polymer composite photonic sensors and (7 ± 2) × 104 CFU/mL on the all-polymer photonic sensors (Table 6.2).

The observed difference in the number of CFUs found on the two types of sensors can be attributed to differences in their wettability, which is known to influence bacterial adhesion.[48] Water contact angle (WCA) measurements (Figure S5, Supporting Information) showed that the pSi-polymer composite photonic sensors, which displayed the higher degree of bacterial attachment, were also substantially more hydrophilic (WCA = 11.6°) compared to the relatively hydrophobic all-polymer photonic sensors (WCA = 113.8°).

Another set of sensors were subjected to the same E. coli incubation procedure and then swabbed with alcohol wipes following the sterilization procedure recommended by the U.S. Center for Disease Control (30 s to 2 min, wipe saturated with 70% isopropyl alcohol).[16] After the sterilization procedure, the surface of the samples was assayed for the presence of live bacteria as described above. No live E. coli were observed to survive this procedure (to a detection limit of

25 CFU/mL). We also analyzed the porous sensor surfaces by electron microscopy to determine the fate of adhered E. coli post-sterilization. Electron microscope images of the surface of the sensor devices after contact with the alcohol swab showed evidence of ruptured E. coli cells; consistent with the lack of CFUs observed after sterilization (Figure 6.9).

The optical changes exhibited by the sensors during the infection and sterilization processes were monitored using reflection spectroscopy and visual assessment. The pSi-polymer composite photonic sensors, being more hydrophilic,[26] were infiltrated by aqueous solutions and thus exposure to the culture media induced a color change (red shift) similar to that observed upon alcohol sterilization. When the samples dried the color blue-shifted back to the original, air-filled values. Subsequent sterilization with alcohol generated the expected red shifts in color, analogous to what was observed with the pristine sensors. Thus, the color changes observed with the pSi-polymer composite photonic sensors could not clearly distinguish between the alcohol sterilization solution and a bacteria-infected liquid medium. By contrast, the all-polymer photonic sensors were more hydrophobic (Figure 6.8); the aqueous culture media did not readily infiltrate the nanopores, and no substantial change in color was observed when this sensor type was incubated with the bacteria culture medium. As with the pSi-polymer composite photonic sensors, the expected color changes were observed upon subsequent sterilization with alcohol. Thus, the all-polymer system is more reliable from the perspective of the colorimetric assay: due to the hydrophobic nature of the sensor, the green-to-red color change was only observed with alcohol solutions and not with water-based solutions.

The nanoporous nature of the sensor elements could be a potential source of leaks in a connector hub. We tested the integrated IV connector hub-sensor units for leakage under simulated infusion conditions and observed no visible fluid leakage after 10 usage cycles. We also evaluated

whether or not silicon (in the form of water-soluble orthosilicate) would leach into the infusate from the pSi-polymer composite photonic devices. The silicon content in the infusate (PBS) was measured using the molybdenum blue assay,[46] which showed no detectable (LOD = 0.5 ppm) silicon in 1 mL of infusate after 30 min of contact with the sensor hub. For comparison, the concentration of silicon in human plasma is 5 ppm.[47-49] It should be noted that the sensor described in this work is designed to function in a specific clinical environment, and a main limitation of the sensor is that it is nonspecific, responding with a color change to essentially any liquid that infiltrates the mesoporous structure. Thus, contamination of the sensor surface with IV fluids that can infiltrate but that are not readily removed from the nanoporous matrix is a concern. It is worth noting that modern IV connectors are designed to minimize the possibility of IV fluid leakage; the BD-MaxPlus Clear IV needleless connector used in this study is an antireflux connector that is specifically designed to minimize the possibility of leakage of IV fluid into the region where the sensor surface is located during priming, flushing, and aspiration. Another concern related to integrating these visual sensors with an IV connector is the mechanical stability of the sensor. Although we did not perform extensive mechanical tests, we did not observe any signs of mechanical wear or degradation during repeated swabbing with alcohol or during repeated infusion of buffer solutions through the sensor-integrated IV device. These latter experiments involved connecting and disconnecting a luer lock syringe to the IV connector for each flushing procedure.

6.5 Conclusion

In summary, this study explored the potential for embedding pSi photonic sensors into reusable medical devices as a visual aid to effective sterilization. We employed needleless IV connector hubs as test fixtures and evaluated two types of sensors consisting of polycarbonate thermally cast into pSi photonic crystal templates: a composite consisting of pSi and polycarbonate, and an all-polycarbonate device from which the pSi template had been selectively removed. Both

types of sensors displayed distinctive color changes that reported on the infiltration and the evaporation of a 70% isopropyl alcohol disinfectant. The pSi-polymer composite sensor displayed more intense colors and color changes that were more visually distinct, but the all-polymer sensor was more effective at repelling water-based solutions that could potentially act as false positives for the presence of the alcohol sterilizing agent. The sensor-embedded IV connector units could be used multiple times without any degradation in optical response, leakage, or leaching of silicon into a test infusate.

Chapter 6, in full, is a reprint of the material as it appears Kumeria, T., Wang, J. (co-first author), Chan, N., Harris, T.J. and Sailor, M.J. A Visual Sensor for Alcohol Sterilization of Plastic Fixtures Using a Porous Silicon Photonic Crystal Template. ACS Sensors 2017, 3 (1), pp 143–150. The dissertation author was the primary investigator and author of this paper.

Table 6.2. Bacterial counts on photonic sensors before and after sterilization.

Sample	Bacteria concentration (CFU/mL)[a]	
	Bacteria Adhered[b]	***After sterilization***
pSi-polymer composite photonic IV connector hub	150000 ± 41000	N.D.[c]
All-polymer photonic IV connector hub	71000 ± 23000	N.D.

[a] Sensors embedded in polycarbonate IV connector hubs were incubated in 2 x 10^6 CFU/mL of non-pathogenic E. coli (FDA strain Seattle 1946) in Luria-Bertani (LB) media for 4 hr. Sterilization performed on sensors by alcohol swab (70% isopropyl alcohol) following published CDC protocol.[16]

[b] Bacteria counts reported from the agar plates inoculated with 1000x dilutions of e-coli.

[c] N.D. = not detected. The LOD for the method was 25 CFU/mL. Error values calculated based on agar plate data from 3 samples, with serial dilutions of 0x, 100x, 1000x, and 10,000x for each e-coli plating test.

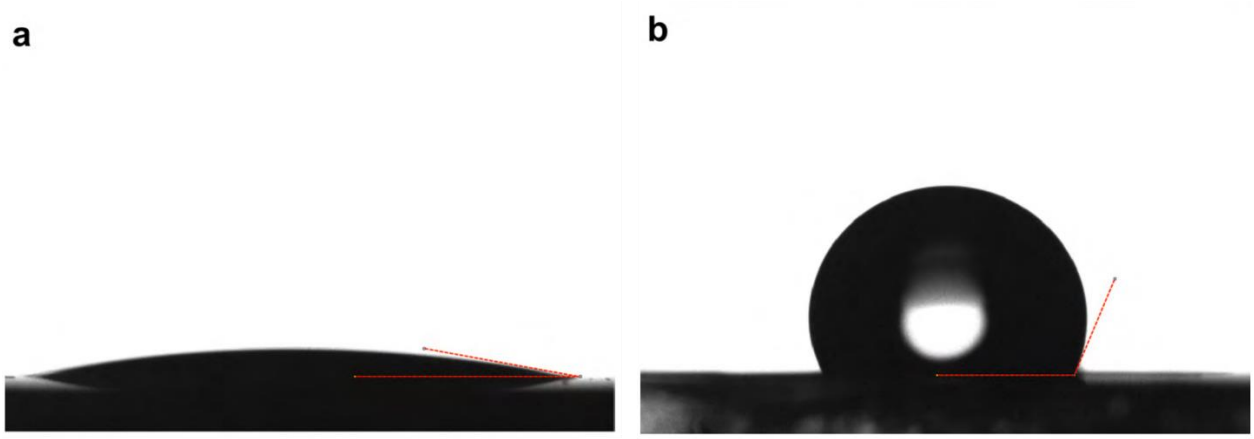

Figure 6.8. Water contact angle measurements of (a) an oxidized porous Si sample and (b) an all polymer porous photonic structure. Digital photograph of a 5-10 µL droplet on the two types of sensors were obtained using a contact angle goniometer (Model No. 190-F2, Ramé-hart instrument co). The average measured contact angle was (a) 11.6° and (b) 113.8°. Error in contact angle values ± 4°

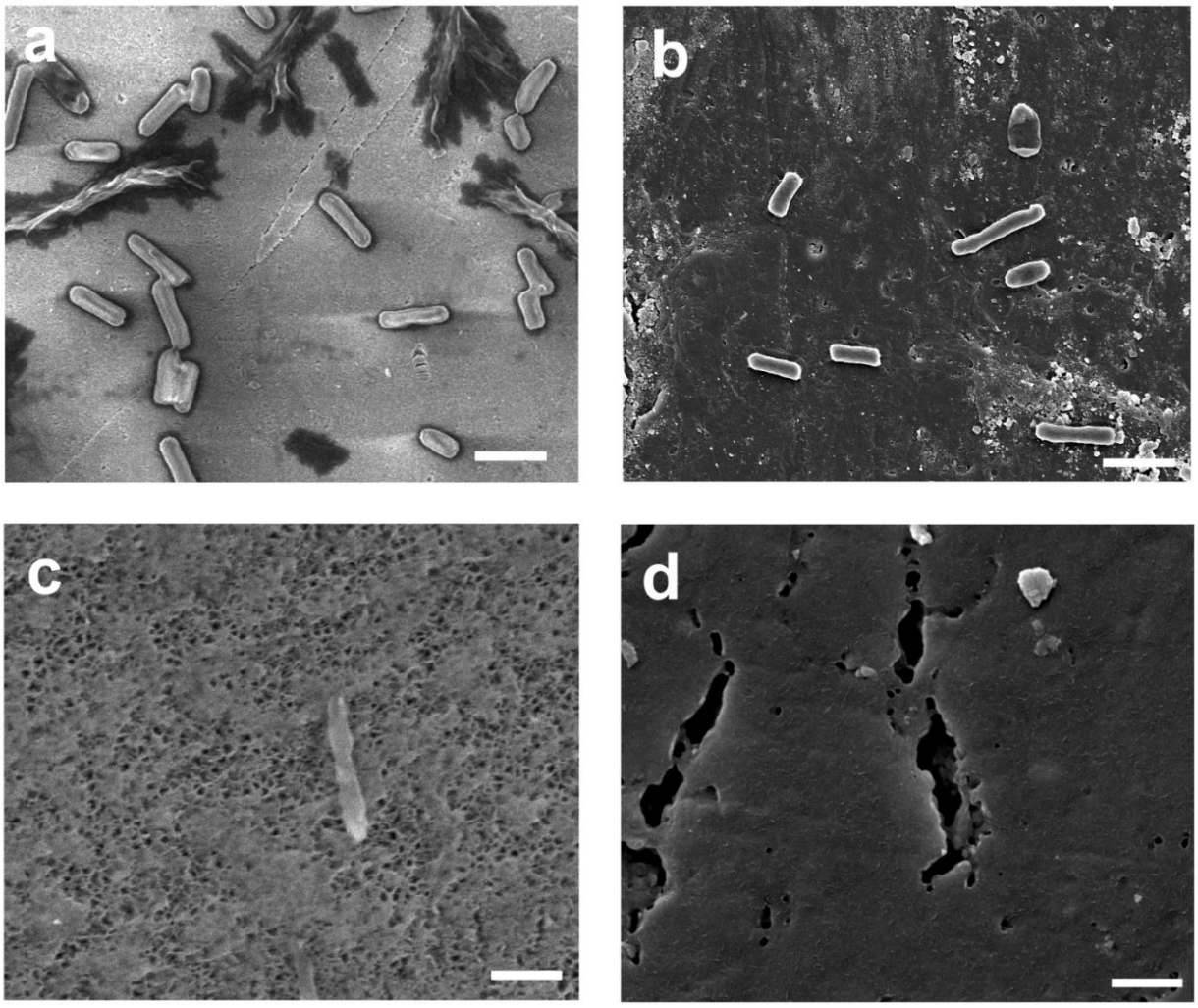

Figure 6.9 Electron microscope images of pSi-polymer composite (a, c) and all-polymer (b, d) IV connector hubs exposed to bacteria. Representative plan-view scanning electron microscope images of Escherichia coli adhered to the surface of the two different sensor types before (a, b) and after (c, d) sterilization with isopropyl alcohol. Sensors were incubated with 2 x 106 CFU. mL-1 of E. coli for images a and b. E. coli counts on both types of sensor displayed no detectable bacteria after swabbing with 70 % isopropyl alcohol-saturated tissue for 30 sec. Images c and d show some evidence of residual debris in the mesopores. Scale bar for a and b: 2 μm, Scale bar for c and d: 200 nm.

6.6 References

1. O'Grady, N. P.; Alexander, M.; Dellinger, E. P.; Gerberding, J. L.; Heard, S.; Maki, D.; Masur, H.; McCormick, R.; Mermel, L.; Pearson, M., Draft guideline for the prevention of intravascular catheter-related infections. *Centers for Disease Control: Atlanta, GA* **2001**.

2. Pronovost , P.; Needham , D.; Berenholtz , S.; Sinopoli , D.; Chu , H.; Cosgrove , S.; Sexton , B.; Hyzy , R.; Welsh , R.; Roth , G.; Bander , J.; Kepros , J.; Goeschel , C., An Intervention to Decrease Catheter-Related Bloodstream Infections in the ICU. *New England Journal of Medicine* **2006,** *355* (26), 2725-2732.

3. Zakhour, R.; Chaftari, A.-M.; Raad, I. I., Catheter-related infections in patients with haematological malignancies: novel preventive and therapeutic strategies. *The Lancet Infectious Diseases* **2016,** *16* (11), e241-e250.

4. Wenzel , R. P.; Edmond , M. B., Team-Based Prevention of Catheter-Related Infections. *New England Journal of Medicine* **2006,** *355* (26), 2781-2783.

5. Grissinger, M., Capping Intravenous Tubing and Disinfecting Intravenous Ports Reduce Risks of Infection. *P&T* **2011,** *36* (2), 62-76.

6. Schilling, S.; Doellman, D.; Hutchinson, N.; Jacobs, B. R., The impact of needleless connector device design on central venous catheter occlusion in children: a prospective, controlled trial. *Journal of Parenteral and Enteral Nutrition* **2006,** *30* (2), 85-90.

7. Niël-Weise, B. S.; Stijnen, T.; van den Broek, P. J., Should in-line filters be used in peripheral intravenous catheters to prevent infusion-related phlebitis? A systematic review of randomized controlled trials. *Anesthesia & Analgesia* **2010,** *110* (6), 1624-1629.

8. Chernecky, C.; Waller, J., Comparative evaluation of five needleless intravenous connectors. *J. Adv. Nurs.* **2011,** *67* (7), 1601-1613.

9. Menyhay, S. Z.; Maki, D. G., Preventing central venous catheter-associated bloodstream infections: Development of an antiseptic barrier cap for needleless connectors. *American Journal of Infection Control* **2008,** *36* (10), S174.e1-S174.e5.

10. Karadeniz, G.; Kutlu, N.; Tatlisumak, E.; Özbakkaloğlu, B., Nurses' knowledge regarding patients with intravenous catheters and phlebitis interventions. *J .Vasc. Nurs.* **2003,** *21* (2), 44-47.

11. Perucca, R.; Micek, J., Treatment of Infusion-Related Phlebitis Review and Nursing Protocol. *Journal of Infusion Nursing* **1993,** *16* (5), 282-286.

12. Maki, D. G.; Ringer, M., Risk factors for infusion-related phlebitis with small peripheral venous catheters: a randomized controlled trial. *Annals of internal medicine* **1991,** *114* (10), 845-854.

13. Grüne, F.; Schrappe, M.; Basten, J.; Wenchel, H.; Tual, E.; Stützer, H., Phlebitis rate and time kinetics of short peripheral intravenous catheters. *Infection* **2004,** *32* (1), 30-32.

14. Macklin, D., Phlebitis: A painful complication of peripheral IV catheterization that may be prevented. *AJN The American Journal of Nursing* **2003,** *103* (2), 55-60.

15. Frank, M. J.; Schaffner, W., Contaminated aqueous benzalkonium chloride - unnecessary hospital infection hazard. *JAMA-J. Am. Med. Assoc.* **1976,** *236* (21), 2418-2419.

16. O'Grady, N. P.; Alexander, M.; Burns, L. A.; Dellinger, E. P.; Garland, J.; Heard, S. O.; Lipsett, P. A.; Masur, H.; Mermel, L. A.; Pearson, M. L.; Raad, I. I.; Randolph, A. G.; Rupp, M. E.; Saint, S., Guidelines for the Prevention of Intravascular Catheter-related Infections. *Clin. Infect. Dis.* **2011,** *52* (9), e162-e193.

17. Curran, E. T.; Coia, J. E.; Gilmour, H.; McNamee, S.; Hood, J., Multi-centre research surveillance project to reduce infections/phlebitis associated with peripheral vascular catheters. *J. Hosp. Infect.* **2000,** *46* (3), 194-202.

18. wide, B. w., MaxPlus™ clear needleless connector in-service video. In *MaxPlus™ clear needleless connector*, 2016.

19. Moureau, N. L.; Flynn, J., Disinfection of needleless connector hubs: clinical evidence systematic review. *Nursing research and practice* **2015,** *doi:10.1155/2015/796762*.

20. Moureau, N. L.; Dawson, R. B., Keeping needleless connectors clean, part 1. *Nursing2015* **2010,** *40* (5), 18-19.

21. Moureau, N. L.; Dawson, R. B., Keeping needleless connectors clean, part 2. *Nursing2015* **2010,** *40* (6), 61-63.

22. Kaler, W.; Chinn, R., Successful disinfection of needleless access ports: a matter of time and friction. *J. Vasc. Access* **2007,** *12* (3), 140-142.

23. Sailor, M. J., *Porous Silicon in Practice: Preparation, Characterization, and Applications*. Wiley-VCH: Weinheim, Germany, 2012; p 249.

24. Lorenzo, E.; Oton, C. J.; Capuj, N. E.; Ghulinyan, M.; Navarro-Urrios, D.; Gaburro, Z.; Pavesi, L., Porous silicon-based rugate filters. *Appl. Optics* **2005,** *44* (26), 5415-5421.

25. Salem, M. S.; Sailor, M. J.; Sakka, T.; Ogata, Y. H., Electrochemical preparation of a rugate filter in silicon and its deviation from the ideal structure. *J. Appl. Phys.* **2007,** *101*, 063503.

26. Wang, J.; Lee, G. Y.; Kennard, R.; Barillaro, G.; Bisiewicz, R. H.; Cortez Lemus, N. A.; Cao, X. C.; Anglin, E. J.; Park, J. S.; Potocny, A.; Bernhard, D.; Li, J.; Sailor, M. J., Engineering the Properties of Polymer Photonic Crystals with Mesoporous Silicon Templates. *Chem. Mater.* **2017,** *29* (3), 1263-1272.

27. Li, Y. Y.; Cunin, F.; Link, J. R.; Gao, T.; Betts, R. E.; Reiver, S. H.; Chin, V.; Bhatia, S. N.; Sailor, M. J., Polymer Replicas of Photonic Porous Silicon For Sensing and Drug Delivery Applications. *Science* **2003,** *299* (5615), 2045-2047.

28. Li, Y. Y.; Kollengode, V. S.; Sailor, M. J., Porous silicon/polymer nanocomposite photonic crystals by microdroplet patterning. *Adv. Mater.* **2005,** *17* (10), 1249-1251.

29. Irani, Y. D.; Tian, Y.; Wang, M. J.; Klebe, S.; McInnes, S. J.; Voelcker, N. H.; Coffer, J. L.; Williams, K. A., A novel pressed porous silicon-polycaprolactone composite as a dual-purpose implant for the delivery of cells and drugs to the eye. *Experimental Eye Research* **2015,** *139*, 123-131.

30. Coffer, J. L., Porous silicon and related composites as functional tissue engineering scaffolds. In *Porous Silicon for Biomedical Applications*, Santos, H. A., Ed. 2014; pp 470-485.

31. Bonanno, L. M.; Segal, E., Nanostructured porous silicon-polymer-based hybrids: from biosensing to drug delivery. *Nanomedicine* **2011,** *6* (10), 1755-1770.

32. Segal, E.; Perelman, L. A.; Cunin, F.; Renzo, F. D.; Devoisselle, J.-M.; Li, Y. Y.; Sailor, M. J., Confinement of Thermoresponsive Hydrogels in Nanostructured Porous Silicon Dioxide Templates. *Adv. Funct. Mater.* **2007,** *17*, 1153–1162.

33. Pal, S.; Tak, Y. K.; Song, J. M., Does the antibacterial activity of silver nanoparticles depend on the shape of the nanoparticle? A study of the gram-negative bacterium Escherichia coli. *Applied and environmental microbiology* **2007,** *73* (6), 1712-1720.

34. Cai, Z.; Kwak, D. H.; Punihaole, D.; Hong, Z.; Velankar, S. S.; Liu, X.; Asher, S. A., A photonic crystal protein hydrogel sensor for Candida albicans. *ANGEWANDTE CHEMIE-INTERNATIONAL EDITION IN ENGLISH* **2015,** *54* (44), 13036-13040.

35. Wang, J.; Joo, J.; Kennard, R. M.; Lee, S.-W.; Sailor, M. J., Thermolytic Grafting of Polystyrene to Porous Silicon. *Chem. Mater.* **2016,** *28* (1), 79-89.

36. Berger, M. G.; Arens-Fischer, R.; Thoenissen, M.; Krueger, M.; Billat, S.; Lueth, H.; Hilbrich, S.; Theiss, W.; Grosse, P., Dielectric filters made of porous silicon: advanced performance by oxidation and new layer structures. *Thin Sol. Films* **1997,** *297* (1-2), 237-240.

37. Bovard, B. G., Rugate filter theory: an overview. *Appl. Optics* **1993,** *32* (28), 5427-5442.

38. Kieser, B.; Dieterle, F.; Gauglitz, G., Discrimination of methanol and ethanol vapors by the use of a single optical sensor with a microporous sensitive layer. *Analytical Chemistry* **2002,** *74* (18), 4781-4787.

39. Shin, K.; Obukhov, S.; Chen, J.-T.; Huh, J.; Hwang, Y.; Mok, S.; Dobriyal, P.; Thiyagarajan, P.; Russell, T. P., Enhanced mobility of confined polymers. *Nat. Mater.* **2007,** *6* (12), 961-965.

40. Pister, K. S. J. Etchants for use in micromachining of CMOS Microaccelerometers and microelectromechanical devices and method of making the same. U.S. Patent #5,726,480, 1998.

41. Anglin, E. J.; Schwartz, M. P.; Ng, V. P.; Perelman, L. A.; Sailor, M. J., Engineering the chemistry and nanostructure of porous silicon Fabry-Pérot films for loading and release of a steroid. *Langmuir* **2004,** *20* (25), 11264-11269.

42. Kelly, T. L.; Gao, T.; Sailor, M. J., Carbon and Carbon/Silicon Composites Templated in Microporous Silicon Rugate Filters for the Adsorption and Detection of Organic Vapors. *Adv. Mater.* **2011,** *23*, 1776–1781.

43. Pervak, V.; Tikhonravov, A. V.; Trubetskov, M. K.; Pistner, J.; Krausz, F.; Apolonski, A., Band filters: two-material technology versus rugate. *Appl. Optics* **2007,** *46* (8), 1190-1193.

44. Massad-Ivanir, N.; Segal, E., Porous silicon for bacteria detection. In *Porous Silicon for Biomedical Applications*, Santos, H. A., Ed. 2014; pp 286-303.

45. Mirsky, Y.; Nahor, A.; Edrei, E.; Massad-Ivanir, N.; Bonanno, L. M.; Segal, E.; Sa'ar, A., Optical biosensing of bacteria and cells using porous silicon based, photonic lamellar gratings. *Appl. Phys. Lett.* **2013,** *103* (3), 033702.

46. Wu, C.-C.; Alvarez, S. D.; Rang, C. U.; Chao, L.; Sailor, M. J., Label-free Optical Detection of Bacteria on a 1-D Photonic Crystal of Porous Silicon. *Proceedings of the SPIE - The International Society for Optical Engineering* **2009,** *7167*, 71670Z-71670Z-10.

47. Letant, S. E.; Hart, B. R.; Van Buuren, A. W.; Terminello, L. J., Functionalized silicon membranes for selective bio-organism capture. *Nat. Mater.* **2003,** *2* (6), 391-396.

48. Lorenzetti, M.; Dogša, I.; Stošicki, T.; Stopar, D.; Kalin, M.; Kobe, S.; Novak, S., The Influence of Surface Modification on Bacterial Adhesion to Titanium-Based Substrates. *ACS Applied Materials & Interfaces* **2015,** *7* (3), 1644-1651.

Appendix A.

Dual Loading of Dexamethasone and Daunorubicin

A.1 Introduction

Chronic intraocular diseases that lead to blindness such as age-related macular degeneration, glaucoma, and macular edema affects millions of Americans annually and projected to increase in the coming years[1-2]. While therapeutic targets such as vascular endothelial growth factor (VEGF) or the inflammation cascade are employed to manage disease progression, continual vision deterioration is inevitable due to the chronic nature of the disease and the complexity of the disease related pathways.

Combination therapy has been shown to be more effective than single drugs alone because, by targeting multiple components of the disease, synergistic effects can be achieved to limit disease progression and symptoms[3]. For example, in wet age-related macular degeneration, fat deposits under the retina leads to inflammation and neovascularization. Better patient outcomes have been observed by using a combination of VEGF inhibitors such as ranibizumab or bevacizumab reduce neovascularization and anti-inflammatory drugs.

Despite these exciting results, the combination therapy presents a pharmacokinetic challenge. Because the primary method of drug administration is by intraocular injection, the therapeutics should be injected simultaneously to prevent leakage and infection to the eye. Both drugs should maintain therapeutic dosage at similar time scales to prevent frequent injections. This is especially challenging because the chemical structure of these drugs has different physical forms of delivery to the eye. For example, Avastin is dispersed in buffer solution while dexamethasone (Retisert) is encapsulated in a PLGA rod. These forms are optimized to the drug and cannot be readily incorporated into a single formulation.

To address these challenges, we loaded both daunorubicin (hydrophilic, anti-proliferative) and dexamethasone (hydrophobic, steroid – anti-inflammatory) into porous silicon carriers via covalent grafting. Porous silicon was selected due to its versatile chemical nature to host different types of molecules ranging from proteins to hydrophobic small molecules. We employed dual loading of the two drugs within a single formulation (instead of cocktail of two formulation) to prevent uneven injection of one drug type and ensure uniform localization of both drugs in the eye. We investigated the role of drug grafting ratio on the release kinetics of both drugs and degradation rate of the particle.

A.2 Materials

Single crystalline silicon wafers (resistivity <0.0011 Ω·cm, 6 in, highly boron doped, (100)) were purchased from siltronix. 2,2-dimethoxy-1,6-diaza-2-silacyclooctane was from Gelest and anhydrous dimethylformamide (DMF), (3-aminopropyl)triethoxysilane and 3-(ethoxydimethylsilyl)propylamine (or aminopropyl dimethyl ethoxy silane, APDMES), succinic anhydride, N-(3-dimethylaminopropyl)-N-ethylcarbodiimide hydrochloride (EDC), N,N-diisopropylcarbodiimide (DIC) and 4-(dimethylamino)pyridine was from Sigma Aldrich. N-hydroxysulfosuccinimide (sulfo-NHS) and phosphate buffered saline (pH 7.4) was purchased from Thermo Fisher Scientific. Dexamethasone was purchased from Tokyo Chemical Industry Co. and daunorubicin from TSZ Chemicals. Dimethyl sulfoxide (DMSO) and dichloromethane (DCM) was purchased from Fisher Scientific.

A.3 Experimental Methods

A.3.1 Synthesis of Porous Silicon Particles

Porous silicon particles were synthesized by full wafer (6 in, 60 cm^2 etching area) electrochemical etching of single crystalline Si wafers (Siltronix) in ethanolic HF (1:1 48% HF to

EtOH) and using three repeats of current density 70 mA/cm^2 for 400 s, 167 mA/cm^2 for 2 s and 0 mA/cm^2 (etch stop) for 2s. Following the etch, the porous layer was removed from the bulk wafer by an electopolishing step of 4.17 mA/cm^2 for 550 s. The films were placed in a glass vial and ultrasonicated for 1-3 hr and, based on settling time, the large and small particles were removed. The particle size ranged from 20-60 μm. Following sonication, the particles were oxidized in a muffle furnace (Thermo Scientific) at 800°C for 1 hr to fully oxidize the particles.

A.3.2 Functionalization with Primary Amines

Prior to grafting, the particles are soaked in Tris buffered saline (TBS, Fisher Scientific) at pH 7.4 for 2 hours at a concentration of 10 mg/mL to activate the OH groups on the surface. The particles were washed with MilliQ water three times (10 mg/mL) and dried in a vacuum desiccator. Particles were functionalized with aminopropyl triethoxy silane (APTES) by soaking in 10 vol% silane in ethanol. The samples were heated in a sand bath at 40-45°C for 24 hours and gently stirred. After amine functionalization, the particles were washed with ethanol (10 mg/mL) three times and dried in a desiccator.

A.3.3 Surface Conversion of Amine to Carboxylate

To convert the surface amine groups to carboxylic acid, the particles (10 mg/mL) were soaked in 50 mg/mL succinic anhydride in anhydrous dimethylformamide (DMF) for 24 hours at 70°C with gentle stirring. Then, the particles were washed three times in DMF, two times in water at 10 mg/mL and dried in a vacuum desiccator.

A.3.4 Covalent grafting of Daunorubicin

To activate the carboxyl groups, the particles were soaked (10 mg/mL) in a solution containing 120 mM of (dimethylaminopropyl)-ethylcarbodiimide hydrochloride (EDC) and 120 mM of hydroxysulfosuccinimide (sulfo-NHS) in PBS with 10 vol% DMSO. The particle solution

was agitated on a rotating wheel for 20 minutes. Daunorubicin (DNR, 10 mg/mL in MilliQ water) was then added to the solution so that the mass ratio of particle to DNR is 10:2. The solution was again agitated on a rotating wheel in the dark for 24 hours, washed three times with MilliQ water (10 mg/mL) and dried in a desiccator.

A.3.5 Covalent grafting of Dexamethasone

Particles were soaked (10 mg/mL) in a solution containing diisopropylcarbodiimide (DIC) and (dimethylamino)pyridine (DMAP) in DCM. Dexamethasone (DEX) dispersed in DCM (20 mg/mL) was added to the solution. Three different mass ratios of DEX to pSi was tested: 3:10, 4:10 and 6:10. The concentration of DIC/DMAP with respect to mass of DEX was 12 mM DIC: 4 mM DMAP: 2 mg of DEX. The particle solution was stirred for 24 hours, washed twice in DCM (10 mg/mL), three times in EtOH (10 mg/mL) and dried in a vacuum desiccator.

A.3.6 Release Experiment and HPLC Sample Analysis

Particles (3 mg) were soaked in 1.5 mL of phosphate buffer at pH 7.4 and incubated at 37°C. Additionally The buffer was replenished daily with the same volume for analysis. The concentration of both DNR and DEX was performed by HPLC-UV Vis. For each sample 0.5-1 mL was placed into glass HPLC sampling vials (2 mL - 9 mm clear glass screw thread vials, Thermo Fisher). The samples were then analyzed with an UltiMate™ 3000 Rapid Quaternary System UHPLC (Thermo Fisher) equipped with a C18 reverse phase column (silica 5 µm particle, 150 mm, max pressure: 4500 psi, Thermo Fisher) and using a gradient flow between water and methanol (with 0.1 vol% triflouroacetic acid). The DEX and DNR concentration in each sample was determined by comparison to a standard calibration curve (freshly prepared for each run).

A.4 Results and Discussion

While previous work has demonstrated covalent loading with dexamethasone[4-5] (DEX) and daunorubicin[6-7] (DNR)within porous silicon, this work seeks to combine the two therapeutics into a single particle formulation. Covalent loading was selected to prevent burst release of both molecules from the particles. Preliminary testing revealed low release concentrations (below the therapeutic window) of DNR[8] despite having comparable loading as single loaded formulations.[6-7] Additionally, the colors appears to have an intense red color at later time points and indicates the presence unreleased DNR. We hypothesized that DEX could be preventing the release of DNR because the hydrophobicity of DEX may inhibit wetting of the silicon surface and prevent the particle from degrading and release DNR.

To test this hypothesis and to encourage the release of DNR, we tested particles that were functionalized using three different concentrations of DEX after DNR grafting. Briefly, porous silicon particles were synthesized by electrochemical etching of single crystalline wafers to create films with high porosity.[7] The porous film was removed by an electropolishing step and the films were broken up into particles between 10-100 μm by ultrasonication. Particles were fully oxidized in a muffle furnace at 800°C for 1 hr to improve the stability of the particles.

The chemistries employed for the grafting process is found in Figure 2.4.1. To activate the OH groups, particles were soaked in Tris buffered saline (TBS) for 2 hrs. After thorough washing in water and drying, particles were functionalized with aminopropyl trimethoxy silane to populate the silicon surface with primary amine groups. The primary amine groups were converted to carboxyl groups using succinic anhydride. EDC/NHS chemistries were performed to graft DNR to the particles and DIC/DMAP chemistries for DEX. The mass ratio of pSi:DNR:DEX were the following: 10:2:3, 10:2:4, 10:2:6. Both molecules were grafted to the carboxyl groups. TGA

analysis revealed the relative grafting masses of each molecule: aminopropyl silane ~7 wt%; succinic anhydride ~7 wt%. The mass loading of DNR/DEX was ~15 wt% for the lowest mass ratio of DEX and further analysis is required to quantify the higher concentrations. It is difficult to distinguish DEX/DNR on TGA because DNR was lost during the DEX grafting, which can be visualized by the red color of the supernatant. This is presumably because some fractions of DNR may graft at the OH site and form ester bonds rather the amine site and may exchange with DEX. It is also possible that some DNR was adsorption loaded but was not removed despite the washing steps or the DMAP that was employed as a catalyst for DEX loading caused degradation that resulted in DNR leaching during the DEX grafting process.

To test the release kinetics, 3 mg of particles for each particle group were soaked in 1.5 mL of phosphate buffered saline (PBS) and incubated at 37°C. The release medium was replenished daily and the concentration was analyzed using HPLC-UV-Vis. The release curve for DEX and DNR is shown in Figure 2.4.2. The pharmacokinetics of DEX followed a typical two component model with initial burst release followed by slow steady state release. Unlike DEX, all formulations of DNR followed a 1st order profile, as shown by the near linear curve. The lowest ratio of DEX loading (3:10 DEX to pSi ratio) maintained the highest DNR concentrations followed by 4:10 and 6:10 DEX:pSi. However, more studies and repeats are required to demonstrate this dependence. Compared to previous studies, we were able to elevate DNR levels to higher concentrations and maintain >20 ng/mL (therapeutic level) for ~25-35 days while retaining therapeutic levels of DEX.

Appendix A, in part is currently being prepared for submission for publication of the material. Wang, J,. Ying, X., Huffman, K., Cheng, L., Freeman, W.R. and Sailor, M.J. Controlling

the Release of Dual-Drug Loaded Porous Silicon for Ophthalmic Combination Therapy. The dissertation/thesis author was the primary investigator and author of this material.

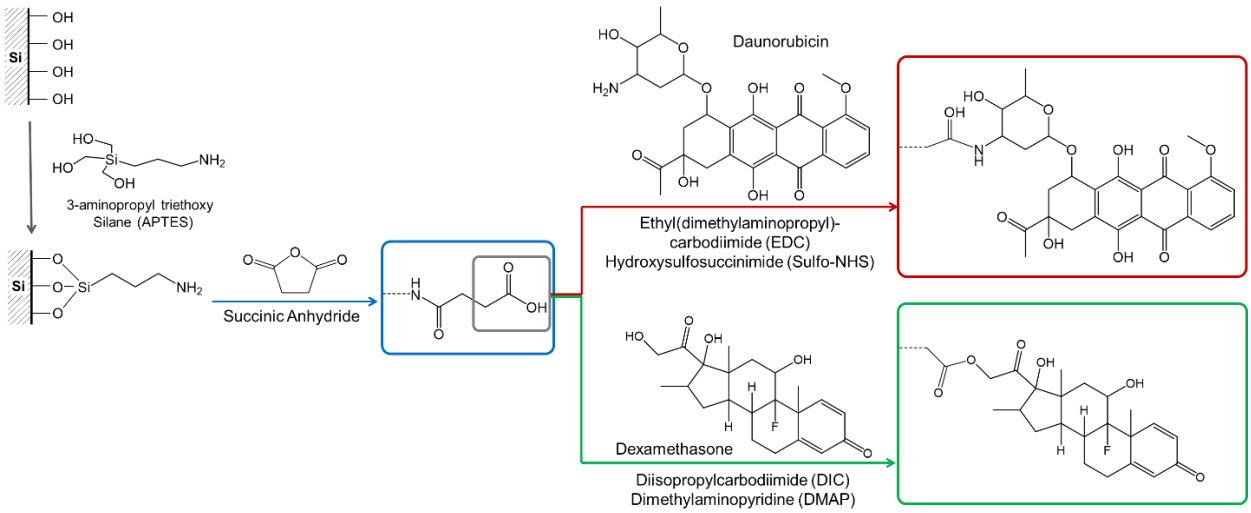

Figure A.1. Schematic of the functionalization steps employed for dual loading of dexamethasone and daunorubicin. Daunorubicin was grafted prior to dexamethasone and the mass ratio of silicon to the added DNR and DEX is 10:2:4, 10:2:6, and 10:2:8.

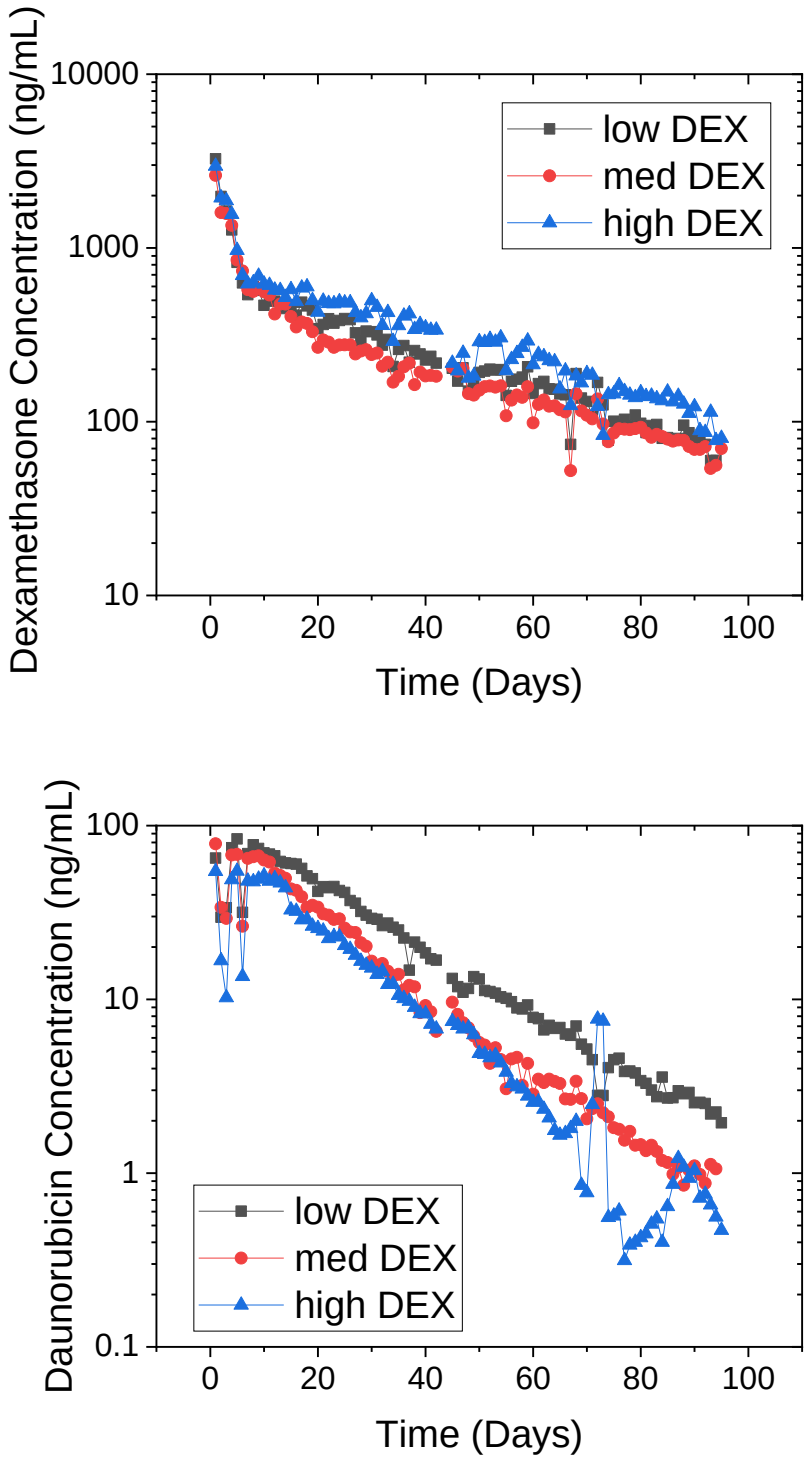

Figure A.2. The concentration of dexamethasone (top) and daunorubicin (bottom) from the dual loaded particles in vitro.

A.5 References

1. Prevalence of Adult Vision Impairment and Age-Related Eye Diseases in America. (accessed Feb 9th).

2. Group*, T. E. D. P. R., Causes and Prevalence of Visual Impairment Among Adults in the United StatesCauses and Prevalence of Visual Impairment Among Adults in the United States. *Archives of Ophthalmology* **2004,** *122* (4), 477-485.

3. Towler, H. M. A.; Whiting, P. H.; Forrester, J. V., Combination low dose Cyclosporin a and steroid therapy in chronic intraocular inflammation. *Eye* **1990,** *4*, 514.

4. Hou, H.; Wang, C.; Nan, K.; Freeman, W. R.; Sailor, M. J.; Cheng, L., Controlled Release of Dexamethasone From an Intravitreal Delivery System Using Porous Silicon DioxideControlled Release of Intravitreal Dexamethasone. *Investigative Ophthalmology & Visual Science* **2016,** *57* (2), 557-566.

5. Wang, C.; Hou, H.; Nan, K.; Sailor, M. J.; Freeman, W. R.; Cheng, L., Intravitreal controlled release of dexamethasone from engineered microparticles of porous silicon dioxide. *Experimental eye research* **2014,** *129*, 74-82.

6. Chhablani, J.; Nieto, A.; Hou, H.; Wu, E. C.; Freeman, W. R.; Sailor, M. J.; Cheng, L., Oxidized Porous Silicon Particles Covalently Grafted with Daunorubicin as a Sustained Intraocular Drug Delivery SystemOxidized Porous Silicon for Delivery of Daunorubicin. *Investigative Ophthalmology & Visual Science* **2013,** *54* (2), 1268-1279.

7. Hou, H.; Nieto, A.; Ma, F.; Freeman, W. R.; Sailor, M. J.; Cheng, L., Tunable sustained intravitreal drug delivery system for daunorubicin using oxidized porous silicon. *J Control Release* **2014,** *178*, 46-54.

8. Warther, D.; Xiao, Y.; Li, F.; Wang, Y.; Huffman, K.; Freeman, W. R.; Sailor, M.; Cheng, L., Porous silicon based intravitreal platform for dual-drug loading and controlled release towards synergistic therapy. *Drug Delivery* **2018,** *25* (1), 1537-1545.